Glacial-interglacial response of the global overturning circulation to southern forcing; carbon cycle applications

University of Exeter

College of Life and Environmental Science

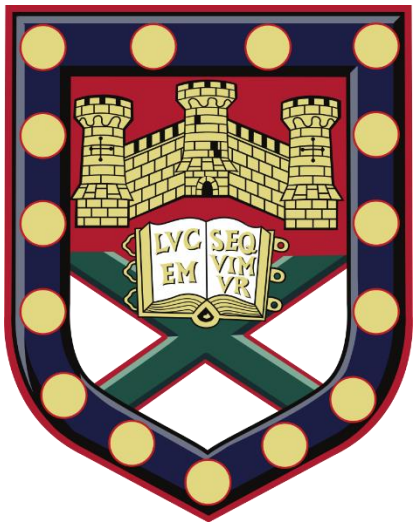

Jonathan Andrew Baker

A thesis submitted for the degree of

Doctor of Philosophy in Geography

September 2019

Glacial-interglacial response of the global overturning circulation to southern forcing; carbon cycle applications

Submitted by Jonathan Andrew Baker to the University of Exeter

as a thesis for the degree of

Doctor of Philosophy in Geography in September 2019

I certify that all material in this thesis which is not my own work has been identified and that no material has previously been submitted and approved for the award of a degree by this or any other University.

Signature: 

ABSTRACT

Over the past one million years, atmospheric CO_2 and Antarctic temperatures covaried over several glacial cycles, with the meridional overturning circulation (MOC) as forced by the climate over the Southern Ocean implicated as a causal factor. This thesis aims to improve our understanding of the mechanisms responsible for glacial-interglacial variations in the MOC and atmospheric CO_2, and also the pathways and mechanisms driving the present-day, glacial and possible future state circulations. Both a semi-analytical ocean model and an idealised general circulation model (GCM) are used.

An idealised two-basin and single-basin GCM connected by a southern circumpolar channel shows the MOC strength and structure is dependent on the Southern Ocean buoyancy and zonal wind forcing, and the ocean's vertical diffusivity. The sensitivity of the MOC to wind and diffusivity perturbations is dependent on the buoyancy forcing, due to the MOC pathways varying with buoyancy forcing. The North Atlantic Deep Water (NADW) cell in the Atlantic basin is driven primarily by the Southern Ocean winds in a glacial state but by Pacific diffusive-driven upwelling in a future 'warm' state.

The single-basin model is shown to have a number of drawbacks, and is unable to simulate a realistic NADW cell strength under realistic wind forcing and vertical diffusivity, regardless of the buoyancy forcing imposed. In contrast, the two-basin model simulates a realistic NADW cell, with a connection between the NADW cell in the Atlantic basin and the Pacific Deep Water (PDW) cell in the Pacific basin under present-day buoyancy forcings.

A transition of the MOC to a glacial state with a weaker, shoaled NADW cell isolated from the Pacific basin is obtained in response to enhanced Southern Ocean sea-ice formation and thus a change in buoyancy forcing. However, reduced Southern Ocean wind forcing leads to only a slight weakening and no shoaling of the NADW cell and thus a glacial state MOC is not obtained.

Changes in the buoyancy forcing between a future warm state and a cool, glacial state lead to a reduction in atmospheric CO_2 of ~30 ppm in the two-basin model when temperature solubility effects are ignored. This is smaller than the ~100 ppm glacial-interglacial change in CO_2, although the model is likely to be highly dependent on the biological parameters, and the effect of sea-ice on biological production and air-sea CO_2 exchange.

A semi-analytical ocean model with a coupled energy-balance model is also used to investigate the glacial cycles. The important role played by climate feedbacks in the MOC transition is apparent, with changes in Southern Ocean sea-ice formation playing a potentially critical role.

Acknowledgements

I would first like to thank my supervisors, Andrew Watson and Geoffrey Vallis for their huge contribution to my research career development and the success of this PhD, through their guidance, enthusiasm and support. They have played a key role throughout the project and I have thoroughly enjoyed working with them, absorbing their expertise and being part of some very interesting discussions. I am very grateful to have been given the opportunity to work with them both and appreciate the trust they have shown towards me.

I would also like to thank Jonathan Lauderdale for giving his time to help in the setup of the MITgcm, particularly the biogeochemistry component of the model, and Tobia Tudino for the initial help in using the supercomputer. I thank my PhD examiners, Andrea Burke (external) and Paul Halloran (internal) for the interesting and useful discussions during my viva and their constructive feedback which has helped to improve this thesis.

Thanks to my lecturers at the University of Reading and Oklahoma for their teaching and support during my degree in the very friendly and stimulating environment of the Meteorology department. In particular, I would like to thank Keith Shine under who I had my first taste of research.

I would like to thank my family and friends, particularly my Mum and Dad for their motivation and interest in my work, and support throughout school and university. My Dad inspired me to become interested in climate change and has motivated me to follow my dream of a career in research.

Thank-you to my friends for many fun and memorable times which has played a large part in my happiness at Exeter. I have had a fantastic four years, while developing as a researcher and I have all of the pre-mentioned to thank for the journey.

Contents

Abstract iii

Acknowledgments iv

List of Tables xi

1. Introduction **1**

1.1. Evidence and Milankovitch Cycles 2

1.1.1. Proxy data 2

1.1.2. Milankovitch Cycles 4

1.2. The Meridional Overturning Circulation (MOC) 8

1.2.1. Theory of the MOC 8

1.2.2. The Glacial MOC 12

1.2.3. Recent idealised modelling studies of the MOC 14

1.3. Glacial-Interglacial processes 15

1.3.1. Terrestrial contribution 15

1.3.2. Oceanic contribution 16

1.3.3. The Southern Ocean's role 19

1.3.4. Oceanic mechanisms: Physical processes 19

1.3.4.1. SST and salinity 20

1.3.4.2. Ocean Circulation 20

1.3.4.3. Ocean stratification 21

1.3.4.4. Sea-ice cover variations 22

1.3.5. Oceanic mechanisms: Chemical processes 23

1.3.5.1. Calcium Carbonate ($CaCO_3$) compensation 23

1.3.6. Oceanic mechanisms: Biological processes- Soft-tissue pump 24

1.3.6.1. Low-latitude mechanisms 25

1.3.6.2. High-latitude mechanisms 26

1.3.7. Conclusions.....29

2. MITgcm ocean-sea-ice-biogeochemistry model configuration 30

2.1. Equations solved.....31

2.2. Model Grid.....34

2.3. Momentum Equations.....37

2.4. Free surface boundary condition.....37

2.5. Active tracer equations 39

2.5.1. Diffusivity profile 40

2.6. Surface Forcing.....42

2.7. Model Geometry 45

2.8. Meridional overturning streamfunction 47

2.8.1. Eulerian-mean overturning streamfunction 48

2.8.2. Eddy-induced overturning streamfunction 48

2.9. Gridding and Interpolation for plotting variables 50

2.10. Physical model parameters 54

2.11. Model Parameterisations.....55

2.11.1. Convection 55

2.11.2. Eddy Parameterisation 55

2.12. Model Data Inputs.....56

2.12.1. Model datasets 56

2.12.2. Conversion to model grid inputs.....57

2.12.3. Bulk Formulae 58
2.13. Sea-ice model 61
2.14. Ocean biogeochemistry model 64
2.14.1. Passive tracer equations 64
2.14.2. Parameterisation of biological production 67
2.14.3. Sources and sinks of passive tracers 68
2.14.3.1. Dissolved Organic Phosphorus and Inorganic Phosphate 68
2.14.3.2. Dissolved Inorganic Carbon and Total Alkalinity 71
2.14.3.3. Oxygen 76
2.14.3.4. Atmospheric box 77
2.15. Passive dye tracer model setup 78

3. Meridional Overturning Circulation in a multi-basin model Part I: Dependence on Southern Ocean buoyancy forcing 79
3.0. Abstract 82
3.1. Introduction 83
3.2. Model Setup and Experiments 87
3.3. General Methodology and Basic Simulation 90
a) Control experiments and MOC upwelling 90
b) Connections between the upper and lower cells of the MOC 92
I) Qualitative considerations 92
II) Quantitative determination of MOC pathways and overturning components 93
3.4. Analysis of Buoyancy Flux Experiments 96
a) Future Circulation 96

b) Present-day Circulation 98
c) Glacial Circulation 100
3.5. Summary and Conclusions 101
3.6. Appendix 106
3.7. Further analysis of MOC variations 117
3.7.1. Deep stratification and surface density 117
3.7.2. MOC components and cell interface depths 121

4. Meridional Overturning Circulation in a multi-basin model Part II: Dependence on Southern Ocean wind forcing and vertical diffusivity 125
4.0. Abstract 126
4.1. Introduction 127
4.2. Model Setup and Experiments 131
4.3. Control simulations 134
4.4. Wind perturbation Experiments 137
i) 'Warm' state 138
ii) Present-day state 145
iii) Glacial state 148
iv) Summary and Comparisons 150
v) Zero wind experiments: A more realistic change in sea-ice 153
4.5. Pacific vertical diffusivity perturbation Experiments 154
i) 'Warm' state 156
ii) Present-day state 159
iii) Glacial state 162
iv) Summary and Comparisons 164

v) MOC driving mechanisms....166
4.6. Conclusions....167
4.7. Further analysis of MOC variations....173
4.7.1. Cell interface depths....173
4.7.2. Deep stratification and surface density....175

5. Single-basin model and tracer release experiments....179
5.1. Questions....180
5.2. Single-basin model buoyancy forcing experiments....180
5.3. Causes of differences between single and multi-basin models....183
5.3.1. Variable geometric configurations of a single-basin model....184
5.3.1.1. Wide single-basin model....187
5.3.1.2. Wide channel single-basin model....189
5.3.2. Single-basin model wind forcing and vertical diffusivity experiments....189
5.3.2.1. Wind forcing perturbations....190
5.3.2.2. Vertical diffusivity perturbations....191
5.4. Tracer release experiments....192
5.5. Conclusions....200

6. Ocean biogeochemistry carbon cycle modelling....203
6.1. Comparison with the original setup....204
6.2. Present-day control experiment....205
6.2.1. DIC, PO_4 and O_2 distributions....205
6.2.2. Preformed and regenerated PO_4....210
6.2.3. Air-sea CO_2 flux....211
6.3. Buoyancy flux perturbation experiments....212

6.2.1. Atmospheric CO_2 variations 212

6.2.2. Glacial state tracer variations 213

6.4. Single-basin model experiments 215

6.5. Conclusions 215

7. Semi-Analytical Model of the Bottom and Upper Cells of the Atlantic (SAMBUCA ocean model) **216**

7.1. Introduction 216

7.2. Energy Balance Model 218

7.3. Coupling of the EBM to SAMBUCA 219

7.3.1. Southern channel 221

7.3.2. Main ocean basin 222

7.3.3. Northern convective region 222

7.4. Further modifications 223

7.5. Results 224

7.5.1. Variation in orbital paramters: obliquity and eccentricity 225

7.5.2. Ice-albedo effect: Northern Hemisphere ice-sheets 230

7.5.3. Changes in Southern Ocean sea-ice formation 232

7.6. Conclusions 235

8. Conclusions **237**

8.1. Summary 237

8.2. Further work 239

Bibliography 241

List of Tables

2.1. Vertical grid of the MITgcm.....36

2.2. Vertical diffusivity profile parameters.....41

2.3. Single- and two-basin model domains.....46

2.4. Physical model parameters 54

2.5. GM-Redi scheme parameters.....55

2.6. Sea-ice model paramteres 63

2.7. Biogeochemistry model paramteres.....66

Chapter 1

Introduction

Over the last two and a half million years (Myrs) the Earth has undergone cyclic variations in its climate, from warm interglacial to cold glacial states, periods often referred to as ice ages. The glacial periods are associated with significantly lower atmospheric carbon dioxide (CO_2) levels than the interglacial periods and the vast expansion of the Northern Hemisphere continental ice sheets and glaciers. Despite the importance of this phenomenon in the climate of Earth's recent past, the mechanisms and climate feedbacks responsible for these large shifts in atmospheric CO_2 and global climate remain uncertain, although numerous theories have been postulated and a great deal of progress has been made.

The ocean is believed to play a vital role in these climatic variations through changes in global ocean carbon storage. The focus of this thesis is on the potential role played by ocean circulation changes during glacial cycles through the implementation of two ocean models. This thesis aims to improve our understanding of the sensitivity of the ocean's large scale meridional overturning circulation (MOC) and consequently atmospheric CO_2 to variations in model forcings and parameters. This enables the mechanisms responsible for ocean circulation changes to be determined and also develops our understanding of the pathways taken by the MOC in various climate states including both a cooler, glacial state and a future warmer state.

This section provides a literature review on glacial cycles and the MOC which provides a broad background and motivates our study before more detailed descriptions of the previous literature (particularly the MOC) is provided in the Results chapters.

This Introduction section is structured as follows: (1.1) the proxy climate record and Milankovitch cycle theory for the glacial cycles, (1.2) the theory of the present-day ocean meridional overturning circulation (MOC) and its glacial-interglacial variation, and (1.3) the major hypothesised glacial cycle mechanisms and their estimated contribution to the glacial-interglacial variation in atmospheric CO_2.

1.1. Glacial cycle evidence and the Milankovitch Cycles

1.1.1. Proxy data

The fluctuations in global climate during glacial-interglacial cycles have been reconstructed from the analysis of ocean floor sediments and trapped air bubbles in the Antarctic and Greenland ice-cores. Ocean floor sediment cores provide indirect records of the temperature and global ice volume over the last 65 million years but at lower resolution than ice-cores (Lisiecki and Raymo [2005]). Antarctic ice-cores provide direct, high resolution records of both Antarctic temperature, and atmospheric greenhouse gas concentrations (i.e. CO_2, methane and nitrous oxide) over the past 750,000 years (the last eight glacial cycles). The Vostok (Petit et al. [1999]) and EPICA (European Project for Ice Coring in Antarctica) Dome C (EPICA community members [2004]) ice-cores provide particularly important records due to the long timescales they cover.

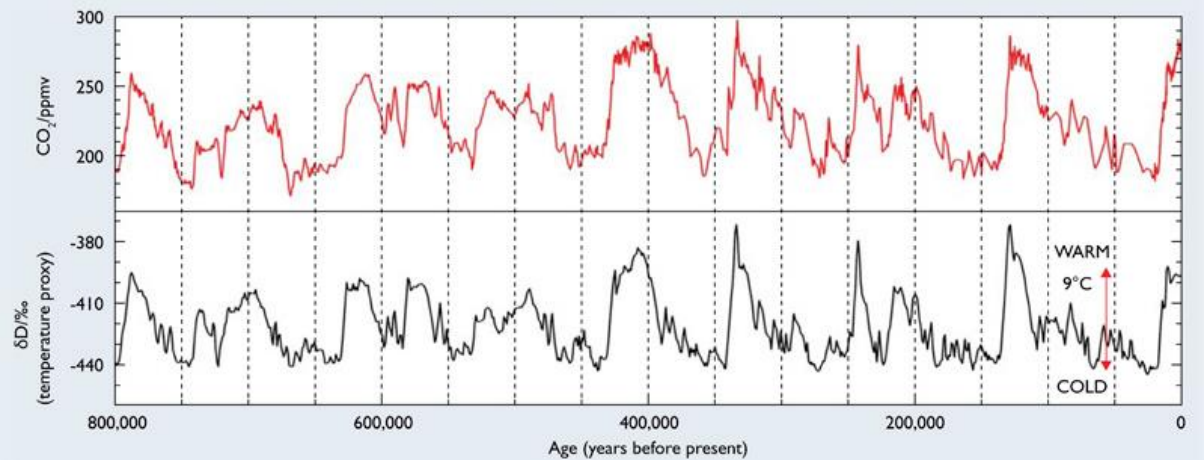

Fig 1.1: Atmospheric CO_2 and Antarctic temperature inferred from the EPICA Dome C ice core record (figure from British Antarctic Survey, Jouzel et al. [2007], Lüthi et al. [2008]).

Atmospheric CO_2 increased from 180 to 280-300 parts per million by volume (ppmv) (which we herein refer to as parts per million (ppm)) during the last four glacial-interglacial transitions (see Fig 1.1), while surface temperatures in the Antarctic covaried by approximately 12°C (Petit et al. [1999]). The global average change in surface temperature is uncertain although most model-based estimates of the temperature variation fall between 3°C and 6°C (Masson-Delmotte et al. [2006]).

The Greenland ice-core record is far shorter than Antarctica's, only extending over the last 120,000 years (120-kyrs) (the last glacial cycle) (Anderson et al. [2004]). It suggests that the Northern Hemisphere climate prior to the Holocene (the current interglacial period which began approximately 11.5-kyrs before present (BP)) was highly unstable, with rapid decadal transitions in climate referred to as Dansgaard-Oeschger events (Bond et al. [1993], Dansgaard et al. [1993]). The Dansgaard-Oeschger events occur on millennial timescales, far shorter than the glacial cycle multiple millennial timescale with 125 Dansgaard-Oeschger events occurring during the last glacial cycle (Grootes et al. [1993]; Li et al. [2019]).

In contrast, the high correlation between Antarctic temperatures and atmospheric CO_2 during the glacial cycles suggests the mechanism responsible for these changes originates in the Southern Ocean.

1.1.2. Milankovitch Cycles

The glacial cycle variations in Earth's climate are believed to be triggered by variations in Earth's orbital characteristics, as described by the Milankovitch theory (Milankovitch [1941], Imbrie and Imbrie [1980]) and calculated by Berger [1978]. The solar irradiance incident at the top of Earth's atmosphere at a given latitude is primarily dependent on three orbital parameters: the Earth's eccentricity, obliquity and precession. Variations in these parameters over long time periods, known as Milankovitch cycles (see Fig 1.2), lead to changes in the intensity and latitudinal distribution of solar irradiance throughout the year (McGehee and Lehman [2012]). These changes in solar radiation alone cannot explain the large changes in global climate during glacial cycles. The processes and climate feedbacks in the Earth system which amplify the insolation signal remain uncertain, although it is believed the growth of Northern Hemisphere ice-sheets (Peltier [2004]) and the greenhouse feedback (a result of a decrease in atmospheric concentrations of global warming inducing greenhouse gases including CO_2 and methane) play a dominant role. One of the aims of this thesis is to improve our understanding of the role played by the ocean, particularly changes in ocean circulation in contributing to the greenhouse feedback.

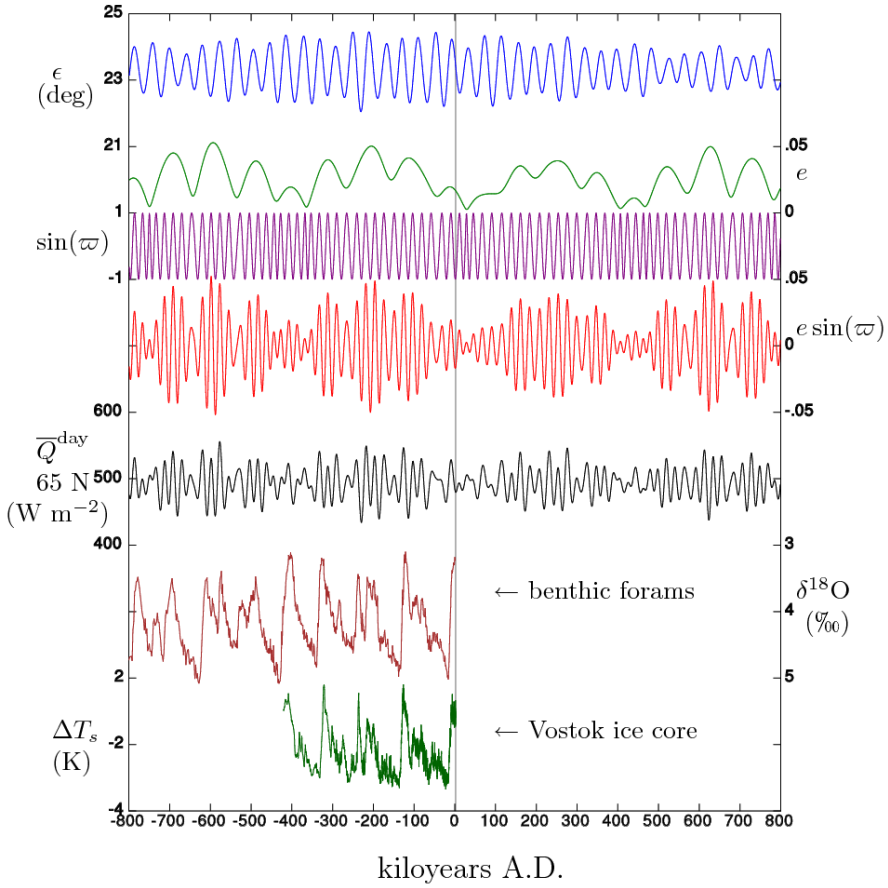

Fig 1.2: Plot of the Milankovitch Cycles over the last 800-kyrs. Variables from top to bottom are: Earth's obliquity, eccentricity, sine of the longitude of perihelion, the precession index, daily averaged solar insolation at 65°N on the day of the summer solstice, $\delta^{18}O$ from ocean sediments and Antarctic temperature from ice cores (Plot created by Incredio: Wikipedia Milankovitch Cycles).

During the late Pliocene and early Pleistocene (between 3-Myrs to 800-kyrs BP), the glacial cycles had a ~40-kyr periodicity and were therefore modulated by the 41-kyr cycle in Earth's obliquity (see Fig 1.2) or axial tilt (Raymo and Nisancioglu [2003]; Shackleton and Hall [1984]). About 800-kyrs BP, the glacial cycle periodiciy transitioned from a 40-kyr to a 100-kyr timescale, which corresponds to the variation in the eccentricity of Earth's orbit around the Sun (Pisias and Moore [1981]; Huybers [2006]). The eccentricity is important due to its modulation of the amplitude of the 23-kyr precession of the equinoxes (Imbrie and Imbrie [1980]) as shown in Fig 1.2.

The obliquity and (eccentricity modulated) precession are believed to control the glacial cycle periodicity during the early and late Pleistocene respectively since they control the intensity of summer insolation at high northern latitudes (see Fig 1.2). When these orbital parameters lead to a decrease in the summer insolation at high northern latitudes, the Northern Hemisphere continental ice sheets can remain throughout the year without melting. The presence of ice-sheets leads to a global cooling by increasing Earth's albedo. Ice-sheets could thus provide the initial positive climate feedback during glacial cycles in response to Milankovitch Cycle changes in insolation. The variations in solar irradiance at high northern latitudes during the late Pleistocene have been shown to be highly correlated with global ice volume reconstructed from the oxygen isotope record in deep-sea sediment cores. This supports the Milankovitch hypothesis for the ice ages (Hays et al. [1976]) and suggests ice-sheets play an important role.

However, as described previously the atmospheric CO_2 greenhouse feedback also played a crucial role in the glacial cycle climatic change as recorded in ice cores. The increase in CO_2 during the transition to an interglacial state may in fact have occurred prior to changes in sea-ice volume and thus may have initialised the amplification of the changes in insolation on the climate (Broecker and Henderson, [1998]).

While the eccentricity modulated precession cycle theory for the 100-kyr glacial cycle periodicity is widely accepted, several other theories have been proposed which include that the glacial-interglacial transitions occur every second or third obliquity cycle (Huybers and Wunsch [2005]) and that stochastic internal climate variability is largely responsible (Wunsch [2003(1)]).

The amplitude of the glacial cycles also increased over time with far larger variations in ice volume during the more recent 100-kyr glacial cycles than prior to this time, as is evident in

the benthic $\delta^{18}O$ stack constructed by Lisiecki and Raymo [2005]. The glacial cycles are not symmetric as would be expected from the Milankovitch Cycle variations in insolation but exhibit a saw-tooth pattern (see Fig 1.1) with long glacial periods and rapid transitions to short interglacial conditions (lasting 10-30 kyrs) (IPCC [2007]) over which climate feedbacks must be large.

As mentioned previously, the changes in the distribution and magnitude of solar insolation associated with the Milankovitch cycles cannot explain the magnitude of the temperature variations which occur over the glacial cycles without positive climate feedbacks. The changes in radiation cause perturbations in the Earth's temperature which are then amplified by changes in climate system processes and the associated climate feedbacks. The relative importance of these amplifiers remains uncertain and it is likely that some important feedbacks have not been identified. Atmospheric CO_2 and Antarctic temperature co-vary in the ice-core records (with CO_2 lagging temperature by a few hundred years (Monnin et al. [2001]), small compared to the glacial-interglacial timescale) which suggests that atmospheric CO_2 is the key driver of the glacial cycles due to its greenhouse warming effect. There is significant uncertainty in the lag due to the gas-ice age difference of the ice core. This gas-ice age difference is a consequence of the air only being enclosed in ice at the bottom of the firn layer, and thus the ice is older than the trapped air (Monnin et al. [2001]). More recently Loulergue et al. [2007] suggest the lag in CO_2 has been overestimated since the gas-ice age difference is in fact smaller than previously estimated, although temperature changes always lead changes in CO_2. Parrenin et al. [2013] use the isotopic composition of N_2 in ice cores to propose a revised age scale of the air bubbles in ice cores which suggest changes in CO_2 and Antarctic temperature in fact vary almost simultaneously with no lag. While the initial feedback in response to changes in solar irradiance remains uncertain, both

changes in albedo due to changes in the ice sheets and changes in atmospheric CO_2 concentrations play a crucial role in the transition of the climate during the glacial cycles.

Finding the mechanisms responsible for the glacial-interglacial changes in atmospheric CO_2 is incredibly important in advancing our understanding of the climate system, particularly given the current anthropogenic induced changes in climate. The main carbon-cycle feedbacks which have been hypothesised to act during glacial-interglacial cycles will be described in Section 1.3. The next section describes the theory of the ocean's meridional overturning circulation (MOC).

1.2. The Meridional Overturning Circulation (MOC)

1.2.1. Theory of the MOC

The large scale MOC of the ocean plays an essential role in redistributing nutrients, carbon, alkalinity, heat and salinity globally throughout the oceans. It also ventilates the deep ocean, enabling CO_2 and heat to be exchanged between the deep ocean and the atmosphere, which is paramount in determining global climate. Thus, understanding the dynamics controlling the sub-thermocline ocean circulation is vital in order to understand how it has varied in the past and how it will change in the future under anthropogenic climate change.

An understanding of the ocean's MOC is essential in many of the mechanisms proposed for the glacial-interglacial changes in atmospheric CO_2 described in Section 1.3. Investigating the nature of the present-day MOC and how it responds to various changes in external forcing along with the resulting change in atmospheric CO_2 is one of the main motivations of this thesis.

The global MOC is characterised by a lower Antarctic Bottom Water (AABW) circulation in the deep ocean, which is formed by the sinking of dense surface waters in the Southern

Ocean (see Fig 1.3). This dense water mass is transported northwards in every ocean basin. Some of this water upwells diffusively to the surface but the majority upwells to mid-depths before being transported adiabatically southwards, upwelling to the surface along sloping isopycnals in the Southern Ocean. In the Atlantic Ocean, there is also an upper NADW overturning cell which circulates in the reverse direction to the AABW cell and is up to 4 Km deep (see Fig 1.3). A brief description of the theory of how these overturning cells are formed and sustained is now described, before a more thorough review of the most relevant literature is provided in Chapter's 3.1 and 4.1.

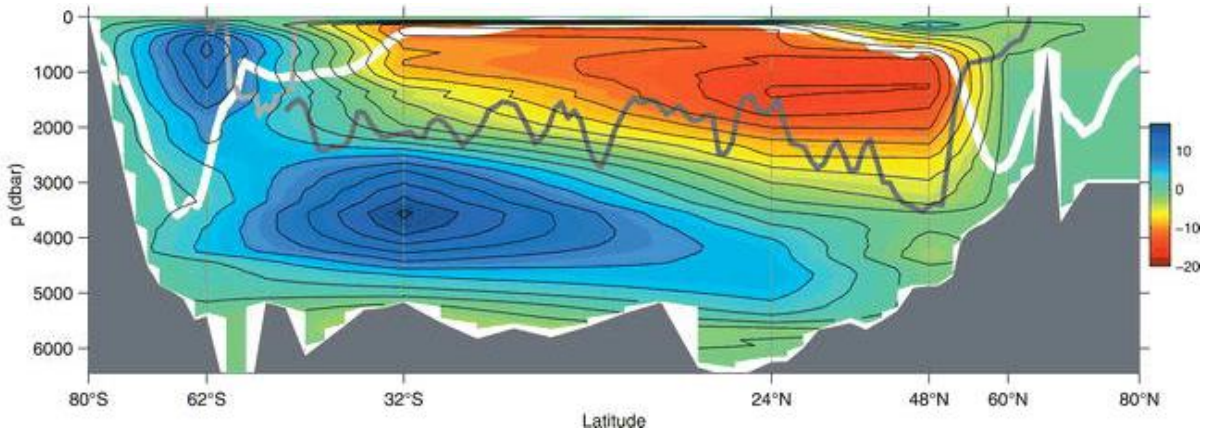

Fig 1.3: Zonally-averaged global MOC. The overturning streamfunction (unit: Sverdrups (Sv)) is plotted, where positive (blue) and negative (red) values correspond to counterclockwise and clockwise overturning circulations respectively (Lumpkin and Speer [2007]).

One of the main uncertainties in understanding the large scale ocean overturning circulation has been determining the mechanism responsible for driving the MOC, specifically the upper NADW cell in the Atlantic Ocean. Originally, it was proposed that the global MOC (which includes the NADW cell) was driven by surface density variations and it was therefore known as the 'thermohaline circulation' (THC), since the density of the ocean is dependent on its temperature and salinity (Sandström [1916]; Jeffreys [1925]). The sinking of NADW in the North Atlantic must be balanced by an upwelling over the remainder of the ocean basin in order to conserve mass. It was hypothesised that this balance is maintained by vertical

diapycnal mixing in the interior of the ocean basin which provides a heat transfer to balance the vertical advection of heat by the upwelling waters. However, a diapycnal diffusivity of about 1 x 10^{-4} m^2s^{-1} (Munk [1966]) is required to balance the upwelling which is an order of magnitude larger than that observed (Rooth and Östlund [1972]; Ledwell et al. [1993]). This view of a MOC driven by diffusive upwelling was further developed by Broecker and Peng [1982], Gordon [1986] and Broecker [1987], who considered the MOC to be a global inter-connected conveyor belt with a transfer of water between all ocean basins. The MOC schematic of Broecker [1987] is shown in Fig 1.4.

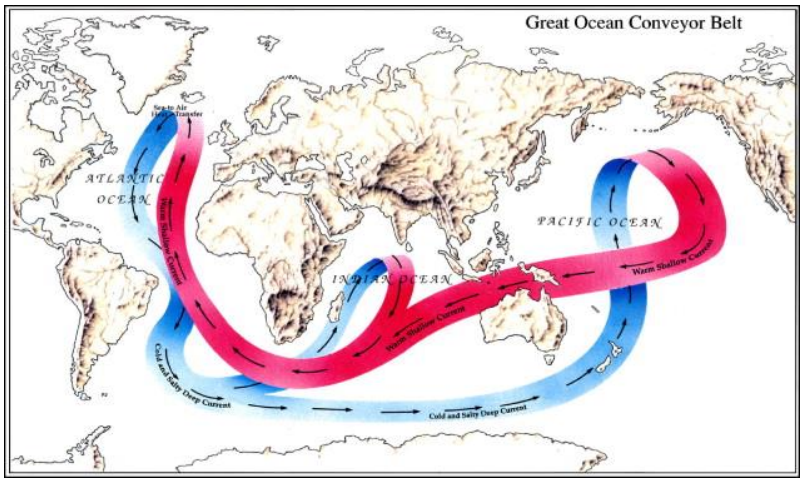

Fig 1.4: The ocean conveyor belt (Broeker [1987]), where warm, less dense waters are shaded red and cooler, dense waters are shaded blue.

More recently, it was proposed that the AMOC is driven by the westerly winds over the Southern Ocean (Toggweiler and Samuels [1993; 1995]) via the 'Drake Passage effect'. They hypothesised that a large proportion of the AMOC upwells in the Southern Ocean where the westerly winds drive a northward surface Ekman flow and a consequent horizontal divergence of water. This causes water to upwell from the deep ocean in order to conserve mass. Thus, the observed diapycnal mixing in the ocean which is inadequate to upwell all of the northern sourced NADW is no longer a dilemma, since a strong NADW circulation persists even in the limit of no vertical mixing (Toggweiler and Samuels [1998]). It is likely

that a combination of both mechanisms act in reality, although this remains an area under debate, with some studies favouring a wind-driven NADW cell (Cessi [2019]) while others stress the importance of diapycnal mixing (Ferrari et al. [2017]). These processes are discussed in more detail later, particularly in Chapter 4. The theory of the MOC with a focus on the most recent literature is discussed in Chapter 3.

Our understanding of the structure and pathways taken by the present-day MOC has since been advanced with the schematics of Schmitz [1995], Lumpkin and Speer [2007] and Talley [2013] providing useful views of the MOC as inferred from observations. The Lumpkin and Speer [2007] schematic is shown in Fig 1.5a, which shows the pathways taken by the MOC between the ocean basins and the Southern Ocean. The connection of the upper and lower cells is clear. Talley [2013] uses a different dataset to emphasise these findings. A schematic of the Southern Ocean upwelling and low latitude Pacific and Indian Ocean upwelling is shown in Fig 1.5b, showing the overlap of the upper and lower cells. The MOC forms one continuous overturning cell (Lumpkin and Speer [2007], Talley [2013], Ferrari [2017]), with most of the NADW which upwells in the Southern Ocean flowing south to form AABW and circumpolar deep water (CDW) in the Pacific and Indian Oceans. The Pacific and Indian Deep Water (PDW and IDW) which form as a result of the diapycnal diffusive-driven transformation of AABW in the respective basins, completes a ‘figure-of-eight’ circulation by returning to the Atlantic via the Southern Ocean.

This three-dimensional nature of the MOC is highlighted in these studies which is not apparent from the two-dimensional global meridional overturning streamfunction shown in Fig 1.3, which features two closed overturning cells.

(a) (b)

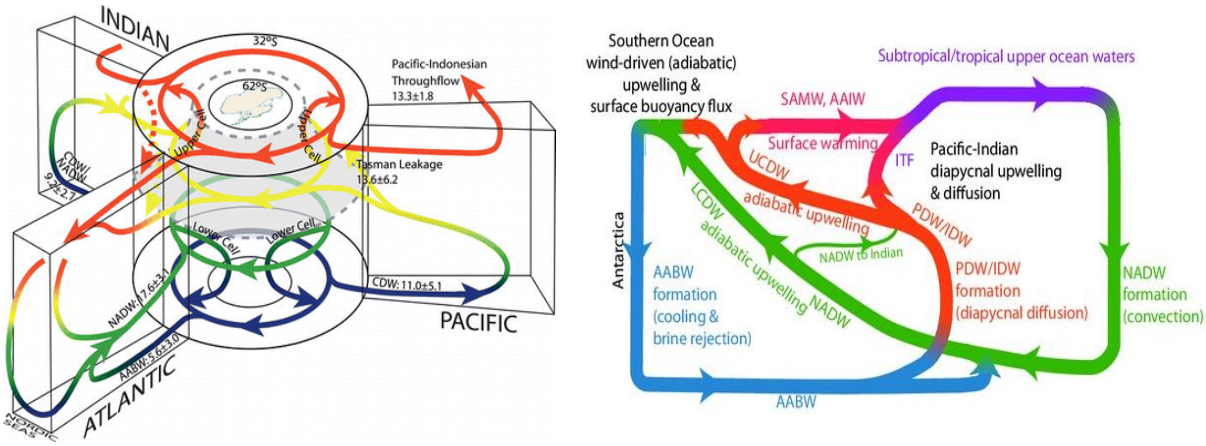

Fig 1.5: Schematic of (a) the global MOC from Lumpkin and Speer [2007], which shows the transfer pathways between basins and the Southern Ocean, and (b) the overlap between the upper and lower cells of the global MOC from Talley [2013].

The remainder of this section describes the glacial structure of the MOC and some of the most recent studies on the transition of the MOC to a glacial state from which Chapter 3 extends this work.

1.2.2. The Glacial MOC

The present-day MOC discussed above is believed to have changed significantly during glacial times. Reconstructions of the MOC of the Last Glacial Maximum (LGM) (approximately 21 kyrs BP) using $\delta^{18}O$ records suggest the NADW circulation became weaker, while benthic foraminifera $\delta^{13}C$ records suggest it became shallower during the LGM, shoaling to a depth of about 2 km and hence it was reduced to intermediate rather than deep levels (Duplessy et al. [1988]; Lynch-Stieglitz et al. [1999]; McManus et al. [2004]; Curry and Oppo [2005]). However, some studies using $^{231}Pa/^{230}Th$ records suggest the NADW shoaled but was also stronger during the LGM (Gherardi et al. [2009]), although the general consensus is that its strength was similar to present or it weakened.

The shoaled NADW became a distinct water mass, known as Glacial North Atlantic Intermediate Water (GNAIW) (Duplessy et al. [1988]). There was a large vertical $\delta^{13}C$ gradient during the LGM, with high $\delta^{13}C$ in the GNAIW above 2 km and low $\delta^{13}C$ in the AABW below this level, contrasting with the high $\delta^{13}C$ NADW distributed throughout the depth of the North Atlantic in the present-day (Curry and Oppo [2005]). This suggests the AABW circulation at the LGM expanded greatly, extending far further north into the deep North Atlantic. The AABW was also saltier than the upper cell at the LGM, according to pore water proxies, in contrast with present-day deviations which have lower salinity in the deep ocean (Adkins et al. [2002]).

Mechanisms used to explain the glacial-interglacial CO_2 variation must account for these paleo-proxy reconstructions of the MOC. A number of climate models are unable to simulate these changes in the MOC under glacial forcings. The Paleoclimate Model Intercomparison Project phase 1 and 2 (PMIP1 and PMIP2) investigate the ability of state of the art climate models to simulate LGM climates. Weber et al. [2007] evaluate nine PMIP1 coupled models forced by LGM conditions. The strength of the North Atlantic overturning cell (i.e. NADW in the present-day) increases in four models, decreases in four models and remains similar in one model relative to the present-day. Similar variations were exhibited among PMIP2 models, with the depth of the North Atlantic overturning cell also unpredictable, deepening in some models and shoaling in others (Otto-Bliesner et al. [2007]). The cause of the deviations are uncertain, although Weber et al. [2007] suggest it is due to differences in the density contrast between NADW and AABW, whereas Otto-Bliesner et al. [2007] hypothesise it is due to variations in the seasonal sea-ice extent. One of the aims of this thesis is to understand how the glacial MOC can be obtained in GCM's (see Chapter's 3 and 4) and the simple semi-analytical model of Nikurashin and Vallis [2011; 2012] (see Chapter 7).

1.2.3. Recent idealised modelling studies of the MOC

Two of the main Southern Ocean mechanisms to transition the MOC to a glacial state are i) reduced atmosphere-ocean buoyancy fluxes (Watson and Garabato [2006], Ferrari [2014], Jansen and Nadeau [2016]; Nadeau et al. [2019]), or ii) a weakening or northward shift in the Southern Hemisphere westerly winds (Toggweiler and Samuels [1993; 1995]; Toggweiler et al. [2006]). The former mechanism is tested in Chapter 3 and the latter mechanism is tested in Chapter 4 using an idealised GCM.

Ferrari et al. [2014], Jansen and Nadeau [2016], Jansen [2017] and Nadeau et al. [2019] argue that changes in Antarctic sea-ice could be a crucial cause of this transition from a geometric and a buoyancy argument respectively. This mechanism can be expected to be significant given the importance of Southern Ocean sea-ice in the water mass transformations of the present-day ocean (Abernathey et al. [2016]).

Ferrari at al. [2014] hypothesise the equatorward expansion of Southern Ocean sea-ice during glacial times as a mechanism to shoal and isolate the NADW cell. They argue that the isopycnal at the summertime sea-ice boundary separates the northward and southward flows at the surface (and the upper and lower overturning branches) of the Southern Ocean. Their theory relies on diffusive-driven upwelling (and thus the PDW cell) being confined below a depth of ~2 Km. If the slope of isopycnals in the Southern Ocean is assumed constant, the depth of the sea-ice boundary isopycnal in the ocean basins north of the channel will shoal above the PDW cell as the sea-ice expands equatorward. Therefore, since PDW only flows into the Southern Ocean below ~2 Km and is therefore confined below the shoaled sea-ice isopycnal, PDW only upwells under sea-ice. It therefore moves polewards at the surface of the Southern Ocean, unable to connect to the less dense NADW cell. The NADW cell in the Atlantic Ocean responds by shoaling above the sea-ice boundary isopycnal. Hence, the upper

and lower overturning cells become isolated. The isolation of these two cells is consistent with the glacial 'mid-depth age bulge' in radiocarbon simulated by Burke et al. [2015] using a semi-analytical single-basin model following on from that used by Nikurashin and Vallis [2012]. The radiocarbon content of mid-depth waters in the South Atlantic decreases in response to an equatorward expansion of Southern Ocean sea-ice and consequent reorganisation of the MOC.

In contrast to the Ferrari et al. [2014] glacial hypothesis, Jansen and Nadeau [2016], and Jansen [2017] argue that enhanced brine rejection due to sea-ice formation increases abyssal stratification, shoaling the NADW cell. A recent paper of Nadeau et al. [2019] studies both mechanisms in a multi-basin model, suggesting both mechanisms work together to shoal the NADW cell with additive effects. Thus, these studies provide a convincing mechanism to obtain the glacial shoaling of NADW via changes in Southern Ocean sea-ice. This Southern Ocean sea-ice induced shoaling of the MOC is investigated in Chapter 7.

Ferrari et al. [2017] use a multi-basin model to investigate the present-day MOC using a multi-basin model. They suggest the ocean circulation is a combination of three limits; the adiabatic, diabatic and inter-basin limits. Thus, diffusive-driven upwelling in the Pacific basin is shown to be important in driving the AMOC in addition to the Southern Ocean westerly winds. The presence of inter-basin geostrophic flows is also seen in the multi-basin analytical model of Thompson et al. [2016] which focuses on the stratification contrasts between the basins.

1.3. Glacial-interglacial processes and their contribution to changes in CO_2

1.3.1. Terrestrial contribution

The pre-industrial terrestrial carbon reservoir (which includes vegetation, soil and detritus) stored between 1950 and 3050 Peta-grams of carbon (PgC) (equivalent to Giga-tonnes of

carbon (GtC)) (Prentice et al. [2000]; Batjes [1996]; IPCC [2013]), which is often approximated to be 2300 PgC (WBGU [1998]; MRS [2001]; De Fries et al. [1999]; Carter and Scholes [2000]; IPCC [2001], [2007]), based on estimates of global plant and soil reservoir sizes. The terrestrial reservoir was a source of carbon to the atmosphere-ocean system during the LGM, with a decrease of between 750-1350 PgC in the terrestrial carbon storage (Adams et al. [1990]; Crowley [1995]), equivalent to as much as a 70% decrease in the terrestrial carbon storage compared to the pre-industrial value. This decrease is hypothesised to be a consequence of the huge expansion of ice-sheets in the Northern Hemisphere, in addition to an expansion of deserts and arid scrub, and a decrease in tropical forest coverage (Adams et al. [1990]).

1.3.2. Oceanic contribution

Sigman and Boyle [2000] show that glacial cycle changes in atmospheric CO_2 must be primarily due to changes in the ocean's carbon storage, since it is the only carbon reservoir which could account for the rate and magnitude of the atmospheric drawdown of carbon to attain the glacial atmospheric CO_2 concentration. The oceans also equilibrate with the atmosphere over thousands of years, the same timescale as glacial-interglacial changes in CO_2 (Sigman et al. [2010]). The ocean contains about 39,000 PgC which is 13 times greater than the atmospheric and terrestrial carbon reservoirs combined (Sigman and Boyle [2000]). The ocean is a large carbon reservoir primarily as a consequence of the chemical properties of CO_2 in seawater. The concentration of dissolved CO_2 which is converted to other compounds depends on the chemical equilibrium between CO_2 and carbonic acid (H_2CO_3) in sea water:

$$CO_2\,(g) + H_2O \leftrightarrow H_2CO_{3\,(aq)} \leftrightarrow HCO_3^- + H^+ \leftrightarrow CO_3^{2-} + 2H^+ \qquad (1.1)$$

When atmospheric CO_2 dissolves in seawater, it is converted to bicarbonate (HCO_3^-) and carbonate (CO_3^{2-}) ions via the equilibrium reaction in (1.1). The ocean has a surface pH of ~8.1 and thus the equilibrium partitioning of these species in the ocean is such that 99% of the dissolved inorganic carbon (DIC) is in the form of bicarbonate or carbonate ions (see Fig 1.6). Thus, only a small fraction of the DIC in the ocean is CO_2. Since in addition to the rate of atmosphere-ocean exchange, the atmosphere-ocean CO_2 flux is determined by the partial pressure of CO_2 (pCO_2) at the sea-surface (IPCC [2007]), the equilibrium carbon content of the ocean is increased significantly by the chemical properties of CO_2 in sea water described by (1). The magnitude of the pCO_2 of seawater required for the ocean to be in equilibrium with atmospheric CO_2 (i.e. for the atmosphere-ocean CO_2 flux to be zero) is dependent on the fugacity (effective partial pressure) of oceanic CO_2, a quantity calculated from well-known chemical equilibria that depend on the ocean's DIC, alkalinity, temperature and salinity (Zeebe and Wolf-Gladrow [2001]). Therefore, many of the mechanisms proposed to alter atmospheric CO_2 described in this review require a change in one of these variables at the surface.

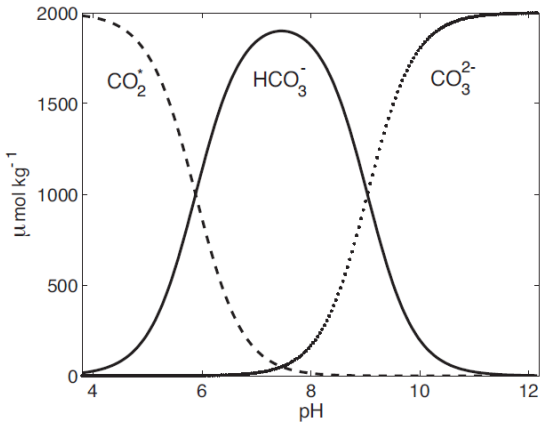

Fig 1.6: Bjerrum plot showing the concentration of the carbonate species (which together give the DIC) as a function of pH (plot from Williams and Follows [2011]).

The vertical distribution of DIC in the ocean is controlled by the efficiency of the solubility, carbonate and soft-tissue pumps which alter the surface pCO_2 by removing DIC from the surface layer. The solubility pump describes the enhanced solubility of CO_2 at high latitudes where the sea surface temperature is lower, and the consequent sequestration of the CO_2 rich water into the ocean interior due to deep water formation at these high latitudes in the Southern Ocean and North Atlantic Ocean (Raven and Falkowski [1999]). The soft-tissue pump describes the transfer of DIC from the surface into the ocean interior due to the sinking of particulate organic carbon (POC) in regions where phytoplankton photosynthesise (see Fig 1.7). Both the solubility and soft-tissue pump act to drawdown atmospheric CO_2. The carbonate pump describes the export of calcium carbonate ($CaCO_3$) produced by species of phyto- and zoo-plankton, into the ocean interior which reduces the surface alkalinity and DIC in a 2:1 ratio. The net effect is an increase in surface fugacity (or partial pressure) of CO_2, increasing atmospheric CO_2. This pump therefore opposes the atmospheric CO_2 sequestration performed by the aforementioned pumps. These processes and the mechanisms proposed to change the efficiency of these pumps as a means to explain the glacial-interglacial CO_2 variation are described in this section.

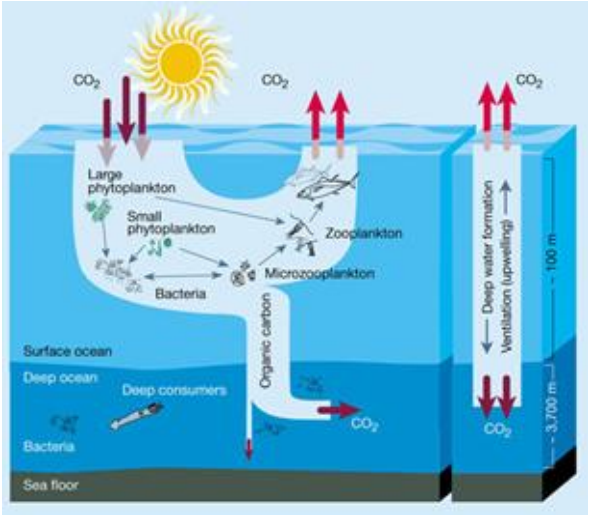

Fig 1.7: Diagram of the soft-tissue pump (left) and solubility pump (right), which both act to maintain a sharp vertical CO_2 gradient in the ocean. (Figure from Chisholm S.W. [2000]).

1.3.3. The Southern Ocean's role

The Southern Ocean appears to play a major role in modulating global climate, through its regulation of atmospheric CO_2, as inferred from the strong correlation between Antarctic temperatures and atmospheric CO_2 in the Antarctic ice core records. However, variations in the concentration of atmospheric methane (CH_4) also increased between the LGM and pre-industrial times increasing from 375 ppb (parts per billion) to 680 ppb (Hopcroft et al. [2017]) with a lag of ~1100 years relative to Antarctic temperatures over the last four glacial cycles (Delmotte et al. [2004]). Hence changes in the tropics and Northern Hemisphere also appear to be significant during glacial cycles due to their modulation of CH_4 (Monnin et al. [2001]), which provides an additional greenhouse climate feedback. As previously described, deep waters upwell to the surface at high latitudes, where the isopycnals outcrop due to the cold surface temperatures. Therefore, polar regions have a larger impact on atmospheric CO_2 than lower latitudes. The Southern Ocean ventilates large volumes of the ocean since both NADW and AABW circulations upwell to the surface in this region. Many of the mechanisms responsible for varying CO_2 are therefore driven by changes in the Southern Ocean carbon cycle.

1.3.4. Oceanic mechanisms: Physical processes

Several physical mechanisms for the glacial-interglacial CO_2 variation have been proposed including a change in sea-surface temperature (SST), changes in the ocean's MOC and stratification, and reduced air-sea CO_2 fluxes as a result of sea-ice expansion around Antarctica (IPCC [2013]).

1.3.4.1. SST and salinity

The glacial-interglacial change in SST and salinity have opposing effects on atmospheric CO_2 due to the solubility of CO_2 decreasing in a warmer ocean but increasing in a fresher ocean. The net increase in atmospheric CO_2 from solubility effects is about 20 ppm (Sigman and Boyle [2000]). The SST in glacial times inferred from CLIMAP [1981] glacial SST reconstructions estimate that the subtropical and tropical SST was up to 3°C cooler during the LGM. Thus, the warming (SST effect) during glacial-interglacial transitions leads to an increase in atmospheric CO_2 of 26 ppm, with a range of 21-30 ppm predicted by intermediate complexity and GCM models (Bopp et al. [2003]; Marchal et al. [1998]). In contrast, the decrease in oceanic salinity during glacial-interglacial transitions is estimated to cause a decrease in CO_2 of 6 ppm (Zeebe and Wolf-Gladrow [2001]), based on a decrease in salinity of 3 parts per thousand (ppt) throughout the ocean, in response to the melting of the Northern Hemisphere ice sheets and consequent increase in sea-level of ~120 m since the LGM.

1.3.4.2 Ocean Circulation

Variations in the ocean's MOC are likely to be vital in causing the glacial-interglacial CO_2 variation as described in Section 2. The effect of changes in circulation on atmospheric CO_2 in a multi-basin model GCM is described in Chapter 6. Circulation changes are required by several of the mechanisms described later. However, changes in the ocean circulation alone (i.e. neglecting the $CaCO_3$ compensation and changes in biological production) have been hypothesised to lead to significant changes in atmospheric CO_2 through the redistribution of carbon with an increase in the deep ocean carbon storage during glacial periods (IPCC [2013]). A central estimate of the impact of ocean circulation changes alone on atmospheric CO_2 is that they caused an increase of 27 ppm (Schmittner et al. [2007]) between the LGM and the Holocene, although model predictions range from 3 to 57 ppm (Kohfeld and

Ridgwell [2009]). Changes in the ventilation of the Southern Ocean is one of the major causes of this CO_2 variation (first proposed by Toggweiler [1999]) and two mechanisms explaining this change are now described, with additional mechanisms described later.

The main theories proposed for the shoaling of the North Atlantic overturning circulation and reduced upwelling in the Southern Ocean during glacial periods (see Section 2) are i) a weakening or northward shift in the Southern Hemisphere westerly winds (Toggweiler and Samuels [1993]; [1995]; Toggweiler et al. [2006]) or ii) reduced atmosphere-ocean buoyancy fluxes (Watson and Garabato [2006]). However, while the impact of changes in the Southern Hemisphere westerly winds have been shown to be significant in numerous ocean model studies (Wunsch [2003]; Oka et al. [2012]), other studies suggest the AMOC's response to wind forcing is eddy compensated (Downes and Hogg [2013]), although this has recently been contradicted by Bishop et al. [2016]. Eddy compensation implies that changes in the wind–induced Deacon circulation are compensated by changes in the competing effect of the eddy-induced circulation (Marshall and Radko [2003]). Also, paleo-proxy data used to infer changes in the Southern Hemisphere westerly winds at the LGM are inconclusive (Kohfeld et al. [2013]) and simulations using GCM's also produce differing changes (i.e. weaker and equatorwards winds (Kim et al. [2003]; Rojas et al. [2009]) to poleward and stronger winds (Wyrwoll et al. [2000]; Otto-Bliesner et al. [2006]). My main focus in this literature review is on the latter buoyancy driven mechanism, since the emphasis of my PhD project is on the effects of changes in the surface buoyancy fluxes on the MOC. This mechanism is described in more detail in Section 4.

1.3.4.3. Ocean stratification

Paleo-proxy evidence suggests that the deep Southern Ocean was more saline at the LGM and thus had a greater stratification (Adkins et al. [2002]), increasing the isolation of deep

waters from the surface. Kohler et al. [2005] estimated from an ocean box model that the enhanced stratification is associated with a 35 ppm decline in atmospheric CO_2. Kobayashi et al. [2015] used a three dimensional ocean general circulation model (OGCM) to investigate the importance of the Southern Ocean stratification on atmospheric CO_2. They used a weaker vertical diffusivity to represent the stronger stratification in the glacial simulation. The increase in stratification only reduced atmospheric CO_2 by 12 ppm in this study. This contrasts with the 40 ppm decrease in CO_2 resulting from the sinking of brine released during sea-ice formation and the consequent decrease in vertical mixing in the Southern Ocean obtained by Bouttes et al. [2011] in simulations using an intermediate complexity model. The large difference in these estimates is primarily due to the AABW circulation strengthening in Kobayashi et al. [2015], whereas it weakens in Bouttes et al. [2011], in response to enhanced Southern Ocean stratification.

1.3.4.4. Sea-ice cover variations

The importance of variations in sea-ice extent on global climate was first studied by Stephens and Keeling [2000]. They showed that changes in the extent of either the annual Antarctic sea-ice coverage, or the wintertime sea-ice extent combined with summer sea-ice melt induced stratification is an important mechanism in the glacial-interglacial CO_2 variations. They hypothesise that the increase in Antarctic sea-ice and summer stratification during glacial periods reduces the deep-ocean ventilation and isolates the Southern Ocean from the atmosphere reducing the air-sea exchange of CO_2. Changes in sea-ice in the Southern Ocean are particularly important given that it ventilates a large volume of the global ocean. In contrast to Stephens and Keeling [2000], Kohler et al. [2005] use an atmosphere-ocean-biosphere box model to show that changes in global sea-ice extent alter atmospheric CO_2 in the opposite direction, with a decrease of approximately 10 ppm occurring during the glacial-interglacial transition. The difference is believed to be partly due to the unrealistically large

increase in sea-ice used by Stephens and Keeling [2000], which is above a threshold at which models become very sensitive to the Southern Ocean sea-ice extent. The main reason for the decrease in Kohler et al. [2005] is the inclusion of changes in sea-ice in the North Atlantic which is a sink for CO_2 and thus sea-ice reduces the air-sea CO_2 flux in this region. GCM simulations also suggest that sea-ice changes lead to a decrease in atmospheric CO_2 during glacial terminations, with the best estimate suggesting a decrease of 5 ppm with an estimated range between 0 and 14 ppm (Kohfeld and Ridgwell [2009]). However, Antarctic sea-ice changes have also been hypothesised to alter the ocean's MOC which could be fundamental in causing the glacial cycle variation in atmospheric CO_2 (Ferrari et al. [2014]). This mechanism will be described in detail in Section 1.4.

Several physical mechanisms have been proposed above to explain the glacial-interglacial variation in CO_2 with some being required to instigate the biological mechanisms which are described in Section 1.4.3.

1.3.5. Oceanic mechanisms: Chemical processes

1.3.5.1. Calcium Carbonate ($CaCO_3$) compensation

One of the major theories for the glacial-interglacial CO_2 variation involves changes in the rate of burial or dissolution of sea-floor $CaCO_3$ which leads to an imbalance between the rate of weathering input to the ocean and deep-sea burial of $CaCO_3$. The subsequent adjustment process known as '$CaCO_3$ compensation' is believed to play a major role in controlling the variation of CO_2 during glacial cycles due to the consequent changes in surface (and whole ocean) alkalinity. During the last glacial period and other cold periods, the carbon isotopic composition ($\delta^{13}C$) of benthic foraminifera implies that there was a net export of CO_2 from the upper to the abyssal ocean, which could be caused by physical or biological mechanisms (Boyle and Keigwin [1987]; Oppo and Lehman [1993]; Kumar et al. [1995]). The '$CaCO_3$

compensation' hypothesis proposes that this increase in CO_2 at depth would cause the dissolution of $CaCO_3$ at the seabed until a steady state was re-established. This would lead to an increase in the total ocean and surface alkalinity, reducing the ocean surface CO_2 fugacity and consequently atmospheric CO_2 (Broeker [1982]; Broeker and Peng [1987]; Marchitto et al. [2005]). In addition to an oceanic rearrangement of CO_2, '$CaCO_3$ compensation' can also be caused by a rearrangement of CO_3^{2-}, or a direct change in the whole ocean carbon and alkalinity inventories, since these changes alter the balance between the ocean's sources and sinks of $CaCO_3$. This mechanism cannot explain the cause of the initial change in atmospheric CO_2 but it is an important carbon cycle feedback, potentially explaining a large proportion of the subsequent change in CO_2 over glacial cycles. The $CaCO_3$ compensation mechanism could account for over a third of the atmospheric CO_2 change during glacial cycles, as shown by the 36 ppm oceanic drawdown of CO_2 in glacial periods in the box model of Toggweiler [1999].

1.3.6. Oceanic mechanisms: Biological processes - Soft-tissue pump

The soft-tissue carbon pump describes the export of organic matter, known as particulate organic carbon (POC) from the surface ocean into the deeper ocean due to biological production as previously described (see Fig 1.7). This is an important process in the ocean carbon cycle since it leads to an increase in DIC at depth, reducing the surface ocean pCO_2 and thus increasing the amount of carbon the ocean can hold. Changes in the magnitude of this process will therefore lead to changes in atmospheric CO_2, a hypothesis first proposed by Broeker [1982]. This could be instigated by changes in the ocean's circulation, surface temperature or sea-ice, and also changes in nutrient concentrations and sunlight availability (Kohfeld and Ridgwell [2009]).

At low- and mid-latitudes, photosynthesis by phytoplankton at the surface of the ocean is limited by the availability of macro-nutrients, whereas at high-latitudes there is an excess of nutrients and thus photosynthesis is limited by the rate of utilisation of these nutrients. Therefore, different mechanisms have been proposed at low and high latitudes to account for the glacial-interglacial CO_2 variation.

1.3.6.1. Low-latitude mechanisms

The organic matter exported by the soft-tissue pump is composed of inorganic carbon, nitrate and phosphate in a 106:16:1 ratio, referred to as the Redfield ratio (Redfield et al. [1934], [1963]), which is the average uptake ratio of these species by phytoplankton during photosynthesis. Thus, in order for biological production to increase the export of DIC from the ocean surface at low- and mid-latitudes and therefore reduce atmospheric CO_2, either the nutrient supply must increase or the Redfield ratio must change at these latitudes.

An increase in the nutrient supply at the surface of the ocean of 30% has been shown to lower atmospheric CO_2 by 30-45 ppm in box-model calculations and could be as high as 50 ppm if the $CaCO_3$ production and therefore the carbonate pump remained constant (Sigman et al. [1998]). Changes in the concentration of phosphate are not believed to be important in causing the glacial cycle CO_2 variations at low latitudes since phosphate has a residence time of 16-kyrs (Ruttenberg [1993]). However, changes in nitrate could play a significant role in controlling the glacial-interglacial variability of atmospheric CO_2, given the dynamic nature of the nitrogen cycle (Gruber and Sarmiento [1997]) and its relatively short residence time of 3-10 kyrs (Codispoti [1995]). Nitrogen proxy data and ocean nitrogen cycle models indicate there was indeed a higher inventory of nitrate during glacial periods (Altabet and Curry [1989]; Altabet and Francois [1994]; Pride et al. [1999]), which could lead to a higher biological production at low latitudes. However, there are major uncertainties regarding the

impact of changes in the availability of nitrate on the soft-tissue pump, since if the Redfield ratio remains constant, phosphate will be the major limiting nutrient during glacial cycles. This would prevent changes in nitrate from altering the rate of export production and consequently atmospheric CO_2 (Broeker and Peng [1982]). Thus, changes in the nutrient supply at low latitudes is not expected to have been a major mechanism due to phosphate limitation and other caveats (Tyrrel [1999]; Farrell et al. [1995]).

An alternative hypothesis for the oceanic drawdown of atmospheric CO_2 during glacial periods is the Redfield ratio changed leading to enhanced biological production (Broeker and Henderson [1998]). They argue an increase in the N:P ratio of organic matter could increase biological production since this ratio determines the transition between nitrate and phosphate limitation (Tyrell [1999]).

1.3.6.2. High-Latitude mechanisms

At high latitudes, nutrients are not fully utilised by phytoplankton at the surface and therefore there is a high surface concentration of preformed nutrients and DIC in these regions. Since the pycnocline (i.e. the layer across which the density increases rapidly) outcrops in cold polar regions, the high latitudes provide a connection between the atmosphere and the deep ocean. In the Southern Ocean, deep water high in CO_2 upwells to the surface and hence a reduction in nutrient utilisation in this region is hypothesised to increase the outgassing of CO_2 to the atmosphere, often referred to as the 'CO_2 leak'. Changes in the efficiency of biological production (or nutrient utilisation) at high latitudes was first proposed as a mechanism for the glacial-interglacial atmospheric CO_2 variation by several researchers independently in 1984 (Knox and McElroy [1984]; Sarmiento and Toggweiler [1984]; Siegenthaler and Wenk [1984]). They each used an ocean box model to show that enhanced nutrient utilisation by phytoplankton at high latitudes leads to a reduction in atmospheric

CO_2. These studies revealed the importance of the 'CO_2 leak' in the Southern Ocean and numerous studies investigating processes in this region followed. The importance of high latitude relative to low latitude regions in controlling atmospheric CO_2, despite their small surface area can be explained by the large proportion of the ocean interior they ventilate.

The mechanism responsible for the increase in Southern Ocean nutrient utilisation during glacial periods could be a result of biological or physical mechanisms. The biological mechanisms include a change in the availability of light and micro-nutrients, particularly iron, which are in short supply and may be limiting biological productivity in this region (Chisholm and Morel [1991]). Both Knox and McElroy [1984], and Sarmiento and Toggweiler [1984] assumed changes in the availability of light alters the utilisation. However, insolation at these latitudes increased by only 10-15% during glacial periods and hence it is unlikely to account for the 500% increase in high latitude productivity (Toggweiler and Sarmiento [1985]). It is now believed that the increase in productivity could be due to an increase in the supply of iron-rich dust at high latitudes during glacial periods (Martin [1990]). This hypothesis requires biological production in this region to be limited by iron deficiency which is supported by iron release experiments (Martin et al. [1991]; Watson et al. [2000]). Thus, if the availability of iron increased, phytoplankton would be able to utilise a greater proportion of the available nutrients, increasing the sequestration of carbon into the deep ocean via the soft-tissue pump. Paleoceanographic reconstructions suggest dust fluxes and therefore the supply of iron to the ocean was two to five times greater during glacial periods relative to interglacial periods (Rea [1994]; Kohfeld and Tegen [2007]) with an increase of 20-fold possible in polar regions (Kohfeld and Ridgwell [2009]). Model studies estimate the 'iron hypothesis' accounts for 15 ppm (central estimate) of the change in atmospheric CO_2, although the range of values varies from 5 ppm (Archer et al. [2000]) to an

observational estimate (using ice core data in which the non-sea-salt calcium flux is used as a proxy for iron) of 28 ppm (Röthlisberger et al. [2004]).

An alternative hypothesis for the increase in nutrient utilisation (as inferred from the higher $\delta^{15}N$ in sediment cores in glacial times (Francois et al. [1997])) invokes a decrease in the transport of nutrients and carbon to the ocean surface which could be instigated by an increase in salinity-driven stratification of the Southern Ocean (Sigman and Boyle [2000]), a decrease in wind-driven upwelling, caused by a decrease in the strength or an equatorward shift of the Southern Ocean winds (Toggweiler and Samuels [1993], [1995]), or changes in the surface buoyancy distribution (Watson and Garabato [2006]; Watson et al. [2015]). In order to model the impact of these mechanisms on the ocean's carbon cycle, Ito and Follows [2005] showed that the fraction of phosphate which is preformed (i.e. not utilised) in the ocean interior can be used to quantify the efficiency of the biological pump and therefore atmospheric CO_2, since it is independent of the model formulation. Watson et al. [2015] used a basic ocean-carbon cycle model, the Nikurashin and Vallis [2012] model with an added carbon cycle which is described in more detail, modified and used in Chapter 7. Watson et al. [2015] use the Ito and Follows [2005] representation of the biological pump to hypothesise that the upwelling of deep waters in the Southern Ocean shifts northwards during glacial periods in response to changes in Southern Ocean buoyancy fluxes. This increases the time phytoplankton at the surface have to utilise the available nutrients through photosynthesis before they return to the abyssal ocean further south via the AABW cell. Since, there is an excess of nutrients available for photosynthesis in this region, the change in circulation increases the uptake of CO_2 by biological activity, increasing the efficiency of the soft-tissue pump. The changes in ocean circulation and biological production in their model can account for 30-60 ppm of the glacial-interglacial atmospheric CO_2 variation.

1.3.7. Conclusions

The glacial-interglacial hypothesis discussed here cannot realistically account for the change in atmospheric CO_2 during the glacial cycles when taken in isolation. Instead it is believed that several of these processes act together, although the exact mechanisms by which this change occurs remains uncertain. However, changes in the ocean's circulation and the consequent changes in biological production are likely to play a major role. Thus, ocean circulation changes and the consequent change in atmospheric CO_2 forms the basis of this thesis.

Chapter 2

MITgcm ocean-sea-ice-biogeochemistry model configuration

The Massachusetts Institute of Technology general circulation model (MITgcm) (Marshall et al. [1997a,b]) is used in the following chapters to simulate the MOC, sea-ice and the ocean carbon cycle under varying forcings and geometrical setups. This will enable us to improve our understanding of the MOC and the mechanisms responsible for the glacial cycles. This complex three dimensional model can provide more realistic simulations than the semi-analytical model used in Chapter 7 since many processes are included and it solves the dynamical equations over the whole domain. Both a single-basin and a two-basin model is used to determine whether multi-basin models are required to attain realistic simulations of the MOC and atmospheric CO_2 variations during glacial-interglacial transitions, and to improve our understanding of the mechanisms driving these changes.

The chapter is organised as follows: firstly the model structure and primitive equations solved by the model are described, followed by a description of the model grid and a more detailed description of the terms and boundary conditions used in the equations. The model setups implemented in subsequent chapters is then described including the forcings, parameters and model settings used in each of the physical, sea-ice and biogeochemistry components of the model.

2.1. Equations solved

The MITgcm is a three dimensional, primitive equation general circulation model used to study atmospheres, oceans and climate. The MITgcm is a flexible model which can be adapted to perform various experiments by changing the packages used, the parameters and the geometrical setup. The packages enable various model options and numerical methods to be selected before building the model. For example, packages responsible for simulating the biogeochemistry, sea-ice and ocean interior and boundary layer processes can be enabled with settings chosen in each package.

The equations used for both the atmosphere and ocean are the Boussinesq Navier-Stokes (N-S) equations, all be it with different quantities represented by the variables in the atmosphere and ocean. The vertical coordinate, r, in the ocean model is depth (in metres). In the setup used in this study, the equations solved are the incompressible Boussinesq, and hydrostatic N-S equations for the ocean (see equations (2.1), (2.3), (2.4), (2.6) and (2.7)), where here we consider the N-S equations to be all of the conservation equations (i.e. momentum, mass and energy). The incompressibility approximation enables the filtering of the insignificant sound waves, while the Boussinesq approximation which assumes $\rho' = (\rho - \rho_0) << \rho_0$ (where ρ is the in-situ density and ρ_0 is the reference density) allows the density to be treated as a constant in all terms except the gravitational acceleration term where the density variations are significant. This increases the linearity of the equations.

The horizontal momentum equation is:

$$\frac{D\vec{\boldsymbol{v}}_h}{Dt} + f\hat{\boldsymbol{k}}\, x\, \vec{\boldsymbol{v}}_h + \frac{1}{\rho_0}\nabla_z p' = \vec{\boldsymbol{F}} \qquad (2.1)$$

where $\vec{\boldsymbol{F}}$ is the forcing term containing the viscous effects which are dissipating terms, and also the wind forcing in the surface layer (see Section 2.6), and where the Coriolis parameter, f, is:

$$f = 2\boldsymbol{\Omega} \tag{2.2}$$

where $\boldsymbol{\Omega}$ is the Earth's angular velocity vector.

The horizontal Coriolis acceleration terms and forcing terms in (2.1) are specified in expanded versions of the zonal and meridional momentum equations in (2.10) and (2.11) respectively. The vertical momentum equation reduces to the hydrostatic balance equation since the hydrostatic approximation is made. Thus:

$$\frac{dP}{dz} = -\rho g \tag{2.3}$$

The incompressible continuity equation in (2.4) is used to diagnostically calculate the vertical velocity, w, from the gradients in the zonal and meridional velocities, u and v respectively.

$$\nabla \cdot \vec{\boldsymbol{v}} = \frac{\partial u}{\partial x} + \frac{\partial v}{\partial y} + \frac{\partial w}{\partial z} = 0 \tag{2.4}$$

The equation of state for the ocean depends on potential temperature, θ, salinity, S and pressure, P:

$$\rho' = \rho\big(\theta, S, P_0(z)\big) - \rho_0 \tag{2.5}$$

where ρ_0 is the reference density.

The heat and salinity equations are:

$$\frac{D\theta}{Dt} = Q_\theta \tag{2.6}$$

$$\frac{DS}{Dt} = Q_S \tag{2.7}$$

where Q_ϑ and Qs are the heat and salinity forcing terms containing the disspating terms due to diffusion, and in the surface layer they also include the surface heat and freshwater fluxes respectively. These are described in the Section 2.5.

The Langrangian rates of change (i.e. following a tracer, x, as it moves) in (2.1), (2.6) and (2.7) can be rewritten as a Eulerian rate of change and an advection term as follows:

$$\frac{Dx}{Dt} = \frac{\partial x}{\partial t} + \vec{\boldsymbol{v}} \cdot \nabla(x) \tag{2.8}$$

These are the primitive equations (hydrostatic form) used by the model. Hydrostatic balance is a good assumption in general in the model setup used here since the depth of the model is far smaller than the horizontal dimensions of the model. Also, the vertical resolution is far smaller than the horizontal resolution of the model and thus the dominant balance in the vertical will be between the vertical pressure gradient and the gravitational acceleration, while the inertial terms (local vertical acceleration, $\frac{\partial w}{\partial t}$, and the advection of vertical velocity, $\vec{\boldsymbol{v}} \cdot \nabla(w)$ are negligible. However, this assumption may break down in unstratified, convective regions where these inertial terms can be large. The convection in this hydrostatic model setup must be paramaterised (see Section 2.11.1).

2.2. Model Grid

The model is spatially discretised using the finite volume method which makes use of the divergence theorem, such that volume integrals of a divergence term are rewritten as surface integrals of a flux. This method is approximately equivalent to using a second order, centred finite difference method over the interior while at the domain boundaries, the method is used to represent 'lopped' cells (i.e. cells with a reduced grid length due to topography) in cases where a boundary is not positioned on a regular or smoothly varying grid (Adcroft et al., [1997]. However, in the experimental setup used here, there are no lopped cells since the bottom topography is flat and at the same level as that dictated by the vertical resolution.

The model implements the Arakawa-C staggered horizontal grid (Arakawa [1966]; Arakawa and Lamb [1977]) in which the horizontal velocities, and the tracer (e.g. potential temperature or salinity) variables are all staggered (see Fig 2.1). The pressure is also co-located with the tracer variables. The zonal and meridional velocity points are staggered half a grid space west and south respectively of the tracer points. The vertical velocity points are also staggered half a vertical grid length below the tracer points using a Lorenz grid (Lorenz [1960]), although the vertical grid spacing is non-uniform since the upper ocean has the greatest vertical variation in the variables and thus needs the highest resolution. The tracer points are located at the centre of each finite volume cell (see Table 2.1). This is advantageous since the divergence within each grid box can easily be determined and must be zero in this non-divergent, incompressible ocean setup. The spherical-polar co-ordinates grid is used in this thesis since this is the most applicable to the spherical Earth without the added complexities of using a curvilinear grid.

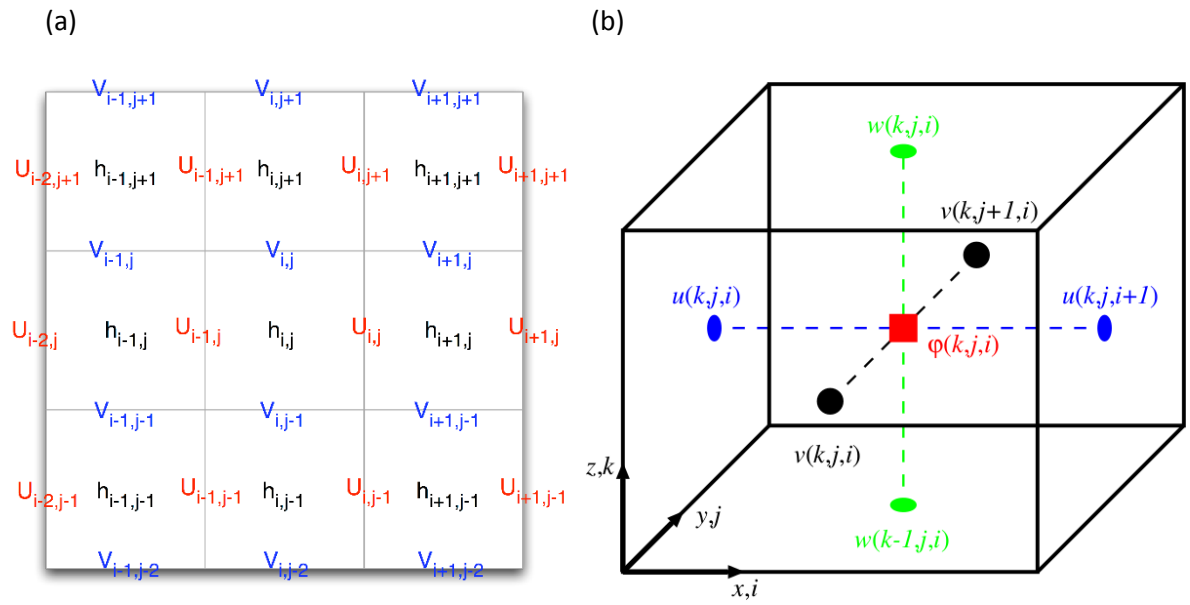

Fig 2.1: a) Arakawa-C horizontal grid with u, v velocities staggered around tracer points, b) Finite volume grid cell showing Arakawa-C staggering of velocities around the cell-centred tracer grid point, with a Lorenz grid in the vertical. ((a) http://www.soest.hawaii.edu/oceanography/courses/OCN681/hw6.html and (b) https://palm.muk.uni-hannover.de/trac/wiki/doc/tec/discret)

The grid in the model setup has an approximate 2.8 degree horizontal resolution and a varying vertical resolution (see Table 2.1). The model has 20 vertical levels in a 4000 m deep ocean. The specified vertical grid (i.e. bottom depth of finite-volume cells) ranges from 50 m deep in the surface layer, to a depth of 4000 m at the bottom of the ocean. The vertical velocity grid points are located at the depths of these specified model grid points, while the tracer points and horizontal (u,v) velocities are staggered above the vertical velocity grid points at mid-depth of the finite-volume cells, since the cell-centred approach is taken.

Level	Bottom depth of cell (m)	Mid-depth of cell (m)	Thickness of cell (m)
1	50	25	50
2	120	85	70
3	210	165	90
4	310	260	100
5	430	370	120
8	590	510	160
6	780	685	190
7	1000	890	220
9	1250	1125	250
10	1500	1375	250
11	1750	1625	250
12	2000	1875	250
13	2250	2125	250
14	2500	2375	250
15	2750	2625	250
16	3000	2875	250
17	3250	3125	250
18	3500	3375	250
19	3750	3625	250
20	4000	3875	250

Table 2.1: Vertical grid spacing showing the bottom and mid-depths of each cell and their corresponding level (where level 1 is the surface layer and level 20 is the lowermost layer) and thickness.

2.3. Momentum Equations

The model solves the momentum equations, tracer equations and equation of state to determine the model variables. Additional equations are solved in the various packages, for example to simulate sea-ice.

The horizontal momentum equations used to determine the evolution of the horizontal velocity components are:

$$\frac{Du}{Dt} - fv + \frac{1}{\rho_0}\frac{\partial P'}{\partial x} - \nabla_h \cdot A_h \nabla_h u - \frac{\partial}{\partial z} A_z \frac{\partial u}{\partial z} = F_u \qquad (2.9)$$

$$\frac{Dv}{Dt} + fu + \frac{1}{\rho_0}\frac{\partial P'}{\partial y} - \nabla_h \cdot A_h \nabla_h v - \frac{\partial}{\partial z} A_z \frac{\partial v}{\partial z} = F_v \qquad (2.10)$$

These terms are the same as in (2.1) except now the zonal and meridional components of the velocity are written separately, and the horizontal and vertical dissipation terms due to the horizontal viscosity, A_h and vertical viscosity, A_z are made explicit (the last two terms on the left handside (LHS) of (2.9) and (2.10)). The surface wind forcing terms on the right handside (RHS) are decribed in Section 2.6, and only apply in the surface layer of the model.

2.4. Free surface boundary condition

The hydrostatic approximation leads to the vertical momentum equation becoming the hydrostatic balance equation, (2.3). (2.3) can be rewritten as a vertical integral over the water column:

$$P'(z) = \int \rho' g \, dz \qquad (2.11)$$

where the atmospheric pressure at depth, z=0 is taken to be the reference pressure at which P'=0.

The choice of boundary condition on the vertical velocity at the surface of the model domain determines how the pressure is solved for to satisfy the continuity equation. In the setup used here, the implicit linear free surface approxmation is implemented.

The vertical velocity, w, is not set to zero since the surface elevation, η, is time dependent in this case, with shallow water waves allowed, although a fixed geometry is still used. Thus, there is an additional contribution to the hydrostatic balance equation due to variations in surface elevation. Thus, (2.11) is rewritten as:

$$P'(z) = \int_{z=-H}^{z=0} \rho' g \, dz + \rho_0 g \eta \tag{2.12}$$

where z = -H is the bottom depth of the ocean and z = 0 is the surface. (2.13) enables the conversion between surface elevation and pressure.

Taking the vertical integral of the continuity equation, (2.4), over the full depth of the water column gives the depth integrated continuity equation:

$$\frac{\partial \eta}{\partial t} + \int_{z=-H}^{z=0} \nabla_h \cdot \boldsymbol{v} \, dz = \mathbf{0} \tag{2.13}$$

where the linear free surface approximation is used (and thus small terms from using z=0 rather than z=η are neglected).

The time variation in surface elevation, $\frac{\partial \eta}{\partial t}$, is equal to the vertical velocity at the surface.

There is no change in the surface elevation due to the net freshwater flux, P-E, in (2.13) since virtual salinity fluxes are used to account for the freshwater flux in our setup, rather than the P-E flux directly changing the surface elevation.

The pressure is solved for by forming an elliptic equation for the surface elevation (which is easily converted to pressure) by substituting the divergence of the horizontal momentum equations into the depth integrated continuity equation, with the pressure in the pressure gradient terms substituted for surface elevation using hydrostatic balance (i.e. P(z=0) = $\rho_0 g\eta$ where the surface depth is zero rather than the free surface elevation) (see Marshall et al. [1997a] for the full equations). The pressure variations due to the free surface perturbations can then be accounted for in the momentum equations which ensures the depth-integrated flow is non-divergent.

The linear free surface approximation does not on its own conserve tracers since the upper level finite volumes (or geometry) are fixed despite the free surface height varying in time to allow for a horizontally divergent depth-integrated flow. Thus, the tracers are not conserved without using a 'surface correction' term which accounts for the surface divergence which now enables both local and global tracer conservation (Campin et al. [2004]; Griffies et al. [2000]) for both the active and passive tracers.

2.5. Active tracer equations

The heat and salinity equations used to determine the evolution of potential temperature, θ, and salinity, S, are:

$$\frac{D\theta}{Dt} - \nabla_h \cdot K_h \nabla_h \theta - \frac{\partial}{\partial z} K_z \frac{\partial \theta}{\partial z} = F_\theta \tag{2.14}$$

$$\frac{DS}{Dt} - \nabla_h \cdot K_h \nabla_h S - \frac{\partial}{\partial z} K_z \frac{\partial S}{\partial z} = F_S \tag{2.15}$$

where the heat and salinity forcing, F_ϑ and F_S respectively are zero except in the surface layer.

The horizontal and vertical dissipative diffusion terms resulting from a horizontal diffusivity, K_h, and a vertical diffusivity, K_z, respectively are written explicitly on the LHS of (2.14) and (2.15). The heat and salinity forcings, F_θ and F_s respectively on the RHS of the equations are zero except in the surface layer. These are decribed in Section 2.6.

2.5.1. Diffusivity profile

The diffusion of heat and salinity smooths out and reduces the spatial gradients in these variables. The horizontal diffusivity is constant throughout the ocean (see Table 2.2). However, the vertical diffusivity varies with depth due to the topographical enhancement of mixing at depth caused by internal wave breaking generating turbulence (Wunsch and Ferrari [2004]), represented using the Bryan and Lewis [1979] background diffusion scheme (BL79) which has a surface vertical diffusivity of approximately 10^{-5} m^2 s^{-1} increasing to approximately $2x10^{-4}$ m^2 s^{-1} at the ocean floor (see Fig 2.2). There is a large increase in vertical diffusivity at about 2 km as observed in the real ocean. The variation in vertical diffusivity with depth using this scheme is calculated as follows:

$$K_z = K_{zsurf} + (K_{zdeep} - K_{zsurf})\left(\frac{\tan^{-1}(-\frac{z - z_{off}}{z_{sc}})}{\pi} + 0.5 \right) \qquad (2.16)$$

where the $\tan^{-1}(x)$ is the inverse tangent function of x, z is the depth taken to be the cell interfaces from the surface to the bottom of the ocean (see Table 2.1), and the remaining parameters are listed in Table 2.2.

Parameter	Value	Units
K_{zsurf}	10^{-5}	$m^2\ s^{-1}$
K_{zdeep}	2×10^{-4}	$m^2\ s^{-1}$
z_{sc} (the depth scale for the inverse tangent function)	150	m
z_{off} (the depth offset for the inverse tangent function)	-2000	m

Table 2.2: Parameters used in the vertical diffusivity profile equation (2.16).

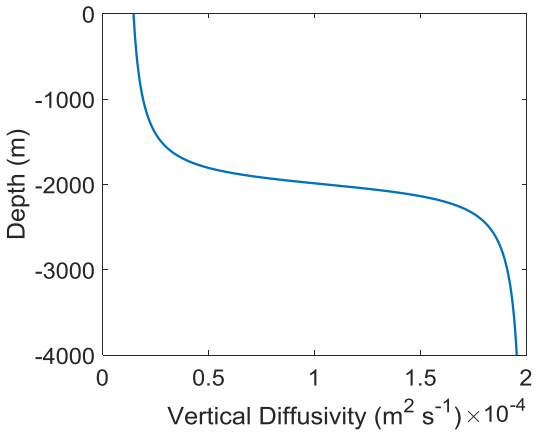

Fig 2.2: The control profile of the Bryan and Lewis [1979] (BL79) vertical diffusivity.

There is also a contribution to the diffusivity from isopycnal diffusion calculated using the REDI scheme described in the Section 2.8.2.

2.6. Surface Forcings

The surface layer of the model is forced by a wind stress (in the momentum equations, (2.9) and (2.10)) and the surface heat and freshwater fluxes (in the heat and salinity equations, (2.14) and (2.15) respectively) with the forcing terms listed below:

$$F_u = \frac{1}{\rho_0}\frac{\partial \tau_x}{\partial z} = \frac{\tau_x}{\rho_0 \Delta z_s} \tag{2.17}$$

$$F_v = \frac{1}{\rho_0}\frac{\partial \tau_y}{\partial z} = \frac{\tau_y}{\rho_0 \Delta z_s} \tag{2.18}$$

$$F_\theta = -\lambda_\theta\,(\theta - \theta^*) + \frac{Q}{C_p \rho_0 \Delta z_s} \tag{2.19}$$

$$F_S = -\lambda_S\,(S - S^*) + \frac{S_0}{\Delta z_s}\,(E - P) \tag{2.20}$$

Each of these forcing terms are functions of time (i.e. seasonal variation) and space which lead to positive or negative time tendencies in the local velocity (m s^{-1}), potential temperature (°C s^{-1}) and salinity ((g/kg) s^{-1}).

The zonal and meridional wind stress (N m^{-2}), τ_x and τ_y respectively, mechanically force the ocean at the sea surface, ρ_0 is the reference density and Δz_s is the depth of the surface layer (50 m in the model setup used here) which represents the depth of the Ekman layer over which the turbulent wind-driven mixing occurs. Thus, the temperature and salinity are assumed to be well mixed in this surface layer and hence the surface heat and salinity forcings act throughout the surface layer.

The surface heat and salinity surface forcings are mixed boundary conditions (Haney [1971] and Mikolajewicz and Maier-Reimer [1994]) with a heat and freshwater flux respectively

(calculated from bulk formulas or prescribed) and a relaxation to a monthly climatological sea surface temperature and salinity respectively. The net heat and salinity fluxes force the ocean by setting the surface buoyancy fluxes. The first terms in (2.19) and (2.20) are the relaxation fluxes to a climatological surface temperature field (ϑ^*) and salinity field (S^*) respectively, with relaxation timescales, τ_ϑ and τ_s. The reciprocal of these relaxation timescales, λ (i.e. $\lambda = 1/\tau$) for sea surface temperature and salinity are λ_θ and λ_S respectively.

The second terms are the temperature and salinity tendencies due to the heat flux, Q (W m^{-2}), and the freshwater flux, E-P (m s^{-1}).

The heat flux, Q, is converted to a temperature time tendency, $\frac{\partial \theta}{\partial t}$, by dividing it by the specific heat capacity of seawater, c_p, the reference density of the ocean, ρ_0, and the surface layer depth, Δz_s. The denominator in (2.19), $c_p \rho_0 \Delta z_s$ is therefore the quantity of heat energy required to increase a unit area of the surface layer by one degree Celsius.

The freshwater flux, E-P, is the net effect of evaporation and precipitation, and also sea-ice effects including brine rejection and freshwater release by the formation and melt of sea-ice respectively (see Section 2.13). The freshwater flux is converted to a virtual salinity flux, $\frac{\partial S}{\partial t}$, by multiplying it by the reference salinity, S_0, and dividing by the surface layer depth, Δz_s. The reference salinity represents the salinity of the surface layer (i.e. rather than the local salinity) which is concentrated or diluted by the fractional rate of change in the water column height, $\frac{\mathrm{E-P}}{\Delta z}$. Thus, if E-P > 0, the salinity flux is positive. The reference salinity rather than the local salinity is used in (2.20) since the virtual salinity flux due to a given air-sea freshwater flux, E-P, will then stay constant even if the local salinity of the surface layer changes which allows us to better ascertain why the circulation changes. The effects of sea-ice can thus be more easily attained since even though the local salinity may change, the air-sea freshwater flux due to evaporation and precipitation will remain the same, except where

sea-ice modifies this flux by reducing the atmosphere-ocean interaction. The virtual salinity flux represents the effects of the freshwater flux on the salinity, rather than the salinity being altered by the direct addition or removal of freshwater which would require the non-linear free surface approximation to be implemented.

The climatological sea surface relaxation temperature, θ^* and salinity, S^*, and the air-sea heat and freshwater fluxes are model inputs, described in more detail in the Section 2.12. The experiments used in Chapter 3, 4 and 5 are slightly different to those in Chapter 6 in which the ocean carbon cycle is simulated. In Chapter 6, the freshwater fluxes (after sea-ice is accounted for) and the relaxation salinity flux are both balanced globally which ensures the salinity is globally conserved, rather than relying on the relaxation flux to prevent the salinity drifting. Although, the change in fluxes using global conservation are likely to be less realistic, it is essential for the virtual salinity flux to be globally balanced when simulating the carbon cycle since it is also used to determine the effects of freshwater fluxes on other passive tracers (McKinley et al. [2004]) as described in Section 2.14**.** The other difference is the use of a small temperature relaxation timescale such that the model surface temperature is equal to the relaxation temperature field. The relaxation temperature is set to the monthly output from the control experiment to cause similar changes in sea-ice and a realistic present-day circulation. This new approach is made so that there are no temperature induced solubility effects on atmospheric CO_2 since the surface temperature is unchanged between experiments. This allows the effects of changes in sea-ice (and consequent circulation changes) on atmospheric CO_2 to be isolated.

The density and thus buoyancy of the ocean is dependent on its temperature, salinity and pressure. The non-linear Jacket and McDougall [1995] equation of state (JMD95z) is implemented in the model, which calculates the density using the potential temperature, salinity and a horizontally homogenous pressure, P, which depends only on depth (i.e.

$P=\rho_0 g\Delta z$). The equation accounts for the non-linear change of density with temperature, salinity and pressure using a high order polynomial. The potential density (i.e. the density a water parcel at a given depth would have at the surface) is used throughout this thesis.

The horizontal velocity components, u and v, potential temperature, ϑ and salinity, S are calculated prognostically using equations (2.9), (2.10), (2.14) and (2.15) while the vertical velocity, w, pressure, P, and density, ρ, is calculated diagnostically (Marshall et al. [1997a]). The vertical velocity is calculated using the continuity equation, (2.4).

The conservation of volume is enforced by the continuity equation, (2.4), and in this case, updating the pressure using the horizontal velocity divergence, accounting for changes in surface elevation, to ensure the flow is non divergent (since the ocean is incompressible).

2.7. Model geometry

As described previously, two geometrical setups are used to simulate the MOC and ocean carbon cycle in this thesis. These are a single-basin and a two-basin model, with a southern circumpolar channel in each model. The model characteristics are described in Table 2.3.

The single-basin model has a basin representative of the Atlantic Ocean with a zonally periodic circumpolar channel in the south between 70°S and 50°S. The basin is confined in the north and south by a zonal boundary. There is a meridional land strip on the western boundary of the basin north of 50°S which closes the basin zonally north of the channel due to the periodic boundary conditions implemented.

Domain characteristics	Model	
	Single-basin	Two-basin
Grid Size of domain(N_x x N_y x N_z)	24 x 52 x 20	68 x 52 x 20
Ocean Depth (m)	4000	4000
Domain Width (degrees)	65°	188°
Single-basin/Atlantic width (degrees)	65°	65°
Pacific width (degrees)	----------	124°
Single-basin/Atlantic latitude range (degrees)	70°S - 73°N	70°S - 73°N
Pacific latitude range (degrees)	----------	70°S - 59°N
Channel latitude range (degrees)	70°S - 50°S	70°S - 50°S
Single-basin/Atlantic area (north of channel) (Km^2)	79 million	79 million
Pacific area (north of channel) (Km^2)	----------	143 million

Table 2.3: Model domain characteristics of the single and two-basin models. All values are given to zero decimal places.

The two-basin model has an Atlantic basin, the same size as that of the single-basin model but with an additional wider Pacific basin and a wider southern channel. The basins are connected by a circumpolar channel which has the same latitudinal extent as in the single-basin model. Both model domains have a meridional land strip with a southernmost latitude of ~50°S, representative of the southern extent of South America, while the two-basin model has an additional meridional land strip, with a southernmost latitude of ~36°S representative

of South Africa. These land strips are referred to herein as the 'South America' and 'South Africa' landstrips respectively, zonally separating the Atlantic and Pacific basins resulting in the same width Atlantic basin of 65 degrees as in the single-basin model, and a wider 124 degrees Pacific basin. The Pacific and Atlantic basin areas are defined as the areas of the ocean north of the circumpolar channel within the Atlantic and Pacific sectors respectively. The basin areas are smaller than reality but a good approximation, with an Atlantic basin area of about 79 million Km^2 and a Pacific basin area of about 143 million Km^2, with average basin widths (since the longitudinal width decreases polewards of the equator) of ~11,770 Km and ~5800 Km. The Atlantic basin has an area about 55% the size of the Pacific basin (i.e. the Pacific is 1.8 times larger). In reality, this percentage is about 66% (i.e. the Pacific is only 1.46 times larger than the Atlantic). Thus, the Pacific is larger relative to the Atlantic than in the real world but the model provides a good approximation and is thus applicable to the present-day and glacial ocean (all be it with many geometric simplifications).

2.8. Meridional overturning streamfunction

Both the Eulerian-mean and eddy-induced meridional overturning streamfunctions must be calculated offline since they are not model outputs. These streamfunctions represent the zonally integrated meridional-vertical transport over the whole domain or a basin by the time-mean flow and eddies respectively. The Eulerian-mean streamfunction is calculated in this thesis by integrating the meridional velocity zonally over the domain or a basin, and vertically from the ocean floor to the surface. The streamfunction is set to zero at the northern and southern boundaries, since there is no flow through the boundaries and thus the conservation of mass is satisfied.

2.8.1. Eulerian-mean overturning streamfunction

The Eulerian mean streamfunction, ψ, is thus calculated at each latitude, φ, defined on the meridional velocity grid as,

$$\psi(\varphi, z) = \int_{z=-H}^{z=0} \bar{v}\, dz \tag{2.21}$$

where $\bar{v}$ is the zonally-integrated meridional velocity over the width of the domain or basin, L, at latitude, φ,

$$\bar{v} = \int_{x=0}^{x=L} v\, dx \tag{2.22}$$

The zonal grid spacing, Δx, is required to calculate the zonal integral of v in (2.22). The zonal grid spacing, Δx, at latitude, φ is:

$$\Delta x = \frac{2\pi R\, cos(\phi)}{nx} \tag{2.23}$$

where R = 6.4×10^6 m is the radius of the Earth,

and nx = 128, the number of zonal grid points required for the model to be global in longitude, given the approximate 2.8° horizontal model resolution.

2.8.2. Eddy-induced overturning streamfunction

The coarse ~2.8° horizontal resolution used in this model setup does not allow mesoscale eddies to be resolved and thus the eddy effects must be parameterised (Gough and Allakhverdova [1998]).

The Gent-McWilliams (GM) eddy parameterisation (Gent and McWilliams [1990]; Gent et al. [1995]) is used to determine the 'bolus' or eddy-induced velocity which represents the advective effect of geostrophic eddies in the flow. This eddy-induced circulation acts to flatten the isopycnals due to baroclinic instability, converting available potential energy to eddy kinetic energy. The Redi scheme (Redi [1982]) is used to diffuse tracers along isopycnals to represent the isopycnal mixing effects of eddies. The Griffie's skew flux (Griffies [1998]) form is applied in the model used here which enables the GM and Redi parameterisations to be combined by rewriting the GM parameterisation as a non-divergent flux (which has no effect on tracers) and a skew-flux. The result is a single tensor, the GM-Redi tensor, which represents the effects of eddies on tracers. This tensor is simplified if the diffusivities used in the GM and Redi mixing schemes are equal which is the case in the model setup used here. The small slope approximation is used to simplify the Redi scheme tensor. Thus, the GM-Redi mixing tensor, $K_{GM\text{-}REDI}$ is a simple tensor containing the thickness diffusivity, κ, (horizontally constant in this model) and the isopycnal slope, S, along with its components in the zonal and meridional planes (S_x and S_y respectively). The parameters used in the GM-Redi parametrisation in the model are described in Section 2.11.2. The GM-Redi tensor is:

$$K_{GM-REDI} = \kappa_{GM} \begin{pmatrix} 1 & 0 & 0 \\ 0 & 1 & 0 \\ 2S_x & 2S_y & |S^2| \end{pmatrix} \tag{2.24}$$

The GM-Redi tensor components, $K_{GM\text{-}REDI}(3, 1)$ and $K_{GM\text{-}REDI}(3, 2)$ (where $K_{GM\text{-}REDI}(i, j)$ is the i^{th} row and j^{th} column of the tensor) in (2.24) are model outputs used to determine the bolus velocity components in the horizontal and vertical. These components are:

$$K_{GM-REDI}(3,1) = 2\kappa_{GM} S_x \tag{2.25}$$

$$K_{GM-REDI}(3,2) = 2\kappa_{GM} S_y \tag{2.26}$$

The bolus velocity vector, **V***, is defined as:

$$\boldsymbol{V}^* = \begin{pmatrix} u^* \\ v^* \\ w^* \end{pmatrix} = \kappa_{GM} \begin{pmatrix} -\partial_z(\kappa_{GM}\, S_x) \\ -\partial_z(\kappa_{GM}\, S_y) \\ \partial_x(\kappa_{GM}\, S_x) + \partial_y(\kappa_{GM}\, S_y) \end{pmatrix} \tag{2.27}$$

Thus, using (2.26) and (2.27), the meridional bolus velocity, v*, is:

$$v^* = -\frac{\partial(\kappa_{GM}\, S_y)}{\partial z} = -\frac{\partial}{\partial z}\left(\frac{K_{GM-REDI}(3,2)}{2}\right) \tag{2.28}$$

The $K_{GM\text{-}REDI}(3, 2)$ component model output is divided by two in (2.28) since we only want the GM skew-diffusive flux, not the Redi-diffusive flux to calculate the eddy-induced velocity and streamfunction.

The eddy-induced streamfunction is calculated in the same way as the Eulerian-mean streamfunction in (2.21) above but now using the bolus meridional velocity, v*, instead of the time-mean meridional velocity, v.

2.9. Gridding and interpolation for plotting variables

Using the correct grid (i.e. the correct vertical and horizontal co-ordinates of variables) is essential when calculating the streamfunction since using an incorrect grid not only leads to an error in the position of the streamfunction, but also an error in its magnitude since grid spacing varies with depth. For example, if the meridional velocity is large at two adjacent vertical grid points, the streamfunction will vary significantly over this depth if the grid spacing between them is large, whereas it will only change slightly if the grid spacing is small. The inaccuracy in the depth rate of change of the streamfunction when using an inaccurate vertical grid is most notable near the bottom of the ocean where the vertical grid

spacing is greatest and also in the region where the meridional velocity has its highest magnitude.

The GM-Redi meridional tensor component ($K_{GM\text{-}REDI}(3, 2)$) described in Section 2.8.2, is defined on the same grid as the vertical velocity points. Thus the eddy-induced velocity (the vertical derivatives of this GM-Redi tensor component) grid points are at the same depth as the time-mean meridional velocitiy points. However, the mean meridional velocity is staggered horizontally by half a grid space to the south of the eddy-induced meridional velocity. The southernmost meridional velocity grid point is half a grid space to the south of the southern boundary of the model. The meridional velocity is therefore always zero at the two southernmost grid points due to the southernmost point within the ocean domain also being zero to prevent a flow through the boundary, whereas only the northernmost point has a value of zero in the north. The eddy-induced meridional velocity is only zero at the southern and northernmost points since these are at the zonal boundaries. The grid used to plot the streamfunction is the meridional velocity grid with the southernmost grid point ignored since it is outside the ocean basin domain. Thus, this grid ranges in latitude from ~68.59°S to ~72.03°N.

The eddy-induced velocity is on the tracer grid, ranging in latitude from 70°S to ~73.44°N. Thus, in order to plot the residual streamfunction, we must know the mean and eddy-induced meridional velocities and their streamfunctions at the same latitudes. In this thesis, this is attained by linearly interpolating (or averaging) both the mean and eddy-induced meridional velocities to the adjacent grid (i.e. half a model grid space meridionally). Therefore, these velocities have interpolated values at a meridional resolution of ~1.4 degrees. The advantage of this approach is that the interpolation does not lead to a reduction in the magnitudes of either of the velocity components or their streamfunctions (the maxima's are maintained). This is significant since the eddy-induced streamfunction was found to vary on the order of a

few Sverdrups when only the values on the meridional velocity grid (i.e. only the interpolated eddy-induced velocities) are used to plot the streamfunction.

The new plotting grid for both the mean and eddy-induced velocities has a latitude range from ~68.59°S to ~72.03°N (i.e. the meridional velocity grid when the southernmost grid point is ignored), but the grid spacing is now ~1.4 degrees. The northern and southern grid points of the original eddy-induced velocity grid are zero since they are located at the ocean basin boundaries. However, the plotting grid ends half a grid point equatorward of these points. Thus, in order to have a zero eddy-induced meridional velocity and streamfunction at the northern and southern boundaries of the interpolated grid, the northern and southernmost eddy-induced meridional velocity values on this grid are also set to zero which closes the eddy-induced streamfunction on this new grid. This also makes physical sense since the time-mean meridional velocity and thus streamfunction are zero at these points.

Both the mean and eddy-induced meridional velocities are interpolated linearly in the vertical to a new grid between depths of 0 and 4000 m with a vertical grid spacing of 10 m. This vertical interpolation smooths the velocities which leads to a more accurate streamfunction being calculated since the velocities vary gradually with depth rather than having sudden jumps, which would be the case if only the model output velocities were used with no interpolation. The vertical rates of change in the streamfunction in particular will be more accurate when using this high resolution vertical interpolation grid and the streamfunction varies smoothly. The vertical grid resolution of the interpolation was chosen to be 10 m since in addition to giving more accurate streamfunction rates of change, the local velocity extrema and hence streamfunction extrema at the grid points are not reduced through the interpolation due to the high resolution relative to the original model grid.

The zonal-average potential density which is imposed on the streamfunction plots is calculated from the potential temperature and salinity using the equation of state described in Section 2.6. It is defined on the tracer grid which is therefore the same grid as the eddy-induced meridional velocity grid prior to interpolation. The same linear vertical interpolation of the zonal average potential density is used as for the meridional velocities with a 10 m vertical resolution. However, it cannot be interpolated to the surface or to the bottom since the values are only output at grid points ranging in depth from 25 m to 3875 m and there is no lower boundary condition in contrast to the meridional velocities (these are zero at the bottom due to a no-slip boundary condition being imposed). The potential density is undefined at the northern and southern boundaries (i.e. where there is no land) and therefore the potential density is only plotted half a grid point equatorward of the northern and southern boundaries of the grid used for plotting the streamfunction described above.

2.10. Physical model parameters

The physical parameter values used in the model are listed in Table 2.4.

Parameter	Value	Units	Symbol
Time step of momentum equations	900	s	Δt_{mom}
Time step of tracer	43200	s	Δt_{tracer}
Vertical diffusivity	BL79 distribution (Surf:10^{-5} m^2 s^{-1}, Base: $2x10^{-4}$ m^2 s^{-1})	m^2 s^{-1}	κ_z
Horizontal eddy viscocity	2 X 10^5	m^2 s^{-1}	κ_h
Vertical eddy viscocity	1 x 10^{-3}	m^2 s^{-1}	A_z
Implicit vertical diffusivity for convection	100	m^2 s^{-1}	κ_{conv}
Reference density of seawater	1035	kg m^{-3}	ρ_0
Density of fresh water	1000	kg m^{-3}	ρ_{fresh}
Reference salinity	35	g/Kg	S_0
Specific heat capacity of water	3994	J kg^{-1} K^{-1}	c_p
Acceleration due to gravity	9.81	ms^{-2}	g
Temperature relaxation timescale	5184000 (3 months)	s	τ_θ (=$1/\lambda_\theta$)
Salinity relaxation timescale	62208000 (2 years)	s	τ_S (=$1/\lambda_S$)

Table 2.4: Physical model parameter values

2.11. Model Parameterisations

2.11.1. Convection

The convection is parameterised by adding a convective diffusivity (the implicit vertical diffusivity for convection, κ_{conv}) to the background vertical diffusivity (i.e. (2.16)) at a particular depth if the density in the two vertically adjacent layers is greater in the upper layer (i.e. if the density decreases with depth). Thus, the enhanced mixing of properties in these convective regions is parameterised in the model.

2.11.2. Eddy parameterisation

The model implementation of the GM-Redi parameterisation which is used to represent eddy effects as described in Section 2.8.2 is now described including the parameters used in the scheme and how eddies are treated in regions of low stratification.

The GM-Redi scheme parameters used in the model are described in Table 2.5.

Parameter	Value
GM 'background' (thickness) diffusivity (κ_{GM})	1×10^3 m^2 s^{-1}
Maximum isopycnal slope (S_{max})	1×10^{-2}
Minimum horizontal diffusivity	100 m^2 s^{-1}
GM Taper scheme	Gerdes et al. [1991]

Table 2.5: GM-Redi scheme parameters

A maximum isopycnal slope, S_{max}, can be set to prevent the vertical GM-Redi isopycnal mixing fluxes becoming unphysically large or infinite in unstratified regions which causes numerical instability. However, even when the magnitude of isopycnal slopes are limited

below a specified maximum slope, the vertical GM-Redi flux can still be very large and lead to unrealistically fast re-stratification, and this also introduces diabatic fluxes (in contrast to the adiabatic nature of the GM-Redi parameterisation). Thus, in the model setup used here the Gerdes et al. [1991] tapering scheme is used in which the whole GM-Redi tensor, (2.24), is scaled down by a tapering function, $f(S)$, if the isopycnal slope, S, is greater than the maximum slope, S_{max}. The direction of the GM-Redi flux is unchanged with only the magnitude reduced to prevent unrealistically large vertical fluxes.

The tapering function, $f(S)$ is:

$$f(S) = min\left[1, \left(\frac{S_{max}}{|S|}\right)^2\right] \tag{2.29}$$

where S_{max} is the maximum isopycnal slope and $|S|$ is absolute value of the actual isopycnal slope.

Thus, $f(S) = 1$ if $S < S_{max}$,

$f(S) = \left(\frac{S_{max}}{|S|}\right)^2$ if $S \geq S_{max}$

The GM-Redi tensor used to determine the GM-Redi diffusive fluxes and the 'bolus' eddy-induced velocity, is scaled by $f(S)$ such that the tensor, $K_{GM\text{-}REDI}$, becomes $f(S)\ K_{GM\text{-}REDI}$.

2.12. Model Data Inputs

2.12.1. Model datasets

The model is forced at the surface by a wind stress (Fig 3.1b), and heat and freshwater fluxes (Fig 3.6b), as described in Section 2.6**.** In the model setup used here, atmospheric quantities must be provided as inputs at the ocean surface to calculate these forcings. The inputs used in the proceeding chapters are zonal-averages (over the real world Atlantic and Pacific basins)

of the climatological monthly averaged National Centers for Environmental Prediction–National Center for Atmospheric Research (NCEP–NCAR) reanalysis data over the period 1981-2010 (Kalnay et al. [1996]), or perturations to these forcings (for the wind and diffusivity experiments in Chapter 4), and the surface temperature and salinity are also relaxed to observed distributions (Levitus and T.P.Boyer [1994a,b]). The NCEP forcings used are the downward shortwave and longwave radiation at the surface, the precipitation and evaporation rate, atmospheric temperature and specific humidity at 2 m, the wind speed and the zonal and meridional wind speed components at 10 m. The NCEP surface heat and freshwater fluxes and relaxation fluxes are combined to form mixed boundary conditions as described by Haney [1971] and Mikolajewicz and Maier-Reimer [1994] (i.e. (2.19) and (2.20)).

2.12.2. Conversion to model grid inputs

The NCEP data has a 2.5° resolution and is therefore interpolated to a 2.8° latitude-longitude grid.

As described above, the inputs are zonal-averages of the NCEP reanalysis data with the zonal averages applied separately over the Atlantic and Pacific sectors of the dataset (the single-basin model uses the same inputs as the Atlantic sector of the two-basin model). The Atlantic and Pacific sector inputs are obtained by zonally-averaging the global data sets over the following areas. For the Atlantic sector inputs, the southern circumpolar channel is closed off in the east at a longitude of 22.5°E corresponding to the southern tip of South Africa, and in the west at 70°W (290°E), corresponding to the southern tip of South America. In the Pacific, the re-entrant channel is closed off at 152.5°E in the west and 70°W (290°E) in the east. The Pacific sector inputs also have to be closed off at the Indonesian throughflow (between Australia and Indonesia) which is closed off at 113°E, north-west of Australia. These land

masks are used to determine the inputs in the Atlantic and Pacific sectors by zonally-averaging the global inputs over the area these masks define. However, only the values between 70°S and 73°N (the latitude range of the models) are used.

Model runs were also performed using inputs covering the full latitude range of the global ocean (e.g. 80°S to 80°N in the Atlantic Ocean) in the model domains described by interpolating and squeezing these global inputs to create new inputs with a reduced number of grid points (appropriate for the model) which are applied over the latitude range of the model (i.e. 70°S to 73°N). The main consequence of this change is the convection in the northern latitudes of the single-basin model and Atlantic sector of the two-basin model occur over several of the most northern grid points, rather than being confined to the northern boundary. This is likely due to the surface being denser at these northern latitudes under these forcing inputs. Since open sea convection is rarely observed in the North Atlantic, convection confined to the northern boundary is more realistic.

2.12.3. Bulk Formulae

The surface wind stress and the various components of the heat flux are calculated using bulk formulae. The freshwater flux is imposed as a virtual salinity flux. The salinity relaxation timescale is set to enable changes in sea-ice brine fluxes to have a realistic effect on the ocean buoyancy, rather than relaxation fluxes dominating the freshwater flux. The bulk formulae and virtual salinity flux are described below.

The wind stress is calculated from the 10 m wind speed and the zonal and meridional wind speed components, rather than being provided as an input since the sea-ice model requires the wind speed. The wind stress is calculated as follows:

$$u_{stress} = \rho_a \, c_d \, |\vec{v}| \, u_{wind} \tag{2.30}$$

$$v_{stress} = \rho_a \, c_d \, |\vec{v}| \, v_{wind} \tag{2.31}$$

where ρ_a is the mean atmospheric density (1.2 Kg m^{-3}), c_d is the neutral drag coefficient which is itself a function of the wind speed and the drag coefficients, and $|\vec{v}|$, u_{wind} and v_{wind} are the 10 m wind speed, and the zonal and meridional wind speed components respectively which are all model inputs.

The net surface heat flux is determined by combining the various atmosphere-ocean heat exchange processes, these are the radiative transfers (net longwave and shortwave radiation) and the latent and sensible heat fluxes.

The net longwave radiation is calculated by combining the downward longwave radiation, LW_{down}, a model input, and the upward longwave radiation, LW_{up}. LW_{up} is calculated using the surface temperature and the surface emissivity as follows:

$$LW_{up} = \varepsilon \sigma T^4 + \beta \, LW_{down} \tag{2.32}$$

where ε is the emissivity of the surface, and β is the reflectivity of the surface to longwave radiation. The transmissivity of the surface layer is set to zero (i.e. longwave radiation does not penetrate the surface) and thus ε = 1 - β to conserve energy.

The net shortwave (or solar) radiation, SW_{net}, absorbed by the surface is more complex to calculate since some of the incoming shortwave radiation is transmitted through the surface to lower layers in the model. The surface albedo is accounted for to determine the amount of solar radiation that is either absorbed by or transmitted through the surface as follows:

$$SW_{net} = -SW_{down}(1 - \alpha) \tag{2.33}$$

where SW_{down} is the downward shortwave radiation at the surface, a model input, and α is the albedo of the ocean (set to 0.066), although it increases in sea-ice regions as described in Section 2.13.

The solar radiation transmitted to depth, z, I(z), is calculated using the model of Paulson and Simpson [1977] which predicts the variation of solar radiation with depth using (2.34), an equation guided by observations which shows the solar radiation has an exponential decay with depth below 10 m depth (Jerlov [1968]). The equation used in the model assumes the surface water type IA (relatively clear) derived by Jerlov [1968] which is characteristic of water deeper than 10 m.

$$\frac{I(z)}{I_0} = \mathrm{Re}^{-\frac{z}{\zeta_1}} + (1-R)\mathrm{e}^{-\frac{z}{\zeta_2}} \qquad (2.34)$$

where I_0 is the solar radiation absorbed by or penetrating the surface (i.e. not reflected) which is equal to SW_{net} in (2.33), R=0.62, and the attenuation lengths are ζ_1 = 0.6 m and ζ_2 = 20 m. It is assumed that no shortwave radiation penetrates below a depth of 200 m. The fraction of shortwave radiation penetrating the 50 m deep surface layer is therefore ~0.03.

The net surface heat flux, Q, is then calculated by adding the latent and sensible heat flux, LH and SH respectively, to the net radiative flux. Thus:

$$Q = SW_{net} + LW_{net} - SH - LH \qquad (2.35)$$

where the following convention is used: $SW_{net} > 0$ if there is a net downward shortwave flux,

$LW_{net} > 0$ if there is a net downward longwave flux,

In this case SW_{net} is the net shortwave radiation after removing the radiation transmitted through the base of the surface layer. The effects of sea-ice on each of these fluxes is

calculated by the sea-ice package (i.e. reducing the exchange between the atmosphere and ocean in sea-ice regions in addition to heat transfer from se-ice growth and melt).

The salinity and temperature flux (both the actual fluxes and the relaxation fluxes described in Section 2.6) are converted to a buoyancy flux, $\frac{\partial b}{\partial t}$, as follows:

$$\frac{\partial b}{\partial t} = g\alpha \frac{\partial T}{\partial t} - g\beta \frac{\partial S}{\partial t} \tag{2.36}$$

which can be rewritten as:

$$\frac{\partial b}{\partial t} = \frac{g\alpha}{\rho_0 c_p \Delta z} (Q + T_{relax}) - \frac{g\beta}{\rho_0 \Delta z} ((E-P)_{flux} + S_{relax}) \tag{2.37}$$

where Q (W m^{-2}) and TRELAX (W m^{-2}) are the net heat flux calculated by the model and the climatological temperature relaxation flux respectively, and $(E\text{-}P)_{flux}$ and SRELAX are the salinity flux due to the freshwater flux, E-P, and the climatological salinity relaxation flux respectively (both with units [g m^{-2} s^{-1}]).

The net freshwater flux, E-P, is imposed in the model as a virtual salinity flux with the $(E-P)_{flux}$ (i.e. the virtual salinity flux [g m^{-2} s^{-1}] due to E-P) in (2.37) calculated from the net freshwater flux [m s^{-1}] as follows:

$$(E-P)_{flux} = S_0 \rho_0 (E-P) \tag{2.38}$$

where S_0 and ρ_0 are the reference salinity and density of seawater listed in Table 2.4.

2.13. Sea-ice model

A sea-ice model is coupled to the ocean model described previously and the biogeochemistry model described later (Section 2.14) enabling the effects of changes in sea-ice on the MOC

and carbon cycle to be studied. Sea-ice is simulated using a fully coupled dynamic-thermodynamic model which accounts for the effects of sea-ice on the buoyancy fluxes. It is based on the non-linear dynamic-thermodynamic sea-ice model with viscous-plastic rheology first employed by Hibler [1979] and modified for efficiency by Zhang and Hibler [1997], and more recently by Losch et al. [2010] for use in coupled ice-ocean models. The ice dynamics assumes a viscous-plastic rheology with the nonlinear momentum equations solved using the Line Successive (over) Relaxation (LSR) algorithm (Zhang and Hibler [1997]), an iterative Picard solver. The zero-layer thermodynamics of Hibler [1980] is used for the sea-ice thermodynamics which assumes a zero heat capacity layer, thus leading to an exaggerated seasonal cycle in sea-ice thickness, since all of the absorbed radiation is used to melt sea-ice.

The sea-ice model alters the surface wind stress, heat and freshwater fluxes in sea-ice regions and hence changes the surface wind and buoyancy forcing.

The net shortwave radiation is calculated from the downward shortwave radiation using (2.33) where the surface albedo determines the magnitude of shortwave radiation reflected at the surface. The albedo is 0.066 over open ocean, whereas in regions of sea-ice the albedo increases, varying from 0.66 for wet ice to 0.84 for dry snow.

The values set for some of the important parameters in the sea-ice model are listed in Table 2.6.

Parameter	Value	Units
Sea-ice freezing point	-1.96	°C
Sea-ice salinity	4	ppt
Number of ice categories (levels) for thermodynamics	7	-------
Wet ice albedo temperature	0	°C

Table 2.6: Parameter values used in the sea-ice model.

The brine and freshwater fluxes from sea-ice formation and melt respectively are determined from the change in the area-averaged thickness of sea-ice, h, a model variable calculated for each grid point at the surface.

The salinity flux due to sea-ice formation and melt assumes a constant sea-ice salinity, S_{ice}, of 4 ppt and also uses the reference ocean salinity, S_0, of 35 ppt rather than the local salinity when calculating the virtual salinity flux (as was also the case in (2.38)). The change in sea-ice thickness, h, (or sea-ice growth) due to various thermodynamic and dynamic processes including sea-ice advection is calculated. The equivalent flux of E-P [m s^{-1}] due to sea-ice growth is then calculated using (2.39) by converting changes in sea-ice thickness, h, to the equivalent change in ocean column depth:

$$E - P = \frac{\partial h}{\partial t} \frac{\rho_{ice}}{\rho_{fresh}} \tag{2.39}$$

where the density of sea-ice, $\rho_{ice} = 0.91 \times 10^3$ Kg m^{-3} and the density of freshwater, $\rho_{fresh}=10^3$ Kg m^{-3}.

Thus, the equivalent E-P flux from sea-ice growth will be positive if sea-ice grows and negative if sea-ice melts. This equivalent E-P flux can be converted to a virtual salinity flux [g m^{-2} s^{-1}] as follows:

$$\frac{\partial S}{\partial t} = (E - P)(S_0 - S_{ice})\rho_0 \tag{2.40}$$

where S_{ice} is the salinity of sea-ice and ρ_0 is the reference density of seawater. This conversion is the same as that used in (2.38) to determine the virtual salinity flux from the actual evaporation and precipitation, except in (2.40) this flux is reduced due to sea-ice being slightly saline in contrast to the precipitated and evaporated freshwater.

2.14. Ocean biogeochemistry model

The physical model described thus far is coupled to a biogeochemistry model (Dutkiewicz et al. [2005]; Parekh et al. [2005]) enabling the advective and diffusive transport of passive tracers to be simulated. The biogeochemistry model used here is based on the setup of Lauderdale et al. [2012] which follows on from the MITgcm biogeochemistry tutorial. It enables the carbon cycle to be represented and thus atmospheric CO_2 concentrations can be calculated.

2.14.1. Passive tracer equations

The biogeochemistry model simulates the distribution of 5 passive tracers, these are the dissolved inorganic carbon (DIC), inorganic phosphate (PO_4), dissolved organic phosphate (DOP), oxygen (O_2) and total alkalinity (A^T or TA).

The equation governing the evolution of these passive tracers is similar to the heat and salinity equations ((2.14) and (2.15)), except the source and sink terms are different for each passive tracer. The evolution equation for passive tracer, A, is:

$$\frac{\partial A}{\partial t} = -\vec{\boldsymbol{v}} \cdot \nabla \mathrm{A} - \nabla_h \cdot K_h \nabla_h A - \frac{\partial}{\partial z} K_z \frac{\partial A}{\partial z} + S_A \qquad (2.41)$$

where $\frac{\partial A}{\partial t}$ is the local time rate of change in tracer A,

$-\vec{\boldsymbol{v}} \cdot \nabla \mathrm{A}$ is the advection of A by the residual velocity, $\vec{\boldsymbol{v}}$,

$\nabla_h \cdot K_h \nabla_h A$ and $\frac{\partial}{\partial z} K_z \frac{\partial A}{\partial z}$ are the horizontal and vertical diffusive transport components of A respectively where the horizontal and vertical components of diffusivity, K_h and K_z, have the same value as in the heat and salinity equations (see Table 2.4),

S_A are the sources and sinks of tracer, A, due to biological and chemical processes.

The key parameters set in the biogeochemistry model used in this thesis are listed in Table 2.7.

Parameter Name	Value	Unit	Symbol
Reciprocal timescale for biological activity	6.43×10^{-11}	s^{-1}	τ_{bio}
Remineralisation power law coefficient	0.9		K_{remin}
Minimum depth of biological activity	500	m	z_{crit}
New production converted to DOP	67	%	f_{DOP}
Remineralisation rate of DOP	6.43×10^{-8}	s^{-1}	λ_{remin}
Rain ratio of inorganic to organic C	0.07		RR
Redfield ratio (C:N:P:O)	117:16:1:-170		R
Half saturation constant of PO_4	5×10^{-4}	mol/m^3	K_{PO4}
Fraction of light that is PAR	0.4		I_{PAR}
Light Attenuation coefficient	0.02	m^{-1}	c_I
Half Saturation constant of Light	30	$W\ m^{-2}$	K_I
Critical O_2 concentration	4×10^{-3}	mol/m^3	O_{2crit}
Scale depth of $CaCO_3$ remineralisation	3500	m	d_{CaCO3}

Table 2.7: Parameters used in the biogeochemistry model. Note: PAR is the photosynthetically active radiation.

2.14.2. Parameterisation of biological production

The biological productivity is parameterised in the model as follows:

$$J_{prod} = \alpha(\ lightlim * nutlim) \tag{2.42}$$

where α is the maximum community production or it can be thought of as the reciprocal of the timescale for biological activity which is how it is referred to throughout this thesis, and lightlim and nutlim are the limitations due to light and nutrient availability respectively. These limitations are calculated as follows:

$$lightlim = \frac{I_{PAR}}{(I_{PAR} + K_I)} \tag{2.43}$$

where I_{PAR} is the photosynthetically active radiation (PAR), (i.e. the fraction of Q_{sw} that is PAR) accounting for sea-ice (computed within the sea-ice model with the option to provide the fraction of sea-ice, f_I, as an input rather than using the sea-ice model), and K_I is the half saturation constant of light.

The limitation due to nutrients, nutlim is:

$$nutlim = \frac{[PO_4]}{([PO_4] + K_{PO4})} \tag{2.44}$$

where $[PO_4]$ is the concentration of PO_4 and K_{PO4} is the half saturation constant of PO_4.

The nutrient limit is only dependent on PO_4 in this setup since iron is not simulated.

Photosynthesis by phytoplankton and other species during biological production uses carbon, nitrogen and inorganic phosphate in the process and releases oxygen. These elements are assumed to be used at a constant ratio, the Redfield ratio (first proposed by Redfield et al.

[1963] with several studies suggesting modifications to this ratio (e.g. Takahashi et al. [1985]; Broecker et al. [1985]; Peng and Broecker [1987]; Martin et al. [1989]; Anderson and Sarmiento [1994])), set at 117:16:1:-170 which is the ratio of Carbon: Nitrogen: Phosphate: Oxygen (C:N:P:O). Thus, the change in PO_4 due to biological production can be used to attain the change in these other elements. The PO_4 used during biological production is exported either as dissolved organic phosphorus (DOP) or as particulate organic phosphorus (POP), which are remineralised at varying rates as described below.

2.14.3. Sources and Sinks of Passive tracers

The sources and sinks for each of the passive tracers in the biogeochemistry model will now be described in turn. The notation used in the following equations to represent the concentration of a tracer, x, is [x].

2.14.3.1. Dissolved Organic Phosphorus (DOP) and Inorganic Phosphate (PO_4)

Firstly, the sources and sinks of DOP, S_{DOP} are:

$$S_{DOP} = f_{DOP} J_{prod} - \lambda_{remin}[DOP] \quad (2.45)$$

where f_{DOP} is the fraction of productivity that remains suspended in the water column as DOP, J_{prod} is the biological productivity, λ_{remin} is the remineralisation rate of DOP to PO_4.

Thus, $f_{DOP} J_{prod}$ is the source of DOP due to biological productivity and $-\lambda_{remin}$[DOP] is the sink of DOP due to the remineralisation of DOP to PO_4.

Inorganic phosphate, PO_4, is removed during biological production with a proportion being converted to DOP, $f_{DOP} J_{prod}$ as in (2.45) above. The remaining PO_4 used during biological production is converted to POP, which sinks through the water column and is instantaneously remineralised in this model, accumulating at different depths. The vertical flux of POP, F_p, is

parameterised using a power law relationship (see (2.49)) set so that the flux decreases with depth due to remineralisation. This instantaneous remineralisation of POP is a reasonable assumption given that the particulate sinking time (about 1 month) is far shorter than the 1-100 year advective timescales over the basin (Najjar and Orr [1998]). The remineralisation of DOP, $\lambda_{remin}[DOP]$, is a source of PO_4, again the opposite sign to the same term in (2.45). The sources and sinks of PO_4 are:

$$S_{PO4} = -f_{DOP}J_{prod} - \frac{\partial F_P}{\partial z} + \lambda_{remin}[DOP] \tag{2.46}$$

where $\frac{\partial F_P}{\partial z}$ is the sum of the accumulation of remineralised POP with depth and the POP flux due to production if the layer is biologically productive, with the net loss or accumulation due to the flux of POP, F_p, from the bottom of a given layer being defined in (2.51).

The PO_4 flux from a given layer due to the flux of POP during biological production, F_{pprod}, is

$$F_{pprod} = (1 - f_{DOP})J_{prod}\Delta z \tag{2.47}$$

where Δz is the depth of the biologically productive layer.

The loss of PO_4 due to the sinking of POP produced in a given layer is determined by assuming a zero flux at the top of the layer since only the production in this layer is being accounted for in F_{pprod}. Thus,

$$-\frac{\partial F_{Pprod}}{\partial z} = \frac{(0 - (1 - f_{DOP})J_{prod}\Delta z)}{\Delta z} = -(1 - f_{DOP})J_{prod} \tag{2.48}$$

The accumulation of remineralised POP in each layer below a specified biologically productive layer, $-\frac{\partial F_{Ptransfer}}{\partial z}$, is now described, where $F_{ptransfer}$ is the POP flux into a given

layer due to production in the biologically productive layer. In the specified biologically productive layer (and all layers above), $F_{ptransfer}$ is assumed to be zero.

In the layers below each biologically productive layer (with bottom depth, z_c, and thickness, Δz) from which the accumulation of remineralised POP is being calculated (Dutkiewicz et al. [2005]), the flux of POP into the layer directly below is equal to F_{pprod} (i.e. $F_{ptransfer} = F_{pprod}$). In all deeper layers, the flux through the upper boundary of the given layer at depth, z, is

$$F_{ptransfer} = (1 - f_{DOP}) J_{prod} \Delta z \left(\frac{z}{z_c}\right)^{-\alpha_{remin}} \tag{2.49}$$

where the power law coefficient, $\alpha_{remin} = 0.9$, a value giving remineralisation length scales of a few hundred metres, determined using sediment trap data (Martin et al. [1987]) and modelled phosphate distributions (Yamanaka and Tajika [1997]).

Thus adding up the flux of POP into each layer from all biologically productive layers gives:

$$F_{ptrantot} = \sum F_{ptransfer} \tag{2.50}$$

Thus, the net source/sink of PO_4 due to POP production, transfer and remineralisation, F_p, is:

$$-\frac{\partial F_P}{\partial z} = -\frac{\partial F_{Pprod}}{\partial z} - \frac{\partial F_{Ptrantot}}{\partial z} \tag{2.51}$$

where $-\frac{\partial F_{Pprod}}{\partial z}$ is the sink of PO_4 due to the production and consequent export of POP from a layer and $-\frac{\partial F_{Ptrantot}}{\partial z}$ is the source of PO_4 due to the accumulation of POP in a layer.

Substituting the equation for $-\frac{\partial F_P}{\partial z}$, (2.51), into (2.46) and using (2.48) to rewrite $-\frac{\partial F_{Pprod}}{\partial z}$ in terms of J_{prod}, (2.46) can be rewritten as

$$S_{PO4} = -J_{prod} - \frac{\partial F_{Ptrantot}}{\partial z} + \lambda_{remin}[DOP] \tag{2.52}$$

where the first term, $-J_{prod}$ is the net biological production of both DOP and POP.

2.14.3.2. Dissolved Inorganic Carbon (DIC) and Total Alkalinity (TA)

The DIC and TA source/sink have several related terms as seen by comparing (2.53) and (2.54):

$$S_{DIC} = r_{C:P}\, S_{PO4} + J_{CaCO3} + V_{CO2} + F_{CO2} \tag{2.53}$$

$$S_{TA} = -r_{N:P}\, S_{PO4} + 2\, J_{CaCO3} + V_{TA} \tag{2.54}$$

where V_{CO2}, V_{TA} and F_{CO2} are boundary conditions which are only applied in the surface layer as described below.

Both DIC and TA have source/sink terms related to the cycling of PO_4 during biological production via the Redfield ratios (the first term in (2.53) and (2.54)) since the elements Carbon, Nitrogen and Phosphate are assumed to be cycled in a constant ratio during photosynthesis. The source term of alkalinity due to biological production has the opposite sign to the source of PO_4, S_{PO4}, since Nitrogen removed in the form of Nitrate (NO_3^-) during photosynthesis decreases TA. The Redfield ratio for Nitrogen, $r_{N:P}$, has been modified to a 16:1 ratio (Anderson and Sarmiento [1994]). Thus, the effects of biology on DIC and TA are determined from the source/sink of PO_4 (i.e. (2.52)) using a simple relation between the elements during photosynthesis.

The formation and subsequent dissolution of $CaCO_3$ shells alters both TA (due to changes in Ca^{2+}) and DIC (due to changes in CO_3^{2-}) in a 2:1 ratio of the change in $CaCO_3$, with the source/sink of $CaCO_3$, J_{CaCO3}, calculated as follows:

$$J_{CaCO3} = -RR\, r_{C:P}(1 - f_{DOP})J_{prod} - \frac{\partial F_{CaCO3}}{\partial z} \quad (2.55)$$

The rate of $CaCO_3$ formation and thus removal of DIC and TA as it sinks is related to the production rate of POP by the rain ratio, RR (the ratio of the soft tissue to the CO_3 pumps). This is the first term in (2.55). The second term, $-\frac{\partial F_{CaCO3}}{\partial z}$, is the accumulation of Ca^{2+} and CO_3^{2-} ions by the dissolution of $CaCO_3$ which is a source of DIC and TA. The flux of $CaCO_3$, F_{CaCO3}, in (2.55) is:

$$F_{CaCO3} = RR\, r_{C:P}(1 - f_{DOP})J_{prod}\Delta z \exp\left(\frac{-(z - z_c)}{d_{CaCO3}}\right) \quad (2.56)$$

Thus, the flux of $CaCO_3$ is assumed to decrease exponentially with depth due to dissolution with a scale depth, d_{CaCO3}. A similar method is used to determine the dissolution of $CaCO_3$ as was used to determine the remineralisation of POP at a given depth in (2.49), with each layer below the $CaCO_3$ formation layer of bottom depth, z_c, accumulating Ca^{2+} and CO_3^{2-} ions at a rate determined by the change in F_{CaCO3} with depth. This is simpler than accounting for the saturation horizon of CO_3^{2-} (the depth below which $CaCO_3$ is undersaturated and dissolves) since $CaCO_3$ can dissolve at any depth.

Both the DIC and TA have a virtual flux at the surface due to the dilution or concentration of these tracers by freshwater fluxes denoted as V_{DIC} and V_{TA}. These virtual fluxes can be neglected for the other passive tracers used in this model but the effects on DIC and TA are significant due to their global-average concentrations being much greater than their variability (Najjar and Orr [1998]). These are related to the virtual salinity flux (in [ppt s^{-1}]) at the surface, $\frac{S_0(\mathrm{E-P})}{\Delta z}$, which is the change in the salinity of the surface layer of thickness, Δz,

due to (negative) freshwater fluxes, E-P (which includes the contributions from the E-P flux, salinity relaxation and sea-ice effects as described in Sections 2.6 and 2.13) as follows:

$$V_{DIC} = \frac{\overline{DIC_s}}{\bar{S}_s} \frac{S_0(\mathrm{E}-\mathrm{P})}{\Delta z} \tag{2.57}$$

$$V_{TA} = \frac{\overline{TA_s}}{\bar{S}_s} \frac{S_0(\mathrm{E}-\mathrm{P})}{\Delta z} \tag{2.58}$$

where $\overline{DIC_s}$, $\overline{TA_s}$ and $\bar{S}_s$ are the global mean surface values of DIC, TA and salinity respectively.

The DIC and TA will not be conserved in the model if the global mean virtual salinity flux is not always zero. This will happen when the model has not reached a steady state which will lead to small variations in the total salinity in the setup described previously. However, to ensure the total salinity of the ocean is conserved, the net freshwater fluxes (including sea-ice effects) and salinity relaxation are balanced by removing the global mean salinity flux at every timestep in the biogeochemistry simulations of Chapter 6, ensuring the global-average DIC and TA virtual fluxes are also zero (Lauderdale at al. [2013]). This ensures the passive tracers including carbon are conserved in the model.

There is an additional contribution to the DIC in the surface layer due to atmosphere-ocean CO_2 exchange,

$$F_{CO2} = k_w([\mathrm{CO_2}^*] - [\mathrm{CO}_{2sat}]) \tag{2.59}$$

where k_w is the gas exchange coefficient for CO_2, and $[CO_2^*]$ and $[CO_{2sat}]$ are the actual and saturated concentrations of CO_2 at the ocean surface respectively. The saturated concentration

of CO_2 is the concentration required for the ocean surface to be in equilibrium with the overlying atmosphere given its specified concentration, [CO_{2atm}].

The gas exchange coefficient, k_w in (2.59) uses the following parameterisation of Wanninkhof [1992]:

$$k_w = (1 - \mathrm{f}_I) a U^2 \left(\frac{Sc(\theta)}{660}\right)^{-\frac{1}{2}} \tag{2.60}$$

Where k_w is dependent on the sea-ice fraction, f_I, the square of the wind speed at 10 m, U, (a climatologically averaged model forcing as described in Section 2.12), the square root of the Schmidt number for CO_2, Sc (which is a function of sea surface temperature, θ), with a proportionality constant, a = 0.337. This constant is computed by determining the gas transfer coefficient required to obtain the natural and bomb radiocarbon distributions (Najjar and Orr [1998]). The effect of sea-ice in (2.60) assumes sea-ice is impermeable to CO_2 and thus the air-sea CO_2 flux is zero under sea-ice.

The sea-ice fractional area is calculated by the sea-ice model, varying in time and with a dependence on the model inputs. It can also be set to a constant distribution enabling the effects of sea-ice on the CO_2 flux to be neglected or held constant, while the physical circulation is still altered in the same way by the sea-ice model.

The concentration of CO_2 and CO_{2sat} at the ocean surface are determined from the actual surface partial pressure of CO_2, pCO_2, and the saturated value, pCO_{2sat} respectively:

$$[\mathrm{CO_2}^*] = k_0 \, pCO_2 \tag{2.61}$$

$$[\mathrm{CO}_{2sat}] = k_0 \, pCO_{2sat} \tag{2.62}$$

where k_0 is the solubility of CO_2 in the ocean.

The actual surface partial pressure, pCO_2, is solved for using the TA, DIC, PO_4 and inorganic Silicate (defined as an input) distributions following the efficient method of Follows et al. [2006] which is an alternative to iterative methods. This method calculates the pCO_2 using the DIC and $[H^+]$ (or pH), where $[H^+]$ is approximated using the positive root of a quadratic equation for $[H^+]$ formed by using the carbonate alkalinity, A_C, and DIC equations,

$$A_C = [HCO_3]^- + 2[CO_3]^{2-} \tag{2.63}$$

$$[DIC] = [CO_2{}^*] + [HCO_3]^- + [CO_3]^{2-} \tag{2.64}$$

and the equilibrium coefficients K_1 and K_2, controlling the partitioning of DIC. The solution for $[H^+]$ is dependent on A_c and DIC. Thus, assuming $A_C \sim A_T$ (or TA) allows an estimate of $[H^+]$ to be made which can be used with TA to obtain an improved estimate of A_C and hence $[H^+]$. The PO_4 and inorganic Silicate are also used to modify the calculated A_C and thus improve the estimate of $[H^+]$ (see Follows et al. [2006] for more detail). The pCO_2 is determined using the DIC concentration and the estimated $[H^+]$ as follows:

$$pCO_2 = \left(\frac{[DIC]}{k_0}\right)\left(1 + \frac{k_1}{[H^+]} + \frac{k_1 k_2}{[H^+]^2}\right)^{-1} \tag{2.65}$$

where $k_1 = \left(\frac{[HCO_3]^-[H^+]}{[CO_2{}^*]}\right)$ and $k_2 = \left(\frac{[CO_3]^{2-}[H^+]}{[HCO_3]^-}\right)$

The saturated pCO_2 is related to the atmospheric CO_2, $[CO_{2atm}]$, by adjusting its value for the surface pressure, P_{0atm}:

$$pCO_{2sat} = P_{0atm}\,[CO_{2atm}] \tag{2.66}$$

where P_{0atm} = 1 atm (1013 hPa).

2.14.3.3. Oxygen

The sources/sinks of oxygen (O_2) include the biological productivity (a sink) and subsequent remineralisation of the organic matter (a source), represented using the source/sink of PO_4, S_{PO4}, from (2.46), and the Redfield ratio of O_2 to PO_4, $r_{O2:P}$, to convert this to a change in O_2.

$$S_{O2} = r_{O2:P} S_{PO4} \quad if\ [O_2] > [O_{2crit}]$$

$$S_{O2} = 0 \quad if\ [O_2] < [O_{2crit}] \tag{2.67}$$

The remineralisation of organic matter only has an effect on the concentration of O_2 if the concentration is greater than the critical level, $[O_{2crit}]$. Below this critical level set at a concentration of 4μmol Kg^{-1}, anoxic respiration occurs since there is a large decrease in the abundance of zooplankton (Saltzman and Wishner [1997]). The change in O_2 due to biological productivity and remineralisation of organic matter is inversely related to that of PO_4 since biological production uses PO_4 and expels O_2 (hence $r_{O2:P}$ is negative with a value of -170 (Anderson and Sarmiento [1994]).

There is an additional source term at the surface due to air-sea exchange of O_2, F_{O2}. This is a surface boundary condition and thus is only applied in the surface layer akin to the CO_2 air-sea exchange, F_{CO2} in (2.59),

$$F_{O2} = k_w([O_2{}^*] - [O_{2sat}]) \tag{2.68}$$

The formula for the exchange coefficient, k_w, is similar to that of CO_2, with the same constant, relation to wind speed and Schmidt number as in (2.59). However, the Schmidt number for O_2 differs from that of CO_2 since different Schmidt number coefficients are used.

The saturated oxygen concentration, $[O_{2sat}]$ is calculated using the formulae of Garcia and Gordon [1992] and the actual surface concentration, $[O_2^*]$, is a model variable.

2.14.4. Atmospheric box

A well-mixed atmospheric box which exchanges CO_2 with the ocean through air-sea CO_2 exchange, F_{CO2} in (2.59), is used to simulate the evolution of atmospheric CO_2 as the buoyancy flux and consequently the ocean circulation is varied (see Chapter 6). The sum of the atmospheric and oceanic carbon is conserved. The volume of the atmospheric box is reduced from that of the real atmosphere of Earth by the factor of reduction in ocean volume in the model relative to the real world. The volume of the real world ocean is taken as 1.332 x 10^9 km^3 (Charette and Smith [2010]). The volume of the single- and two-basin models (see Table 2.3) used in this thesis have volumes of ~349.2 and ~982.8 billion km^3 respectively, which equates to a fractional volume of 0.262 and 0.738 relative to the real world ocean. Therefore, the total number of atmospheric moles in the Earth's real (dry) atmosphere (assuming an atmospheric mass of 5.1352 x 10^{18} kg (Trenberth & Smith [2005]) is changed by this fractional factor giving 4.74 x10^{19} moles and 1.34x10^{20} moles in the single and two-basin models respectively.

Reducing the atmospheric box by the surface area of the ocean gives slightly smaller atmospheric boxes in both model configurations and thus the results would be very similar if this was used instead of volume. The changes in CO_2 in these models should therefore be comparable since the atmospheric boxes are scaled according to their ocean volumes, with differences between the models being due to differences in the variation in ocean circulation when there is an additional basin.

The number of moles of CO_2 required for an atmospheric concentration of 278 ppm (parts per million) in the single- and two-basin models would be 1.32 x10^{16} and 3.71x10^{16} moles

respectively. However, it has proved difficult to obtain this exact atmospheric CO_2 concentration and thus the control experiments described in Chapter 6 have some variation from this pre-industrial concentration.

2.15. Passive dye tracer model setup

The model has also been setup with a single passive tracer simulated rather than using the biogeochemistry model. This passive tracer can be initialised with a specified distribution and concentration but with no sources or sinks i.e. a dye tracer release experiment. The advection and diffusion schemes implemented are the same as that of temperature and salinity. This model setup is used for visualisation of the overturning circulation to aid our understanding of the pathways taken in the models as described in Chapter 5.

Chapter 3

MOC in a multi-basin model Part I: Dependence on Southern Ocean buoyancy forcing

This chapter contains the original draft of a paper which has been accepted (since the initial submission of this thesis) in the Journal of Physical Oceanography: Baker J. A., A. J. Watson and G. K. Vallis, 2020: Meridional Overturning Circulation in a multi-basin model Part I: Dependence on Southern Ocean buoyancy forcing. https://doi.org/10.1175/JPO-D-19-0135.1 (Accepted, awaiting publication).

The focus of this chapter and the following chapter (which contains a second paper, Part II of this two paper study) is on the physical processes controlling the MOC strength and structure, and thus how changes in the model forcings lead to changes in the overturning. The study helps improve our understanding of the pathways taken by the MOC under varying forcings and its driving mechanisms in the multi-basin model as described further in Chapter 4. It improves our understanding of the cause of transitions in the MOC between present-day, glacial and potential future states. The effect of these circulation changes on atmospheric CO_2 is then later analysed in Chapter 6.

This chapter was motivated in part by the results described in Chapter 5 in which the single-basin model is shown to have a similar residual overturning structure to the multi-basin

model's global-average circulation but with a far weaker NADW cell, despite the same model forcings being used as in the Atlantic sector of the multi-basin model. The circulations in the individual Atlantic and Pacific basins of the multi-basin model vary significantly in structure from the global-average circulation. Thus, the importance of using a multi-basin model to realistically simulate the overturning circulation is described in Chapter 5. These differences between the individual basin and global-average overturning circulations of the multi-basin model enable a method to be proposed in this chapter to separate the MOC pathways in the model.

As shall be discussed in this chapter, the studies of Ferrari et al. [2014] and Jansen and Nadeau [2016] address a similar area to our research, improving our understanding of the transition of the MOC to a glacial state. However, our study differs in a number of ways from these previous studies. Firstly, we do not distinguish between the mechanisms of Ferrari et al. [2014] and Jansen and Nadeau [2016] to shoal the NADW cell. Instead, we vary the sea-ice freezing point which alters both the Southern Ocean sea-ice formation rate and sea-ice extent, with both of these mechanisms therefore being possible. Ferrari et al. [2014] was a theoretical study with no model simulations to support their theory. Jansen and Nadeau [2016] use a single-basin model to show the importance of sea-ice induced changes in abyssal stratification on the MOC. Our approach differs in that we use a multi-basin model which has important consequences on the structure and pathways taken by the MOC as discussed in these chapters and later in Chapter 5. In particular, we propose a method to separate the wind and diffusive-driven pathways of the MOC, enabling a deeper understanding of the changes in the strength and structure of the MOC with changes in buoyancy and wind forcing, and vertical diffusivity. Our method to vary the Southern Ocean sea-ice through changes in the sea-ice freezing point enables the gradual transition of the MOC to a glacial state in response to buoyancy perturbations to be analysed, in addition to changes to a warmer than present-

day low-ice state. A recent study of Nadeau et al. [2019] uses a multi-basin model to investigate the Ferrari et al. [2014] and Jansen and Nadeau [2016] sea-ice mechanisms in causing the transition of the MOC to a glacial state. They find both these mechanisms act together with additive effects. The work presented in this chapter was carried out independently of this study, although there is unsurprisingly some overlap since both studies investigate the effect of Southern Ocean sea-ice on the MOC in a multi-basin model. The major differences of our work compared to this study are highlighted in Section 3.5.

The final accepted version of this paper has some significant changes and additions from the version in this thesis. However, the main results and conclusions remain unchanged. This is not the original submitted manuscript with some of the changes made in the revision process added here and it has also been updated with some changes suggested by my PhD examiners.

3.0. ABSTRACT

The variation in the strength and structure of the overturning circulation under varying Southern Ocean buoyancy forcing, corresponding to present day, a cooler (glacial) state, and a possible future warmer state is analysed in an idealised two-basin general circulation model connected by a southern circumpolar channel.

A connection between the North Atlantic Deep Water (NADW) cell in the Atlantic basin and the Pacific Deep Water (PDW) cell in the Pacific basin is proposed to occur via a direct flow of NADW into the channel's lower cell, while PDW upwelled in the Pacific basin can flow directly into the upper wind-driven cell in the channel. The intersection of these cells along with direct zonal flows between the basins completes the inter-basin circulation.

The present-day Atlantic Meridional Overturning Circulation (AMOC) in the model is driven both by wind-driven upwelling in the Southern Ocean and by diffusion in the Pacific and Atlantic. In a cooler climate with enhanced sea ice and Antarctic Bottom Water (AABW) formation, the NADW cell shoals which can then no longer flow directly into the channel's lower cell, reducing the Pacific diffusively-driven pathway of NADW. This leads to a substantial weakening of the AMOC, suggesting buoyancy forcing changes can play a substantial role in the transition of the AMOC to a glacial state. In contrast, in a future warmer climate with reduced AABW formation, the NADW cell strengthens and deepens, becoming increasingly driven by diffusive upwelling in the Pacific basin, with a smaller role played by wind-driven upwelling.

3.1. Introduction

Over the past 20 years a great deal of progress has been made in our understanding of the processes responsible for driving the Meridional Overturning Circulation (MOC), and the corresponding structure of and pathways taken in the ocean. Numerous studies have contributed to this endeavour, including Toggweiler and Samuels [1995], Gnanadesikan [1999], Vallis [2000], Ito and Marshall [2008], Wolfe and Cessi [2009; 2011], Nikurashin and Vallis [2011; 2012], Shakespeare and Hogg [2012], Jansen and Nadeau [2016], Thompson et al [2016] and Ferrari et al. [2017]. Reviews and syntheses of many of these ideas are given by Vallis [2017] and Cessi [2019].

To a large degree the global-average MOC is composed of two separate overturning cells. In a latitude-depth cross section with south to the left (this orientation is used throughout the paper), a clockwise upper North Atlantic Deep Water (NADW) cell, stemming from deep water formation in the North Atlantic Ocean, overlies an anti-clockwise Antarctic Bottom Water (AABW) cell in the abyssal ocean that is associated with a sinking of dense surface waters in the Southern Ocean. A large volume of the water in these cells upwells adiabatically to the surface along sloping isopycnals in the Southern Ocean.

The ocean circulation was perhaps first considered to be a global inter-connected conveyor belt by Broecker and Peng [1982], Gordon [1986] and Broecker [1987], who all provided schematics of the MOC with a transfer of water between all ocean basins, with diffusive upwelling generally imagined to be the main driver. (Numerous such schematics followed, as reviewed by Richardson [2008].) An alternative notation, that the MOC is largely driven by westerly winds in the Southern Ocean, predates these ideas – it was discussed by Eady [1957] – but the idea languished until Toggweiler and Samuels [1995] and Doos and Coward [1997] independently suggested the Southern winds as a mechanism to upwell NADW to the surface

and thus drive the MOC. Most subsequent theoretical studies considered the MOC in the global average, ignoring inter basin flows, although observations suggest that the present-day MOC forms one continuous overturning cell, as anticipated in the Broecker and Gordon references above and better quantified by Schmitz [1995], Lumpkin and Speer [2007] and Talley [2013], rather than two separate cells as might be inferred from the global-average streamfunction. In these later descriptions, much of the NADW which upwells adiabatically in the Southern Ocean is believed to flow south at the surface to form AABW and Circumpolar Deep Water (CDW) before flowing into the Pacific and Indian Oceans. The Pacific and Indian Deep Water (PDW and IDW) which form as a result of the diffusive upwelling of AABW in these basins, complete the inter-basin circulation by flowing into the Atlantic Ocean via the Southern Ocean or Indian Ocean.

These pathways may have been different in the past. Proxy data suggest the AMOC became weaker during the Last Glacial Maximum (LGM), with NADW becoming shallower, perhaps no deeper than about 2 km (Lynch-Stieglitz et al. [1999]; McManus et al. [2004]; Curry and Oppo [2005]). The glacial shoaled NADW is sometimes referred to as Glacial North Atlantic Intermediate Water (GNAIW) (Duplessy et al. [1988]) since it is no longer 'deep'. Consistent with this picture, the AABW cell during the LGM expanded greatly, as suggested by a large vertical $\delta^{13}C$ gradient in the Atlantic Ocean during the LGM, with low $\delta^{13}C$ in the older, CO_2-rich waters below about 2 km. The AABW was also saltier than the upper cell during the LGM, according to sediment pore waters, in contrast with the present day salinity distribution (Adkins et al. [2002]). The change in circulation has been linked to the decrease in atmospheric CO_2 observed from ice core records in glacial time (Watson et al. [2015]) and the ageing of deep water masses (Burke et al. [2015]).

Two of the main mechanisms proposed to cause the glacial shoaling and weakening of the NADW cell during glacial periods are: i) reduced atmosphere-ocean buoyancy fluxes

(Watson and Garabato [2006], Ferrari [2014], Jansen and Nadeau [2016]), or ii) a weakening or northward shift in the Southern Hemisphere westerly winds (Toggweiler and Samuels [1993, 1995]; Toggweiler et al. [2006]). In this paper we further investigate the first mechanism; more specifically, we perturb the Southern Ocean buoyancy forcing in a two-basin model. Overturning schematics of the present-day, glacial and a warmer state MOC are used to depict how the MOC pathways change with variations in Southern Ocean buoyancy loss. A follow-up paper (Part II or Chapter 4) will investigate the sensitivity of the MOC to changes in Southern Ocean wind and vertical diffusivity under varying buoyancy forcings.

We choose only to vary the Southern Ocean boundary conditions in part for simplicity and in part because such changes are believed important in the transition to glacial climates (e.g., Shin et al. [2003], Liu et al. [2005], Ferrari et al. [2014], Sun et al. [2016], Jansen and Nadeau [2016], and Jansen [2017]). The mechanism can be expected to be significant given the importance of Southern Ocean sea-ice in the water mass transformations of the present-day ocean (Abernathey et al. [2016]). However, it should be understood that the MOC is not driven solely by the value of the surface boundary conditions in the Southern Ocean. Rather, it depends on the difference in density between the high latitude surface waters in the Northern and Southern Hemispheres. Thus, Vallis [2000] explicitly showed that the depth of the NADW cell depends on the density of the northern-sourced water relative to that produced in the south (and so on the surface buoyancy forcings, among other things), as is implicit in the theory of Nikurashin and Vallis [2012].

The exact mechanisms whereby changes in Southern Ocean boundary conditions affect the MOC are not wholly clear. At a basic level, Shakespeare and Hogg [2012] find an enhanced abyssal cell as the Southern Ocean buoyancy flux becomes more negative. Relatedly, Jansen and Nadeau [2016] and Jansen [2017] argue that enhanced brine rejection due to sea-ice formation effectively acts as a negative buoyancy flux and indeed find an enhanced lower cell

as sea-ice expands in the Southern Ocean. In some contrast, Ferrari at al. [2014] hypothesise the equatorward expansion of Southern Ocean sea-ice during glacial times as a mechanism to shoal and isolate the NADW cell, using a geometric argument building from Nikurashin and Vallis [2012]. Nadeau et al. [2019] use a multi-basin model to propose both mechanisms can work together by varying the Southern Ocean buoyancy fluxes, both in magnitude and in latitude, to represent enhanced buoyancy fluxes and extended sea-ice. The study confirms the Jansen and Nadeau [2016] enhanced stratification mechanism in a two-basin model, extending the theory of the original study, and also validates the Ferrari et al. [2014] hypothesis. In any case, it is clear that changes in Southern Ocean sea-ice can have a large impact on the MOC and potentially lead to shoaling of NADW in cold climates, as observed.

In this paper our main focus is on the change in the pathways taken by the MOC in response to Southern Ocean buoyancy flux changes, rather than on the exact process and mechanisms which act to shoal the NADW cell. We use a model with two basins because of the potential importance of diffusive upwelling in the Indo-Pacific Oceans, and because of the evident inter-hemispheric nature of the overturning circulation, which as noted may have been different in glacial climates. For example, in the present climate diffusive upwelling in the Pacific basin drives the AMOC in addition to the Southern Ocean winds, but whether that was so in the LGM is less clear. In Section 3.2 we describe the model that we use (an ocean model coupled to sea ice), in Section 3.3 we describe the control simulation and the methodology we use to analyse the results. In Section 3.4 we describe the results of the experiments in which we vary the buoyancy forcing, and in Section 3.5 we summarize and conclude.

3.2. Model Setup and Experiments

The Massachusetts Institute of Technology general circulation model (MITgcm) (Marshall et al. [1997a,b]) is used with a 2.8 degree horizontal resolution and 20 vertical levels in a 4000 m deep ocean, with decreasing resolution with depth. An idealised domain (Fig 3.1a) is used with two basins connected by a circumpolar channel in the south. The basins have an area representative of the Atlantic and Pacific Oceans, and for brevity we refer to them as "Atlantic" and "Pacific". The domain extends from 70°S to 73°N in the Atlantic basin and 65°N in the Pacific basin. The model has a longitudinal extent of 188 degrees, with an Atlantic basin of 63.5 degrees and a Pacific basin of 123.5 degrees. There are two meridional land strips extending from the north of the model which represent and are referred to herein as the South American and South African land strips, extending to a latitude of 53°S and 36°S respectively. The Southern Ocean south of the South Africa land strip is herein referred to as the channel. The full non-linear equation of state for seawater is used to calculate density.

The model is forced at the surface by a wind stress (Fig 3.1b), and heat and freshwater fluxes. The inputs used in all of the model buoyancy flux experiments to calculate these forcings are zonal-averages (over the real world Atlantic and Pacific basins) of the climatological monthly averaged National Centers for Environmental Prediction–National Center for Atmospheric Research (NCEP–NCAR) reanalysis data over the period 1981-2010 (Kalnay et al. [1996]) and the surface temperature and salinity are also relaxed to observed distributions (Levitus and T.P.Boyer [1994a,b]). The NCEP forcings used are the downward shortwave and longwave radiation at the surface, the precipitation and evaporation rate, atmospheric temperature and specific humidity at 2 m, the wind speed and the zonal and meridional wind speed components at 10 m. The NCEP surface heat and freshwater fluxes and relaxation

fluxes are combined to form mixed boundary conditions as described by Haney [1971] and Mikolajewicz and Maier-Reimer [1994].

The inputs used to determine the heat and freshwater fluxes and the relaxation fluxes are zonal averages of the NCEP reanalysis data described above but with the zonal averages applied separately over the Atlantic and Pacific sectors of the dataset. This results in zonal contrasts in the temperature and salinity forcings between the Atlantic and Pacific sectors of the model as in the real ocean (see Fig 3.1c). Thus, the sea-ice expands further north in the cooler Atlantic sector of the Southern Ocean than in the Pacific sector. The surface wind stress and the various components of the heat flux are calculated using bulk formulae. The freshwater flux is imposed as a virtual salinity flux. The salinity relaxation timescale is set to enable changes in sea-ice brine fluxes to have a realistic effect on the ocean buoyancy.

The vertical ocean diffusivity is set using the Bryan and Lewis [1979] diffusion scheme (BL79) with a surface diffusivity of approximately 10^{-5} m^2 s^{-1} increasing to approximately $2x10^{-4}$ m^2 s^{-1} at depth and it is horizontally uniform (Fig 3.1d). There is a large increase in vertical diffusivity at about 2 km to represent the topographical enhancement of mixing at depth caused by the generation of turbulence by internal wave breaking (Wunsch and Ferrari [2004]). Convection is parameterised by adding a convective diffusivity of 100 m^2s^{-1} to the vertical diffusivity coefficient if the ocean is statically unstable due to a decrease in density with depth.

The Gent-McWilliams (GM) eddy parameterisation (Gent and McWilliams [1990]; Gent et al. [1995]) is used to determine the 'bolus' or eddy-induced velocity which represents the advective effect of geostrophic eddies in the flow. This eddy-induced circulation acts to flatten the isopycnals due to baroclinic instability, converting available potential energy to eddy kinetic energy. The Redi scheme (Redi [1982]) is used to diffuse tracers along

isopycnals to represent the isopycnal mixing effects of eddies. The eddy transfer coefficient is set to 1000 $m^2 s^{-1}$.

Sea-ice is simulated using a fully coupled dynamic-thermodynamic model which accounts for the effects of sea-ice on the buoyancy fluxes. It is based on the non-linear dynamic-thermodynamic sea-ice model with viscous-plastic rheology first employed by Hibler [1979] and modified for efficiency by Zhang and Hibler [1997], and more recently by Losch et al. [2010] for use in coupled ice-ocean models. The zero-layer thermodynamics of Hibler [1980] is used for the sea-ice thermodynamics which assumes a zero heat capacity layer.

We effect changes in the Southern Ocean buoyancy flux by changing the sea-ice freezing point globally according as to whether we seek to simulate present-day conditions, a glacial state or a future warm state. Specifically, a constant sea-ice freezing point is set in each experiment, with values ranging from -1.96°C to 1°C to represent increases in Southern Ocean sea-ice formation and thus changes in the surface buoyancy flux mediated through the sea ice formation rate. In the descriptions below we refer to experiments with freezing points of -1.96°C, 0°C and 1°C as 'warm', 'present day' and 'glacial' climates respectively, noting that the experiments with high freezing point produce more sea ice, resembling a glacial climate. The heat flux and relaxation temperature field remain unchanged. Therefore, surface temperature and heat flux changes are a result *only* of changes in ocean circulation and sea-ice cover, so enabling the effect of changes in sea-ice formation on the MOC to be isolated. Another advantage of this technique is that small perturbations to the sea-ice formation rate can be made by slowly changing the sea-ice freezing point. Thus, the gradual transition of the MOC in response to sea-ice formation can be obtained. The surface temperature would have to be perturbed gradually to obtain a similar transition in the MOC. The effect of sea-ice changes on the circulation would no longer be isolated since there would also be effects due

to the surface temperature perturbations. The Southern Ocean buoyancy flux perturbation experiments are performed in Section 3.4.

The model is spun up over about twenty thousand years to a steady state for the control state. Perturbation experiments are integrated for a further 10,000 years to ensure a steady state is reached.

3.3. General Methodology and Basic Simulation

In this section we first describe the overturning circulation obtained from the control experiment. Then, in Section 3.3b, we describe how a connection between the upper and lower cells of the MOC is enabled. We do this first in a somewhat qualitative way and then, in 3.3b.(II) describe a method to quantitatively separate the wind and diffusive-driven pathways and the various components of the MOC.

a. Control experiment and MOC upwelling

The control experiment uses the forcings described in Section 3.2, with a sea-ice freezing point of 0°C. This produces a MOC which is most comparable with the present-day circulation. Although this is not the true sea-ice freezing point, the model has an idealised bathymetry and forcings and so some adjustment to these to obtain a good fit is not unexpected. The control experiment residual circulation is shown for each basin and for the global-average in Fig 3.2. The residual circulation shown is the sum of the time-averaged Eulerian-mean and the 'eddy-induced' circulations produced by the GM parameterization, and it is this flow that is responsible for the net advective transport of tracers.

In the Atlantic basin there is a clockwise upper NADW cell of about 13 Sverdrups (Sv , or 10^6 m^3 s^{-1}) with deep water formation at the northern boundary, and an anti-clockwise lower

AABW cell at depth. In the Pacific basin, the MOC is dominated by the AABW cell, which upwells diffusively to form PDW. The global-average circulation is similar to the Atlantic basin overturning, but with a stronger and slightly expanded lower AABW cell. The expansion is due to the PDW cell in the Pacific basin upwelling to shallower depths than the lower cell in the Atlantic basin. This difference in the MOC structure in the global-average compared to in the individual basins shows the importance of analysing each basin separately to determine the ocean pathways. The global-average circulation in the channel is primarily controlled by the Southern Ocean westerly winds. They drive a clockwise Eulerian-mean Deacon cell and indirectly an anti-clockwise eddy-induced cell.

The AMOC, specifically the circulation associated with NADW, is associated with convection in the North Atlantic basin where deep water formation occurs. For a given North Atlantic surface density distribution, the two-basin model experiments performed here suggest the volume of NADW which can be upwelled to near the surface (and thus drive the NADW cell) depends on both Southern Ocean winds and diffusion, as discussed more below. And although the NADW cell in the control experiment is likely weaker than the present-day overturning, this is not surprising given there is no Indian Ocean diffusive upwelling and the model circumpolar channel is about half the longitudinal width of the global ocean.

In the experiments performed in this paper, the wind and diffusivity profile are not altered from the control setup described in Section 3.2 (the effects of wind and diffusivity variations are discussed in Part II.) The remainder of this section introduces the methods used to determine the magnitude of the transports due to the various mechanisms, for a given circulation.

b. Connections between the upper and lower cells of the MOC

b. I. Qualitative considerations

We propose the upper (lower) cell in each basin is able to flow into the lower (upper) cell in the channel (i.e. all latitudes south of the South Africa meridional land strip), depending on the forcings. We can see this from an inspection of Fig 3.3, which shows the MOC in the Atlantic and Pacific basins with the global-average streamfunction added to the channel, for the experiment with a sea-ice freezing point of -1.96°C. This freezing point is chosen to highlight the intersection of the overturning cells, since it leads to a deep NADW cell (with almost no AABW cell in the Atlantic basin), and thus the overlap between the upper and lower cells at the channel-basin boundary is particularly clear.

In the channel, the zonal circumpolar current flows rapidly over the whole depth of the water column, with a speed that greatly exceeds that of the meridional overturning flows, so that the density structure is more-or-less uniform over all longitudes. Similarly, the overturning circulation is driven by the wind-induced Eulerian-mean and eddy-induced circulations in the channel and these are similar in structure and strength per unit longitude in each sector. The global-average channel residual overturning circulation is thus, to a first approximation, representative of the flow in both the Atlantic and Pacific sectors.

The global-average residual circulation's cell interface (i.e. the interface between the upper and lower cells) at the channel-basin boundary (labelled as 'z_interface' in Fig 3.3) may then be used in a calculation of the MOC components: flows coming from the northern basins which enter the channel join the upper cell if they enter above this depth, and the lower cell if they are below it. The cell interface depth ('z_interface') can be altered by changes in the depth of NADW flowing into the channel, since (for example) the shoaling of the NADW cell can in turn shoal the cell interface depth. However, the shoaling of the cell interface

depth as the NADW cell shoals and AABW cell expands in the Atlantic basin is limited by the presence of the clockwise upper wind-driven cell in the channel and also by changes in the flow of PDW out of the Pacific basin, since in the glacial state this anti-clockwise cell only returns to the channel at mid depths rather than all the way to the surface.

b. II . Quantitative determination of MOC pathways and overturning components

The NADW cell in the Atlantic basin and the PDW cell in the Pacific basin of a multi-basin model can flow into the global-average lower and upper cells of the channel respectively at the channel-basin boundary (i.e. the upper and lower cells intersect). Thus, NADW in the upper cell, flowing into the channel from the Atlantic basin (referred to in this paper as NADW_channel and labelled (2) in Fig 3.3) remains in the upper cell of the channel if it is above the interface depth, or flows directly into the lower cell of the channel if it is dense enough to be below that depth: we refer to these components as NADW_wind and NADW_pac_lower respectively, where the suffixes refer to the return pathways they take (see below). They are labelled (3) and (4) in Fig 3.3.

The NADW flowing into the channel must upwell to a shallower depth before it can flow north in the Atlantic basin as less dense intermediate waters. The two components described above follow different pathways to upwell, either (1) the direct wind-driven pathway in the channel, or (2) the diffusive-driven pathway via upwelling in the Pacific basin.

The NADW_wind, entering above the channel's cell interface at the channel-basin boundary, flows into the channel's upper wind-driven cell. It is consequently upwelled adiabatically in the Southern Ocean, where it is lightened at the surface by positive buoyancy fluxes and flows northwards back into the Atlantic basin.

The remaining component, NADW_pac_lower, entering below the channel cell interface, also upwells adiabatically in the Southern Ocean, before downwelling further south. The

water upwells towards the surface where it densifies by negative buoyancy fluxes, flows southwards and sinks forming AABW. This is believed to occur in the present-day ocean (Cessi [2019]). The AABW formed in the far south of the model domain flows north into the Pacific basin at depth (in the present day ocean some also flows into the Atlantic basin, but in the circulation of Fig 3.3 this is negligible). The AABW upwells diffusively in the Pacific basin to form PDW before returning to the channel at shallower depths.

There is also a direct zonal pathway for NADW to enter the Pacific basin via the circumpolar channel, as discussed by Ferrari et al. [2017]. Any direct zonal flow of NADW below the 'z_interface' will already be included in the NADW_pac_lower component. However, if there is a zonal flow of NADW into the Pacific basin above the 'z_interface', a proportion of the NADW_wind component defined above is instead upwelling in the Pacific basin. Therefore, a slight modification is made to NADW_wind to account for this zonal flow (if present). The zonal flow is equal to the northward flow into the Pacific basin above the 'z_interface', and is referred to as NADW_pac_upper. If the streamfunction has two maxima in the south of the Pacific basin, any NADW which flows north above the lower maxima in the Pacific is included in NADW_pac_upper. Thus, NADW_pac_upper and NADW_pac_lower separate the upper and lower pathways of NADW origin waters into the Pacific basin. Combining these components gives the total Pacific diffusive-driven pathway, referred to herein as NADW_pac.

The sum of the direct wind and Pacific diffusive-driven components of NADW (NADW_wind and NADW_pac respectively) is equal to the flow of NADW into the channel (NADW_channel).

There is a third component to the NADW in our model, which does not however enter the channel. A significant volume of NADW formed in the north Atlantic in Fig 3.3 upwells

within the Atlantic basin due to the clockwise eddy-induced circulation in the north where isopycnals outcrop and also due to diffusive upwelling in this basin. The NADW upwelling in the Atlantic basin is smaller in the present-day state (Fig 3.4b) than in the 'warm' state (Fig 3.3) but remains significant with a similar Atlantic upwelling as observed in the present-day overturning (Lumpkin and Speer [2007]; Cessi [2019]). However, in the model's present-day state Atlantic residual circulation, the eddy-induced component is weak as in these observations.

The PDW flowing into the channel from the Pacific basin can flow along three possible routes with all three likely to be important in the present-day ocean. PDW can flow into the channel below the channel-basin cell interface and thus flow into the channel's lower cell. This water is completely isolated from the Atlantic basin's NADW cell and thus does not contribute to the NADW cell strength (the Atlantic basin lower AABW cell is also completely isolated in this way). It is herein referred to as PDW_sep (component (5) in Fig 3.3). The remainder of the PDW, entering above the channel cell interface, is either upwelled further in the channel by the upper wind-induced circulation before flowing northwards into the Atlantic basin, or it flows directly into the Atlantic basin without further upwelling via the direct zonal pathway. These latter pathways of PDW into the Atlantic basin are referred to here as PDW_at (component (6) in Fig 3.3). This component is not displayed in later figures since by continuity, it should equal the NADW_pac component. This is found to be approximately (within 0.4 Sv) the case in all experiments, providing a check on the method proposed.

Using the approach outlined above to separate the direct wind-driven and Pacific diffusively-driven components of the AMOC, the variation in the MOC with varying Southern Ocean buoyancy forcing will now be described.

3.4. Analysis of Buoyancy Flux Experiments

In this section we describe various experiments that transition the circulation from a potential future "warm" low-ice state, to a "present-day" state, and finally a "glacial" state. In all cases we change the buoyancy fluxes in the Southern Ocean. As mentioned earlier, these fluxes are varied by altering the sea-ice freezing point to bring about changes in sea-ice formation and brine rejection. All other forcings remain unchanged. The expansion of sea-ice with an increased freezing point leads to brine rejection in regions of sea-ice formation, and freshwater release further north where the sea-ice melts. Thus, the buoyancy fluxes in the far south become more negative while just to the north they become more positive. The experiments performed enable the effects of changes in sea-ice formation to be analysed with any temperature changes being only a result of the effect of sea-ice on the circulation. The atmospheric temperature and incoming radiative fluxes are not changed (although sea-ice reduces the atmosphere-ocean heat transfer).

Fig 3.4 shows the overturning circulation simulated in the model with sea-ice freezing points of -1.96°C, 0°C and 1°C. The distribution of sea-ice in the Southern Ocean and the zonal average buoyancy fluxes in these experiments are shown in Figs 3.5 and 3.6 respectively. The variation of the MOC components under varying Southern Ocean sea-ice freezing rates (and also varying Southern Ocean buoyancy fluxes) are shown in Fig 3.7, while Fig 3.8 displays the variation of the Atlantic NADW cell and global-average cell interfaces at the channel-basin boundary. Fig 3.9 shows schematics of the major pathways in the three simulations shown in Fig 3.4.

3.4.a. Future Circulation

Using a sea-ice freezing point of -1.96°C generates a circulation which has no AABW cell in the Atlantic basin in contrast to the present-day control circulation (see Section 3.3a). This

simulation could be indicative of a future circulation in a warmer climate in which there is much reduced sea-ice formation, and reduced AABW formation, in the Southern Ocean.

Fig 3.4a shows the overturning streamfunction in this -1.96°C freezing point experiment (the same as Fig 3.3) and Fig 3.9a depicts the primary overturning circulation pathways.

The buoyancy flux is slightly positive in the far south of the domain (Fig 3.6a), and thus AABW formation is non-existent resulting in a weakly stratified abyssal ocean. The lower anti-clockwise eddy-induced cell in the channel therefore does not upwell to the surface in the far south of the domain (in contrast to the control), since a negative buoyancy flux is required for a poleward surface flow. The water mass flowing into the Pacific basin therefore has approximately the same density as the NADW flowing into the channel's lower cell. The NADW cell strengthens to 19.5 Sv, flowing into the channel almost all the way to the ocean floor, with no AABW cell. Therefore, there is a significant difference between the depths of the Atlantic NADW cell (~3650 m) (which is the cell interface between the upper and lower cells in the Atlantic basin) and the global-average cell interface, 'z_interface' (~2250 m), at the channel-basin boundary (see Fig 3.8), and thus a large ~1400 m overlap between the NADW cell and the channel's lower cell.

Most of the ~11 Sv of NADW flowing into the channel is below the 'z_interface' and thus the primary pathway followed by ~7 Sv of 'NADW_channel' is along the lower route of the Pacific diffusive-driven pathway ('NADW_pac_lower', which is equal to 'NADW_pac' in this case). Only a small volume (4.1 Sv) of NADW flows along the direct wind-driven pathway ('NADW_wind') (see Figs 3.7 and 3.9a). The main cause of the increase in the strength of the AMOC relative to the more present-day like control circulation (described in Section 3.3a) is the ~5 Sv increase in upwelling of NADW in the Atlantic basin to 8.4 Sv (see Fig 3.7). This is due in an equal part to enhanced diffusive upwelling as the NADW cell

deepens into a region of higher diffusivity, and an increase in the clockwise eddy-induced cell in the convective region of the north Atlantic. This increase in the eddy-induced circulation is due to the north Atlantic surface density being equal to the surface density at a more southern latitude in the Southern Ocean in this state leading to a deepening and steepening of the isopycnals which outcrop in the north Atlantic.

Despite the lack of AABW formation, the anti-clockwise PDW cell in the Pacific basin maintains its strength and expands over the full depth of the Pacific basin below the wind-driven gyres. Since isopycnals do not outcrop in the north of the fresher Pacific basin, in contrast to the Atlantic basin, there is no upper cell to contract the anti-clockwise lower cell. The connection between the upper NADW cell in the Atlantic basin and the lower cell in the Pacific basin provides most of the source water for the PDW cell and this must return to the Atlantic basin to conserve volume in each basin. The upwelled PDW which flows into the channel is almost entirely connected to the channel's upper cell (i.e. above the 'z_interface') at the channel-basin boundary. Thus, it is connected to the NADW cell in the Atlantic basin, rather than being an isolated cell ('PDW_sep' is zero). The PDW returns to the Atlantic basin either directly via the zonal flows or after further upwelling by the wind-driven upper cell in the channel (the latter pathway increases in this case).

3.4.b *Present-day Circulation*

The sea-ice formation rate increases (non-linearly) with an increased sea-ice freezing point, reducing the buoyancy fluxes in the far south of the domain (see Fig 3.6b) to negative values. This increases the density in the south of the model and increases the formation of AABW altering the abyssal stratification. Thus, the lower AABW cell expands in the Atlantic basin while the NADW cell shoals. The NADW cell weakens as it is shoaled, with the greatest

sensitivity to the sea-ice formation rate (and buoyancy flux) between freezing points of -1°C and 0.5°C (Fig 3.7).

The control experiment (described in Section 3.3a) with a freezing point of 0°C looks most representative of the present-day circulation in this study (Fig 3.4b). The NADW cell weakens by 6.6 Sv relative to the future -1.96°C freezing point experiment, to ~13 Sv, somewhat weaker than the real ocean, while the AABW cell probably upwells to shallower depths than in the present-day ocean, but the pathways taken by the present-day MOC are therefore likely to be similar to this case, with the pathways depicted in Fig 3.9b.

The depths of the NADW cell interface and the 'z_interface' in this experiment decrease to ~2000 m and ~1700 m respectively (see Fig 3.8), and thus the ~300 m overlap between the Atlantic NADW cell and the channel's lower cell is far smaller than in the 'warmer' climate MOC. Therefore, the main change in the pathways taken in this present-day case relative to the 'warmer' climate MOC is that a greater proportion of the NADW flows into the upper wind-driven cell rather than the lower cell at the channel-basin boundary due to the shoaling of the NADW cell (see Fig 3.4b). This leads to an increase in the volume of NADW flowing into the channel that is directly wind-driven ('NADW_wind'), which partially compensates for the decrease in the volume of NADW diffusively-driven by Pacific upwelling ('NADW_pac') (see Fig 3.7). The relative importance of these pathways in the present-day MOC is particularly sensitive to changes in Southern Ocean buoyancy forcing. There is now a direct zonal flow of NADW from the Atlantic to the Pacific basin above the 'z_interface' ('NADW_pac_upper') which also compensates for the large decrease in 'NADW_pac_lower'. The 'NADW_pac_lower' pathway now involves NADW upwelling adiabatically to the surface in the channel's lower cell before being transformed to denser AABW. The volume of NADW flowing into the channel ('NADW_channel') only decreases by 1.7 Sv, with most of the NADW cell weakening due to reduced Atlantic upwelling.

The PDW cell responds to these changes in NADW pathways to conserve volume in each basin. There is an increase in the PDW flowing into the channel's lower cell ('PDW_sep'), which is therefore isolated from the Atlantic basin. The volume of PDW which is upwelled further by the channel's upper wind-driven cell must decrease significantly regardless of changes in PDW cell strength and structure, since the 'NADW_wind' component increases and there is also a slight decrease in the global-average upper cell flow at the channel-basin boundary. Thus, a greater proportion of the PDW returning to the Atlantic must be via the direct zonal pathway. The PDW cell still upwells over the full depth of the Pacific basin (Fig 3.4b).

3.4.c Glacial Circulation

As the sea-ice freezing rate is increased further, the NADW cell is shoaled further and the AABW cell in the Atlantic basin expands, until the NADW cell is more or less completely isolated from the channel's lower cell and the Pacific basin (see Fig 3.4c). The negative buoyancy flux in the south of the domain has increased significantly (Fig 3.6c).

The NADW cell weakens by 4.4 Sv in the 1°C freezing point experiment relative to the control, to 8.5 Sv (see Fig 3.7). The mechanism responsible for the weakening and the change in pathways may well reflect the real world glacial circulation changes. The pathways taken in the glacial state are depicted in Fig 3.9c. The overlap between the Atlantic NADW cell interface and the channel's lower cell is now only ~50 m (see Fig 3.8). The flow of NADW into the channel ('NADW_channel') decreases by 3.1 Sv, explaining over two-thirds of the decrease in cell strength. Of this reduced flow, the lower Pacific diffusive pathway ('NADW_pac_lower') decreases by 2.5 Sv to approximately zero due to the shoaling of the NADW cell. Thus, the AABW and NADW cells are virtually isolated (see Fig 3.9c) with

almost all of the upwelled PDW now flowing into the channel's lower cell ('PDW_sep' increases).

The Atlantic AABW cell expansion appears to be the primary cause of a 1.1 Sv reduction in the direct wind driven pathway ('NADW_wind') to 4.6 Sv due to the 'z_interface' being shoaled (all be it less so than the Atlantic NADW cell at the channel-basin interface). The NADW flowing into the channel is now almost all upwelled along the direct wind-driven pathway (i.e. 'NADW_wind' is approximately equal to 'NADW_channel'). There is also a weak 1.4 Sv direct zonal flow of NADW into an isolated PDW cell in the upper ocean (NADW_pac_upper'), which maintains a small 'NADW_pac' component. The volume of NADW upwelling in the Atlantic basin also decreases by 1.3 Sv. Thus, changes in Atlantic basin upwelling play only a secondary role in the weakening between the present-day and glacial states. The shoaling of the NADW cell by enhanced sea-ice formation provides a mechanism to both isolate the upper and lower cells and to weaken the NADW cell during glacial times.

3.5. Summary and Conclusions

In this paper we have explored the dependence of the MOC strength and structure on variations in Southern Ocean buoyancy forcing, which is known from general theoretical considerations to play a major role in determining the relative sizes of the two main overturning cells in the ocean (Nikurashin and Vallis [2012]). Specifically, we have used a two-basin ocean model with idealised topography to analyse the sensitivity of the MOC to varying Southern Ocean sea ice formation, one of the main mechanisms proposed to cause the transition of the ocean circulation to a glacial state (Watson and Garabato [2006], Ferrari et al. [2014], Jansen and Nadeau [2016]).

We find that enhanced sea-ice formation in the Southern Ocean, and thus more negative Southern Ocean buoyancy fluxes, can explain the transition of the MOC from a present-day to a glacial state (in agreement with the aforementioned studies) with an expanded AABW cell and weakened, shallow, NADW cell. In this glacial state the upper and lower cells are effectively isolated from each other and, in particular, the NADW is largely wind-driven, with little influence of diffusive upwelling in the Pacific. In contrast, in a potential future climate, with more positive Sothern Ocean buoyancy fluxes, the ocean is characterized by a weaker or non-existent AABW cell in the Atlantic and a deeper and stronger NADW cell (in agreement with the Jansen [2018] warming-induced response of the steady state MOC). The NADW (in the Atlantic) and the abyssal water mass in the Pacific (analogous to AABW) then have similar densities, with the deep ocean being only very weakly stratified.

A shoaling of the depth of the isopycnal defining the northern boundary of summertime Southern Ocean sea-ice due to the equatorward expansion of sea-ice (Ferrari et al. [2014]), and enhanced abyssal stratification as Southern Ocean sea-ice formation increases (Jansen and Nadeau [2016]) are likely to both play an important role in causing the NADW cell to shoal (Nadeau et al. [2019]). The change in the MOC pathways described here is a consequence of the sea-ice induced shoaling of the NADW cell (whatever the cause of the shoaling may be).

We have argued that the pathways taken by the MOC and the mechanisms driving the NADW cell in these aforementioned regimes may be determined from the volume flow rates between the residual circulations in each basin and the global-average residual circulation in the channel. The diffusive and wind-driven components of the MOC can thus be separated. The direct wind-driven component of the NADW cell is equal to the volume of NADW flowing into the channel above the interface between the channel's upper and lower cells at the channel-basin boundary (i.e. into the channel's upper cell). Conversely, the volume of

NADW which sinks in the Southern Ocean and ultimately upwells diffusively in the Pacific basin is equal to the volume of NADW flowing into the channel below the cell interface (i.e. into the channel's lower cell). An additional pathway of NADW directly into the Pacific basin via zonal flows as discussed by Ferrari et al. [2017] is also accounted for. The role played by both wind and diffusive upwelling in driving the present-day AMOC then becomes apparent, and will be further quantified in Part II. In the present-day climate, wind driven upwelling in the Southern Ocean has about the same importance as diffusive upwelling in the Pacific and, secondarily, the Atlantic basin, although this result of course depends on the precise values of the parameters chosen.

As the Southern Ocean sea-ice formation rate is increased (leading to enhanced negative buoyancy fluxes in regions of sea-ice growth because of seasonal brine rejection), the proportion of NADW driven directly by the winds relative to that driven by Pacific basin upwelling increases. For small changes in sea-ice formation the direct wind-driven pathway increase partially compensates for the decrease in the Pacific diffusive-driven pathway. As the sea-ice formation rate continues to increase, the connection between the upper and lower cells, and thus between the Atlantic and Pacific basins is reduced further. Eventually the cells are completely isolated with the Pacific diffusive-driven upwelling by the dominant PDW cell no longer contributing to the NADW cell strength. This is our glacial state.

The changes in these pathways are caused by the shoaling of the NADW cell as the Southern Ocean sea-ice formation rate is increased, causing the NADW flowing into the channel to be confined to shallower regions. In the modern ocean, NADW can in principle either flow directly into the channel's wind-driven upper cell, or into the lower cell which ultimately upwells diffusively in the Pacific basin. But as the NADW cell is shoaled, the volume of NADW flowing into the channel's lower cell decreases and the cell therefore becomes increasingly wind-driven as the Southern Ocean buoyancy flux becomes more negative. The

relative size of the aforementioned pathways under a given Southern Ocean buoyancy forcing depends on the strength of the Southern Ocean winds and the vertical diffusivity profile within the basins, as will be further explored in Part II of this study.

In the present-day MOC both the direct wind-driven and the Pacific diffusive-driven pathways of NADW are important, and the relative size of these pathways is very sensitive to perturbations in the Southern Ocean buoyancy forcing. There is also a weak direct zonal flow of NADW into the upper Pacific. A proportion of the upwelled PDW flows into the Atlantic basin via zonal flows and the channel's upper wind-driven cell, in order to conserve volume in each basin. The remainder flows into the channel's lower cell which is isolated from the Atlantic basin's NADW cell. The upwelling of PDW to shallow depths is possible despite a far lower diffusivity in the upper ocean.

The potential future warmer climate MOC, in which Southern Ocean sea-ice formation almost ceases leads to a deepening and slight strengthening of the NADW cell relative to the present-day, predominately due to enhanced Atlantic basin upwelling. The circulation is primarily diffusively-driven under these forcings with most NADW flowing directly into the channel's lower cell and thence into the Pacific basin. The PDW cell responds by returning all of the upwelled PDW to the Atlantic basin via the same pathways as in the present-day MOC.

In the glacial state MOC, the NADW cell weakens and is shoaled significantly. Thus, it can only flow into the channel's upper wind-driven cell (and the upper Pacific). There is no longer any flow into the channel's lower cell and hence the lower Pacific diffusive-driven pathway of NADW reduces to zero. The direct wind-driven flow also decreases slightly due to the shoaling of the global-average cell interface at the channel-basin boundary as the AABW cell expands. The NADW cell is therefore primarily weakened by a reduced flow

into the channel. The AABW cell in the Pacific basin responds by shoaling to the deep ocean rather than upwelling to the surface, with all of the upwelled PDW in the deep ocean flowing into the channel's lower cell. This again conserves volume in each basin. The NADW and AABW cells are therefore completely isolated.

This study extends our understanding of the pathways taken by the MOC under varying buoyancy forcings, following on from the study of Ferrari et al. [2014] and Nadeau et al. [2019]. It improves our understanding of the transition of the MOC between varying buoyancy states through eight varying Southern Ocean sea-ice formation simulations including a warmer than present-day state. Most previous studies only show a present-day and glacial state MOC. In particular, the pathways taken by PDW in addition to NADW are made explicit (Nadeau et al. [2019] focused on the NADW pathways), including the response of the PDW cell to changes in the NADW pathways. Our calculation of the NADW and PDW pathways by analysing the volume flow rates of these water masses into the channel's upper and lower cells is first considered in this study. Our analysis of these pathways helps us to explain the buoyancy induced changes in the strength and structure of the MOC. The meridional overturning streamfunction is shown to be a very useful tool to quantitatively evaluate the MOC pathways.

We end with a general remark. The transition to an ocean circulation resembling the one at the last glacial maximum, with a larger bottom cell (at least in the Atlantic) and weaker NADW cell, is undoubtedly influenced by many factors, including ice formation in the Northern Hemisphere and, possibly, an overall reduction in temperature changing the relative importance of buoyancy and salinity terms in the equation of state. Here we have shown that changes in Southern Ocean sea ice almost certainly play a major role in that transition.

ACKNOWLEDGEMENTS

We greatly appreciate and thank Jonathan Lauderdale for his advice on using the MITgcm, and Tobia Tudino for his help in using the university supercomputer.

3.6. APPENDIX

Methods: Calculation of the overturning components

The streamfunction components described below are analysed at the latitude bounding the north of the channel (36°S). ψ_{chan} is the global-average streamfunction at 36°S while ψ_{NADW} and ψ_{PDW} are the absolute values of the NADW and PDW streamfunctions at the south of the Atlantic and Pacific basins respectively (i.e. at 36°S). The subscript 'max' is the maximum value at 36°S. The ocean depth, z increases below the surface (z=0). The following formulas are used to determine the MOC components labelled in Fig 3.3 and used throughout this study. It should however be noted that the upper maxima of PDW (present in some cases) is only accounted for in these equations if the upper maxima is isolated above 'z_interface', otherwise a slight modification to (3.3), (3.4), (3.6) and (3.7) is required.

$$\text{Z\_interface} = z|_{\psi_{chan}} = 0 \tag{3.1}$$

$$\text{NADW\_channel} = T_{NADW\_channel} = \psi_{NADW\_max}\big|_{y=36°S} \tag{3.2}$$

$$\text{NADW\_pac\_lower} = T_{NADW\_pac\_lower} = \psi_{NADW}|_{z=interface} \tag{3.3}$$

$$\text{NADW\_pac\_upper} = T_{NADW\_pac\_upper} = \psi_{PDW\_max}\big|_{z \le z\_interface} - T_{NADW\_pac\_lower} \tag{3.4}$$

$$\text{NADW\_pac} = T_{NADW\_pac} = T_{NADW\_pac\_lower} + T_{NADW\_pac\_upper} \tag{3.5}$$

$$\text{NADW\_wind} = T_{NADW\_wind} = T_{NADW\_channel} - T_{NADW\_pac} \tag{3.6}$$

$$\text{PDW\_sep} = T_{PDW\_sep} = \psi_{PDW\_max}\big|_{y=36°S} - \psi_{PDW}|_{z=interface} \tag{3.7}$$

PDW_at $= T_{PDW\_at} = \psi_{PDW\_max}\big|_{y=36°S} - T_{PDW\_sep} + T_{NADW\_pac\_upper}$ (3.8)

Theoretically, $T_{NADW\_pac} = T_{PDW\_at}$ (3.9)

in order to satisfy the conservation of volume, since the flow of PDW which returns to the Atlantic basin to form NADW, T_{PDW_at}, should be equal to the volume of NADW which ultimately flows into the Pacific basin, T_{NADW_pac}. This formula is based on the assumption that the global-average circulation is applicable throughout the channel.

Substituting (3.5) and (3.8) into (3.9), and rearranging gives:

$\psi_{PDW\_max}\big|_{y=36°S} = T_{NADW\_pac\_lower} + T_{PDW\_sep}$ (3.10)

The sum of $T_{NADW\_pac\_lower}$ and T_{PDW_sep} is compared to the magnitude of the PDW cell maxima at the channel-basin boundary, $\psi_{PDW\_max}\big|_{y=36°S}$ to test the method. These should be equal if (3.8) is satisfied.

The sum of the components on the RHS of (3.10) are consistently greater than the maxima of the PDW cell, although only by about 0.3-0.4 Sv, decreasing to 0.1 Sv at the highest sea-ice freezing points. This is a small difference considering the size of the transports involved in this calculation and is always in the same direction. This is despite large changes in the transport components between experiments. This difference could either be due to the NADW_wind component being larger in reality and thus NADW_pac would be smaller, or it could be due to the PDW_sep component being smaller, perhaps a combination of these. This could be due to slight zonal differences in the channel residual circulation. It could also be in part due to error from vertical interpolation of the streamfunction. However, since the discrepancy is small and always in the same direction, it does not alter the conclusions drawn in this paper.

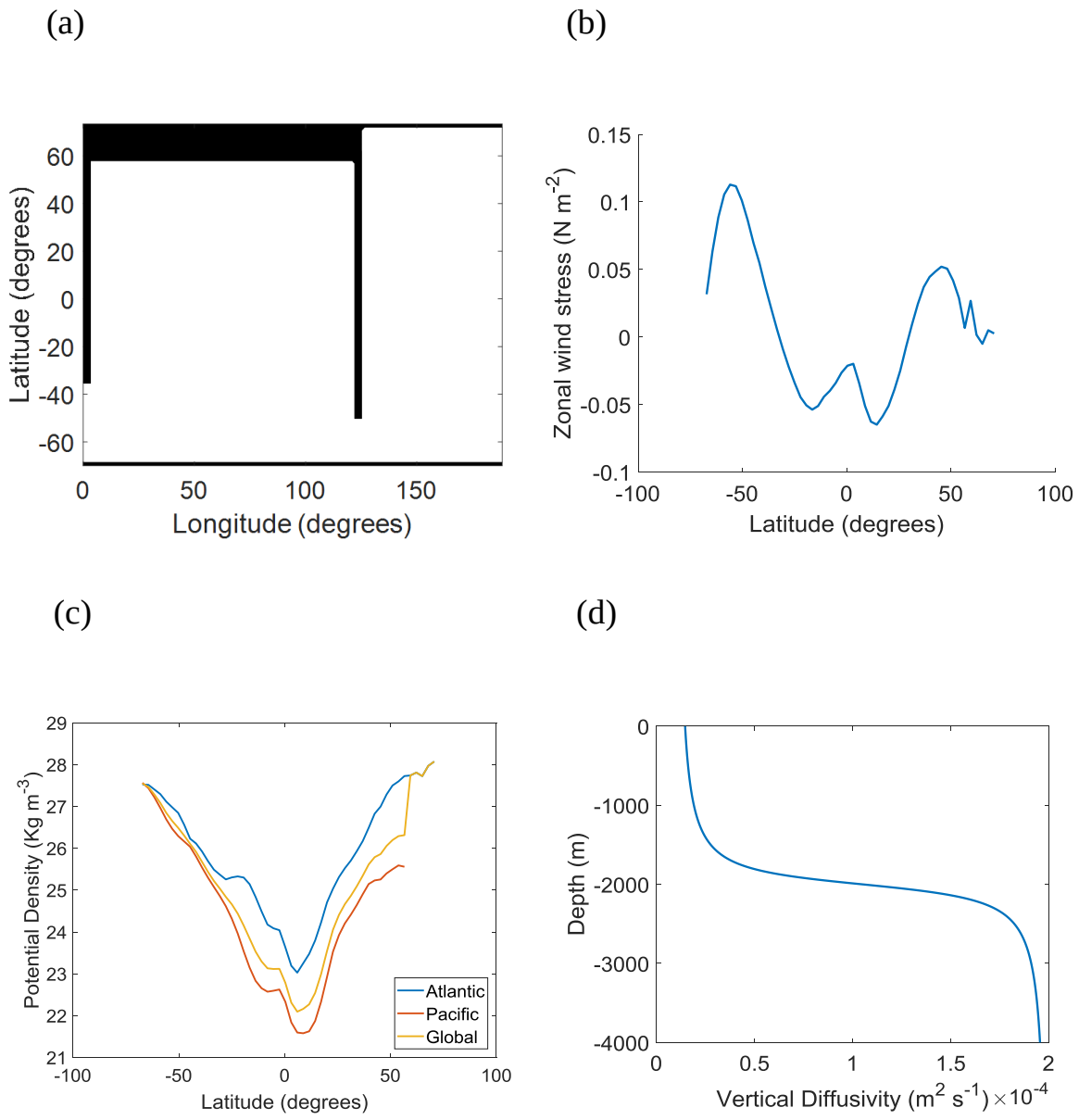

Fig 3.1: (a) Bathymetry of the multi-basin model. The ocean, shaded in white, has a depth of 4000 m, while land is shaded black. The basin on the left and right represent the Pacific and Atlantic Ocean's respectively. The meridional land strips in the west and centre of the domain represent the South Africa and South America land strips respectively. (b) Zonal average zonal wind stress (N m^{-2}). (c) Potential density (Kg m^{-3}) of surface waters in the control experiment, zonally-averaged over the Atlantic sector (blue), Pacific sector (red) and over the whole domain, referred to as global (orange). (d) Vertical profie of the vertical ocean diffusivity (m^2 s^{-1}) used in all experiments increasing from 0.1 x 10^{-4} m^2 s^{-1} at the surface to 2 x 10^{-4} m^2 s^{-1} at the ocean floor.

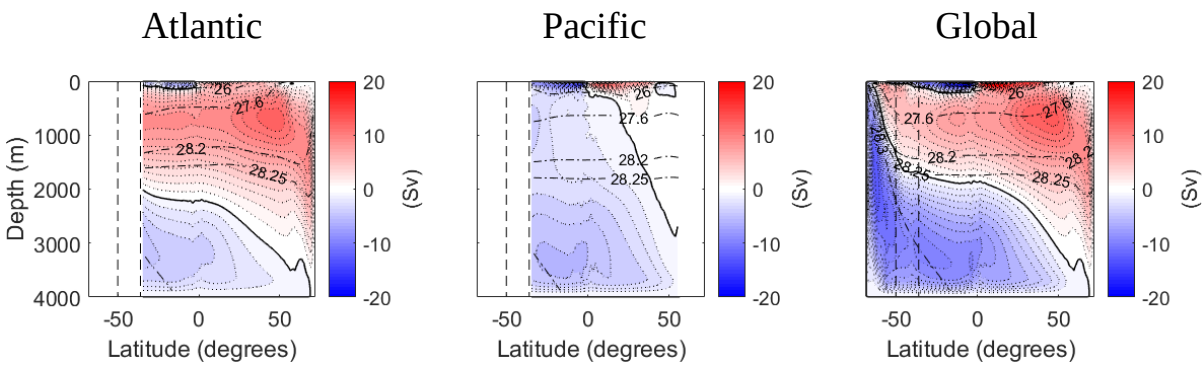

Fig 3.2: Zonal-average residual overturning streamfunction (Sverdrups) in the control experiment. A sea-ice freezing point of 0°C is imposed generating a MOC with a structure closest to the present-day. Plots from left to right are the Atlantic, Pacific and global-average circulations respectively. The red (positive) and blue (negative) streamfunctions are clockwise and anti-clockwise circulations respectively. The streamline contour intervals are 1 Sv. The thick solid black contour bordering the blue-shaded, anti-clockwise cell is the 0 Sv streamline, separating the clockwise and anti-clockwise cells. Potential density contours are represented by thin dash-dot black lines. The vertical dashed lines in the south of the domain are from left to right, the southernmost latitudes of the South America and South Africa landstrips respectively.

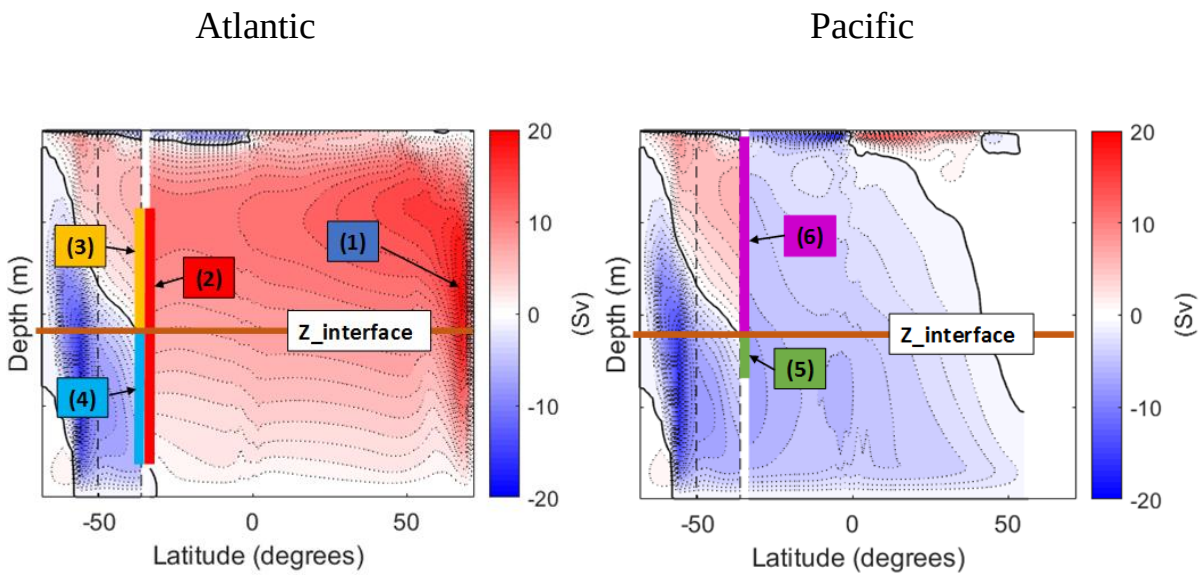

Fig 3.3: Zonal-average residual overturning streamfunction in the Atlantic (left) and Pacific (right) sectors when using the control forcings but with a sea-ice freezing point of -1.96°C. The global-average streamfunction is used in the channel. Colours and contours are as in Fig 3.2**.** The components of the overturning circulation (described in Section 3.3c) are labelled and represented by a vertical coloured line at the channel-basin boundary. Each component is equal to the net flow into the channel from the applicable basin to the north over the depth of the vertical line. The components labelled are (1) NADW cell strength, (2) NADW_channel, (3) NADW_wind, (4) NADW_pac_lower, (5) PDW_sep and (6) PDW_at. The depth of the interface between the upper and lower cells (i.e. the depth of the 0 Sv contour) of the global-average circulation at the channel-basin boundary, labelled 'z_interface' is represented by the horizontal line at mid-depth. Component (3) is modified slightly when there is a net zonal flow of NADW into the Pacific basin above 'z_interface'.

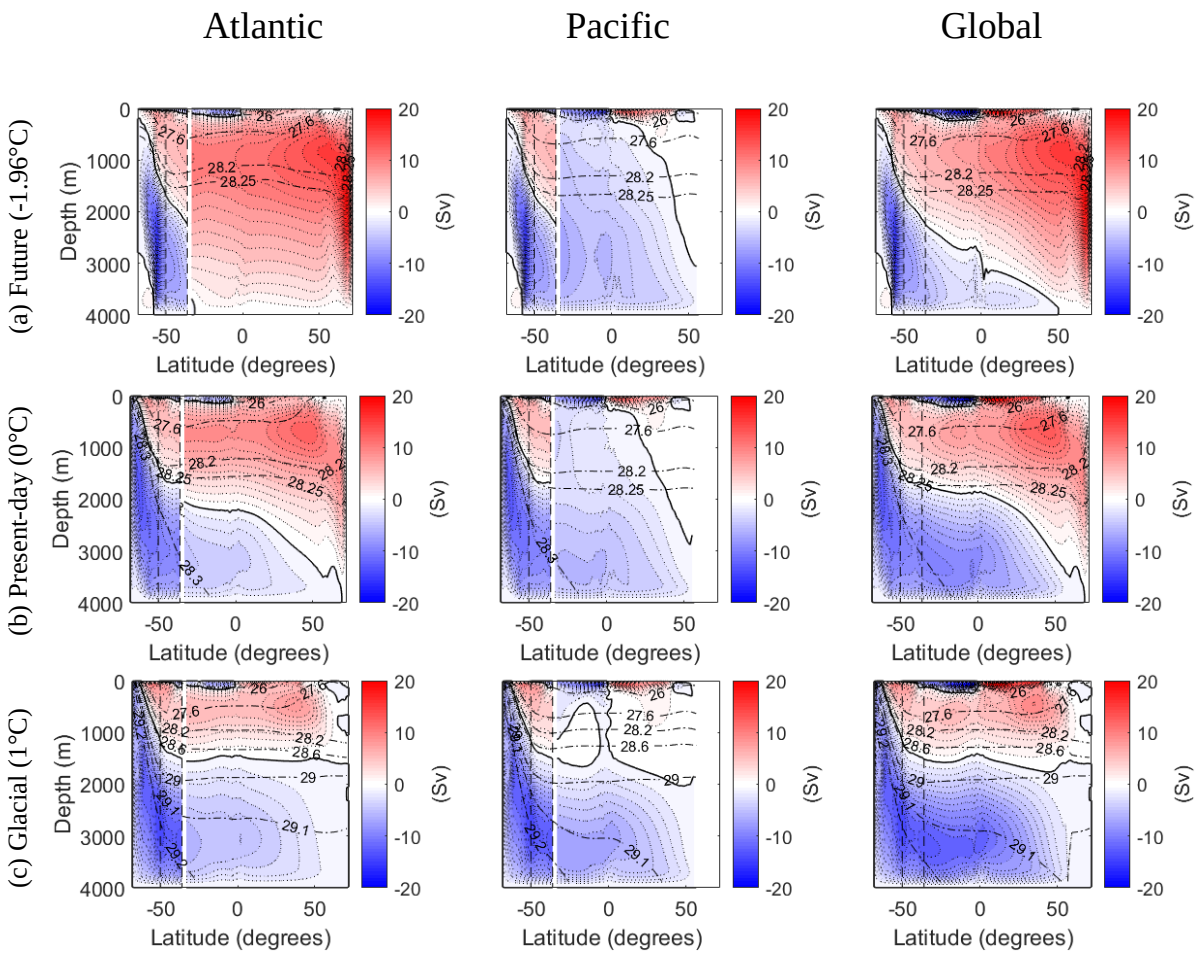

Fig 3.4: Zonal-average residual overturning streamfunction (1 Sv contour intervals) for varying sea-ice freezing points (and MOC states) from top to bottom of (a) -1.96°C (future 'warmer' state), (b) 0°C (present-day state) and (c) 1°C (glacial state) respectively. Plots from left to right are the Atlantic, Pacific and global-average circulations respectively. The global-average streamfunction is plotted in the channel in all plots. Colours and contours are as in Figs 3.2 and 3.3. Potential density contours are represented by thin dash-dot black lines (note the contour intervals above a potential density of 28.6 Kg m^{-3} are greater in (c) than in (a) and (b)). The vertical dashed lines are from left to right, the southernmost latitudes of the South America and South Africa landstrips respectively.

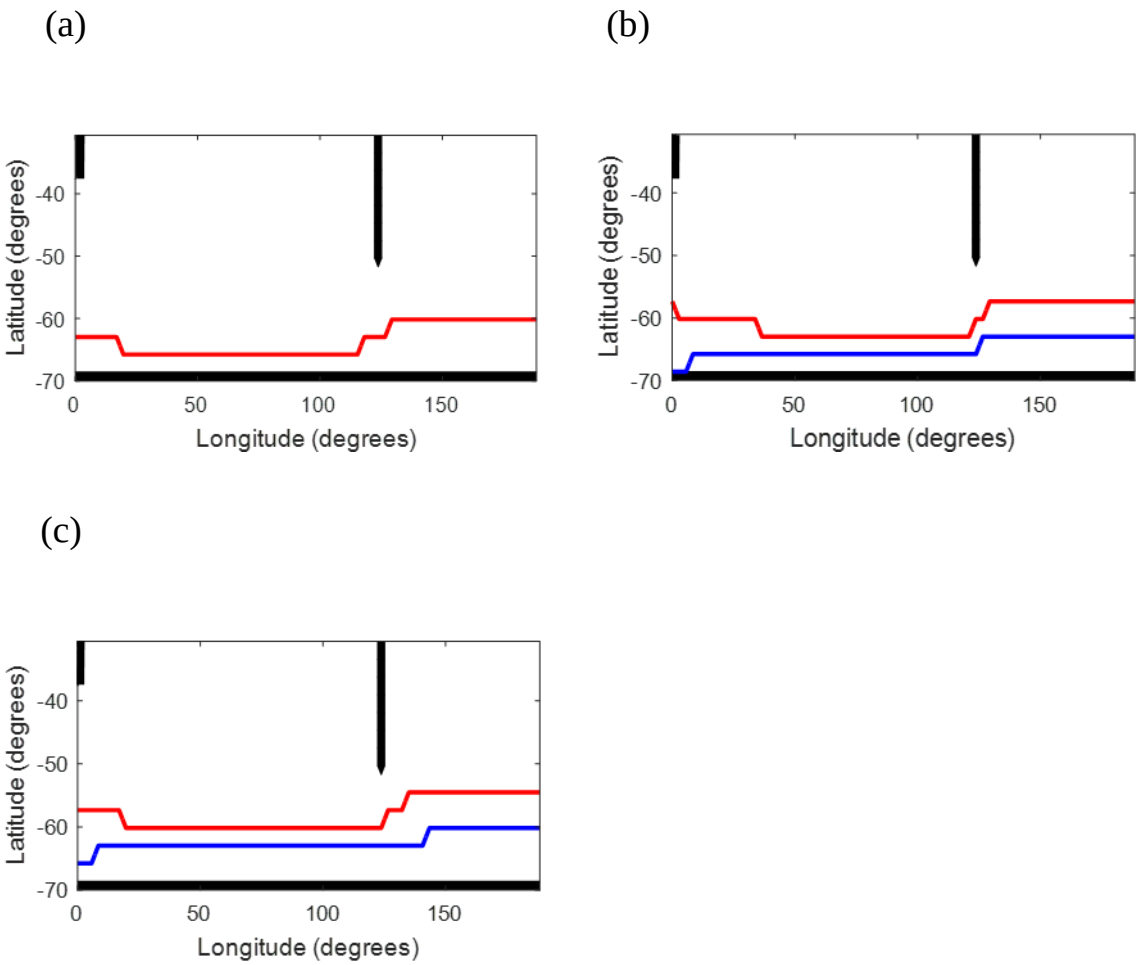

Fig 3.5: Southern Ocean annual-average sea-ice concentration for experiments with sea-ice freezing points of (a) -1.96°C (future 'warmer' state), (b) 0°C (present-day state) and (c) 1°C (glacial state). The sea-ice concentration northern boundaries displayed are 0.1 (red) and 0.8 (blue) implying an ocean surface coverage by sea-ice of 10% and 80% respectively.

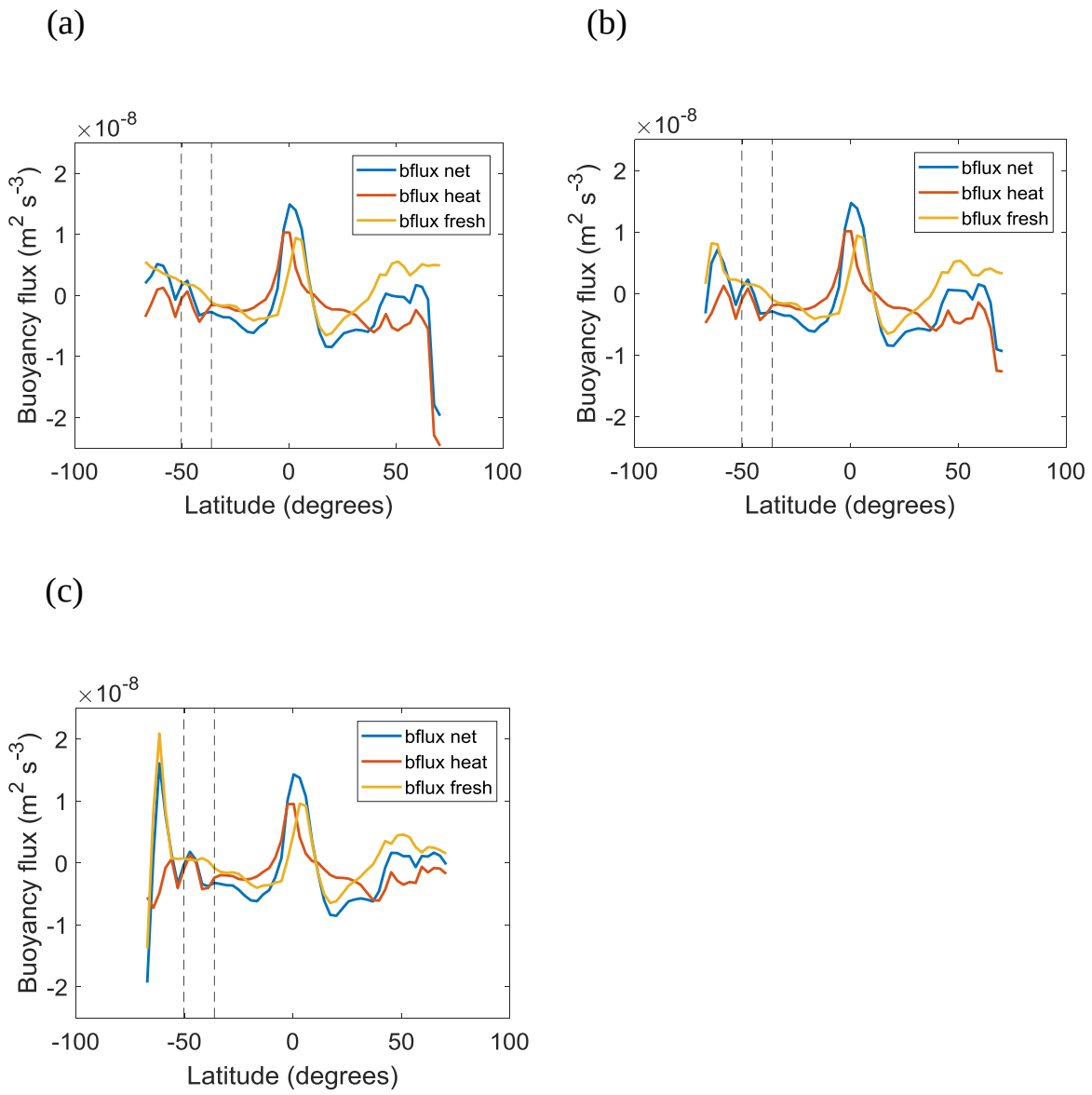

Fig 3.6: Zonal-average surface buoyancy flux ($m^2 s^{-3}$) against latitude over the whole model domain; plotted is the net buoyancy flux (blue), and the heat (red) and freshwater (orange) flux contributions to the net buoyancy flux. The plots correspond to the experiments with a sea-ice freezing point of (a) -1.96°C (future 'warmer' state), (b) 0°C (present-day state) and (c) 1°C (glacial state). The most notable changes are in the north Atlantic and in the Southern Ocean; in the north Atlantic the large negative buoyancy flux becomes more positive as the glacial state is approached. This is due to the net heat flux becoming less negative due to a reduced northerly flow speed as the NADW cell weakens. In the Southern Ocean, the buoyancy flux changes from positive in the far south to an increasingly negative buoyancy flux as the sea-ice formation rate and thus salinity flux increases towards a glacial state. In contrast, just to the north of these large salinity fluxes is a region with large freshwater fluxes from the melting of sea-ice formed further south, as it is forced northwards by the surface Ekman flow.

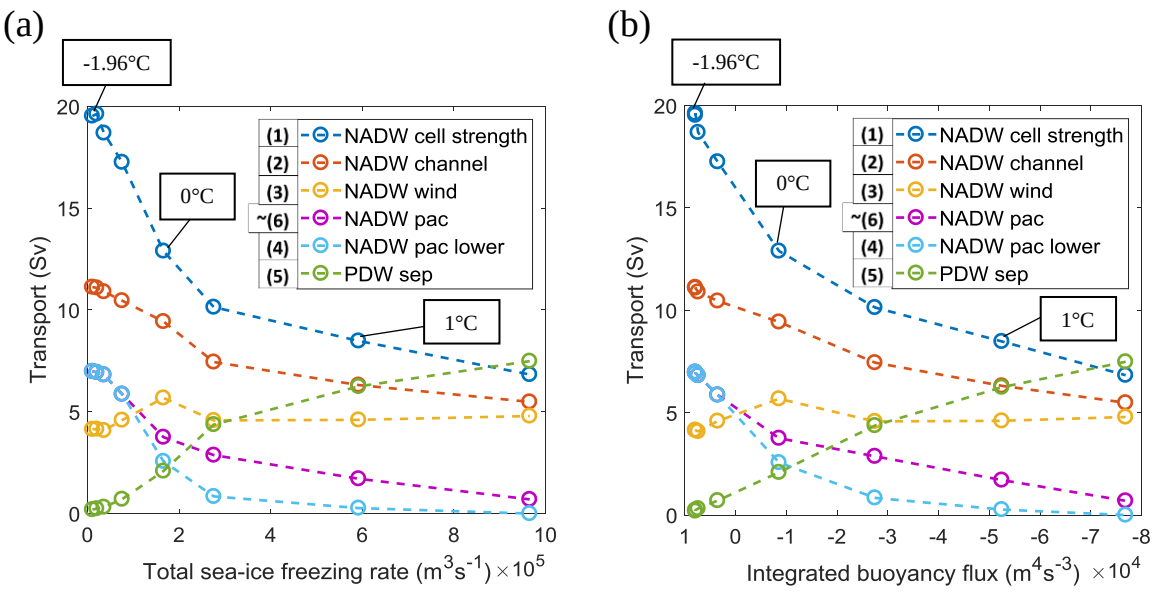

Fig 3.7: Zonal-average residual MOC overturning transport components as a function of (a) the total sea-ice freezing rate in the Southern Ocean and (b) the area integrated buoyancy flux in the southernmost latitudes where the zonal-average buoyancy flux becomes negative as the sea-ice formation rate increases. The dots on each component represent experiments with varying freezing points (see Methods) increasing from -1.96°C to 1.5°C (corresponding to the lowest and highest freezing rates respectively) with 0.5°C perturbations above -1.5°C. The colours and bracketed numbers next to the components plotted correspond to the components labelled in Fig 3.3. The components plotted are as follows: (i) NADW cell strength (dark blue (1)), (ii) NADW flow into the channel from the Atlantic basin (red (2)), (iii) NADW directly upwelled by the Southern Ocean winds (yellow ((3) after removing any zonal flow into the Pacific basin above 'z_interface')), (iv) NADW upwelled diffusively in the Pacific basin (purple (~6)), (v) the proportion of 'NADW_pac' flowing into channel's lower cell which subsequently upwells diffusively in the Pacific basin (light blue ((4) after removing any direct zonal flows into the Pacific below 'z_interface' due to the Pacific's upper ocean streamfunction maxima, if present)) and vi) the PDW flowing out of the Pacific basin which is isolated from the upper NADW cell and thus returns to the Pacific basin after densification in the Southern Ocean (green (5)). The difference between the NADW cell strength (dark blue) and NADW_channel (red) is the volume of NADW upwelling in the Atlantic basin and flowing back to the north before reaching the channel. The difference between 'NADW_pac' (purple) and 'NADW_pac_lower' (light blue) is equal to 'NADW_pac_upper', the proportion of 'NADW_pac' which is due to zonal flows into the Pacific basin above the 'z_interface' (and below it if a proportion of the flow into the Pacific basin below the 'z_interface' is a consequence of the Pacific's upper streamfunction maxima).

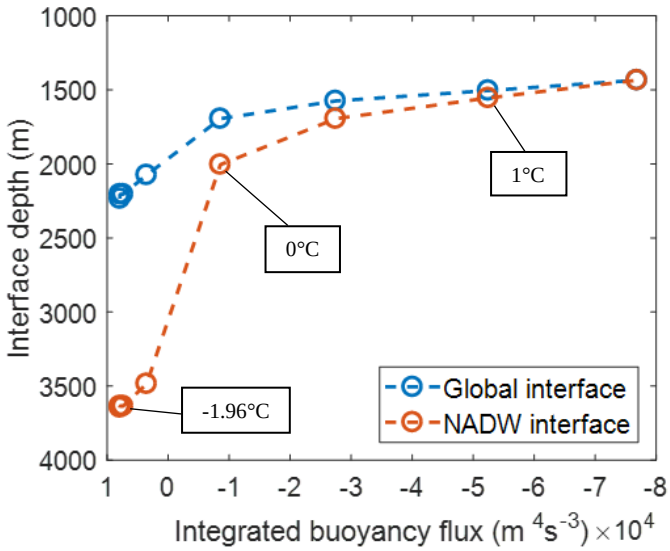

Fig 3.8: Interface depth of the global-average circulation (blue) referred to as 'z_interface' in this paper and the NADW cell (red) at the channel-basin boundary against the area integrated buoyancy flux in the southernmost latitudes where the zonal-average buoyancy flux becomes negative as the sea-ice formation rate increases. Each dot corresponds to a varying freezing rate experiment (see Fig 3.7).

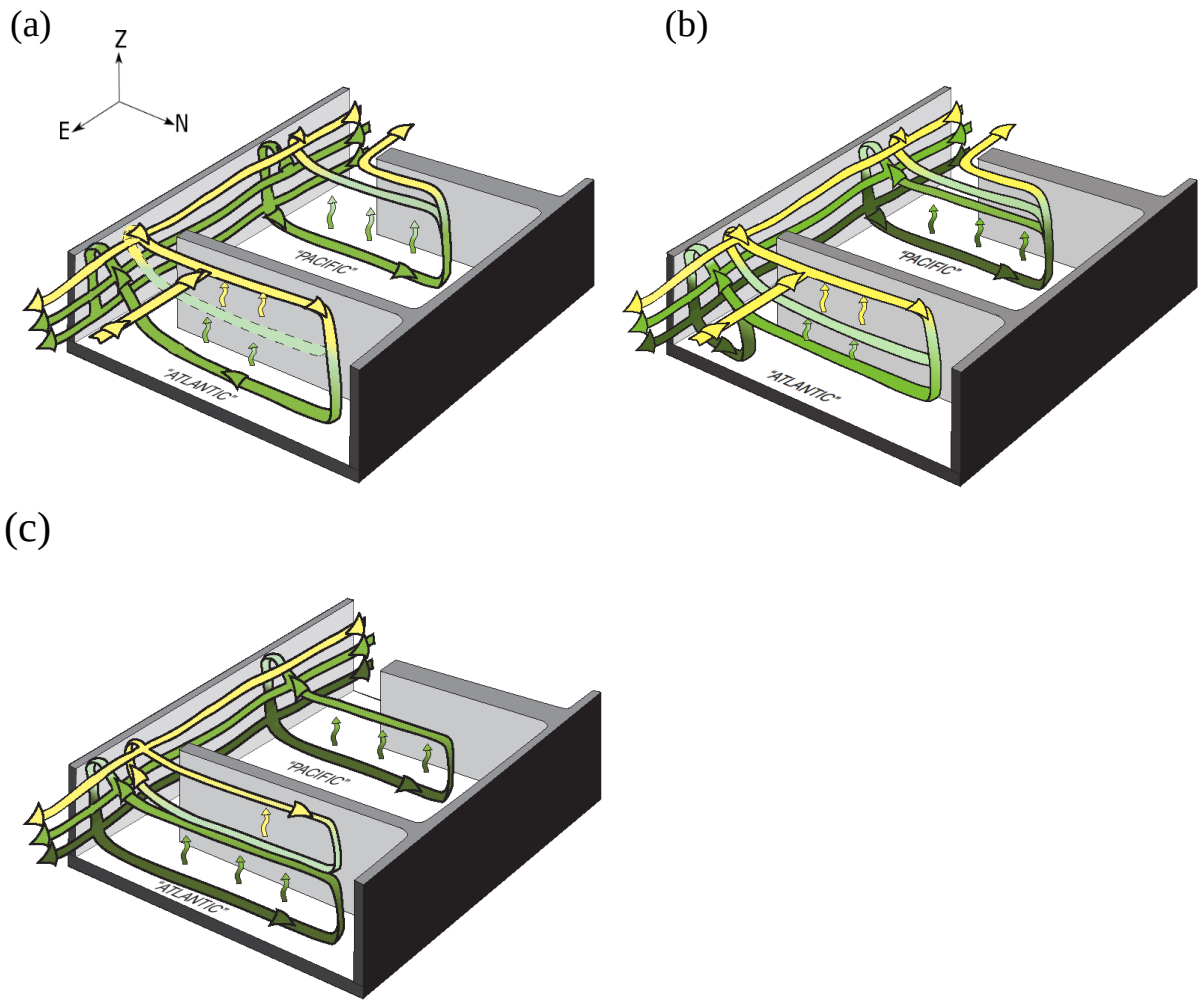

Fig 3.9: Schematics of MOC pathways in (a) the future 'warmer', (b) 'present-day' and (c) 'glacial' states of the two-basin model. Colours represent increasing density of flows from yellow (least dense) through lightest green to darkest green (most dense). Diffusive upwelling is indicated by small vertical wavy arrows. In (a) there is almost no Southern Ocean sea-ice formation, which however increases progressively in (b) and then (c). The meridional pathways represent the zonal-average flow in each basin and over the channel. The figures illustrate the shoaling of the NADW cell in the Atlantic in response to progressively greater buoyancy forcing in the south. For detailed explanation, see the text. The dashed line pathway (in (a)) of less dense NADW in the Atlantic basin flowing into the upper wind-driven cell in the channel represents the fact that the flow along this pathway is weaker than along the deeper pathway of NADW into the channel's lower cell.

3.7. Further analysis of MOC variations

In this section we perform an analysis of the changes in deep stratification and north-south (N-S) density differences in the southern buoyancy forcing perturbation experiments performed previously in this chapter. The aim of this additional analysis is to improve our understanding of the cause of the MOC changes in response to buoyancy forcing perturbations. In particular, we are interested in how the change in the MOC pathways and cell interface depths vary with deep stratification and density differences. We do not attempt to separate the effects of the sea-ice mechanisms of Ferrari et al. [2014] (i.e. a geometric argument), and Jansen and Nadeau [2016] (i.e. a buoyancy flux argument) as this has already been analysed in the multi-basin model study of Nadeau et al. [2019] as described in Section 3.1.

3.7.1. Deep stratification and surface density

The stratification averaged over the Atlantic sector of the model is shown against depth in Fig 3.10 for each of the buoyancy states in the buoyancy perturbation experiments performed previously. The stratification in the 'warm' and present-day states is very similar. However, the stratification in the glacial state increases significantly between a depth of about 800 m and 2000 m, with a local maxima in stratification at about 1250 m. The stratification profile therefore changes greatly in the glacial state at these depths. The NADW cell in the glacial state (Fig 3.4c) has shoaled to approximately the depth of this local maxima in stratification suggesting an important role for stratification in causing the shoaling as in Jansen and Nadeau [2016]. However, the change in the stratification profile in a glacial state differs from that shown in the single-basin model experiments performed by Jansen and Nadeau [2016]. In the former study, the stratification increases significantly over the full depth below 2000 m whereas the changes below 2000 m in Fig 3.10 appear fairly small. On closer inspection, the

stratification below 2000 m does increase by about 10^{-6} s^{-1} on average (Fig 3.11a), about five times smaller than the increase in Jansen and Nadeau [2016], all be it with a different variation in buoyancy forcing and also a vertically varying rather than a constant vertical diffusivity. The very large increase in stratification at 1250 m (~10^{-5} s^{-1}) in our model is not present in Jansen and Nadeau [2016]. The reason for these differences is beyond the scope of our study although this enhancement in stratification at 1250 m is a particularly interesting feature in our model. It raises more questions about the differences between single and multi-basin models, some of which we will discuss in Chapter 5.

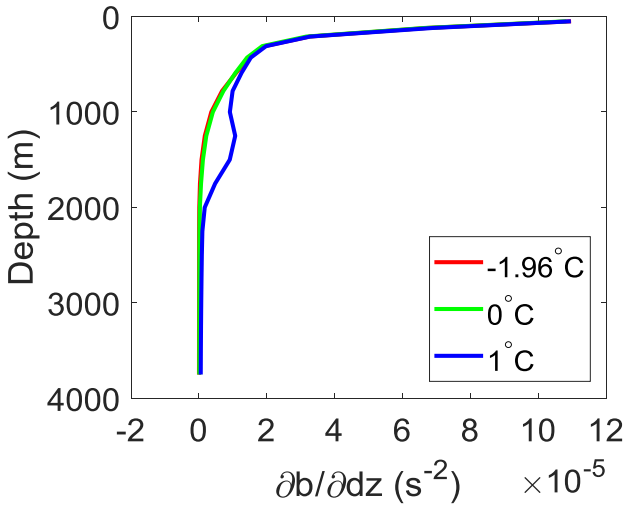

Fig 3.10: Atlantic sector averaged stratification (s^{-2}) against ocean depth for varying sea-ice freezing points (and buoyancy states) of -1.96°C (red), 0°C (green) and 1°C (blue) corresponding to the 'warm', present-day and glacial states respectively.

The deep stratification, N-S surface density contrast and depth of the most northerly and southerly outcropping isopycnals at the channel-basin boundary are plotted against the integrated buoyancy flux over the south of the domain in Fig 3.11. The deep stratification increases as the integrated buoyancy flux becomes more negative (Fig 3.11a) and thus with an enhanced Southern Ocean sea-ice formation rate. The change is relatively linear when averaged over all depths below 2 km, whereas the increase in stratification at 2 km is less

linear with a far larger increase. This is not unexpected since the stratification in Fig 3.10 increases towards the surface with a significant enhancement at a depth of around 1250 m in the glacial state. However, it is the change in the ocean's deep stratification that is believed to be most important for the changes in the MOC (Jansen and Nadeau [2016]) and thus we focus on depths below 2000 m.

(a)

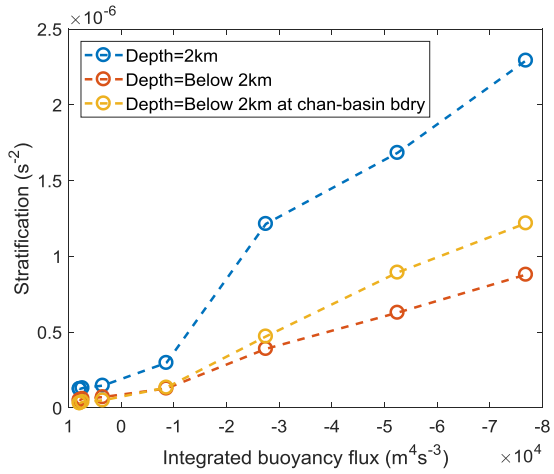

(b)

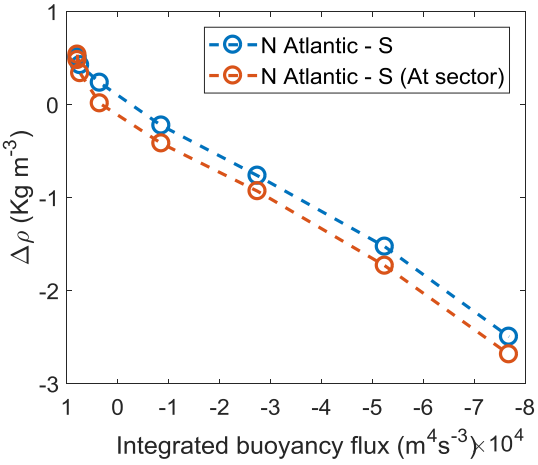

(c)

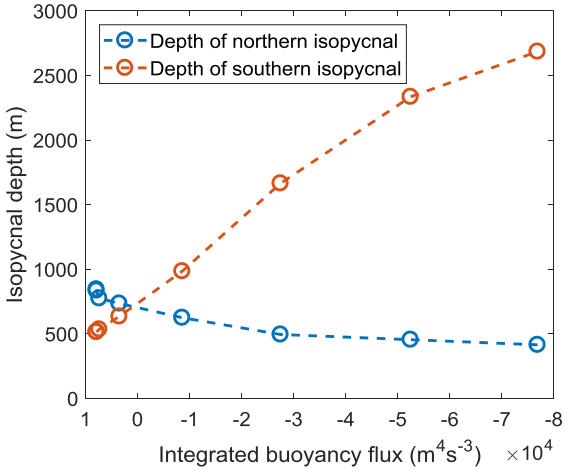

Fig 3.11: Plots of (a) Atlantic sector stratification (at various depths), (b) surface density difference between the North Atlantic and south of model (Atlantic sector average (red) and global-average (blue)) and (c) depth of northern and southernmost outcropping isopycnals at the channel-basin boundary against the integrated buoyancy flux in the far south of the domain.

The annual-average surface density in the south of the domain relative to the North Atlantic increases linearly as the integrated buoyancy flux in the south of the domain becomes more negative and a glacial state is approached (Fig 3.11b). In the 'warm' state, the North Atlantic is slightly denser than the Southern Ocean, whereas the Southern Ocean is denser than the North Atlantic in the present-day state. These density changes are expected since enhanced Southern Ocean sea-ice brine rejection leads to a more negative southern buoyancy flux, increasing the surface density in the south of the domain. This north-south density difference is likely important in the shoaling of the NADW cell, and expansion of the AABW cell between the 'warm' and glacial states.

The depth at the channel-basin boundary of the most northerly isopycnal outcropping in the North Atlantic (Fig 3.11c) is far shallower than the depth of the NADW cell in all buoyancy states, with the greatest discrepancy in the 'warm' state. Thus, the annual-average surface density in the North Atlantic is lower (i.e. buoyancy is higher) than the densest NADW formed. This suggests seasonal variations in NADW formation lead to this difference with significant NADW in the Northern Hemisphere winter when the North Atlantic surface density is lower. The depth of the globally-averaged southernmost outcropping isopycnal, at the channel-basin boundary, deepens significantly with a more negative southern buoyancy flux, increasing from ~500 m in the 'warm' state to ~2400 m in the glacial state (Fig 3.11c). This is a significant deepening coinciding with the increase in the deep stratification (Fig 3.11a) and is most likely due to the increase in southern sea-ice brine rejection which increases the density over all depths of the Southern Ocean.

3.7.2. MOC components and cell interface depths

We now plot the MOC components and cell interface depths against the deep stratification and N-S density contrast to determine the relationship between the MOC variations and these variables.

The MOC components vary in a similar way with changes in the N-S density difference (Fig 3.12b) and deep stratification (Fig 3.12c and d) to changes in the southern buoyancy flux (Fig 3.12a) between the 'warm' and glacial states. However, the initial large decrease in NADW cell strength between the 'warm' and present-day states occurs for only a small increase in deep stratification and thus there is a far more rapid decrease with enhanced stratification than with reduced southern buoyancy fluxes (compare Fig 3.11a with Fig 3.11c, d). This decrease between the 'warm' and present-day states is primarily due to reduced Atlantic upwelling which is therefore unlikely due to changes in deep stratification. However, the reduction in NADW cell strength with further increases in deep stratification above the present-day state value varies far more slowly with increased stratification. The components vary more linearly with enhanced stratification than the response to changes in the southern buoyancy flux and north-south density difference. The NADW cell is here primarily weakened by a reduction in the Pacific pathway. The enhanced deep stratification likely plays a significant role in these changes by shoaling the NADW cell.

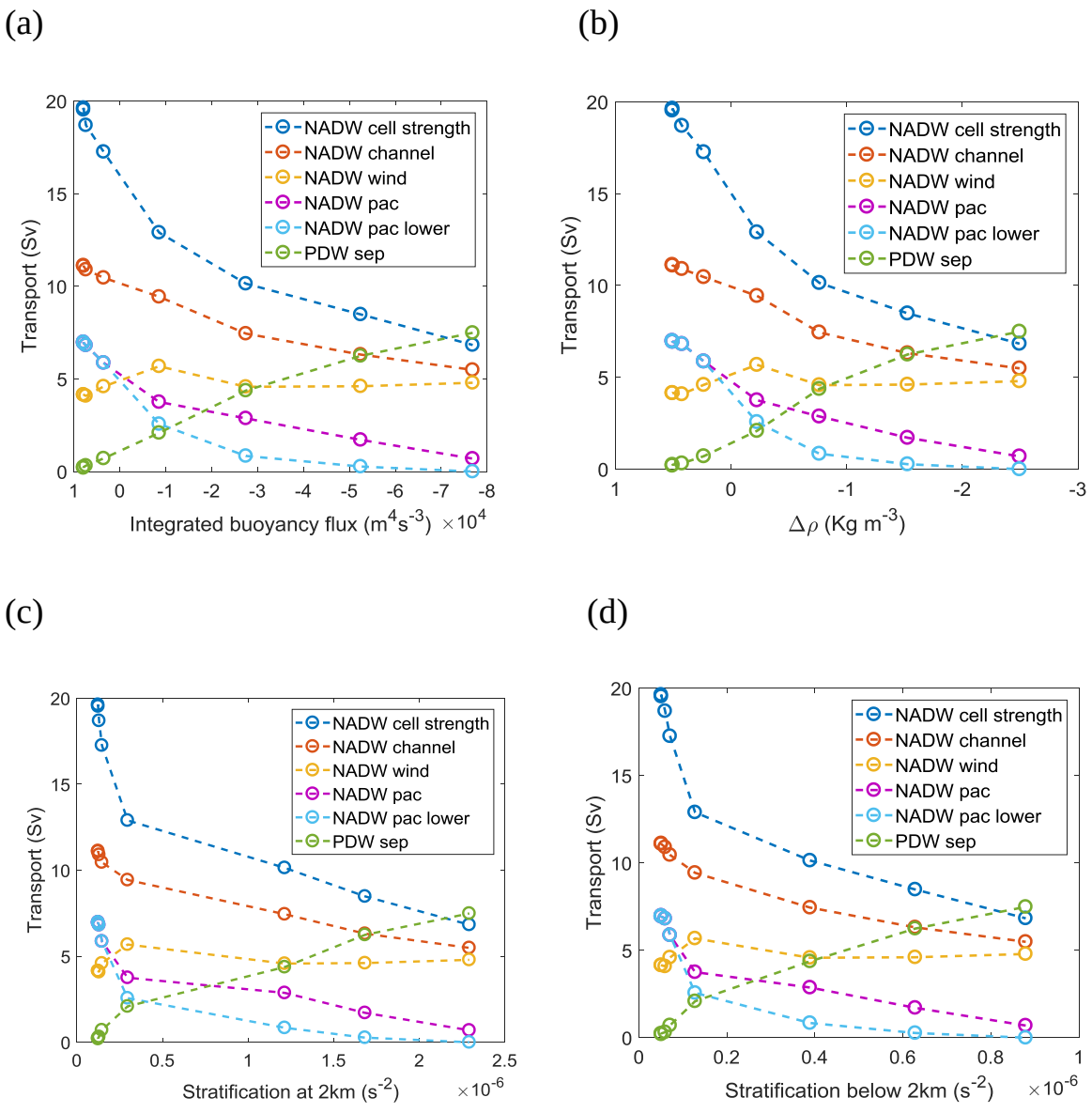

Fig 3.12: Zonal-average residual MOC overturning transport components as a function of (a) the area integrated buoyancy flux in the southernmost latitudes, (b) the North Atlantic-south of domain density difference, (c) Atlantic sector stratification at 2 km, and (d) Atlantic sector stratification averaged below 2 km. The dots on each component represent experiments with varying freezing points increasing from -1.96°C to 1.5°C (corresponding to the lowest and highest freezing rates respectively) with 0.5°C perturbations above -1.5°C. See Fig 3.7 for further details.

The change in the NADW and global-average cell interface depths at the channel-basin boundary are plotted against the variables of interest in Fig 3.13. As in Fig 3.12, the changes are similar between all variables with the NADW cell interface shoaling at a faster rate than

the global-average cell interface as the glacial state is approached. The variation of the interface depths with enhanced deep stratification is highly linear for values greater than in the present-day state (Fig 3.13c and d).

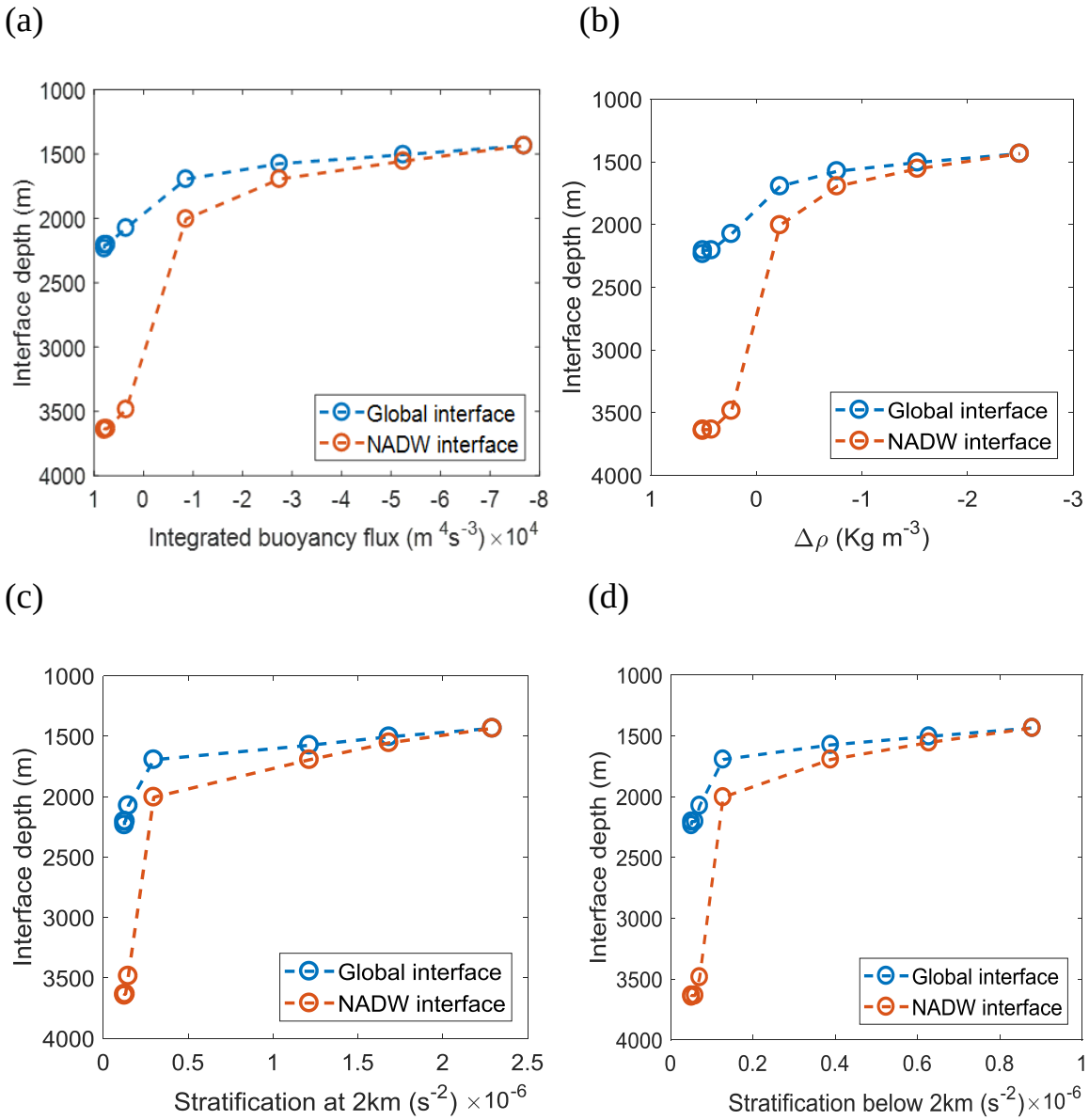

Fig 3.13: Interface depth of the global-average circulation (blue) and the NADW cell (red) at the channel-basin boundary against (a) the area integrated buoyancy flux in the southernmost latitudes, (b) the North Atlantic-south of domain density difference, (c) Atlantic sector stratification at 2km, and (d) Atlantic sector stratification averaged below 2km. Each dot corresponds to a varying freezing rate experiment (see Fig 3.7).

This analysis highlights the complexity of the changes in stratification in response to varying buoyancy forcing and also suggests there may be a difference between the stratification changes in single and multi-basin models. It suggests deep stratification changes play an important role in the MOC changes, along with the simultaneous change in the north-south density contrast. It is however difficult to separate these factors in their contribution to the MOC changes given how they are both highly linked to the changes in sea-ice and buoyancy forcing.

Chapter 4

Meridional Overturning Circulation in a multi-basin model Part II: Dependence on Southern Ocean wind forcing and vertical diffusivity

This work is a first draft of a paper which will form the second part of the study in Chapter 3. Significant further work will be needed to cut down this manuscript prior to submission. However, here we provide greater detail which will not be possible in the final version we submit.

4.0. ABSTRACT

The strength and structure of the Meridional Overturning Circulation (MOC) under varying Southern Ocean zonal wind stress and Pacific basin vertical diffusivity is investigated in a two-basin general circulation model connected by a southern circumpolar channel. As in Part I (Chapter 3), the variation of the wind and diffusively-driven pathways of the MOC are quantified. The Southern Ocean buoyancy forcing is also varied, corresponding to a varying sea-ice formation rate.

The North Atlantic Deep Water (NADW) cell strengthens (weakens) with enhanced (reduced) Southern Ocean wind stress and Pacific diffusivity under all buoyancy forcings; the 'warm', present-day and 'cold' glacial states.

The sensitivity of the NADW cell to Pacific diffusivity increases as the buoyancy forcing is varied from a 'cold' glacial to a 'warm' state, due primarily to a greater change in the Pacific diffusively-driven pathway of NADW in the 'warm' state and also a greater change in Atlantic upwelling as the NADW cell deepens. In contrast, the NADW cell is more sensitive to changes in wind stress when the buoyancy forcing is varied from a 'warm' to a present-day or glacial state due to a greater variation in the wind-driven pathway of NADW in these latter states.

The changes in diffusivity and wind speed significantly alter the structure of the MOC, the latter leading to changes in the channel circulation. At low wind speeds, the NADW cell only weakens slightly in the 'warm' and present-day states due to the maintenance of the Pacific diffusively-driven pathway through zonal flows of NADW between the Atlantic and Pacific basins, and the expansion of the channel's lower cell respectively. The NADW cell is not shoaled implying reduced Southern Ocean wind forcing alone cannot lead to a glacial state MOC.

4.1. Introduction

In Part I (Chapter 3) of this study, changes in buoyancy forcing was shown to have a significant impact on the Meridional Overturning Circulation (MOC). In this paper the impact of changes in Southern Ocean wind forcing and Pacific vertical diffusivity on the MOC is analysed under varying buoyancy states.

North Atlantic Deep Water (NADW) formation in the North Atlantic must be balanced by an upwelling of these dense waters elsewhere in the ocean. This was believed to be provided by diffusive-driven upwelling by interior vertical mixing throughout the ocean (Munk [1966], and Munk and Wunsch [1998]) maintaining the deep stratification via the advective-diffusive balance. However, more recently wind-driven adiabatic upwelling in the Southern Ocean has been proposed as an alternative mechanism to upwell NADW and believed to play a dominant role (Toggweiler and Samuels [1995]; Doos and Coward [1997]). As shown in Part I (Chapter 3) of this study and a number of previous studies (e.g. Vallis [2000]; Kuhlbrodt et al. [2007]; Ferrari et al. [2017]) both of these processes appear to play an important role in the present-day ocean.

A number of studies have looked at the importance of the Southern Ocean winds and vertical diffusivity on the MOC in both global **(**e.g. Lauderdale et al. [2013]; Jochum and Eden [2015]**)** and idealised ocean models (e.g. Gnandesikan [1999]; Nikurashin and Vallis [2011; 2012]**)**. The response of the MOC to changes in the Sothern Ocean wind forcing has been of particular interest, since it is an alternative mechanism to the reduced Southern Ocean atmosphere-ocean buoyancy fluxes (Watson and Garabato [2006], Ferrari [2014], Jansen and Nadeau [2016]) discussed in Part I to instigate the glacial shoaling and weakening of the NADW cell during glacial periods. A weakening or northward shift in the Southern Hemisphere westerly winds (Toggweiler and Samuels [1993, 1995]; Toggweiler et al.

[2006]) could cause this transition to a glacial state MOC. In this paper, the Southern Ocean wind strength mechanism is investigated.

The theory of the dependence of the NADW cell on the Southern Ocean winds (and other parameters) is studied by Gnandesikan [1999], Gnandesikan et al. [2007], Shakespeare and Hogg [2012], Nikurashin and Vallis [2012] using idealised models. The models all suggest a strong relation between Southern Ocean winds and the strength of the NADW cell.

The Southern Ocean westerly winds have been shown to be significant in numerous other ocean model studies (Wunsch [2003]; Oka et al. [2012], Lauderdale at al. [2013], Munday et al. [2013]). However, other studies suggest the AMOC's response to wind forcing may be eddy compensated (Downes and Hogg [2013]), although only some of the course-resolution CMIP5 climate models used in this study show full eddy-compensation. Eddy compensation implies that changes in the wind-induced Deacon circulation are compensated by changes in the opposing eddy-induced circulation in the Southern Ocean (Marshall and Radko [2003]). Bishop et al. [2016] find the NADW cell strengthens in response to enhanced Southern Ocean wind speed in a high resolution eddy-resolving global coupled climate model although the simulation was only run for ~20 years and thus only the transient response of the MOC is obtained. In contrast to many of these studies, Jochum and Eden [2015] suggest the NADW cell is almost insensitive to changes in the wind, maintaining its strength in a global model even if the wind is reduced to zero by instead upwelling diffusively in the Indo-Pacific. The importance of Southern Ocean upwelling on the Atlantic Meridional Overturning Circulation (AMOC) and climate is reviewed by Marshall and Speer [2012], while Gent [2016] provides a review of eddy saturation and eddy compensation in studies which used differing models and horizontal resolution.

Timmermann and Goose [2004] show that wind forcing is essential for the maintenance of the NADW cell. However, they only look at the effect of changing the wind forcing globally, rather than the Southern Ocean winds, thus the results are likely to differ substantially.

The importance of mixing on the NADW cell in the real world remains under debate. Although, early theories of the MOC used diffusive upwelling in all ocean basins to close the circulation (Broecker and Peng [1982]; Gordon [1986]; Broecker [1987]), observational estimates of the vertical mixing of ~10^{-5} m^2 s^{-1} would be too small to maintain the present-day strength of NADW (Gregg [1987]; Ledwell et al. [1993]; Toole et al. [1994], Wang and Huang [2005]). More recent research suggest this discrepancy could be at least partly explained by enhanced mixing over bathymetry which leads to the bottom enhancement of diffusivity in the ocean by internal wave breaking (Wunsch and Ferrari [2004]; Nikurashin and Ferrari [2010]). The connection of the MOC in the present-day between the Atlantic and Indo-pacific basins is believed to be a major route of the MOC (Lumpkin and Speer [2007]; Talley [2013]; Cessi [2019]).

A higher vertical diffusivity has been shown in numerous model studies to strengthen the NADW cell (e.g. Bryan [1987]; Zhang et al. [1999]; Marotzke [1997]; Vallis [2000]; Mignot et al. [2006]; Nikurashin and Vallis [2012])

The theoretical models of Gnandesikan [1999] and Nikurashin and Vallis [2012] also predict a strong sensitivity of the NADW cell to changes in vertical diffusivity. However, these models have single ocean basins and thus the importance of Pacific upwelling cannot be separated from Atlantic upwelling.

Mignot et al. [2006] analysed the effect of global changes in a uniform vertical profile of vertical diffusivity on the MOC in a global model, separating the Atlantic upwelling of NADW and the export to the south out of the basin. They find the NADW cell strength is

linearly dependent on and highly sensitive to the diffusivity but the southward export of NADW out of the Atlantic basin varies only weakly with diffusivity, a surprising result given the apparent importance of Pacific diffusive upwelling in driving the present-day NADW cell. However, the effect of buoyancy fluxes were not considered in this study which as shown in Part I (Chapter 3) can change the MOC pathways significantly with an increase in the direct wind component relative to the diffusive component as the MOC transitions from a 'warm' to a glacial state.

In contrast to these previous studies, only the diffusivity in the Pacific basin is varied in our study enabling the importance of this interbasin exchange and Pacific upwelling on the NADW cell to be isolated.

In Part I (Chapter 3), we separated the wind and (Atlantic and Pacific) diffusive-driven components under varying surface buoyancy forcings. In this paper, the variation of these components with Southern Ocean wind forcing and Pacific vertical diffusivity is analysed in the two-basin configuration under varying initial buoyancy forcings. The aim of this paper is to further develop our understanding of the structure and resulting pathways taken by the MOC, and its driving mechanisms under varying forcings, following on from Part I. It will also further our understanding of the sensitivity of the MOC to wind and diffusivity, and allow us to investigate the plausibility of the Southern Ocean wind speed mechanism in inducing the transition to a glacial state.

The key questions we seek to answer are:

1) How does the sensitivity of the MOC and its components vary with Southern Ocean wind speed and Pacific diffusivity under varying initial buoyancy forcings? In particular, how does the strength and structure (or pathways) of the NADW cell vary, and can the upwelling mechanisms which sustain the MOC be separated?

2) Can reduced Southern Ocean wind speeds explain the transition of the MOC to a glacial state?
3) How does the dependence of the MOC on Southern Ocean buoyancy forcing studied in Part I change if a different wind forcing or Pacific vertical diffusivity is used?

This paper is organised as follows: the model (an ocean model coupled to a sea ice model) and experiments performed using it are described in Section 4.2, in Section 4.3 we describe the control simulations, in Sections 4.4 and 4.5 we describe and compare the results of the experiments in which we vary the Southern Ocean wind forcing and the Pacific vertical diffusivity respectively, and in Section 4.6 we summarize and conclude.

4.2. Model Setup and Experiments

As in part I, the Massachusetts Institute of Technology general circulation model (MITgcm) (Marshall et al. [1997a,b]) is used with a 2.8 degree horizontal resolution and 20 vertical levels in a 4000 m deep ocean. An idealised domain is used with two basins (referred to as "Atlantic" and "Pacific") connected by a circumpolar channel in the south.

The model is forced at the surface by a wind stress (Fig 4.1a), and heat and freshwater fluxes. Further details of the forcings used and geometry of the model are described in Part I.

Sea-ice is simulated using a fully coupled model based on the non-linear dynamic-thermodynamic sea-ice model with viscous-plastic rheology first employed by Hibler [1979] and modified for efficiency by Zhang and Hibler [1997], and more recently by Losch et al. [2010] for use in coupled ice-ocean models. The sea-ice model accounts for the effects of sea-ice on the buoyancy fluxes with the sea-ice freezing point set to values of -1.96°C, 0°C and 1°C to obtain buoyancy fluxes which simulate a MOC representative of a 'cold' glacial, a

present-day and a future ‘warm’ state respectively. Increases in the sea-ice freezing point lead to an enhanced Southern Ocean sea-ice formation rate and thus changes in the surface buoyancy flux mediated through the rate of sea ice brine rejection. We refer to experiments with freezing points of -1.96°C, 0°C and 1°C as ‘warm’, ‘present day’ and ‘glacial’ climates respectively throughout this paper. Further reasoning for this approach and details are provided in Part I.

The vertical ocean diffusivity is set using the Bryan and Lewis [1979] diffusion scheme (BL79) with a surface diffusivity of approximately 10^{-5} m^2 s^{-1} increasing to approximately $2x10^{-4}$ m^2 s^{-1} at depth and it is horizontally uniform (Fig 4.1b). There is a large increase in vertical diffusivity at about 2 km to represent the topographical enhancement of mixing at depth caused by the generation of turbulence by internal wave breaking (Wunsch and Ferrari [2004]).

The Gent-McWilliams (GM) eddy parameterisation (Gent and McWilliams [1990]; Gent et al. [1995]) is used to determine the ‘bolus’ or eddy-induced velocity which represents the advective effect of geostrophic eddies in the flow. This eddy-induced circulation acts to flatten the isopycnals due to baroclinic instability, converting available potential energy to eddy kinetic energy. The Redi scheme (Redi [1982]) is used to diffuse tracers along isopycnals to represent the isopycnal mixing effects of eddies. The eddy transfer coefficient is set to 1000 m^2 s^{-1}. The eddy compensation to changes in wind forcing is dependent on this GM-Redi parameterisation scheme. Although, it may not be a true representation of reality, it does provide a reasonable estimate of the eddy-induced circulation for our purposes.

(a) (b)

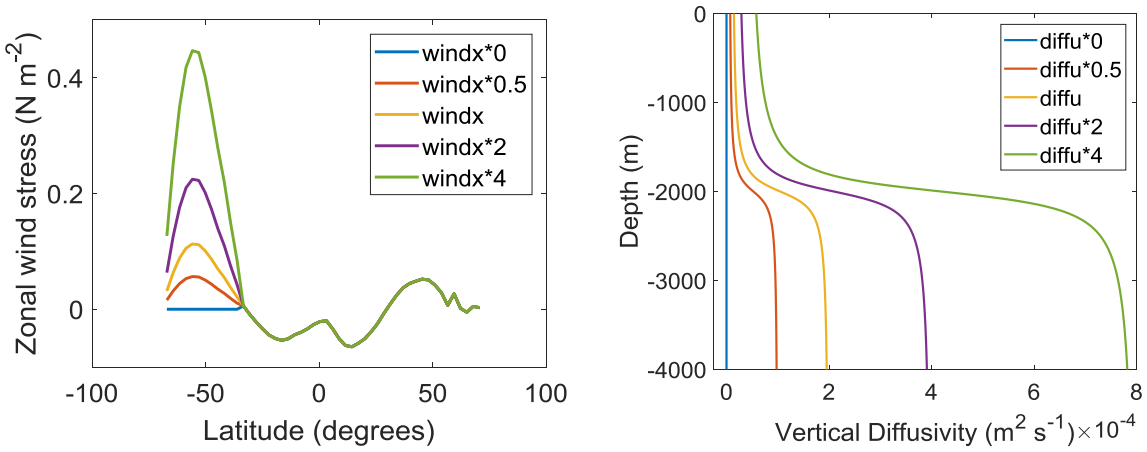

Fig 4.1: (a) Zonal wind stress (zonally-averaged over the domain) against latitude and (b) Vertical profile of the background vertical diffusivity ($m^2\ s^{-1}$) in the Pacific basin of the model, in the control (windx and diffu), and the zero (var*0), half (var*0.5), two-fold (var*2) and four-fold (var*4) Southern Ocean zonal wind stress and vertical diffusivity perturbation experiments (where var is the windx or diffu variables in the respective experiments).

The experiments performed in this study perturb either the Southern Ocean wind speed (south of 36°S), leading to a similar change in wind stress (Fig 4.1a), or the vertical diffusivity in the Pacific basin (Fig 4.1b), by factors ranging from zero to four-fold relative to the control. There are three control experiments from which the wind or diffusivity is perturbed. These use varying sea-ice freezing points and thus Southern Ocean buoyancy forcing, as described above to represent the 'warm', present-day and glacial states.

The wind speed is only perturbed south of 36°S (referred to as the channel in this study), the latitude of the southern extent of the 'South Africa' meridional land strip in the model since the Deacon cell, a consequence of the northward surface Ekman transport is mainly localised to the region south of this latitude, which has only one or no meridional boundaries to obstruct the resulting zonal ocean transport. This wind-induced upwelling of NADW therefore is restricted to the south of this latitude. The wind speed also becomes westerly

south of this latitude, enabling the wind perturbation profiles to maintain approximately the same shape and the zero wind experiment to have no discontinuity at the channel-basin boundary.

The model is spun up over several thousand years before a steady state is reached for the control state. Perturbation experiments are integrated for a further 10,000 years to ensure a steady state is reached.

4.3. Control simulations

The future 'warm', present-day and 'cold' glacial MOC states obtained in Part I by using a sea-ice freezing point of -1.96°C, 0°C and 1°C respectively and thus with an increasing Southern Ocean sea-ice formation rate are our three control experiments (see Fig 4.2). These control experiments all use the control wind speed and diffusivity. The zonal wind speed and Pacific vertical diffusivity perturbations described in Section 2 are applied in each control experiment. Thus, the response of the MOC to these perturbations is obtained for varying initial buoyancy forcings.

As described in Part I, in contrast to a single-basin model (or the global-average circulation), the NADW cell in the Atlantic basin and the PDW cell in the Pacific basin of a multi-basin model can flow into the global-average lower and upper cells of the channel respectively at the channel-basin boundary (i.e. the upper and lower cells intersect).

The control experiments are described in detail with the differences explained in Part I and thus we do not describe these experiments in detail here.

In Part I, NADW flowing into the channel was shown to either upwell in the channel's upper wind-driven cell before returning to the Atlantic (referred to as the 'direct wind-driven pathway') or it can flow into the lower cell and consequently upwell diffusively in the Pacific

basin before returning to the Atlantic basin (referred to as the 'Pacific diffusively-driven pathway'). There is also an upper pathway of NADW flowing zonally into the Pacific basin via the channel in some cases. The MOC components in each of the experiments performed here can be separated by analysing the meridional overturning streamfunction in each basin and in the channel, using the method described in Part I.

The main difference between the MOC in the control experiments is the depth and strength of the NADW cell (and the AABW cell) in the Atlantic basin. As AABW formation increases with the enhanced sea-ice formation rate between the warm and glacial states, the NADW cell is shoaled. This leads to a significant change in the pathways of NADW, as summarised below.

The present-day like AMOC is driven by both Pacific diffusively-driven (NADW_pac) and Southern Ocean direct wind-driven (NADW_wind) upwelling. There is also a significant contribution by Atlantic upwelling. In the 'warm' state with reduced AABW formation, the NADW cell strengthens and deepens, becoming increasingly driven by diffusive upwelling in the Pacific, with a reduced role played by the direct wind-driven pathway. The increased Atlantic upwelling also strengthens the NADW cell. In contrast, in the cold glacial state with enhanced sea-ice and Antarctic Bottom Water (AABW) formation, the NADW cell shoals and weakens. NADW can no longer flow directly into the lower cell in the channel, isolating it from the Pacific basin. The Pacific diffusively-driven pathway of NADW is diminished, while the direct wind-driven pathway does not change.

The difference in the magnitude of the Pacific diffusively-driven and direct wind-driven pathways of NADW between the control buoyancy states is expected to cause differing MOC responses in each state to perturbations in Pacific vertical diffusivity and Southern Ocean wind stress.

Since the direct wind-driven pathway increases at the expense of the Pacific diffusively-driven pathway as the Southern Ocean buoyancy forcing is varied from a ‘warmer’ to a ‘cooler’ state, it is expected that the NADW cell strength will have a greater sensitivity to changes in wind and a lower sensitivity to changes in Pacific diffusivity as the MOC approaches the ‘cooler’ glacial state.

However, the structure of the MOC may also be effected by the change in forcing which would change the other components of the MOC beyond the direct predictable changes. Additionally changes in sea-ice in response to the change in forcings could lead to further changes in the circulation.

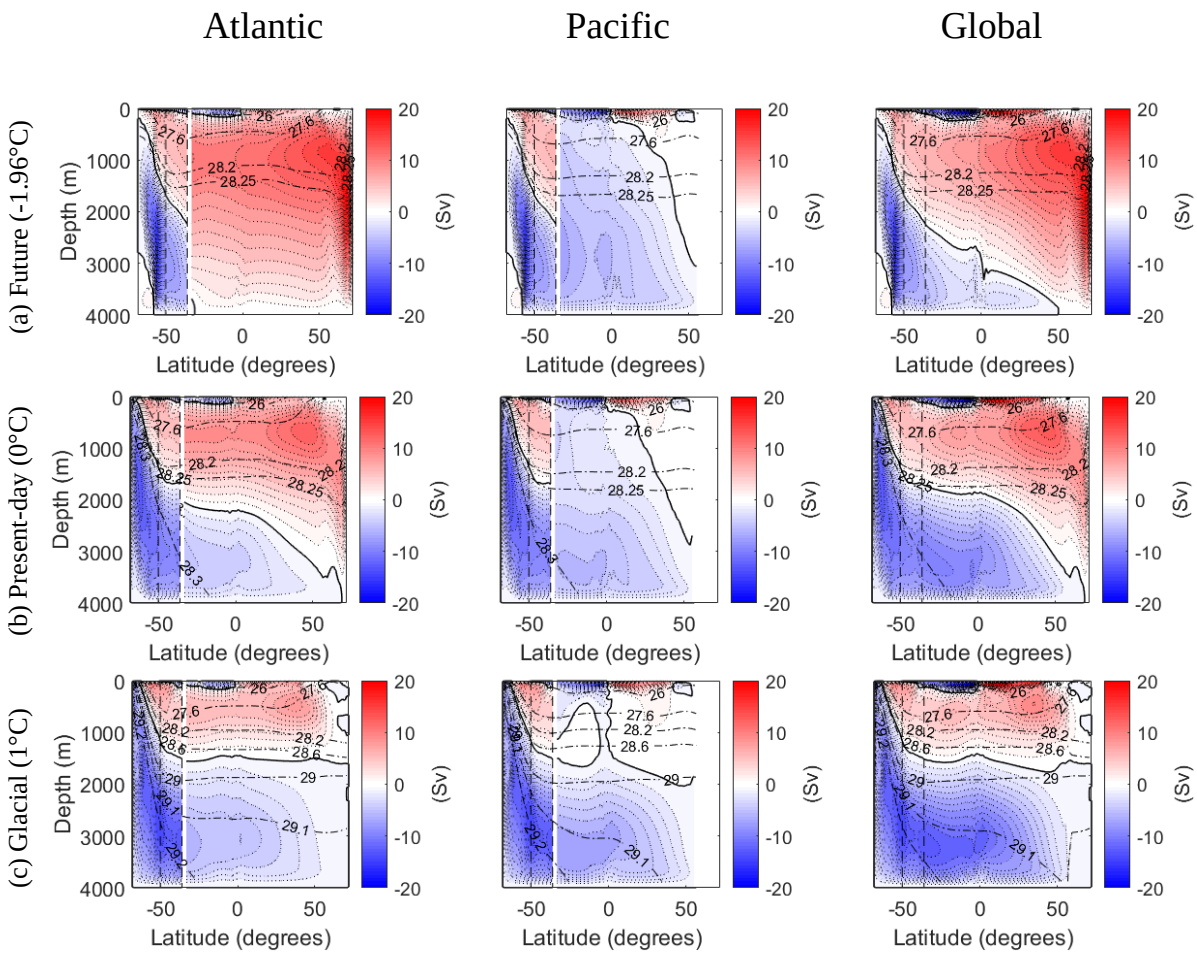

Fig 4.2: Zonal-average residual overturning streamfunction (1 Sv contour intervals) of the control states which have varying sea-ice freezing points (and MOC states) from top to bottom of (a) -1.96°C (future ‘warmer’ state), (b) 0°C (present-day state) and (c) 1°C (glacial state) respectively. Plots from left to right are the Atlantic,

Pacific and global-average circulations respectively. The global-average streamfunction is plotted in the channel in all plots. The red (positive) and blue (negative) streamfunctions are clockwise and anti-clockwise circulations respectively. The thick solid black contour bordering the blue-shaded, anti-clockwise cell is the 0 Sv streamline, separating the clockwise and anti-clockwise cells. Potential density contours are represented by thin dash-dot black lines (note the contour intervals above a potential density of 28.6 Kg m^{-3} are greater in (c) than in (a) and (b)). The vertical dashed lines are from left to right, the southernmost latitudes of the South America and South Africa landstrips respectively.

The model response of the MOC and its pathways to: a) varying Southern Ocean wind stress; b) varying vertical diffusivity in the Pacific basin, shall now be described in Sections 4.4 and 4.5. The experiments are performed using each of the control MOC states to determine how the dependence of the MOC on the wind and diffusivity changes with the initial sea-ice formation rate and thus surface buoyancy forcing. This is followed by a Discussion section on the driving mechanisms of the MOC.

4.4. Wind perturbation experiments

In this section, the Southern Ocean zonal wind speed is perturbed from zero to a four-fold increase relative to the control (Fig 4.1a), in each of the control experiments. However, the buoyancy forcing is not held constant in these experiments but is allowed to respond to changes in the circulation and sea-ice.

An increase in Southern Ocean zonal wind speed increases the northward Ekman transport, increasing the sea-ice export rate. This is expected to increase the Southern Ocean sea-ice formation rate and lead to more negative buoyancy fluxes in this sea-ice formation region. The opposite change is expected to occur when the wind speed is reduced. Thus, the effects of changes in the buoyancy forcing along with the direct effects of the wind itself on the MOC must be considered.

(a) (b)

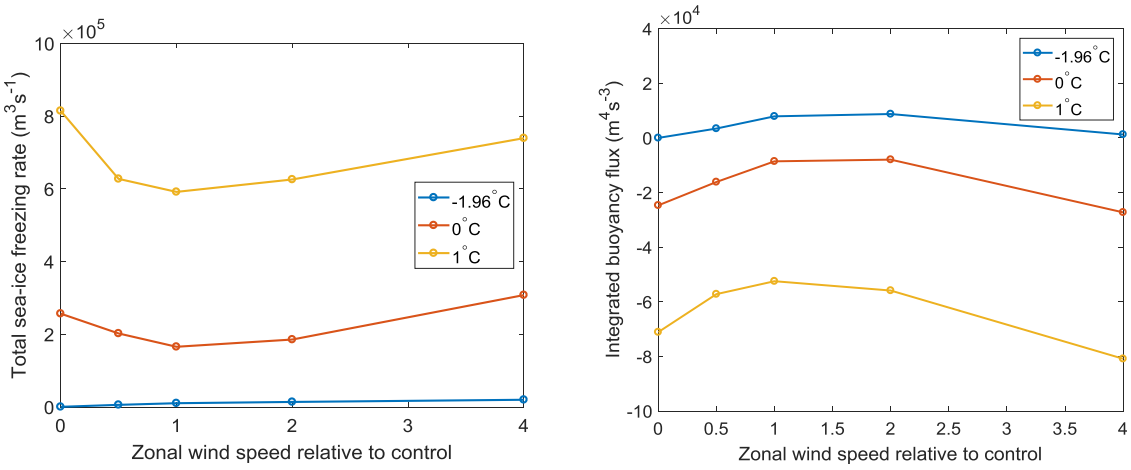

Fig 4.3: Variation of (a) the total sea-ice freezing rate in the Southern Ocean and (b) the area-integrated buoyancy flux in the southernmost latitudes where the zonal-average buoyancy flux becomes negative as the sea-ice formation rate increases, as a function of Southern Ocean zonal wind speed relative to the control. The lines plotted are for varying sea-ice freezing points of -1.96°C (blue), 0°C (red) and 1°C (yellow), corresponding to the 'warm', present-day and glacial states in the control experiments. The dots on each line represent experiments with varying wind speeds relative to the control of zero, half, control, two and four-fold.

The total Southern Ocean sea-ice freezing rate and the area-integrated buoyancy flux in the south of the domain where the zonal-average flux is negative (south of 67°S except in the 'warm' state where it is positive in the far south) is analysed in each of the perturbation experiments (see Fig 4.3). The changes in these variables with wind speed is described for each of the MOC states in the subsections below.

i) Warm state

The 'warm' climate control MOC in which there is almost no Southern Ocean sea-ice (or AABW) formation has a 19.5 Sv NADW cell (see Fig 4.2a), with a large overlap between the NADW cell and the channel's lower cell at the channel-basin boundary. The primary route taken by NADW flowing into the channel is via the Pacific diffusive-driven pathway

('NADW_pac'), with the direct wind-driven pathway ('NADW_wind') playing a smaller role (see Fig 4.5a).

As the Southern Ocean zonal wind speed is varied, both the sea-ice formation rate and the buoyancy flux in the south of the domain remain fairly constant at zero or a small positive value (see Fig 4.3). However, there is a small increase (decrease) in sea-ice formation rate with enhanced (reduced) wind speed due to changes in the northward sea-ice export rate, although it is always an order of magnitude lower than the present-day control. The reduced surface flow reduces the buoyancy flux from a small positive value to zero in the zero wind experiment, while at four-fold wind the small increase in sea-ice formation also reduces the buoyancy flux to zero due to enhanced brine rejection.

The area-integrated buoyancy flux is always positive or zero and thus the buoyancy regime is approximately the same in all cases with the direct effect of changes in wind on the circulation (rather than sea-ice (or buoyancy) changes) dominating the MOC changes.

The overturning streamfunction for the zero and two-fold wind experiments are shown in Fig 4.4 while Fig 4.5a shows the variation in the MOC components with Southern Ocean wind speed (which also includes the half and four-fold wind speed experiments).

The NADW cell in the Atlantic basin dominates the basins circulation in all experiments, flowing into the channel almost all the way to the ocean floor due to there being almost no AABW formation. The main change in the MOC is in the channel as described below.

At zero wind speed, the channel's wind-driven upper cell is no longer present and thus 'NADW_wind' is zero. The anti-clockwise eddy-induced lower cell is replaced by a clockwise eddy-induced cell due to the isopycnals becoming slightly positively tilted without the wind-induced negative tilting of the isopycnals. The pathways of the MOC therefore change significantly as the wind speed is reduced towards zero, with the NADW flowing into

the Pacific directly via zonal flows (which are no longer wind-induced but driven by density differences between the basins (e.g. Thompson et al. [2016]; Ferrari et al. [2017])) rather than upwelling in the channel's lower cell and sinking further south as in the control. These zonal flows maintain the Pacific diffusive pathway of NADW ('NADW_pac'), enabling a strong ~16 Sv NADW cell at zero wind speed (see Fig 4.4a and Fig 4.5a), decreasing by only ~3.5 Sv relative to the control. Thus, the NADW cell is fairly insensitive to reduced wind speed under the 'warm' climate buoyancy forcings as predicted.

The return pathway of PDW to the Atlantic basin is only possible via zonal flows around South Africa and South America, since it can no longer be upwelled further by the channel's wind-driven upper cell. The PDW therefore only flows into the channel at shallow depths and NADW now flows north into the Pacific basin over a greater depth range.

Halving the wind leads to an approximate halving (~1.8 Sv decrease) of the 'NADW_wind' component in the control to ~2.3 Sv, weakening the NADW cell to ~17.5 Sv. The NADW flows into the Pacific via the lower cell in the channel and also via zonal flows since the lower cell is now too weak to transport all of the NADW into the Pacific basin.

A two and four-fold increase in Southern Ocean wind speed leads to an increase of ~4.3 Sv and ~13.7 Sv in 'NADW_wind' respectively, slightly greater than a two and four-fold increase, while the 'NADW_pac' component decreases only slightly (~1 Sv). The Atlantic upwelling also increases slightly. Thus, the NADW cell strengthens by ~4.7 Sv and ~14.4 Sv in the two and four-fold wind experiments respectively to ~24 Sv and ~33.9 Sv (see Fig 4.4b). The direct wind-driven pathway of NADW becomes slightly greater than the Pacific diffusive-driven pathway in the two-fold wind case (see Fig 4.5a). The MOC in the channel is therefore not eddy compensated in this model as expected since the GM parametrisation employed uses a time and spatially constant GM eddy coefficient (Gent [2016]). The MOC

structure remains similar to the control in these enhanced wind cases, except the upper wind-driven cell in the channel expands, deepening the 'z_interface' (the depth of the interface between the global-average upper and lower cells at the channel-basin boundary) from ~2230 m in the control to ~2660 m and ~3220 m in the two and four-fold experiments respectively. As in the control, about 2-3 Sv of PDW is upwelled further by the wind-driven cell in the channel before flowing north into the Atlantic basin.

The model used here is clearly only partially eddy compensated with significant increases in NADW cell strength, and the strength and depth of the channel's upper wind-driven cell with enhanced wind speed. This is not unexpected since the model is not eddy resolving, instead using the GM eddy parameterisation (Gent and McWilliams [1990]; Gent et al. [1995]) to simulate the effects of mesoscale eddies. The increased slope of the Southern Ocean isopycnals as the wind speed is enhanced leads to a partial eddy compensation as the eddy-induced circulation strengthens although the enhancement is smaller near the surface. However, our use of a constant eddy thickness diffusivity likely leads to reduced eddy compensation compared with a time and spatially varying eddy diffusivity (Danabasoglu and Marshall [2007]; Farneti et al. [2015]). The model significantly underestimates the degree of eddy compensation relative to higher resolution eddy-permitting models (Gent [2016]) which tend to lead to a far weaker NADW cell sensitivity to enhanced wind speeds. However, the degree to which eddies compensate the enhanced Eulerian-mean wind-induced circulation remains uncertain with some eddy-resolving models showing complete compensation (Henning and Vallis [2005]; Abernathey et al. [2011]), while others are only partially compensated (Hallberg and Gnanadesikan [2006]; Wolfe and Cessi [2010]; Dufour et al. [2012]; Munday et al. [2013]), although they all show considerably greater eddy compensation with enhanced wind speeds than in the non eddy-resolving model used here.

The almost linear increase in ‘NADW_wind’ with zonal wind speed is clear in Fig 4.5a. The ‘NADW_pac’ component is approximately constant and is equal to ‘NADW_pac_lower’ (i.e. only the lower pathway of NADW into the Pacific is present with no separate upper maxima in the Pacific streamfunction (and thus no upper pathway into the Pacific)). However, ‘NADW_pac’ decreases slightly (~1.6 Sv) between a two- and a four-fold wind speed as the ‘z_interface’ deepens due to an enhanced upper wind-driven cell in the channel. This reduces the depth over which NADW can flow into the channel’s lower cell and Pacific basin. The ‘PDW_sep’ component (i.e. the PDW flowing into the channel’s lower cell, isolated from the Atlantic basin) remains approximately zero as expected under these ‘warm’ climate buoyancy forcings since the ‘NADW_pac’ component must be balanced by the PDW returning to the Atlantic, and the PDW cell strength and ‘NADW_pac’ are approximately equal for all wind speeds. The ‘NADW_channel’ component also has an approximately linear dependence on the wind speed due to the linear change in ‘NADW_wind’. However, it remains constant when the wind speed relative to the control is reduced from half to zero. This higher than expected value at zero wind speed despite a reduction in ‘NADW_wind’ is due to the generation of a clockwise eddy-induced cell in the channel which upwells ~2 Sv of NADW, reducing the weakening of the NADW cell at zero wind speed. There is only a relatively small increase (~3.3 Sv) in Atlantic upwelling between zero and four-fold wind due to the depth of the NADW cell being fairly constant with changes in wind speed. The NADW cell strength varies approximately linearly with wind speed, although the rate of change does increase slightly with wind speed.

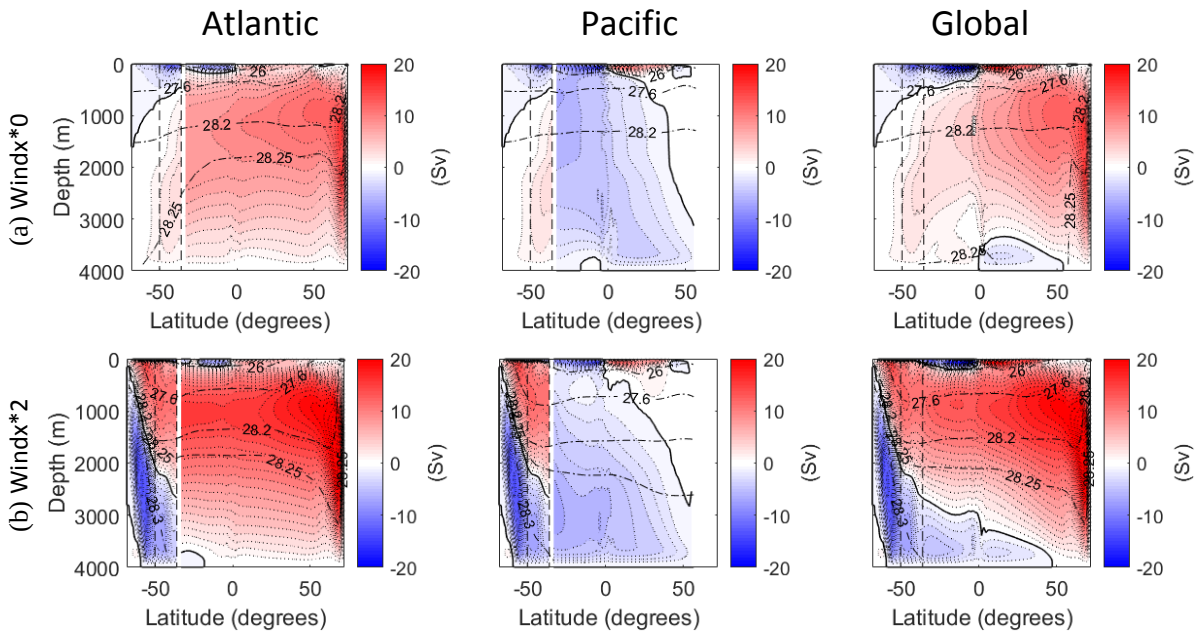

Fig 4.4: Zonal-average residual overturning streamfunction (1 Sv contour intervals), for the future 'warm' state control experiment (-1.96°C freezing point) with a Southern Ocean zonal wind speed of (a) zero and (b) a two-fold increase relative to the control. Plots from left to right are the Atlantic, Pacific and global-average circulations respectively. The global-average streamfunction is plotted in the channel in all plots. Colours and contours are as in Fig 4.2.

(a)

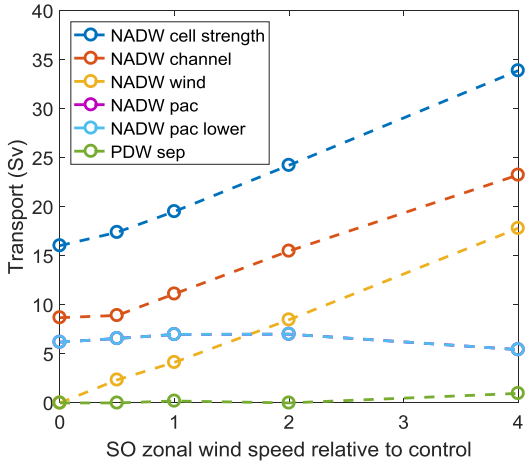

(b)

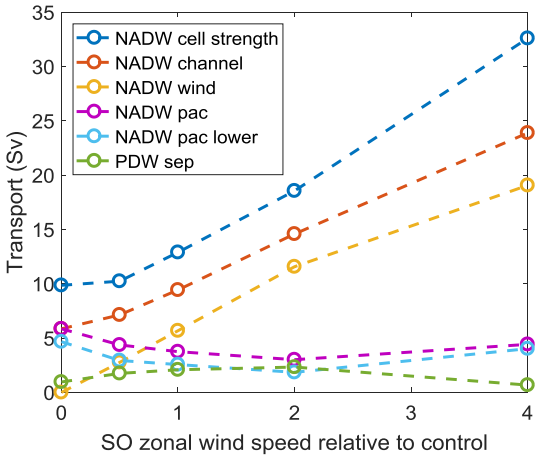

(c)

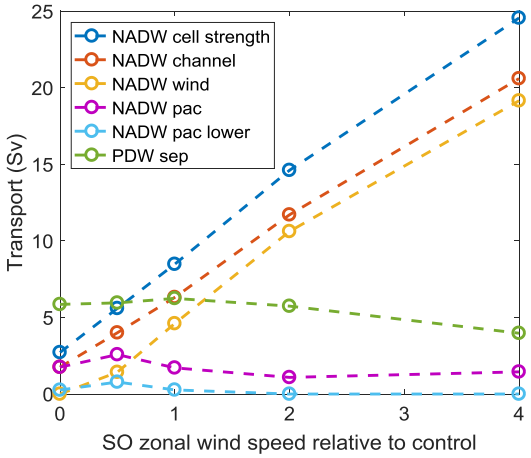

Fig 4.5: Zonal-average residual MOC overturning transport components as a function of Southern Ocean zonal wind speed relative to the control, in experiments with a sea-ice freezing point of (a) -1.96°C, (b) 0°C and (c) 1°C, representative of the 'warm', present-day and glacial states respectively under the control forcings. The dots on each component represent experiments with zonal wind speeds varying from zero to four-fold relative to the control wind speed. The components plotted are as follows: (i) NADW cell strength (dark blue), (ii) NADW flow into the channel from the Atlantic basin (red), (iii) NADW directly upwelled by the Southern Ocean winds (yellow), (iv) NADW upwelled diffusively in the Pacific basin (purple), (v) the proportion of 'NADW_pac' flowing into the channel's lower cell which subsequently upwells diffusively in the Pacific basin (light blue) and vi) the PDW flowing out of the Pacific basin which is isolated from the upper NADW cell and thus returns to the Pacific basin after densification in the Southern Ocean (green). The difference between the NADW cell strength (dark blue) and NADW_channel (red) is the volume of NADW upwelling in the Atlantic basin and flowing back to the north before reaching the channel, 'NADW_at'. The difference between 'NADW_pac'

(purple) and 'NADW_pac_lower' (light blue) is equal to 'NADW_pac_upper', the proportion of 'NADW_pac' which is due to zonal flows into the Pacific basin above the 'z_interface' (and below it if a proportion of the flow into the Pacific basin below the 'z_interface' is a consequence of the Pacific's upper streamfunction maxima). 'NADW_pac_upper' is zero in the 'warm' state, (a), and thus 'NADW_pac' and 'NADW_pac_lower' overlap.

ii) Present-day state

The Southern Ocean sea-ice formation rate increases in the present-day control (using a freezing point of 0°C), shoaling the NADW cell and expanding the AABW cell relative to the 'warm' climate control (as described in Part I (Chapter 3)) (see Fig 4.2b). The NADW flowing into the channel is primarily wind-driven under this buoyancy forcing, although Pacific diffusively-driven upwelling remains important (see Fig 4.5b).

The sea-ice formation rate increases with wind speed, although the increase relative to the control is only large at four-fold wind speed, which results in an approximately three-fold increase in the magnitude of the negative buoyancy flux (see Fig 4.3), a consequence of the enhanced northward wind-driven export of sea-ice. The buoyancy forcing therefore changes by about 43% of that needed to reach the glacial state control forcing. While these buoyancy flux changes are significant and likely play a small role in the change in MOC components, the direct effect of the wind at these high wind speeds dominate the MOC changes. These changes in sea-ice formation are expected and a comparison with the glacial state enhanced wind experiments can still be made since the buoyancy forcing remains significantly different from the enhanced wind glacial state experiments.

In contrast to the 'warm' state, as the wind speed is reduced relative to the control the sea-ice formation rate increases, by about 50% at zero wind speed with a consequent increase in the magnitude of the negative buoyancy forcing of just under three-fold, smaller than the four-fold wind experiment and only about 36% of the increase needed to reach the glacial control

buoyancy forcing. The increase is due to sea-ice becoming unrealistically thick (5 m at half the control wind speed and ~400 m at zero wind speed) enabling a significant sea-ice export despite a very small sea-ice velocity. However, since there is only a small buoyancy forcing change, it allows the effect of reduced wind speed on the MOC with a present-day buoyancy state to be investigated since the direct effect of the wind on the MOC components will dominate with the sea-ice induced buoyancy forcing changes playing only a minor role. The changes we expect to occur with a realistic change in the buoyancy forcing in response to reduced wind speed are discussed later.

The NADW cell is expected to be more sensitive to changes in the Southern Ocean wind speed in this case, since the control has a greater direct wind-driven component of ~5.5 Sv (~1.5 Sv greater than the 'warm' state control).

Fig 4.6 shows the MOC streamfunction for the zero and two-fold wind experiments and Fig 4.5b shows the MOC components for varying wind speed from zero to four-fold relative to the control.

The depth of the NADW cell at the channel-basin boundary is similar with wind perturbations except at four-fold wind where it deepens significantly despite the enhanced Southern Ocean buoyancy flux. This appears to be due to the steepening of the Southern Ocean isopycnals by the enhanced wind speed, deepening the isopycnals in the Atlantic basin. At zero wind speed, the channel's upper wind-driven cell is no longer generated but in contrast to the 'warm' state, the channel is dominated by an anti-clockwise eddy-induced cell, despite there no longer being wind-induced tilting of the channel isopycnals. Instead, the enhanced sea-ice formation leads to enhanced brine rejection in the south of the domain and freshwater fluxes from sea-ice melt further north leading to a buoyancy forcing induced tilting of the isopycnals.

A reduction in the Southern Ocean wind speed to zero only weakens the ~12.9 Sv control NADW cell by ~3 Sv, which is 0.5 Sv lower than in the 'warm' state despite the wind-driven component being greater in the present-day control (see Fig 4.6a). Indeed, 'NADW_wind' is more sensitive to a reduced wind speed (~1.5 Sv greater decrease relative to the control) in the present-day state than in the 'warm' state. The decrease in the direct wind-driven upwelling of NADW is partially compensated by an increase in the volume of NADW flowing via the Pacific diffusive pathway from ~4 Sv to ~6 Sv (see Fig 4.5b). This is due to NADW flowing into the channel being able to flow into the channel's anti-clockwise cell at all depths, and subsequently into the Pacific basin at depth. There is also a direct zonal flow of NADW into the Pacific basin of ~0.5 Sv at ~1500 m depth. However, 'NADW_channel' decreases by ~3.5 Sv compared to ~2.5 Sv in the 'warm' state. The smaller weakening of the NADW cell in the 'warm' state is explained by a ~0.5 Sv increase in Atlantic upwelling due to a slight deepening of the NADW cell (and perhaps changes in stratification) increasing diffusive upwelling, whereas it decreases by ~1 Sv in the 'warm' state.

The weakening of the NADW cell suggests the reduced wind speed could be a mechanism to obtain a glacial state MOC. However, in this case there is still a significant connection between the upper and lower cells, and the NADW cell is not shoaled in contrast to the glacial shoaling of the MOC. Thus, this mechanism cannot instigate a transition to a glacial MOC in these simulations. A more realistic wind-induced change in sea-ice at low wind speeds is discussed later, which also cannot produce a glacial MOC.

When the wind is increased two and four-fold relative to the control, the NADW cell strengthens by ~5.7 Sv and ~19.7 Sv respectively, with a corresponding increase in the wind-driven component of NADW of ~5.9 Sv and ~13.4 Sv respectively (see Fig 4.5b and Fig 4.6b). The 'NADW_pac' variations are small, with the other major change in the four-fold

wind experiment being an increase of ~5 Sv in Atlantic upwelling due to the deepening of the NADW cell.

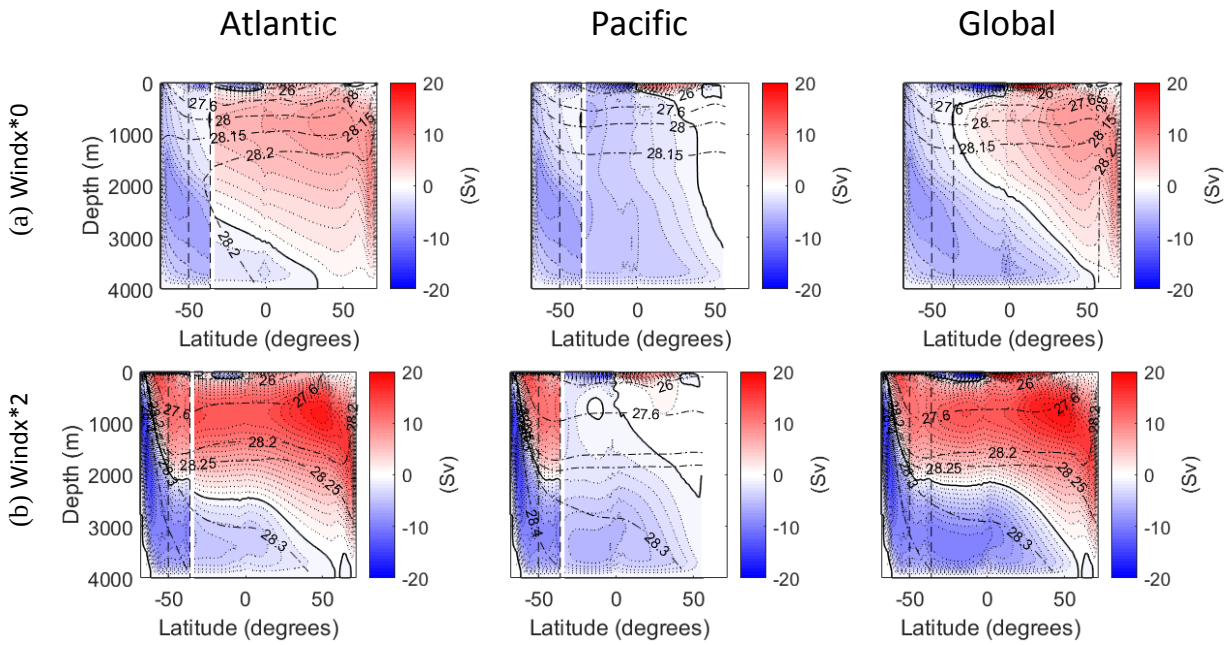

Fig 4.6: Zonal-average residual overturning streamfunction (1 Sv contour intervals), for the present-day state control experiment (0°C freezing point) with a Southern Ocean zonal wind speed of (a) zero and (b) a two-fold increase relative to the control. Colours and contours are as in Fig 4.2.

iii) Glacial State

The glacial state control (using a sea-ice freezing point of 1°C) has a Southern Ocean sea-ice formation rate and a negative area-integrated buoyancy flux enhanced by factors of 3.6 and 6.5 respectively relative to the present-day control. This leads to an expanded AABW cell in the Atlantic basin and a weaker, shoaled NADW cell of ~8.5 Sv. The upper and lower cells of the MOC are now more or less separated at the channel-basin boundary, with almost no NADW flowing into the channel's lower cell and Pacific basin via the lower pathway, and thus 'NADW_pac_lower' has reduced to ~0.3 Sv (see Fig 4.5c). The NADW cell is primarily wind-driven and thus expected to be highly sensitive to the Southern Ocean wind speed, although the absolute value of the direct wind-driven pathway is ~1 Sv smaller than the

present-day control. The change in the sea-ice formation rate and buoyancy flux in response to wind perturbations is similar to that of the present-day state, except the magnitude of the changes are slightly greater (see Fig 4.3).

Reducing the wind to zero leads to a ~5.8 Sv weakening of the NADW cell from ~8.5 Sv to ~2.7 Sv, a larger decrease than in the 'warm' and present-day state experiments, despite the control NADW cell strength being far weaker (see Fig 4.5c and Fig 4.7a). This is due to the wind-driven pathway (~4.6 Sv) decreasing to zero as in the previous experiments but the Pacific diffusively-driven pathway remaining constant at ~1.7 Sv (see Fig 4.5c) rather than increasing as in the present-day state. The lack of compensation by Pacific upwelling is likely due to the NADW cell being shoaled and confined to near the surface such that only a very small volume of NADW can flow into the channel's anti-clockwise cell (which dominates the channel circulation as in the present-day zero wind case). The Atlantic upwelling also decreases from ~2.2 Sv to ~1 Sv due to the shoaling of the NADW cell.

A two and four-fold increase in wind speed increases 'NADW_wind' approximately two and four-fold respectively from ~4.6 Sv to ~10.6 Sv and ~19.2 Sv respectively (see Fig 4.7b). The Atlantic upwelling also increases from ~2.2 Sv to ~2.9 Sv and ~4 Sv in the two and four-fold experiments respectively due to the deepening of the NADW cell. These changes result in a ~14.6 Sv and ~24.6 Sv NADW cell despite there being almost no connection of this cell to the Pacific basin ('NADW_pac' is small and does not change significantly). The NADW cell is therefore highly sensitive to the Southern Ocean wind speed under these buoyancy forcings as predicted, with no major changes in the pathways of NADW.

The deepening and shoaling of the NADW and AABW cells respectively as the wind increases is a response to the deepening of the 'z_interface' as the channels upper wind-driven cell deepens. We suggest this deepening of the NADW cell is a result of continuity

since without the expansion of the NADW cell, the Atlantic AABW cell would flow into and upwell in the channel's upper cell and thus connect to the NADW cell, but the NADW would have no pathway to return to the lower cell. Thus, the NADW cell deepens despite the increase in Southern Ocean sea-ice formation.

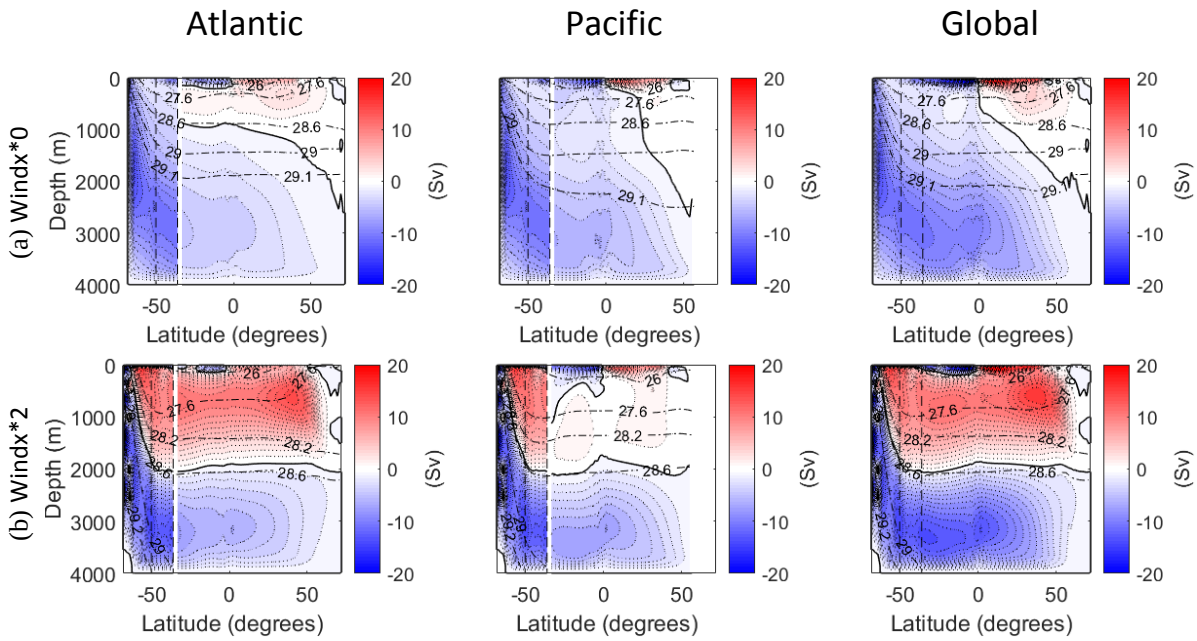

Fig 4.7: Zonal-average residual overturning streamfunction (1 Sv contour intervals), for the glacial state control experiment (1°C freezing point) with a Southern Ocean zonal wind speed of (a) zero and (b) a two-fold increase relative to the control. Colours and contours are as in Fig 4.2.

iv) Summary and Comparisons

A comparison between the MOC components for the wind (and diffusivity) experiments for each buoyancy state are shown in Fig 4.8. The changes in wind speed significantly alter the strength of the NADW cell under all buoyancy forcings, primarily due to the change in the wind-driven component. The increase in this component of the MOC from zero at zero wind speed to a four-fold wind speed is similar in each experiment, although it is greatest in the present-day and glacial states. While the present-day state has the greatest wind-driven component in the control, this component has a greater magnitude at four-fold wind in the

glacial state. The present-day and ‘warm’ state MOC’s are similar at four-fold wind speed. This is a consequence of a structural change in the ‘warm’ state MOC, since the increased wind speed also deepens the ‘z_interface’ which increases ‘NADW_wind’ at the expense of ‘NADW_pac’. The deepening of the NADW cell in the present-day state despite an enhanced negative buoyancy flux also causes the pathway ratios to converge, increasing ‘NADW_at’ significantly, although they still differ somewhat. The similarity of the MOC in these experiments despite the difference in buoyancy forcing is interesting. It suggests the wind at these high magnitudes can in some cases dominate over the buoyancy forcing differences, with the Atlantic AABW cell being shoaled in the present-day case. The deepening of the NADW cell in the present-day case could be due to the increase in the depth of the ‘z_interface’.

The change in the relative contribution of the various components to the NADW cell strength highlight these structural changes to the MOC and the consequent change in NADW pathways (see Fig 4.8). This highlights the importance of wind speed changes in determining the structure of the MOC, in addition to the buoyancy forcing.

(a)

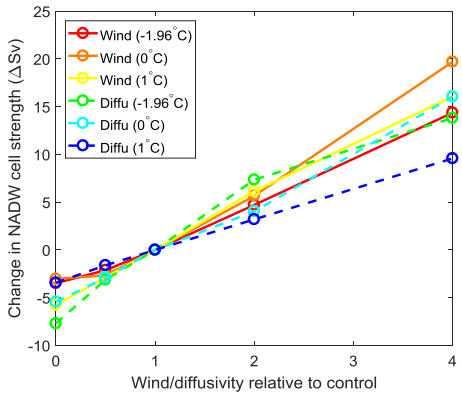
Change in NADW cell strength (ΔSv)
Wind/diffusivity relative to control
Wind (-1.96°C)
Wind (0°C)
Wind (1°C)
Diffu (-1.96°C)
Diffu (0°C)
Diffu (1°C)

(b)

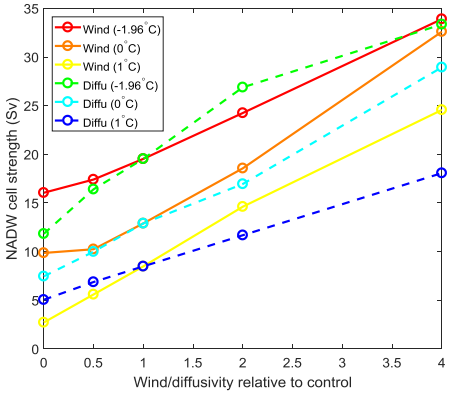
NADW cell strength (Sv)
Wind/diffusivity relative to control
Wind (-1.96°C)
Wind (0°C)
Wind (1°C)
Diffu (-1.96°C)
Diffu (0°C)
Diffu (1°C)

(c)

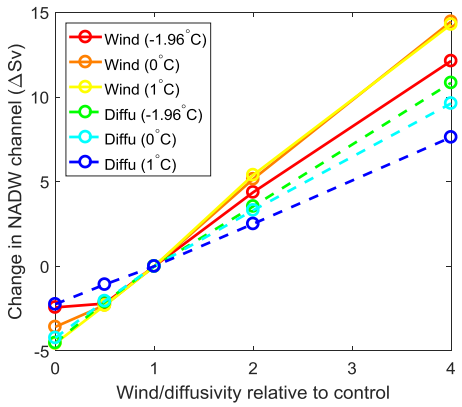
Change in NADW channel (ΔSv)
Wind/diffusivity relative to control
Wind (-1.96°C)
Wind (0°C)
Wind (1°C)
Diffu (-1.96°C)
Diffu (0°C)
Diffu (1°C)

(d)

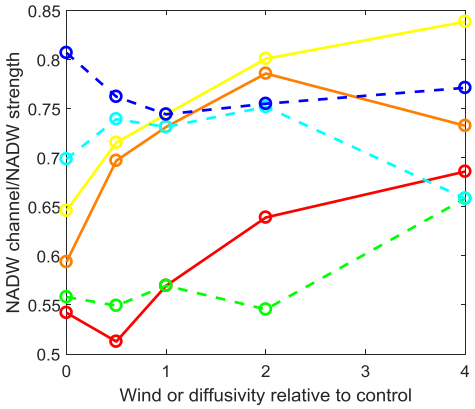
NADW channel/NADW strength
Wind or diffusivity relative to control

(e)

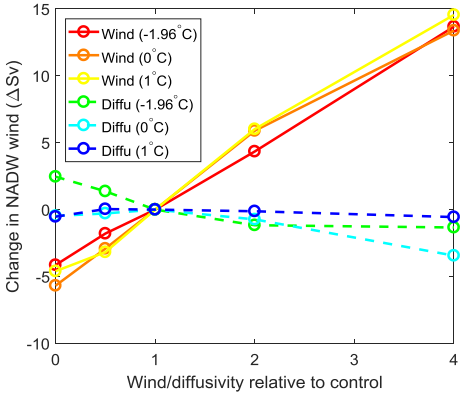
Change in NADW wind (ΔSv)
Wind/diffusivity relative to control
Wind (-1.96°C)
Wind (0°C)
Wind (1°C)
Diffu (-1.96°C)
Diffu (0°C)
Diffu (1°C)

(f)

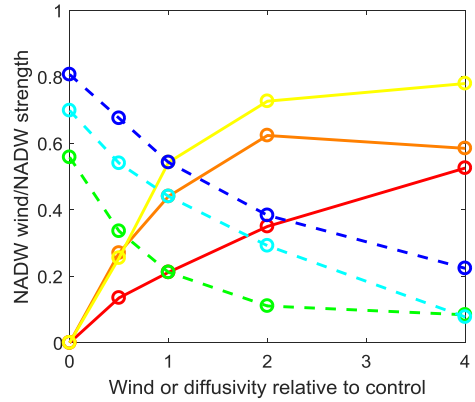
NADW wind/NADW strength
Wind or diffusivity relative to control

(g) (h)

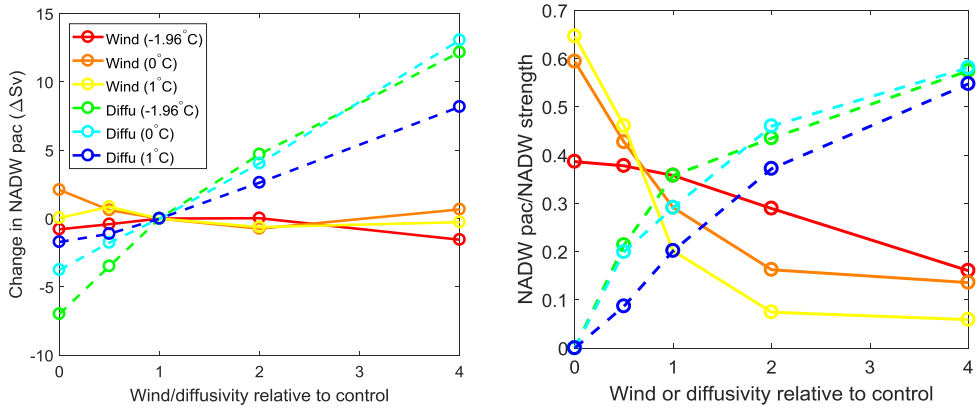

(i) (j)

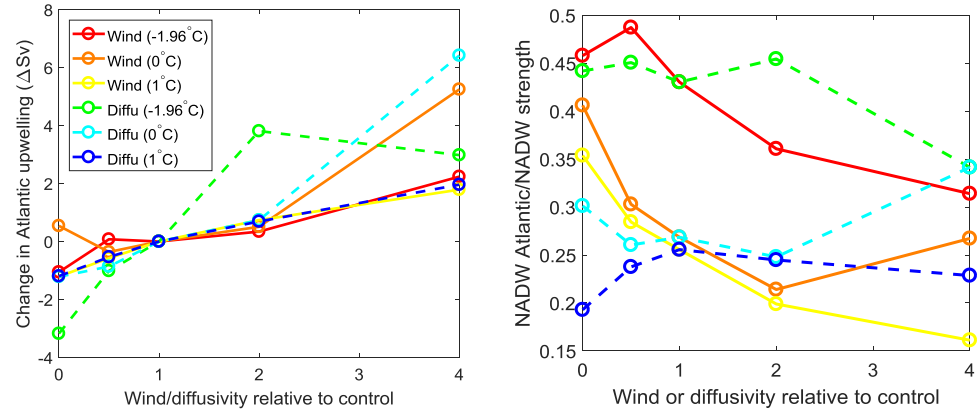

Fig 4.8: (a) Change in NADW cell strength relative to the control, (b) NADW cell strength, (c),(e),(g),(i) change in NADW_channel, NADW_wind, NADW_pac, NADW_at respectively relative to the control, (d),(f),(h),(j) the ratio (or relative contribution) of NADW_channel, NADW_wind, NADW_pac, NADW_at respectively to the NADW cell strength, against Southern Ocean wind speed (solid lines) or Pacific vertical diffusivity (dashed lines) relative to the control. The varying wind and diffusivity experiments, labelled 'Wind' and 'Diffu' are plotted for each of the three control buoyancy forcings (i.e. for the 'warm', present-day and glacial states labelled as '-1.96°C', '0°C' and '1°C' respectively, the freezing points corresponding to each of these states).

v) Zero wind experiments: A more realistic change in sea-ice

The present-day and glacial state zero wind experiments both have an anti-clockwise eddy-induced cell dominating the channel since there is no longer an upper clockwise wind-driven cell but the isopycnals remain negatively tilted due to the sea-ice formation rate and negative

buoyancy fluxes in the south of the domain remaining significant (and actually increasing). However, the sea-ice becomes unrealistically thick in the south of the domain in these experiments enabling the northward advective volume transport of sea-ice to be maintained despite only a very small advective velocity. In reality, the sea-ice would be significantly thinner and thus the buoyancy flux would be far smaller (perhaps even zero) due to virtually no sea-ice export. Thus, there would likely be negligible AABW formation and thus the channel isopycnals would no longer be negatively tilted. The channel circulation would then be zero or a clockwise eddy-induced cell could form as in the 'warm' state. The tendency of the Southern Ocean buoyancy flux towards zero (and thus towards the 'warm' state) with almost no AABW formation would lead to an expansion of the NADW cell as in the 'warm' state, with direct zonal flows into the Pacific basin maintaining 'NADW_pac'. The MOC would therefore transition to that of the 'warm' state at zero wind, deepening and potentially strengthening the NADW cell. Thus, a reduced wind speed would still be unable to transition the MOC to a glacial state, as in the experiments which have buoyancy forcings relatively similar to the controls.

4.5. Pacific vertical diffusivity perturbation experiments

In this section experiments are performed with a vertical diffusivity profile perturbed by a factor from zero to four-fold relative to the control in the Pacific basin (i.e. latitudes north of the South Africa landstrip in the Pacific sector), while it is held at the control diffusivity elsewhere (see Fig 4.1b). The profiles have a bottom enhancement in diffusivity with a large increase at a depth of ~2000 m, except in the zero diffusivity case.

As in the wind experiments, each of these experiments are performed using varying sea-ice freezing points representative of varying Southern Ocean sea-ice formation rates and thus buoyancy fluxes as described in Section 4.2.

(a) (b)

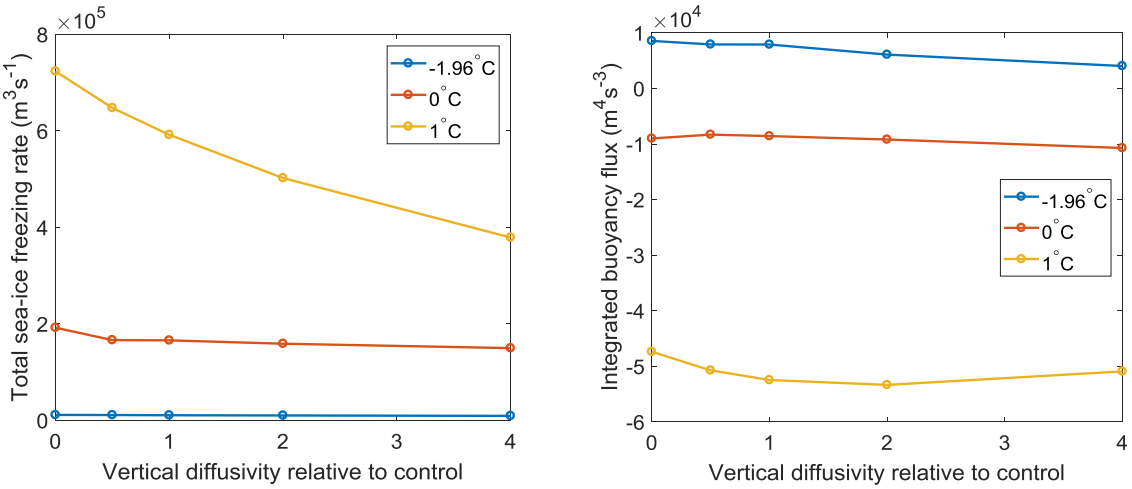

Fig 4.9: Variation of (a) the total sea-ice freezing rate in the Southern Ocean and (b) the area integrated buoyancy flux in the southernmost latitudes where the zonal-average buoyancy flux becomes negative as the sea-ice formation rate increases, as a function of Pacific vertical diffusivity relative to the control. The lines plotted are for varying sea-ice freezing points of -1.96°C (blue), 0°C (red) and 1°C (yellow), corresponding to the 'warm', present-day and glacial states in the control experiments. The dots on each line represent experiments with varying Pacific vertical diffusivity profiles relative to the control of zero, half, control, two and four-fold.

The variation of the Southern Ocean sea-ice freezing rate and area-integrated buoyancy flux is approximately constant for varying vertical diffusivity **(**see Fig 4.9), except for a large decrease (increase) in the sea-ice freezing rate with enhanced (reduced) diffusivity relative to the control in the glacial state. However, as the diffusivity is reduced in the glacial state, there is a corresponding decrease in the magnitude of the negative area-integrated buoyancy flux, the opposite direction to the change expected from an increase in the sea-ice freezing rate. We suggest the cause of this change is due to the stratification being greatest in the glacial control state, which causes the diffusivity perturbations to cause far larger changes in stratification than in the other buoyancy states, with the Atlantic density profile also changed. The channel becomes less dense with the surface cooler and saltier. This changes the

relaxation fluxes, maintaining or slightly decreasing the buoyancy flux despite the enhanced sea-ice formation rate.

The Southern Ocean buoyancy forcing thus remains fairly constant in each buoyancy state, as the diffusivity is perturbed. Our main assumption from this is that changes in Pacific diffusivity (and the consequent effects it has on the stratification) rather than perturbations in the buoyancy flux are primarily responsible for the changes in the MOC. Changes in the diffusivity alter the buoyancy contrast between the north Atlantic and Southern Ocean which has significant effects on the NADW cell depth, in addition to the changes in the Pacific basin circulation. However, the changes in the MOC may result in these buoyancy changes.

In contrast to the wind perturbation experiments, the structure of the channel circulation and the depth of the 'z_interface' is fairly insensitive to diffusivity in each buoyancy state, with changes in the Atlantic and Pacific basin circulations causing the changes in the MOC pathways. There is only a small decrease (<1 Sv) in the strength of the channel's upper wind-driven cell at the channel-basin boundary in all experiments for an increase in Pacific diffusivity from zero to four-fold, and thus this is not the primary cause of changes in 'NADW_wind'.

i) 'Warm' state

The control NADW cell is predicted to have the greatest sensitivity to the Pacific basin diffusivity in this 'warm' state, since the NADW flowing into the channel ('NADW_channel') primarily flows along the Pacific diffusively-driven pathway ('NADW_pac').

The meridional streamfunction of the zero and two-fold diffusivity experiments is shown in Fig 4.10, and the magnitude of the MOC components under varying diffusivity is shown in Fig 4.11a.

The depth of the NADW cell at the channel-basin boundary varies significantly with Pacific diffusivity, shoaling (deepening) with reduced (enhanced) diffusivities. We propose this is primarily due to the change in circulation in the Pacific basin, although stratification changes may also play a role.

As the diffusivity is decreased from the control, the NADW cell weakens substantially, decreasing by ~7.7 Sv at zero diffusivity (see Fig 4.10a), the greatest decrease of all perturbation experiments performed in this study (see Fig 4.8a). The Pacific circulation is then negligible with no structure, and thus 'NADW_pac' is zero, a decrease of ~7 Sv. However, this decrease is partially compensated by an increase in 'NADW_wind' of ~2.5 Sv (see Fig 4.11a). This is in response to the wind-driven cell now only upwelling NADW, whereas in the control, PDW flowing into the channel was also upwelled by this upper cell in the channel. The NADW can no longer flow into the channel's lower cell since there is no pathway for it to return to the upper cell or surface of the Atlantic basin without Pacific basin upwelling. The NADW cell therefore shoals at the channel-basin boundary, to the depth of the 'z_interface' to conserve volume. The NADW can thus only upwell in the Atlantic basin or via the upper wind-driven cell in channel in all of the zero diffusivity experiments. The lower cell expands in the Atlantic basin to fill the void (contrasting with the buoyancy forced shoaling of NADW in Part I). The shoaling of the NADW cell also reduces Atlantic upwelling by ~3.2 Sv.

The NADW cell strengthens by ~7.4 Sv and ~13.8 Sv at two and four-fold Pacific diffusivity respectively relative to the control. The change is primarily due to an increase in 'NADW_pac' of ~4.7 Sv and ~12.2 Sv respectively, and also due to an increase in Atlantic upwelling of ~3.8 Sv and ~3 Sv respectively. The large increase at two-fold diffusivity in Atlantic upwelling is due to the NADW cell deepening slightly to the very bottom of the

ocean throughout the Atlantic basin. The wind-driven pathway decreases by ~1 Sv relative to the control in both perturbations.

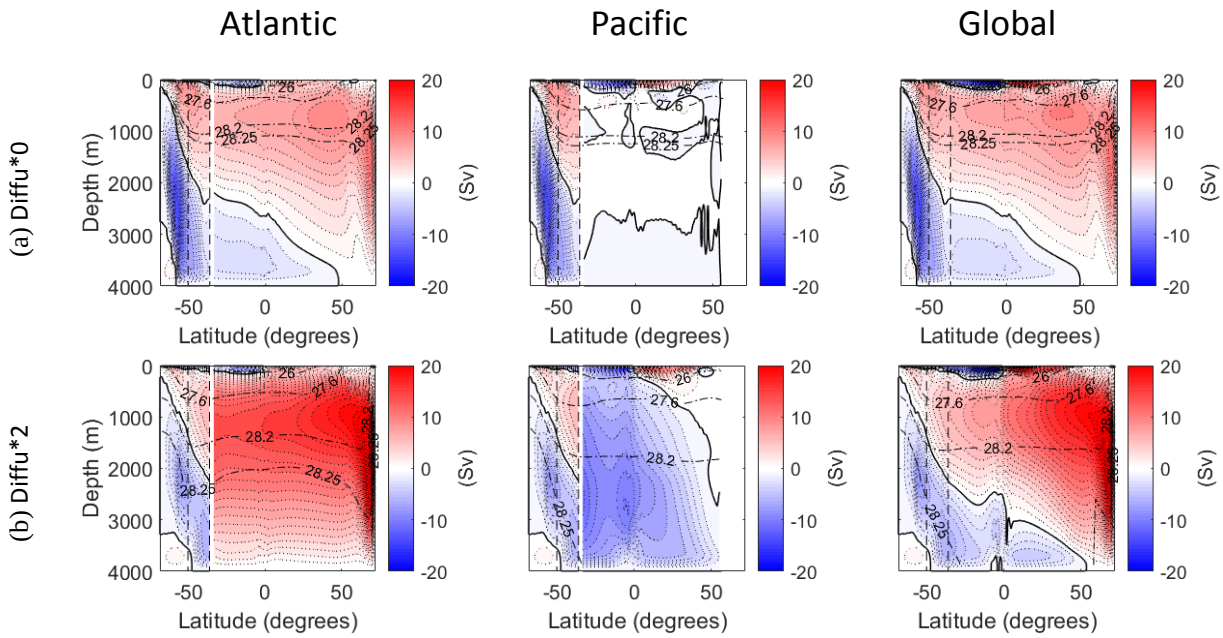

Fig 4.10: Zonal-average residual overturning streamfunction (1 Sv contour intervals), for the future 'warm' state control experiment (-1.96°C freezing point) with a Pacific vertical diffusivity of (a) zero and (b) a two-fold increase relative to the control. Colours and contours are as in Fig 4.2.

(a)

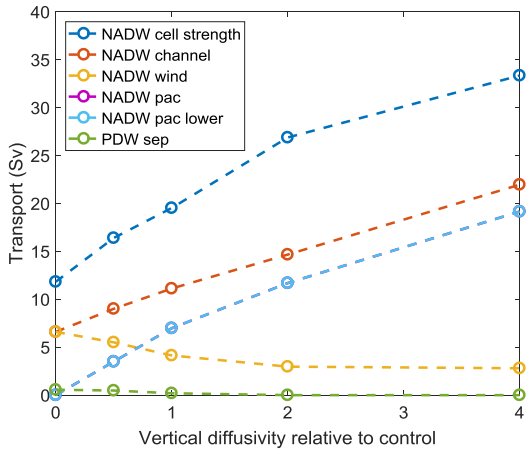

(b)

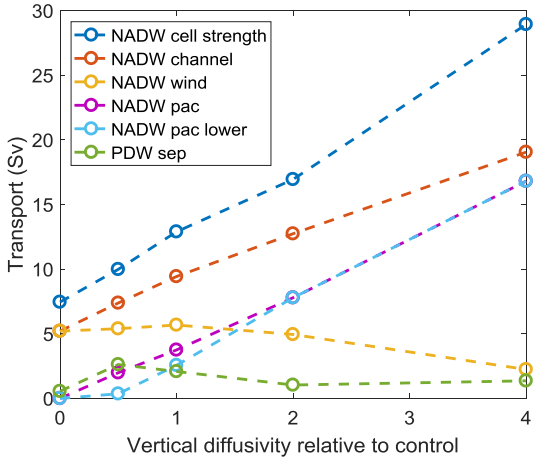

(c)

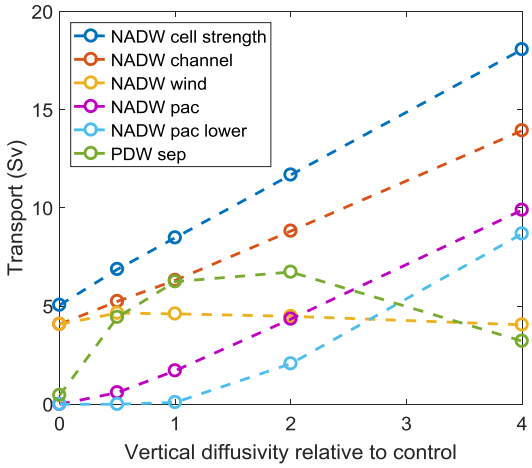

Fig 4.11: Zonal-average residual MOC overturning transport components as a function of Pacific basin vertical diffusivity relative to the control, in experiments with a sea-ice freezing point of (a) 1.96°C, (b) 0°C and (c) 1°C, representative of the 'warm', present-day and glacial states respectively under the control forcings. For further details, see Fig 4.5.

ii) Present-day state

The change in MOC structure with Pacific diffusivity perturbations is similar in the present-day state to the 'warm' state with a shoaling (deepening) of the NADW cell at the channel-basin boundary with reduced (enhanced) Pacific diffusivity. The change in MOC components is therefore similar, although there are some differences in the sensitivity of these components to the diffusivity.

The NADW cell is expected to have a lower sensitivity to changes in Pacific diffusivity since only ~3.8 Sv of NADW flows along the Pacific diffusively-driven pathway in the control (compared to ~7 Sv in the 'warm' state). Reducing the Pacific basin diffusivity to zero decreases the strength of the NADW cell by ~5.4 Sv, ~2.3 Sv less than in the 'warm state as expected (see Fig 4.12a). This smaller change is due to a smaller decrease in 'NADW_pac' (which decreases by ~3.8 Sv to zero) and Atlantic upwelling (which decreases by ~1.2 Sv) (see Fig 4.8 and Fig 4.11b). The NADW cell is less deep in the control state compared to the 'warm' state control, and thus the reduction in Atlantic upwelling is smaller. However, the 'NADW_wind' component does not compensate for the decrease in 'NADW_pac' in contrast to the 'warm' state, instead remaining approximately constant. This is due to 'NADW_wind' being approximately equal to the channel's upper wind-driven cell flow across the channel-basin boundary since only a small volume of PDW is upwelled further by the winds in the channel in this case due to the presence of an upper maxima in the PDW cell.

The zero diffusivity case is similar to the glacial state control, with all the NADW flowing into the channel's upper cell, and only ~1 Sv weaker at ~7.5 Sv. The only difference is in the pathways taken with a small upper Pacific diffusive pathway in the glacial state case of ~1.7 Sv, and 'NADW_wind' in this present-day experiment is ~0.6 Sv greater, with a deeper 'z_interface' in this experiment.

Increasing the diffusivity relative to the control strengthens the NADW cell by ~4.1 Sv and ~16 Sv in the two (see Fig 4.12b) and four-fold experiments respectively, the latter being a ~2 Sv greater increase than in the 'warm' state **(**see Fig 4.8a**).** As in the 'warm' state, the deepening of the NADW cell increases the overlap between the upper and lower cells at the channel-basin boundary (since the 'z_interface' is approximately constant), increasing 'NADW_pac' in the respective experiments by ~4 Sv and ~13.1 Sv, with the Atlantic upwelling increasing by ~0.74 Sv and ~6.4 Sv, the latter a large increase (see Fig 4.11b). In

contrast, ‘NADW_wind’ decreases by ~0.7 Sv and ~3.4 Sv in these experiments, due to an increase in PDW being upwelled by the wind-induced cell in the channel. The ‘PDW_sep’ decreases and ‘NADW_pac_upper’ is zero at high diffusivity. The structure of the MOC in the four-fold case is the same as in the corresponding experiment in the ‘warm’ state. The component composition of these four-fold experiments is more or less identical (see Fig 4.8), despite a smaller magnitude of ‘NADW_pac’, ‘NADW_wind’ and ‘NADW_at’, and thus a ~4.4 Sv weaker NADW cell (see Fig 4.8b). The difference in buoyancy forcing no longer leads to differences in the overturning structure in the Atlantic and Pacific basins. However, the stratification differences lead to a weaker eddy-induced lower cell in the channel and the global-average circulation still has a stronger, more expansive lower AABW cell, leading to differences between experiments.

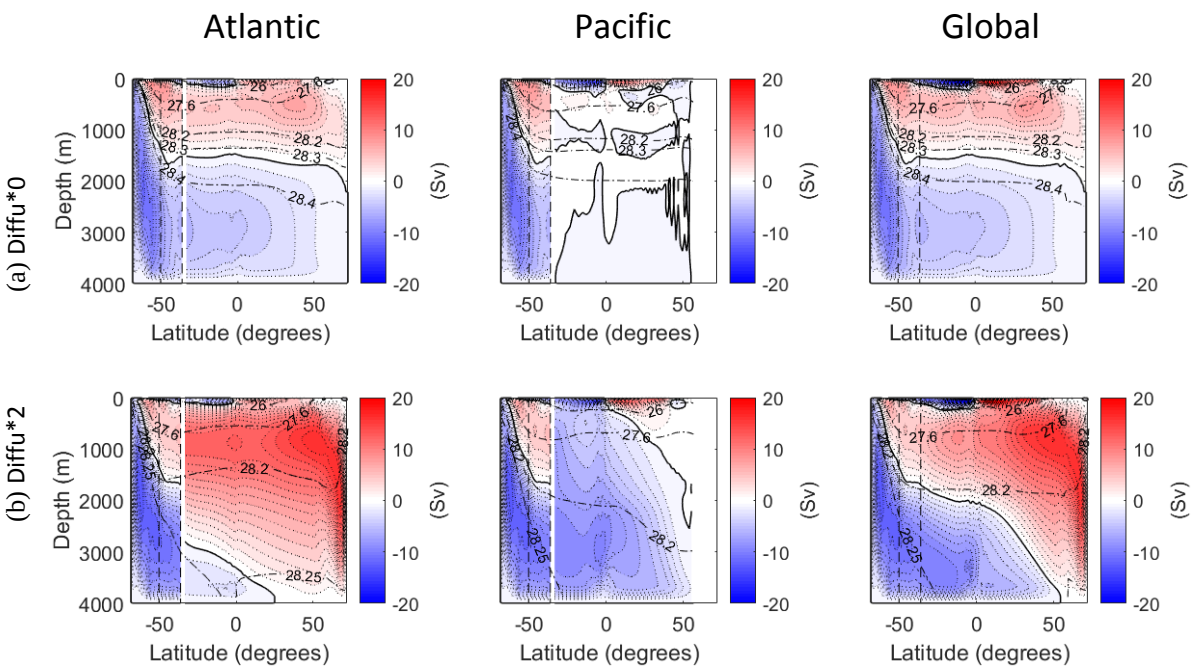

Fig 4.12: Zonal-average residual overturning streamfunction (1 Sv contour intervals), for the present-day state control experiment (0°C freezing point) with a Pacific vertical diffusivity of (a) zero and (b) a two-fold increase relative to the control. Colours and contours are as in Fig 4.2.

iii) Glacial state

Almost all of the NADW flowing into the channel in the glacial state control flows along the wind-driven pathway with only a small 'NADW_pac' component of ~1.7 Sv due to the upper Pacific diffusively-driven pathway in which NADW flows zonally into the upper Pacific basin above the 'z_interface'. Thus, the glacial NADW cell is expected to be the least sensitive to changes in Pacific vertical diffusivity.

The NADW cell deepens (shoals) slightly with enhanced (reduced) Pacific diffusivity, although the change in depth is far smaller than in the previous experiments.

The NADW cell weakens by ~3.4 Sv from ~8.5 Sv to ~5.1 Sv when the diffusivity is reduced to zero (see Fig 4.13a), primarily due to 'NADW_pac' decreasing to zero and the Atlantic upwelling reducing by ~1.2 Sv, as the NADW cell shoals. 'NADW_wind' is ~4.1 Sv

(remaining approximately constant with changes in diffusivity) accounting for almost all of the NADW cell strength (see Fig 4.11c).

As the diffusivity is increased, the NADW cell strengthens by ~3.2 Sv and ~9.6 Sv for a two (see Fig 4.13b) and four-fold increase in diffusivity respectively. The NADW cell at the channel-basin boundary deepens below the 'z_interface', increasing the overlap between the upper and lower cells. This increases 'NADW_pac_lower', and thus 'NADW_pac' increases by ~ 2.6 Sv and ~8.2 Sv in the respective experiments, with a small increase in Atlantic upwelling. Although, the relative contribution of 'NADW_pac' at four-fold diffusivity to the NADW cell strength is similar to the previous experiments (all be it a far smaller magnitude), the relative contribution of Atlantic upwelling is far smaller while that of wind-driven upwelling is greater (see Fig 4.8). The direct wind-driven flow is maintained since the PDW flowing into the channel above the 'z_interface' is confined to near the surface due to the presence of the upper Pacific maxima (even in the four-fold experiment), and is therefore not upwelled further by the upper wind-driven cell.

The 'PDW_sep' component increases from ~0.5 Sv to ~6.2 Sv between zero and the control diffusivity due to the enhanced Pacific upwelling. However, it only increases by a further ~0.5 Sv at two-fold diffusivity before decreasing to ~3.2 Sv at four-fold diffusivity. This change at higher diffusivities is due to the increase in the lower Pacific diffusively-driven pathway of NADW causing the same volume of PDW to return to the Atlantic by continuity.

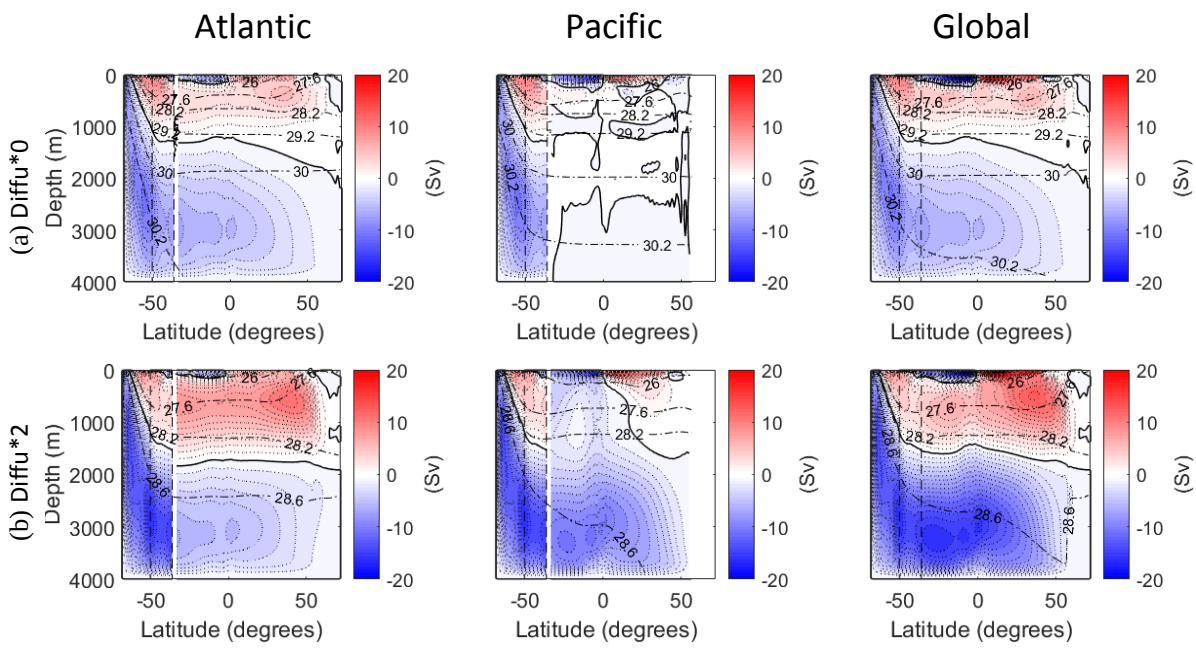

Fig 4.13: Zonal-average residual overturning streamfunction (1 Sv contour intervals), for the glacial state control experiment (1°C freezing point) with a Pacific vertical diffusivity of (a) zero and (b) a two-fold increase relative to the control. Colours and contours are as in Fig 4.2.

iv) Summary and Comparisons

The sensitivity of the NADW cell strength to varying Pacific diffusivity is highly dependent on the initial buoyancy forcing, with a clear increase in sensitivity as the buoyancy forcing is varied from a glacial to a 'warm' state. The exception is at very high diffusivity where the present-day state becomes more sensitive due to a significant deepening of the NADW cell (see Fig 4.8). This contrasts with the wind experiments in which the present-day state is most sensitive to an increase in wind speed, and the glacial state is most sensitive to a reduction in wind speed. The wind changes are more complex since the wind speed also alters the channel circulation and the 'z_interface' significantly. The differences in the size of the wind-driven pathway between the control buoyancy states is also significantly smaller than the differences in the magnitudes of the Pacific diffusively-driven pathway. The greater difference in the response of NADW cell strength between buoyancy states to diffusivity than wind is therefore expected. Indeed, the difference in the sensitivity of 'NADW_wind' to wind

perturbations between buoyancy states is small compared with the difference in the sensitivity of 'NADW_pac' to diffusivity perturbations (see Fig 4.8).

However, the NADW cell strengthens at a greater rate with enhanced wind speed than Pacific diffusivity, except in the 'warm' state where the increase is equal (see Fig 4.8). In contrast, the NADW cell weakening is greatest in response to reduced Pacific diffusivity in the 'warm' and present-day states but in response to reduced wind stress in the glacial state.

Some of the variation in the rate of response to wind and diffusivity at a given buoyancy state, is due to the accompanying changes in MOC structure. In particular changes in the depth of the NADW cell lead to significant changes in upwelling of NADW in the Atlantic basin which also play an important role in the changes in NADW cell strength in response to perturbations. Also, changes in the wind alter the channel circulation structure and thus the depth of the 'z_interface' which changes the MOC pathways.

There is also a small compensation by the Pacific diffusively-driven pathway or wind-driven pathway in response to changes in wind speed or Pacific diffusivity respectively in the zero and four-fold perturbations, opposing the net change in NADW cell strength. The Pacific diffusively-driven pathway decreases (increases) in the 'warm' (present-day) state in response to enhanced (reduced) wind speed. The same compensation by the wind-induced pathway to changes in Pacific diffusivity are seen except with the 'warm' and present-day states above reversed. There is no compensation in the glacial state due primarily to there being no lower Pacific diffusively-driven pathway of NADW.

An analysis of the change in the MOC components against the area-integrated Southern Ocean buoyancy flux for each of the wind and diffusivity perturbations (not shown), suggests the change in the MOC components with buoyancy forcing is similar to the control wind and diffusivity forcings (as described in Part I), with only small changes in the wind-driven

pathway but a large decrease in the Pacific diffusive-driven pathway as the buoyancy flux becomes more negative (i.e. more glacial). However, only three different buoyancy fluxes are available for each set of forcings and thus further research is needed in this area.

v) MOC driving mechanisms

Although, we have separated the pathways taken by NADW in this study (i.e. 'NADW_wind', 'NADW_pac' and 'NADW_at'), the driving mechanisms do not necessarily equate to these pathways. However, from these perturbation experiments we can conclude that these pathways do in general equate to the drivers of the NADW cell as described below.

The separation of the NADW flowing into the channel's lower cell which ultimately flows into the Pacific basin ('NADW_pac'), from that which flows into the channel's upper cell along the wind-driven pathway ('NADW_wind') is a very important distinction in this study. If this was not separated, the Southern Ocean wind-driven upwelling could be assumed to drive the AMOC in its entirety with only a minor role played by the Pacific diffusive upwelling. However, the assumption in this work is that the 'NADW_pac' component of the NADW cell would not be present without diffusive upwelling in the Pacific basin (i.e. the NADW cell would weaken). Instead, the eddy-induced lower cell would be isolated in the Southern Ocean with no NADW flowing into it, and this is shown to be the case in the zero Pacific diffusivity experiments. Thus, the 'NADW_pac' component is no longer present. However, the 'NADW_wind' component may increase slightly even if the wind remains constant, compensating for some of the reduction in 'NADW_pac'. This is due to there no longer being any PDW upwelled further in the upper wind-driven cell in the channel. Instead, the wind-driven cell can only upwell NADW. Thus, while 'NADW_wind' and 'NADW_pac' do give a good approximation to the wind and Pacific diffusive driving mechanisms of the

NADW cell, a small proportion of the 'NADW_pac' component in some cases includes waters which are both diffusively and later wind-driven to the surface.

The wind does of course also have a significant impact on the channel circulation and thus could alter the Pacific pathway if the winds are reduced, since the wind-induced tilting of isopycnals is the main factor generating the eddy-induced lower cell. Thus, the wind could still be important in enabling this Pacific diffusive mechanism to drive the NADW cell. However, in the zero wind experiments performed here, 'NADW_pac' is not significantly changed from the control experiments due to the direct zonal flows of NADW into the Pacific basin, or the buoyancy-induced tilting of the isopycnals maintaining the eddy-induced cell.

The Atlantic upwelling, 'NADW_at' is NADW which upwells via diffusive upwelling or the north Atlantic clockwise eddy-induced cell.

4.6. Conclusions

In this two part study, the dependence of the strength, structure and pathways of the MOC on Southern Ocean buoyancy forcing and wind stress, and vertical diffusivity has been investigated using a two-basin model with a southern circumpolar channel. In Part I, the Southern Ocean buoyancy forcing was shown to lead to a transition of the MOC from a future 'warm' low ice state to a present-day state and finally a 'cold' glacial state through a sea-ice induced increase in AABW formation, and thus a shoaling of the NADW cell. This changes the magnitudes of the wind-driven and Pacific diffusively-driven pathways of NADW by changing the overlap between the upper and lower cells at the channel-basin boundary. The Pacific diffusively-driven pathway decreases as the MOC transitions from a 'warm' to a 'glacial state, whereas the wind-driven pathway is greatest in the present-day state and smallest in the 'warm' state. In Part II, the variation of the MOC with Southern Ocean wind speed and Pacific vertical diffusivity is studied. The same method used in Part I

to separate the MOC components is used, enabling the importance of diffusive upwelling in the Pacific and Atlantic basins, and wind-driven upwelling in the channel to be determined.

The variation in Southern Ocean wind speed and Pacific vertical diffusivity leads to significant changes in the wind and Pacific diffusive-driven pathways as expected due to the ability of these mechanisms to upwell water being directly modified by these perturbations. However, there are further adjustments in these pathways due to the wind and diffusivity also influencing the depth of the NADW cell at the channel-basin boundary. The magnitude of Atlantic upwelling also increases as the NADW cell deepens.

The wind changes have the added complexity of changing the southern channel circulation and the depth of the interface between the upper and lower cells, both directly (through changes in the Deacon cell) and indirectly through isopycnal tilting and sea-ice export (which effect the eddy-induced lower cell).

Despite these additional changes, there is a clear dependence of the sensitivity of the NADW cell strength to variations in Southern Ocean wind speed and Pacific vertical diffusivity on the initial Southern Ocean buoyancy forcing. While the NADW cell strengthens (weakens) with enhanced (reduced) wind speed or Pacific diffusivity under all buoyancy forcing states, the magnitude of this change varies.

The sensitivity of the NADW cell strength to Pacific diffusivity increases as the Southern Ocean buoyancy forcing is varied from a glacial to a ‘warm’ climate state, as expected given the Pacific diffusively-driven pathway of NADW increases as the buoyancy forcing is perturbed towards a ‘warm’ state. In contrast, the ‘warm’ state has the lowest sensitivity to wind forcing, with the glacial and present-day states most sensitive to reduced and enhanced wind forcing respectively.

The key cause of these changes is due to the direct change in the wind-driven or Pacific diffusively-driven pathways, although changes in the wind speed and Pacific diffusivity also alter the NADW cell depth in some cases, increasing Atlantic upwelling non-linearly with enhanced wind speed or diffusivity. The structural changes also lead to small compensating changes by the wind-driven or Pacific diffusively-driven pathways in the 'warm' and present-day states, particularly at zero and four-fold perturbations, which oppose the change in NADW cell strength.

The main change in structure of the MOC with enhanced (reduced) Pacific diffusivity is a deepening (shoaling) of the NADW cell at the channel-basin boundary which alters the overlap between the upper and lower cells. This must happen since at zero Pacific diffusivity, all NADW flowing into the channel must be shallow enough to be upwelled by the wind-driven upper cell. This leads to large changes in Atlantic upwelling particularly in the 'warm' state, which undergoes the greatest structural changes with significant shoaling at low diffusivities, despite no change in buoyancy forcing.

The response of the NADW cell depth to wind forcing is less clear, with no change in the 'warm' state and only a deepening at high wind speeds in the present-day state. The deepening occurs at all wind speeds in the glacial state, due to the deepening of the channel's wind-driven upper cell. The increase in Atlantic upwelling with wind speed is therefore smaller in the wind experiments. However, in the present-day state at both a four-fold wind and diffusivity, the NADW cell deepens substantially leading to a large change in this component, with this state becoming most sensitive to changes in both wind and diffusivity at these high values.

The structure of the NADW cell is therefore dependent on wind and diffusivity, in addition to buoyancy forcing.

The experiments performed have a similar Southern Ocean buoyancy forcing in the zero wind experiments to the corresponding control, and therefore simulate the direct effect of wind changes with only small buoyancy (and sea-ice) perturbations. Changes in wind are shown to be unable to shoal the NADW cell to a glacial state, with a predicted strengthening and deepening of the NADW cell if the sea-ice was realistically simulated which would enable the reduced wind speed to reduce Southern Ocean sea-ice formation.

The Southern Ocean sea-ice formation rate and therefore buoyancy forcing also varies with wind speed since it exports sea-ice northwards. However, at low wind speeds the buoyancy forcing tends to remain similar in each of the buoyancy state experiments due to an increase in sea-ice thickness. The channel's lower cell is maintained in the present-day state due to buoyancy forced tilting of the Southern Ocean isopycnals, which maintains the Pacific diffusively-driven pathway.

A weakening of the Southern Ocean zonal wind stress has been proposed as a mechanism to instigate the transition of the MOC to a glacial state, characterised by a weaker, shoaled NADW cell and a more expansive Atlantic AABW cell. However, the experiments performed in this study suggest that while reduced wind speeds lead to a weakening of the NADW cell due to a reduced wind-driven pathway of NADW, it does not shoal the NADW cell (in either the 'warm' or present-day states). The only plausible mechanism to both weaken and shoal the NADW cell as in glacial times is a change in the buoyancy forcing, with a decrease in the negative Southern Ocean buoyancy fluxes due to enhanced sea-ice formation shown to be capable of causing this change in Part I.

We identified the simulation of unrealistically thick Southern Ocean sea-ice in the zero wind speed experiments of the present-day (and glacial) buoyancy states, which enables the sea-ice formation rate and buoyancy forcing to remain fairly unchanged at low wind speeds.

However, if the Southern Ocean buoyancy flux becomes more negative as may be expected at low wind speeds, the buoyancy forcing would tend towards the 'warm' state, potentially leading to a deepening and strengthening of the NADW cell even at zero wind speed. Thus, this mechanism would still be unable to cause a transition to a glacial state MOC.

Both a reduction in the magnitude of the Southern Ocean wind speed and buoyancy forcing (shown in Part I) reduce the NADW cell strength from a state representative of the present-day, one of the key changes in the transition to a glacial MOC. However, only a perturbation in the buoyancy forcing leads to a shoaling of the NADW cell, the other characteristic of the glacial state MOC.

Our results contrast with Jochum and Eden [2015], in which the NADW cell strength is shown to be highly insensitive to enhanced Southern Ocean wind speed in a global climate model, whereas there is a large strengthening of the NADW cell in each buoyancy state in our experiments. However, they do appear to validate their suggestion that the NADW cell is insensitive to reduced wind speed. In our present-day and 'warm' states, NADW upwells via Pacific diffusively-driven upwelling at reduced wind speeds as in the pre-mentioned study, reducing the NADW cell sensitivity. The cause of the difference in sensitivity to enhanced wind speed between these studies is difficult to fully ascertain. The experiments of Jochum and Eden [2015] were only partially eddy compensated with a significant increase in the wind-driven upper cell in the channel with wind speed as in our experiments. However, the increase in this cell is primarily and thus this is likely not the cause of the difference. Instead, the divergence may lie with the varying wind used in the models and perhaps other model parameters. In the control experiment of Jochum and Eden [2015], the Pacific pathway seems to be almost zero as in our glacial state. However, in contrast to our experiments, a large volume of the increase in this cell is isolated within the Southern Ocean rather than increasing the upwelling NADW flowing into the channel. This is likely either due to

differences in the zonal wind speed profile, with the Deacon cell located further south in the channel of Jochum and Eden [2015], or it may be due to the eddy compensation by the enhanced eddy-induced cell strength being locally larger in the north of the channel in Jochum and Eden [2015]. This reinforces the uncertainties associated with the magnitude of eddy compensation and model differences. However, our results for reduced wind speeds and sensitivity differences between varying buoyancy forcings should hold regardless of the models representation of mesoscale eddies so long as the control experiments have a realistic channel circulation. The change at zero wind speed is akin to our 'warm' state, with very little weakening or shoaling of the NADW cell, and the presence of a weak clockwise cell in the north of the channel. This is the response we predict would also occur in the present-day state if the sea-ice model responded realistically to reduced wind speed in this state.

This study highlights the complexity of the MOC and the importance of simulating realistic changes in both Southern Ocean winds and buoyancy forcing, and obtaining an accurate vertical diffusivity profile to accurately model MOC variations in past and future climates. The initial state taken to be the present-day MOC will also significantly impact the sensitivity of the MOC to these forcings. However, the direction of variation of the MOC components to varying buoyancy forcings described in Part I (Chapter 3) appears to hold for a wide range of Southern Ocean wind and Pacific diffusivities. However, simultaneous variations in both of these latter parameters and experiments with smaller freezing rate perturbations are needed to confirm this and quantify any differences.

The importance of both Pacific (and Atlantic) diffusive-driven upwelling and wind-driven upwelling in driving the NADW cell varies both with the buoyancy forcing (as shown in Part I) and also with changes in the Southern Ocean wind speed and Pacific vertical diffusivity.

4.7. Additional analysis of MOC variations

While our focus in this chapter has been on the change in the overturning streamfunction in response to changes in Southern Ocean wind speed and Pacific vertical diffusivity, we now perform an analysis of the changes in stratification and N-S density differences which accompany the MOC changes in response to the wind and diffusivity perturbations. This will enable us to determine the impact these changes may have on the MOC. This may improve our understanding of the cause of the MOC variations since the wind-induced sea-ice changes alter the stratification and N-S density differences, while the wind and diffusivity also directly alter the ocean's density distribution.

4.7.1. Cell interface depths

(a) (b)

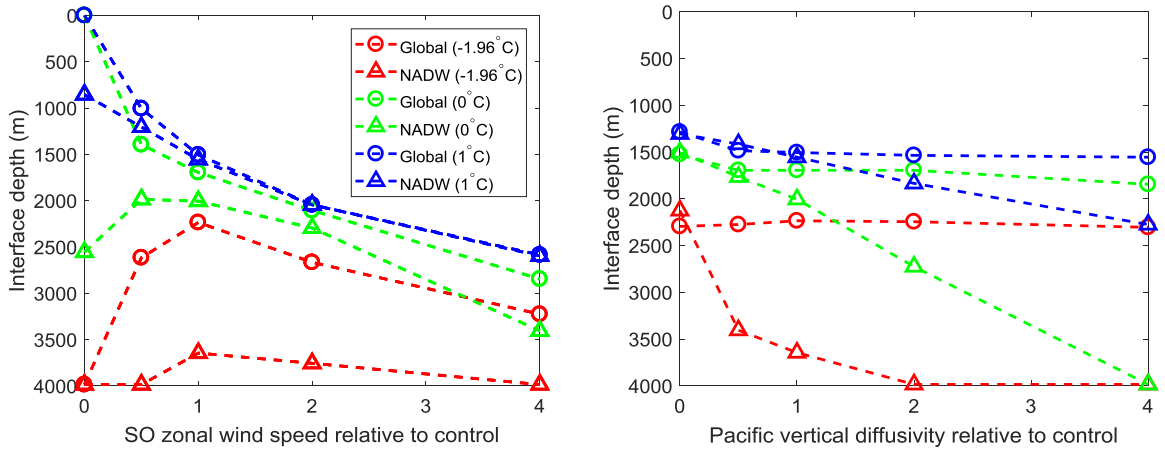

Fig 4.14: Interface depth of the global-integrated circulation (circle markers) and the NADW cell (triangle markers) at the channel-basin boundary against (a) the Southern Ocean wind speed and (b) Pacific vertical diffusivity, relative to the control values. Each marker on a line corresponds to an experiment with a varying wind or diffusivity. In each plot, the interface depths are plotted for each of the three control buoyancy forcings; the 'warm', present-day and glacial states labelled as '-1.96°C' (red), '0°C' (green) and '1°C' (blue) respectively, the sea-ice freezing points corresponding to each of these states.

Before analysing the changes in stratification and density, we calculate the changes in NADW and global-average interface depths at the channel-basin boundary with perturbations in Southern Ocean wind speed (Fig 4.14a) and Pacific diffusivity (Fig 4.14b). These plots help to highlight the changes in the MOC components described previously in this chapter since the overlap between the upper and lower cells at the channel-basin boundary is the dominant factor determining the magnitude of the Pacific pathway of NADW.

The changes in response to Pacific diffusivity are the most straightforward with the NADW cell deepening with enhanced diffusivity under all buoyancy states while the global-average cell interface depth remains approximately constant. Thus, the overlap increases with Pacific diffusivity, increasing the Pacific pathway. There is no overlap at zero diffusivity, as is required to satisfy continuity since any NADW flowing into the channel's lower cell would no longer be able to return to the surface of the Atlantic without Pacific upwelling.

However, the changes with wind speed are more complex as the global-average interface depth also varies and is dependent on the initial buoyancy forcing. For increases in wind speed relative to the control, both the NADW and global-average interfaces deepen. The changes tend to increase the overlap slightly in the present-day state and reduce it in the 'warm' state. In response to reduced wind speed relative to the control, the global-average interface shoals to the surface in the present-day and glacial states due to the reduction in the wind-driven upper cell, while the anti-clockwise eddy-induced channel circulation dominates due to the unrealistic maintenance of Southern Ocean sea-ice formation. The NADW cell also shoals in the glacial state whereas it deepens in the present-day state. This contrast leads to a large difference in the response of the MOC to reduced wind speed due to contrasting Pacific pathway magnitudes. In the 'warm' state, the global-average interface increases significantly and the NADW cell also increases, both deepening to the ocean floor due to the presence of a clockwise eddy-induced cell in the channel. However, this is relatively weak with the Pacific

pathway maintained via zonal flows. This additional analysis helps to visualise the changes in the MOC pathways with wind and diffusivity perturbations.

4.7.2. Deep stratification and surface density

(a) (b)

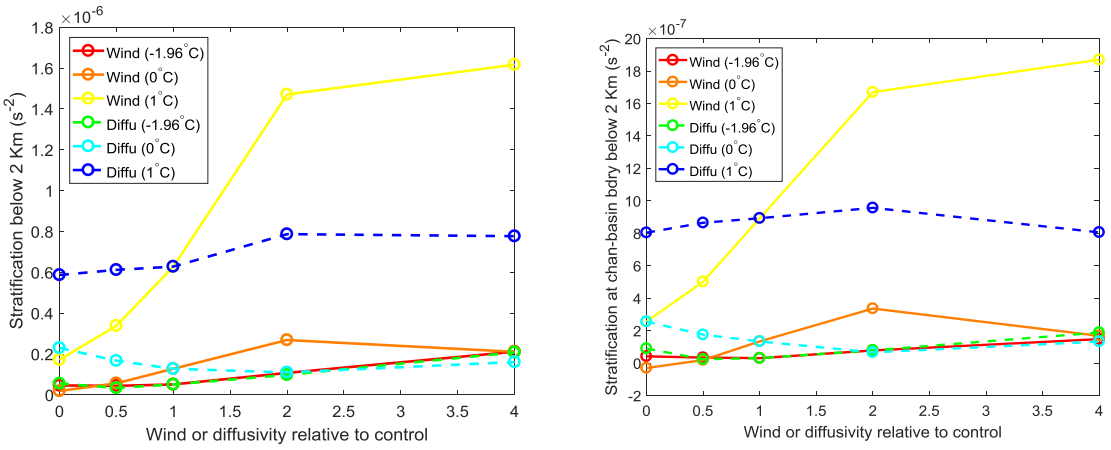

(c)

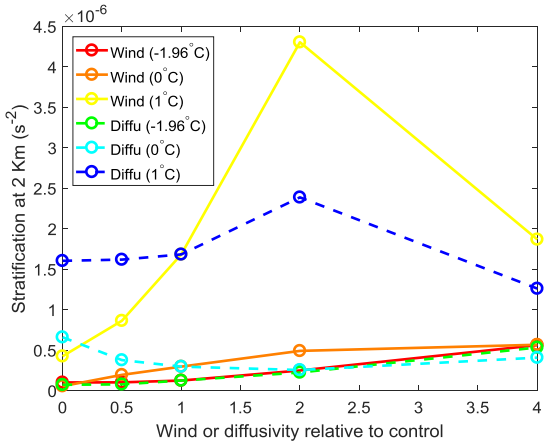

Fig 4.15: Stratification (s^{-2}) in the Atlantic sector averaged (a) over depths below 2 km, (b) over depths below 2 km at the channel-basin boundary, and (c) over depths of 2 km, plotted against wind or diffusivity relative to the control. As in Fig 4.14, the wind and diffusivity perturbation experiments are plotted for each of the buoyancy states, with sea-ice freezing points of -1.96°C, 0°C and 1°C.

In Fig 4.15, the variation of the deep stratification (i.e. at depths of 2 km and below) with wind and diffusivity perturbations tends to be small, except in the glacial state wind

perturbation experiments where the changes are far greater (the yellow line). The enhanced wind speed increases the tilt of the Southern Ocean isopycnals (in latitude-depth space) which primarily causes the changes in stratification with wind speed in this glacial state (Fig 4.16d). It is interesting to note that the NADW cell deepens with wind speed in this glacial state despite the deep stratification increasing. This suggests changes in stratification play only a secondary role on the NADW cell structure in these experiments while the direct effects of changes in wind speed on the MOC dominate.

The isopycnal slope also increases with wind speed in the present-day and 'warm' states (Fig 4.16d), and with diffusivity in the glacial state. However, the changes in deep stratification are small. This difference is likely due to the stratification being far smaller in the present-day and 'warm' state control experiments, reducing the impact of the isopycnal slope changes. In the glacial state, enhanced Pacific diffusivity reduces the density difference between the North Atlantic and south of the model which leads reduces the changes in stratification (Fig 4.15c). Clearly, the changes in stratification are not significant in the other wind and diffusivity experiments with only small changes (see Fig 4.15).

(a) (b)

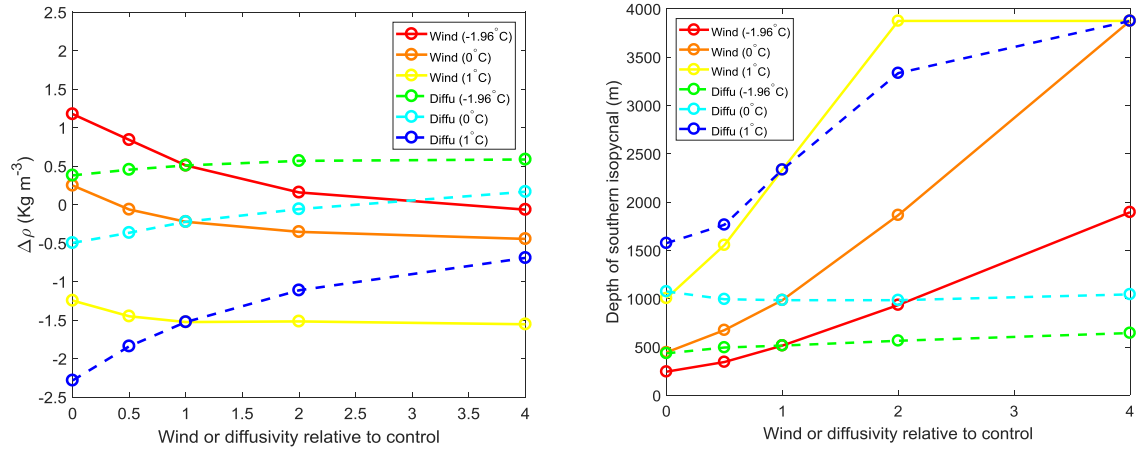

(c) (d)

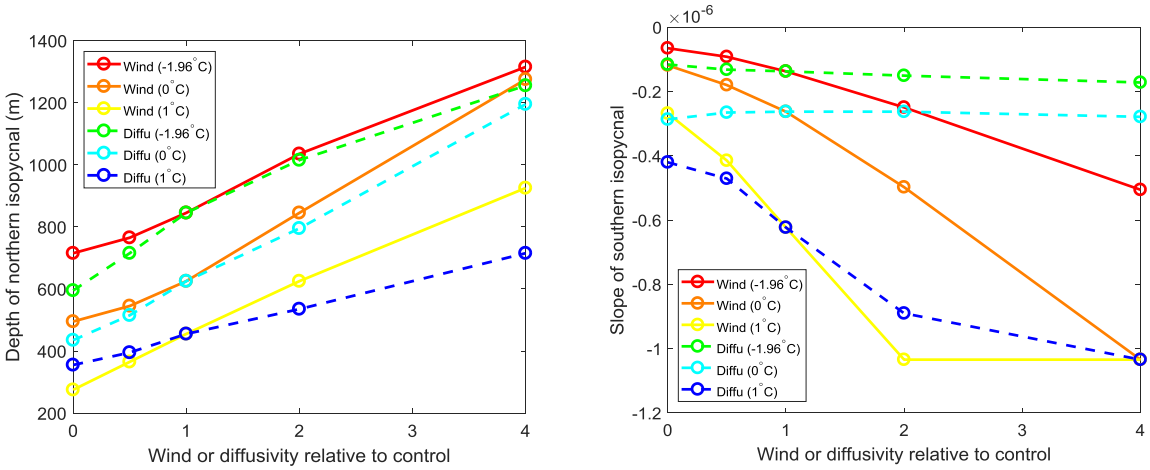

Fig 4.16: Plots of (a) surface density difference between the North Atlantic and the south of model (globally-averaged), (b) and (c) depth of the northern and southernmost outcropping isopycnals respectively at the channel-basin boundary, and (d) slope of the southernmost outcropping isopycnal averaged over the channel, all plotted against wind or diffusivity relative to the control. As in Fig 4.14, the wind and diffusivity perturbation experiments are plotted for each of the buoyancy states, with sea-ice freezing points of -1.96°C, 0°C and 1°C.

The variation in the N-S density difference with wind and diffusivity perturbations (Fig 4.16a) is far smaller than when the southern buoyancy forcing is perturbed (Fig 3.11b) as expected since we are no longer directly altering the surface buoyancy. The density in the north decreases relative to the south with enhanced wind speed due to the increased Southern

Ocean sea-ice formation rate but it increases with enhanced Pacific diffusivity. The change in the N-S density difference with enhanced wind speed therefore opposes the strengthening and deepening of the NADW cell. The N-S density increases with Pacific diffusivity are small except in the glacial state. We therefore do not believe changes in stratification or density are a major factor controlling the response of the MOC to wind and diffusivity perturbations. Thus, we do not plot these variables directly against the MOC component changes or the cell interface depths as we did in chapter 3. These plots of the stratification or the cell interface depths would also become very difficult to interpret since the stratification and cell interface depths are almost constant at varying wind speeds and diffusivities in some cases (Fig 4.15) or vary inconsistently (see Fig's 4.14 and 4.15).

This additional analysis improves our understanding of the changes in the MOC components with the wind speed and Pacific diffusivity perturbations described previously. In particular, the cell interface depth plots help us to understand the consequent changes in the direct wind and Pacific pathways. The effects of stratification and N-S density differences have only a secondary role in the MOC changes with the direct effects of wind and diffusivity changes on the MOC structure appearing to be the primary factor in the changes seen. Of course, the degree to which stratification and N-S density differences change varies between the different buoyancy states. Changes in the depth of the northernmost isopycnal and slope of the Southern Ocean isopycnals with wind and diffusivity may also play an important role.

Chapter 5

Single-basin model simulations and tracer release experiments

The aims of this section are to determine the differences between single- and multi-basin model simulations of the MOC to gain further insight into the overturning pathways taken in ocean models and the drawbacks of using a single-basin model compared with a multi-basin model.

The transition of the MOC from present-day to glacial states (through buoyancy forcing changes) will be discussed as in the multi-basin model simulations, and experiments with varying Southern Ocean winds and vertical ocean diffusivity are performed. This section is less detailed since the main findings on the physical circulation have already been discussed using the more realistic multi-basin model.

This section is divided as follows: firstly questions that we seek to answer are stated, followed by an analysis of the MOC in single-basin models under varying buoyancy forcing and geometrical setups which are compared with multi-basin models. Single-basin model experiments are then performed with enhanced Southern Ocean wind forcing and varying vertical diffusivity. Finally tracer release experiments are performed in both the single- and multi-basin models.

5.1. Questions

The main questions this research seeks to understand are listed below:

- Why do single-basin models have a weaker NADW circulation than multi-basin simulations under all buoyancy forcings?
- How are single-basin models setup to attain a realistic overturning circulation, representative of the global-integrated MOC?
- How do variations in vertical ocean diffusivity, Southern Ocean winds and surface buoyancy fluxes alter the circulation in single-basin models?

5.2. Single-basin model buoyancy forcing experiments

The single-basin model configuration is described in Chapter 2. The model is forced at the surface with the same control buoyancy and wind forcings used in the Atlantic basin of the multi-basin model simulations. This enables a direct comparison between the circulation in the single-basin model and the Atlantic basin of the multi-basin model. The sea-ice freezing point is varied between -1.96°C and 1°C as in the multi-basin model experiments, to represent varying Southern Ocean sea-ice formation rates and thus buoyancy forcings.

In contrast to the multi-basin model, the sea-ice freezing point most representative of the present-day MOC in the single-basin model is the -1.96°C experiment. The residual overturning circulation has a NADW cell and lower AABW cell with a strength of ~7.5 Sv and ~8.3 Sv respectively (the lower cell strength maximum being in the channel due to the eddy-induced circulation) (see Fig 5.1a). The NADW cell is slightly weaker than the glacial state (1°C freezing point) multi-basin model experiment and significantly weaker than the ~19.5 Sv NADW cell in the corresponding multi-basin model freezing point experiment. This difference is due to the differing geometry of these models. The single-basin model has no

Pacific basin over which diffusive-driven upwelling of NADW origin waters can occur and also a narrower channel, reducing the wind-driven upwelling component of NADW. The wind-induced upwelling of NADW is ~2.5 Sv (i.e. the volume of NADW flowing south of the latitude of the South Africa landstrip (not present in the single-basin model) where the zonal wind speed becomes strong. The remaining ~5 Sv of NADW is upwelled in the basin before reaching the channel. The lower 'AABW' cell in this experiment is primarily a consequence of the eddy-induced overturning in the channel, with almost no AABW formation and thus a highly unstratified deep ocean.

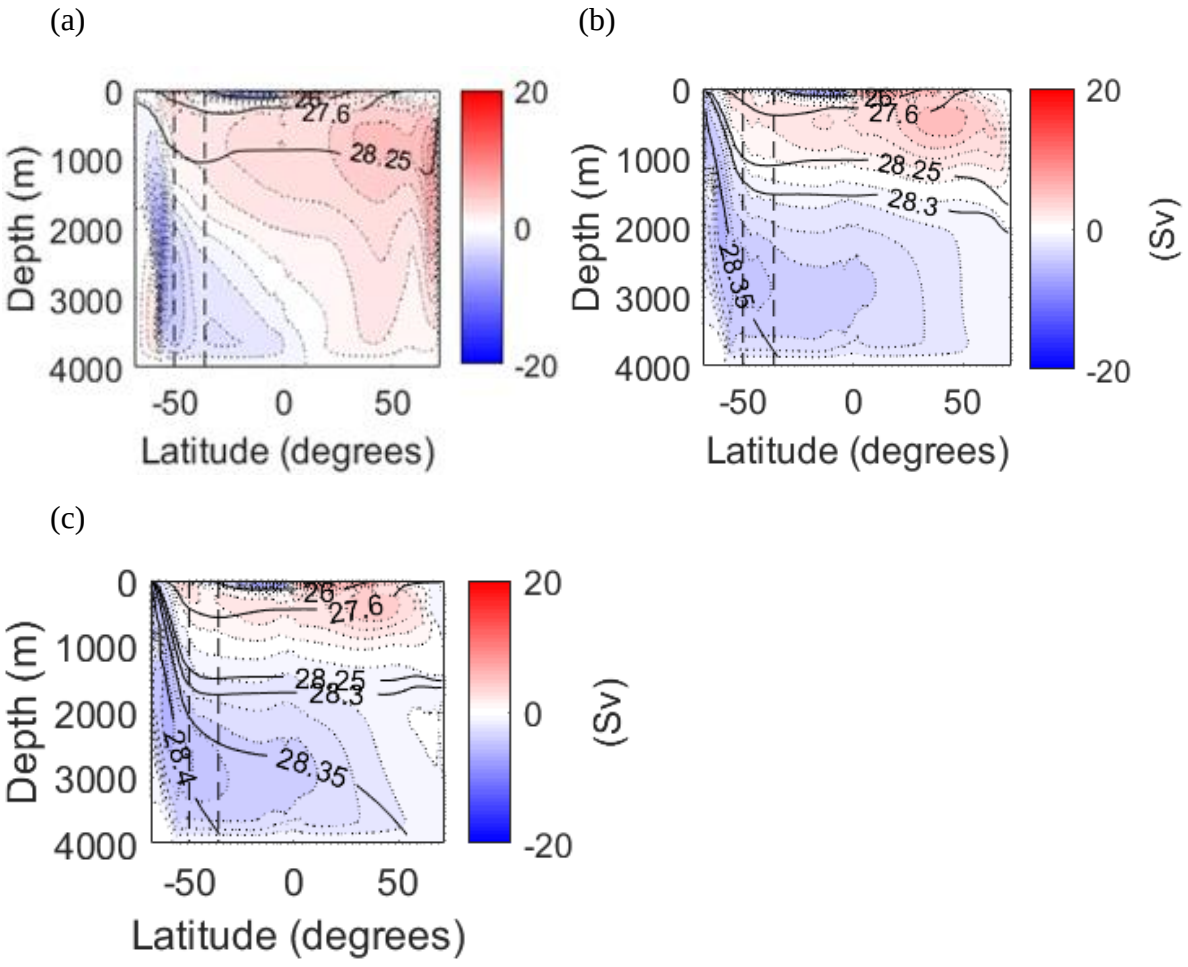

Fig 5.1: Zonal-average residual overturning streamfunction in the single-basin model when using the control forcings with a sea-ice freezing point of (a) -1.96°C, (b) 0°C and (c) 1°C. The red (positive) and blue (negative) streamfunctions are clockwise and anti-clockwise circulations respectively. The streamline contour intervals are 1 Sv. Potential density contours are represented by black solid lines. The vertical dashed lines in the south of the

domain are from left to right, the southernmost latitudes of the South America and South Africa landstrips respectively (the latter landstrip not present in the single-basin model).

As the sea-ice freezing point is increased, the AABW formation rate increases and the deep stratification increases. This leads to a shoaling of the NADW cell as described by Jansen and Nadeau [2016] and the expansion of the lower AABW cell. In the 0°C freezing point experiment, the NADW cell weakens by ~1.8 Sv to ~5.7 Sv (Fig 5.1b). Although the lower cell weakens to ~5.9 Sv, this is due to a reduced eddy-induced circulation but a stronger Eulerian-mean component due to the enhanced AABW formation. The NADW cell has shoaled to a glacial state with most of the decrease in NADW cell strength due to reduced upwelling in the basin north of the channel.

The residual NADW cell weakens further to ~4.7 Sv when the sea-ice freezing point is increased to 1°C (Fig 5.1c), leading to enhanced Southern Ocean sea-ice and AABW formation.

The single-basin model simulations using the average of the forcings over the Atlantic and Pacific sectors generates a similar MOC to using the Atlantic forcings. However, it does lead to a small strengthening of the NADW cell (by ~3 Sv in the -1.96°C experiment) due to the buoyancy gradient in the north Atlantic then being greater.

The MOC in the -1.96°C sea-ice freezing point experiment is similar to the structure of the global-integrated streamfunction in the corresponding multi-basin model experiment. This is despite the NADW cell being significantly weaker in the single-basin model. The similarity in the overturning structure with most of the NADW upwelling to the upper ocean as it flows southwards to the channel (in contrast to the Atlantic only circulation) is due to the significant Pacific basin upwelling in the multi-basin model. This shall be described in more detail later.

5.3. Causes of differences between single and multi-basin models

While the single and multi-basin models have similarities in the structure of the global-average multi-basin and the single-basin model residual circulations, the multi-basin model has a stronger upper NADW and lower AABW cell than the single-basin model. The circulations in the individual basin also differ greatly from the global-average circulation as described in Chapters 3 and 4.

The global-average NADW cell in the multi-basin model is ~19.5 Sv which is ~12 Sv greater than in the single-basin model (despite the same Atlantic basin forcings). Given the findings in Chapters 2 and 3, this is likely due to the enhanced model domain size. The hypothesis is:

- The volume of water in the wider multi-basin model is greater than the single-basin model, and is therefore able to upwell a greater volume of water and drive a stronger NADW cell. Therefore, a wide single-basin model (with a reduced northern extent in the Pacific basin) will have the same strength as the multi-basin model unless the additional meridional boundary in the multi-basin model (with a narrow Atlantic basin) is important. The main mechanisms that could act to increase the NADW cell strength would be enhanced wind-driven or diffusive-driven upwelling. To determine how much of the strengthening is due to enhanced wind-driven upwelling, a wide channel single-basin model simulation is also used.

The simulations shown below were performed prior to obtaining the results in Chapters 3 and 4. We therefore only performed these varying geometry single-basin model simulations with a sea-ice freezing point of -1.96°C (i.e. the ‘warm’ state in the multi-basin model and present-day state in the single-basin model). However, it enables us to further understand the cause of differences between the single and multi-basin model circulations.

5.3.1. Variable geometric configurations of a single-basin model

The MOC in a single-basin model with varying geometries are described in this section. A single-basin model with the same width as the multi-basin model and with a reduced latitudinal extent over a longitude range equal to the Pacific basin width (i.e. the multi-basin model with no South Africa land strip) is used to see the effect of basin width on the MOC, particularly on the strength of the upper NADW cell. This is referred to as the wide single-basin model (Fig 5.2a). A single-basin model with the original Atlantic basin width but with a channel the same width as the multi-basin model is also used to determine the importance of channel width. This is referred to as the wide channel single-basin model (Fig 5.2b). In the MOC calculations, the velocities in the separated Pacific basin are removed (i.e. the Pacific basin can be considered to be land).

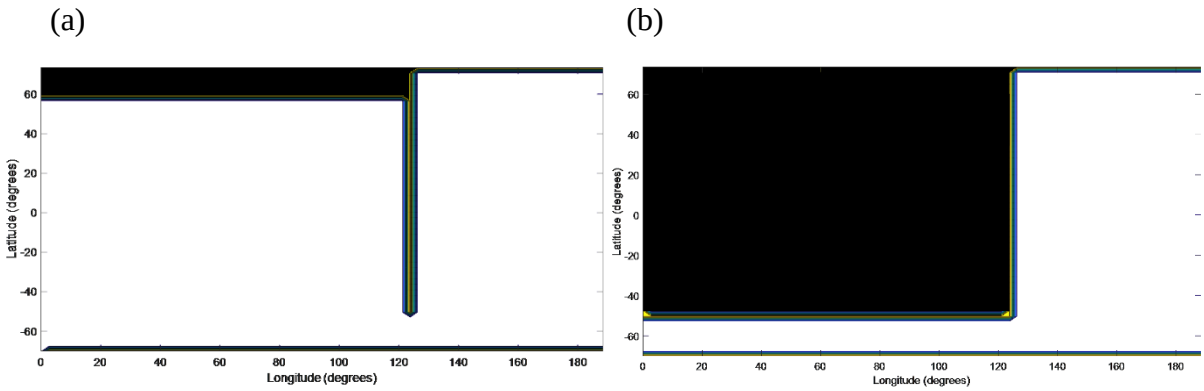

Fig 5.2: Bathymetry of (a) the wide single-basin model with a reduced northern extent over a longitude range equal to the Pacific basin width, (b) the single-basin model with a wide southern channel. The ocean is white, while land is black (or yellow and blue at the border between ocean and land).

The forcings used in each model domain are now changed. The surface temperature and salinity averaged over the Atlantic sector of the multi-basin model -1.96°C freezing point experiment from Chapter 3 is used as the temperature and salinity relaxation forcings. The relaxation timescales for temperature and salinity are set to 6 days, such that the surface

temperature and salinity in these simulations are approximately equal to the relaxation temperature and salinity.

To enable a direct comparison of the effect of changes in geometry on the circulation (with no other effects), the MOC in the original single and multi-basin models with freezing points of -1.96°C were also simulated using the same forcings (i.e. relaxation forcings using the surface temperature and salinity from the Atlantic sector of the multi-basin model everywhere).

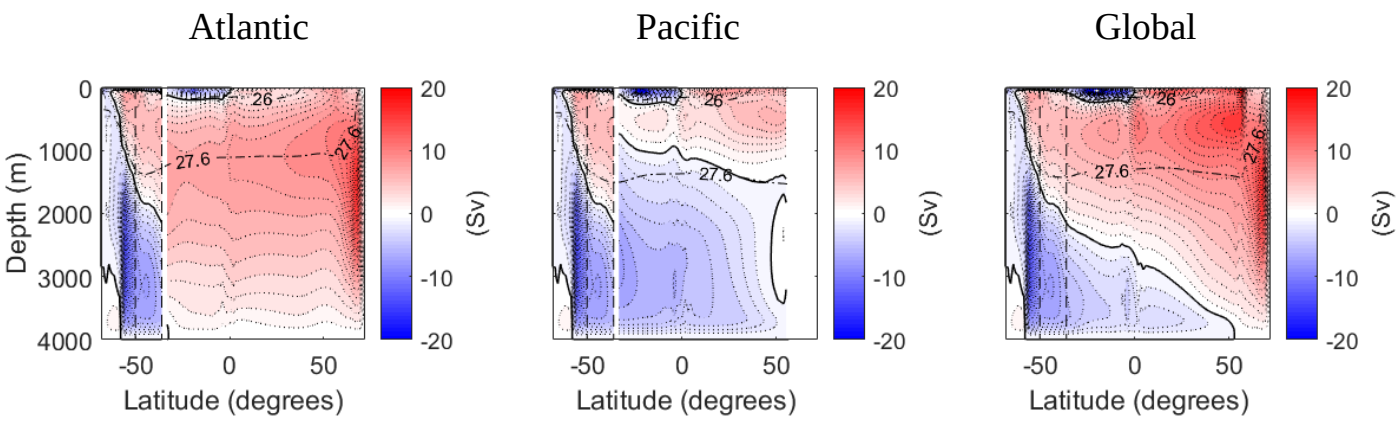

Fig 5.3: Multi-basin model zonal-average residual overturning streamfunction using a sea-ice freezing point of -1.96°C forced using strong temperature and salinity relaxation forcings representative of the Atlantic Ocean throughout the domain. Plots from left to right are the Atlantic, Pacific and global-average circulations respectively. Colours and contours as in Fig 5.1.

Fig 5.3 shows the multi-basin model MOC using these forcings. The upper NADW cell strength in the Atlantic sector and in the global-average is ~16.5 Sv, ~3 Sv weaker than the ~19.5 Sv upper cell strength in the -1.96°C freezing point experiment from Chapter 3 which used different forcings in the Pacific and Atlantic sectors of the model. The Pacific basin now has an upper cell due to the north of the Pacific basin being denser due to Atlantic forcings being applied throughout the whole domain. The flow into the channel, 'NADW_channel' is now only ~8 Sv compared to ~11.1 Sv using the more realistic forcings. This decrease is due to 'NADW_wind' now reduced to ~1.2 Sv from ~4.1 Sv. It therefore seems likely the

reduced NADW cell strength is primarily a consequence of the Pacific basin being denser in the north and thus producing an upper cell. This prevents the PDW cell upwelling to the surface and therefore this PDW must be upwelled by the wind-driven upper cell in the channel before returning to the Atlantic. Therefore 'NADW_wind' is reduced.

The same Atlantic forcings and strong temperature and salinity relaxation imposed in the original single-basin model generates a NADW cell strength of ~10.3 Sv, with ~2.5 Sv upwelled in the channel by the Southern Ocean zonal winds (see Fig 5.4a). The NADW cell is ~2.8 Sv stronger than the single-basin model control experiment described previously. This is primarily due to the north of the model being slightly denser than in the control experiment under these forcings.

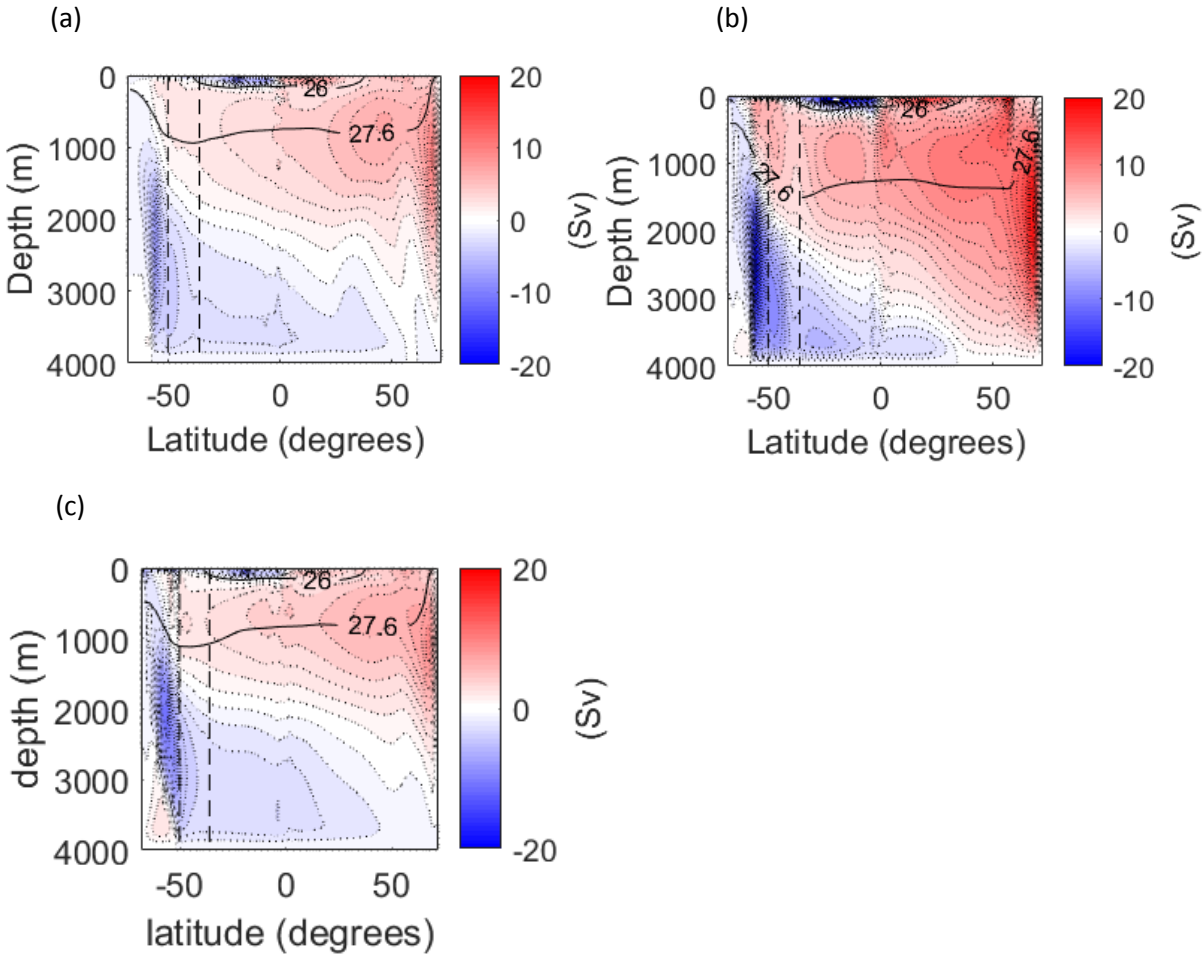

Fig 5.4: Single-basin model zonal-average residual overturning streamfunction using varying geometrical setups forced using strong temperature and salinity relaxation to forcings representative of the Atlantic Ocean throughout the domain. The model domains are (a) the original single-basin model, (b) the wide single-basin model with reduced northern latitude in the Pacific sector and (c) the wide channel single-basin model. Colours and contours as in Fig 5.1.

5.3.1.1. Wide single-basin model

The MOC in the wide single-basin model is now described and compared to these simulations. The wide single-basin model (Fig 5.2a) has the same width as the multi-basin model which is 2.9 times wider than the original single-basin model. The effect of this increased width and ocean basin volume on the MOC can now be determined.

In the wide single-basin model, there is a ~19.1 Sv NADW cell with ~5 Sv driven by upwelling along the direct wind-driven pathway ('NADW_wind') in the channel, and ~14 Sv

upwelled by diffusive-driven upwelling and the eddy-induced cell in the basin to the north (see Fig 5.4b). This is ~2.5 Sv stronger than the multi-basin model NADW cell strength under the same Atlantic only forcings. The direct wind-driven pathway is ~4 Sv greater in the wide single-basin model, while the total upwelling in the basin north of the channel is actually greater in the multi-basin model. The difference in NADW cell strength is likely due to the NADW which flows into the channel in the multi-basin model primarily upwelling in the Pacific basin before being upwelled further by the wind in the channel. Thus, the wind and diffusive-driven upwelling work together rather than both contributing separately to the NADW cell strength. This could also be the case in the wide single-basin model since only the global-average MOC can be plotted in single-basin models, in which the NADW cell must connect to the upper cell in the channel. However, it is more likely that the NADW that upwells in the basin does not flow into the channel, since there is no longer two separate basins preventing zonal flows between the Atlantic and Pacific sectors north of the channel. The clockwise eddy-induced circulation is approximately the same strength and thus this is not contributing to the strength difference.

Comparing, the global-average MOC in the multi-basin model (Fig 5.3) and the wide single-basin model (Fig 5.4b), the MOC structure looks very similar and has a similar strength. In contrast, the Atlantic width single-basin model NADW cell (Fig 5.4a) is ~9 Sv weaker than the wide single-basin model. Thus, we can conclude that the wider domain size is the most important factor in generating a stronger NADW cell in the multi-basin model compared to the original narrow single-basin model, while the separation of the domain into two basins appears to play only a small role. The enhanced strength in the multi-basin model is therefore due both to an enhanced wind-driven upwelling in a wider channel and a larger volume basin which can diffusively upwell a greater volume of water.

5.3.1.2. Wide channel single-basin model

The wide channel single-basin model is the original single-basin domain but with a channel width the same as in the multi-basin model (Fig 5.2b). The MOC in the wide channel single-basin model (Fig 5.4c) is similar to that of the original single-basin model (Fig 5.4a). The NADW cell unexpectedly weakens from ~10.3 Sv to ~6.3 Sv due to a reduced eddy-induced circulation in the far north of the basin. The wind-driven upwelling of NADW in the channel increases by ~0.6 Sv from ~2.5 Sv to ~3.1 Sv. While the wider channel does not strengthen the MOC in this case, if the Southern Ocean winds were significantly stronger, the NADW cell would be expected to strengthen and overcome the decrease in the eddy-induced circulation.

It should also be noted that the wide single-basin model and the multi-basin model have a wider domain north of the southern end of the South America land strip than the wide channel single-basin model, over which the Southern Ocean westerly winds are still strong and the channel's wind-driven upper cell is present (i.e. between 50°S and 36°S). Thus, the wider domain in these cases leads to a far greater increase in the wind-driven upwelling and thus plays an important role in the strengthening of the NADW cell relative to that of the original single-basin model.

5.3.2. Single-basin model wind forcing and vertical diffusivity experiments

The original Atlantic width single-basin model experiments were also performed with varying Southern Ocean zonal wind speed and vertical diffusivity. While a number of wind perturbation experiments were performed, only the enhanced wind experiment is shown here. The control wind and vertical diffusivity are the same as those used in the Atlantic sector of the multi-basin model control experiments of Chapter 3 and 4, with the single-basin model control experiment shown in Fig 5.1a (i.e. closest to the present-day state).

5.3.2.1. Wind forcing perturbations

The Southern Ocean westerly winds were only varied south of the South America landstrip (i.e. between 70°S and 50°S). A two-fold increase in the Southern Ocean winds at these latitudes leads to an increase in Southern Ocean zonal wind stress from a maximum of 0.11 N m^{-2} at 50°S to 0.22 N m^{-2} (similar to the maxima in the Trenberth et al. (1989) climatological zonal wind stress which is far larger than the NCEP-NCAR dataset, and larger than satellite scatterometer measurements (Lee et al. [2013]).

The residual NADW cell increases by ~2.8 Sv to ~10.3 Sv in the two-fold wind experiment (Fig 5.5a), with the volume of NADW upwelled in the channel's upper wind-driven cell increasing from ~2.5 Sv to ~4.3 Sv. While this shows the NADW cell is sensitive to changes in Southern Ocean wind speed, a far larger increase would be required to obtain a stronger, more realistic NADW cell.

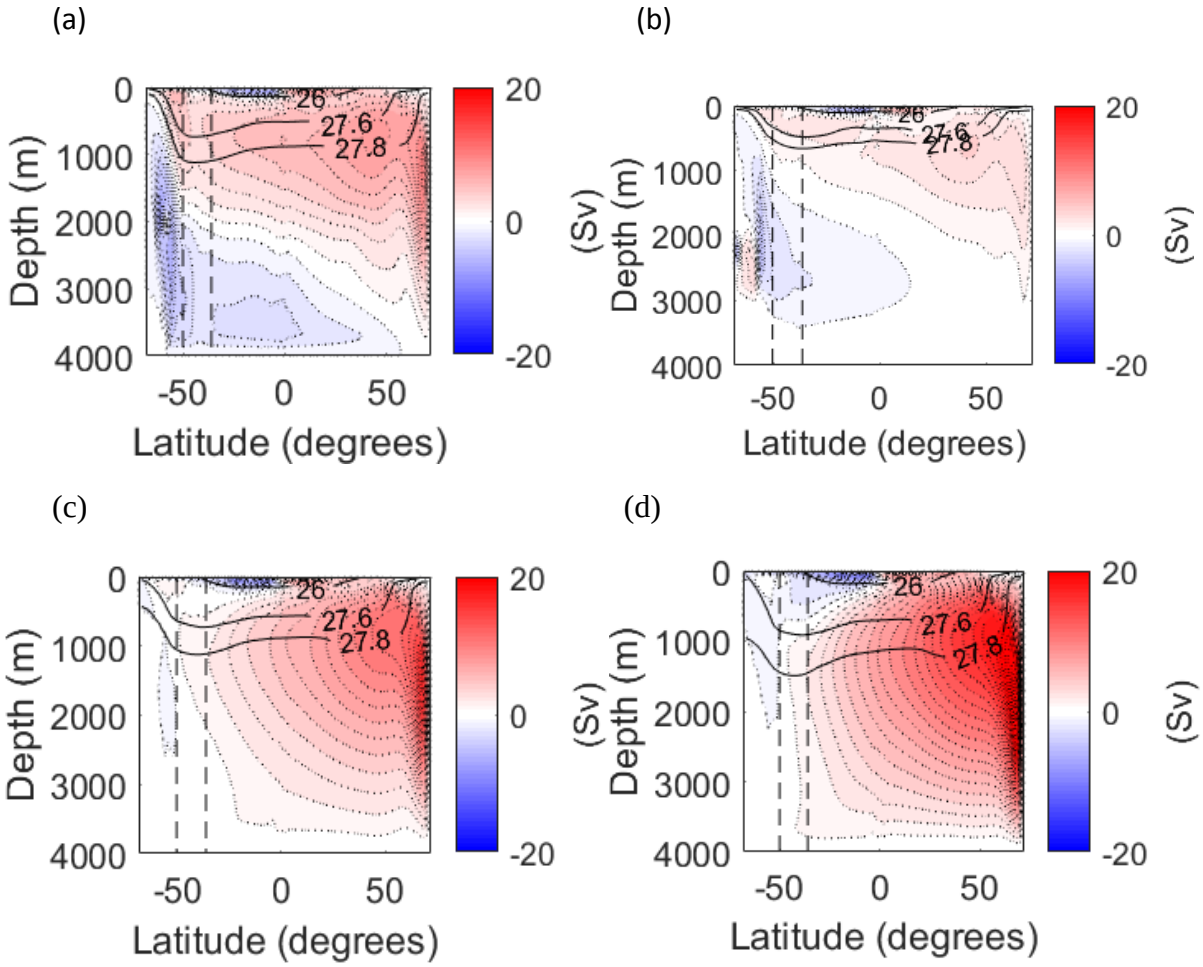

Fig 5.5: Original Atlantic width single-basin model zonal-average residual overturning streamfunction for experiments with perturbations to the -1.96°C freezing point control simulation. The control is perturbed by (a) a two-fold increase in the zonal wind stress in the circumpolar channel (70°S to 50°S), (b) a constant vertical diffusivity of 10^{-5} m^2 s^{-1}, (c) a constant vertical diffusivity of $5x10^{-5}$ m^2 s^{-1}, (d) a constant vertical diffusivity of 10^{-4} m^2 s^{-1}. Colours and contours as in Fig 5.1.

5.3.2.2. Vertical diffusivity perturbations

A constant vertical diffusivity profile was used in the vertical diffusivity perturbation experiments, despite the control experiment using the Bryan and Lewis [1979] diffusivity scheme (BL79), with an increase in diffusivity from 0.1 x 10^{-4} m^2 s^{-1} at the surface to 2 x 10^{-4} m^2 s^{-1} at the ocean floor (an average of about 10^{-4} $m^2 s^{-1}$). While similar changes in NADW cell strength can be obtained when using perturbations of the original BL79 diffusivity profile, the constant diffusivity profile is also of interest since this has been used in a number

of single-basin model studies (e.g. Jansen and Nadeau [2016] use a constant diffusivity of 6 x 10^{-5} m^2 s^{-1}).

Using a constant diffusivity of 10^{-5} m^2 s^{-1} generates a NADW cell of ~4.2 Sv (Fig 5.5b), ~3.3 Sv weaker than the ~7.5 Sv control simulation (Fig 5.1a) due to reduced diffusive-driven upwelling in the basin. In contrast, a constant diffusivity of 5x10^{-5} m^2 s^{-1} and 10^{-4} m^2 s^{-1} generates a NADW cell with a strength of ~17.2 Sv and ~25.7 Sv respectively (Fig 5.5c and d). The NADW cell in these experiments is highly diffusive. This suggests that using a constant diffusivity rather than a profile with a more realistic large increase at ~2000 m despite a similar average vertical diffusivity, generates a significantly stronger NADW cell. Thus, the enhanced diffusivity in the upper 2000 m, where the NADW is formed appears to significantly strengthen the NADW cell despite there being a decrease in the diffusivity in the lower 2000 m.

Another characteristic of the constant diffusivity experiments is the lower cell weakens and shoals or is non-existent. This is due to the control buoyancy forcing producing a very weak Eulerian-mean AABW cell while the anti-clockwise eddy-induced circulation contributes most to the lower residual cell strength. However, in these constant vertical diffusivity profile experiments, the eddy-induced circulation weakens dramatically due to reduced Southern Ocean isopycnal slopes. A more realistic lower AABW cell would likely be obtained in these experiments if the buoyancy forcings are changed to make the buoyancy fluxes more negative in the south of the model and thus the surface of the Southern Ocean denser.

5.4. Tracer release experiments

A number of passive tracer release experiments provide a visual aid to the ocean pathways in the single and multi-basin models. The passive tracer is transported through the models by advection from the residual circulation and is also redistributed by diffusion. This provides a

useful insight into the transport of a passive tracer such as carbon or phosphate through the model, in addition to the pathways taken by the MOC. However, these tracer transports will of course differ from that of a passive tracer such as phosphate in the real ocean since the concentration of phosphate is already spread throughout the ocean and thus the diffusion will be smaller.

In the multi-basin model 'warm' state (-1.96°C freezing point) experiment, the tracer is released at the bottom of the north Atlantic and at mid-depth in the south of the Pacific basin (see Figs 5.6 and 5.7). In the single-basin model -1.96°C freezing point experiment, the tracer is released at the bottom of the ocean in the far north of the domain (see Fig 5.8).

The multi-basin model tracer release simulations show the upwelling pathway of NADW or PDW flowing into the channel towards the surface along the negatively tilted isopycnals in the Southern Ocean, as expected from the residual meridional overturning streamfunction. It is important to note the different units in the Atlantic and Pacific sectors of these figures which in some cases mean the blue shading representing low concentration in one sector equates to a red shading representing high concentrations in the other sector. The units also change with time since the model diffuses the tracer over time and it is also spread by the advective flows, reducing its concentration.

In Fig 5.6, the tracer released at the bottom of the north Atlantic flows south through the Atlantic basin and diffuses upwards from the ocean floor. It then upwells adiabatically in the Southern Ocean (at T=222 years) and sinks in the south before flowing north through the deep Pacific. However, as predicted from the 'warm' state MOC, most of the upwelling NADW does not actually reach the surface, instead upwelling towards the surface and sinking via the anti-clockwise eddy-induced circulation in the channel. The dominant pathway taken by the tracer flowing south into the channel is into the Pacific basin along the

Pacific diffusive-driven pathway, with very little upwelling in the Southern Ocean and returning north to the Atlantic basin along the direct wind-driven pathway. This is expected given the dominance of the Pacific pathway in the 'warm' state.

The dye does not simply follow the streamlines of the flow due both to zonal asymmetries and the diffusion of the tracer in all directions, including against the flow. The diffusion is clear at T= 28 years and T= 222 years in the Atlantic basin since the dye spreads towards the surface despite the streamlines being predominantly horizontal.

In Fig 5.7, the tracer is released at a depth of 1500 m in the south of the Pacific basin at the channel-basin boundary. The tracer flows south into the channel and predominately upwells adiabatically via the upper wind-driven cell, since the global-average residual cell interface at the channel-basin boundary is 2265 m. The rapid transfer of the tracer zonally through the channel is clear from the fast transport to the Atlantic sector at T=28 years. The upwelled tracer then moves north near the surface of the Atlantic basin via the NADW cell before sinking in the north Atlantic.

An interesting and unexpected feature is the relatively high concentration of tracer located in the upper Pacific basin at T=625 years and T=958 years. While this is lower than the concentration in the north Atlantic, it is significant. This is likely due to the proximity of the tracer release site to the upper levels of the Pacific basin, with diffusion spreading it southwards. The wind-driven gyres may then trap the tracer near the surface.

Atlantic

Pacific

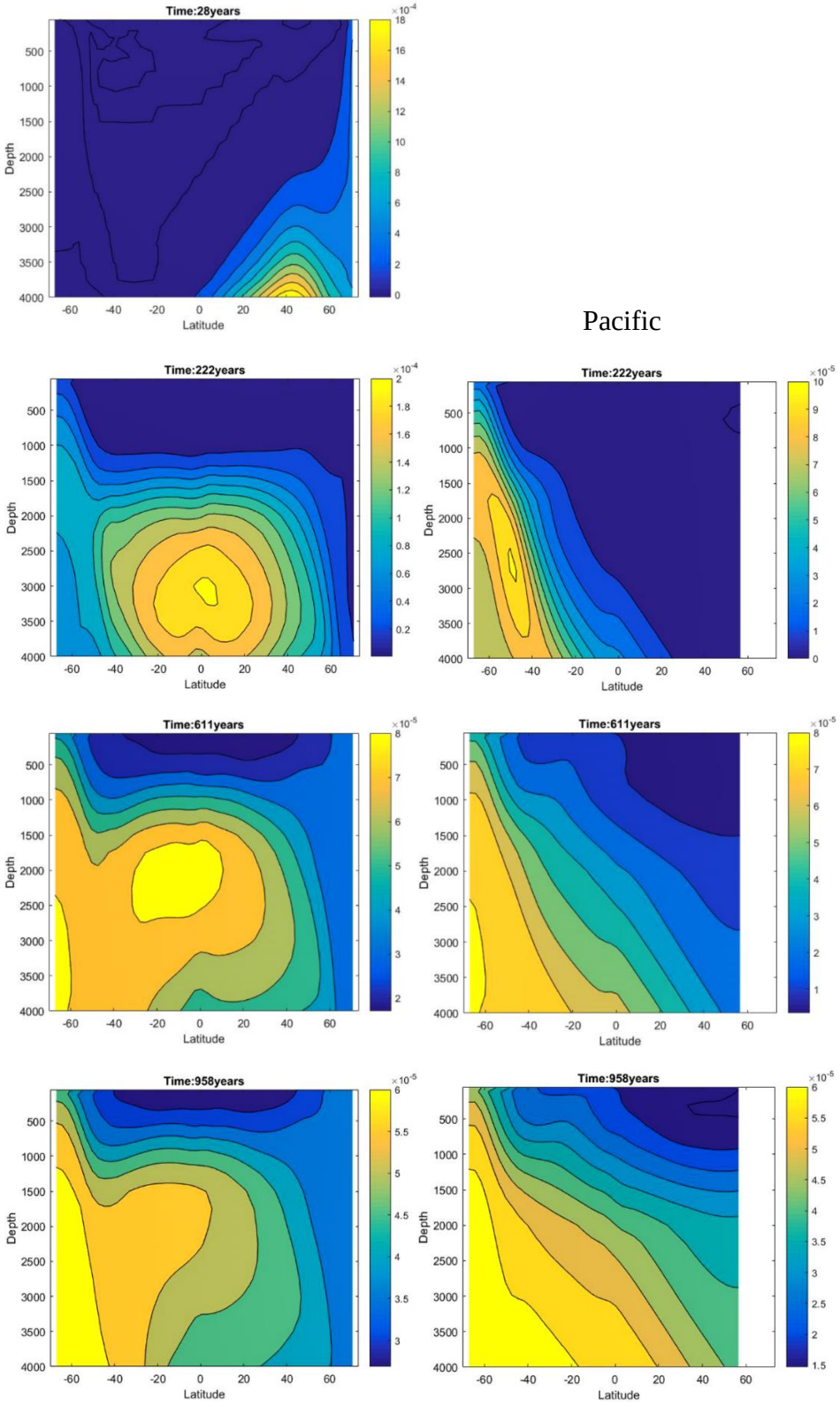

Fig 5.6: Multi-basin model 'warm' state experiment latitude-depth cross-sections showing the evolution of a passive tracer released at the bottom of the north Atlantic at time T=0 years. The Atlantic and Pacific sectors are displayed on the left and right respectively. From top to bottom the plots show the tracer distribution at 28 years,

222 years, 611 years and 958 years after release. Note: the tracer concentration scale varies in each plot and decreases over time due to the advection and diffusion of the tracer through the model. The concentration unit is taken to be [g m^{-3}], although this is arbitrary, with the initial concentration at the time of release being 1 g m^{-3}.

Atlantic Pacific

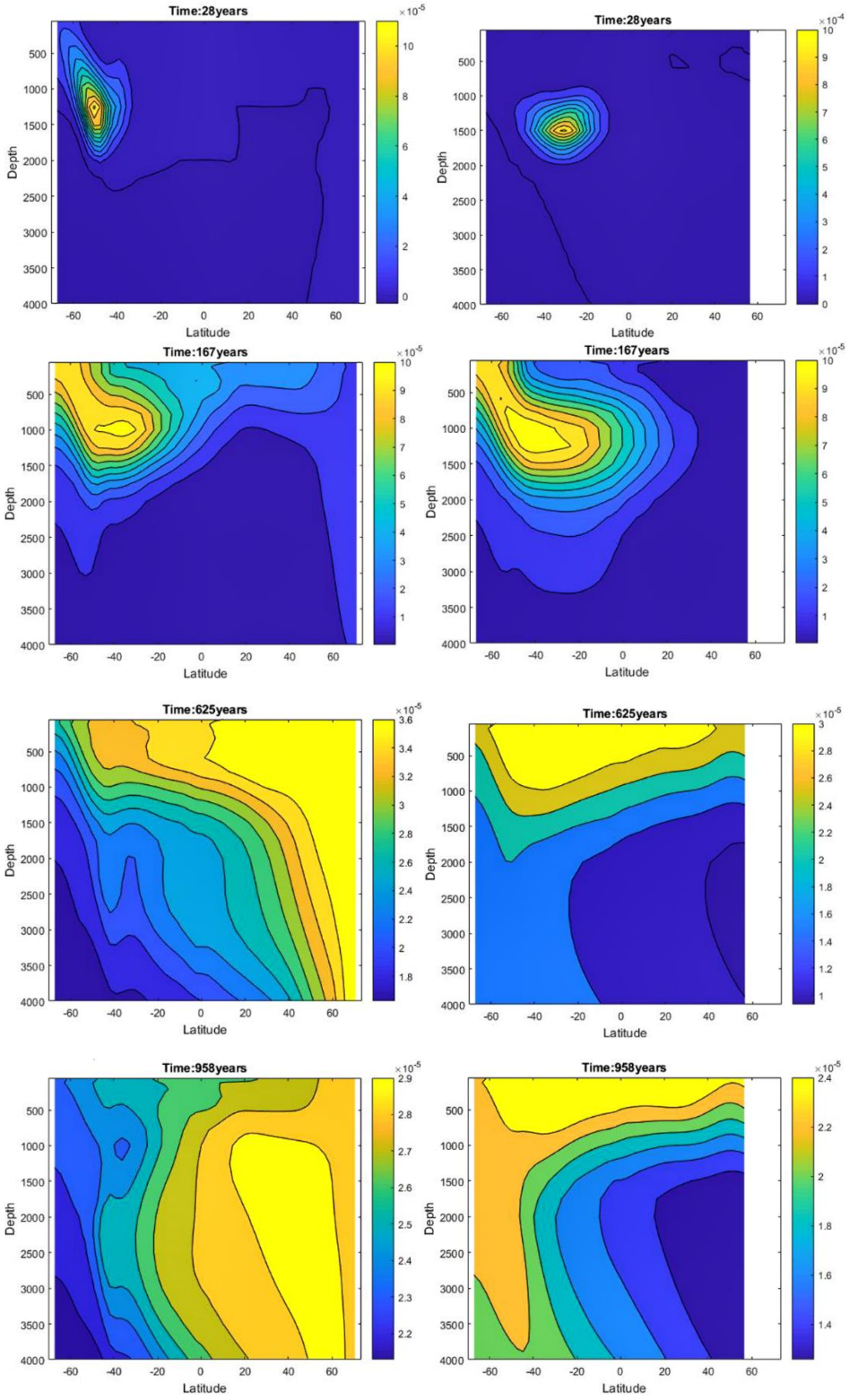

Fig 5.7: Multi-basin model ‘warm’ state experiment latitude-depth cross-sections showing the evolution of a passive tracer released at 1500 m in the south of the Pacific basin at a time, T= 0 years. The Atlantic and Pacific basins are displayed on the left and right respectively. From top to bottom shows the tracer distribution at 28 years, 167 years, 625 years and 958 years after release. Note: the tracer concentration scale varies in each plot.

A tracer release experiment was performed in the single-basin model with a -1.96°C freezing point as in the control experiment (see Fig 5.1a) with the tracer released at the ocean floor in the north of the basin (see Fig 5.8). As in Fig 5.6, the tracer is advected southwards by the NADW cell and rapidly diffused upwards. However, the NADW cell is weaker and upwells within the basin in contrast to the equivalent NADW flow in the multi-basin model which is into the channel all the way to the ocean floor. This leads to the tracer being upwelled to slightly shallower depths in the single-basin model and being transported northwards at a quicker rate. Despite this difference, the tracer transport is similar with adiabatic upwelling in the Southern Ocean. However, in contrast to the multi-basin model, a significant volume of the tracer flows north near the surface back towards the north of the basin, rather than sinking or flowing out of the Atlantic sector as in the multi-basin model. This difference is expected since in the multi-basin model ‘warm’ state most NADW flows into the channel’s lower cell and then into the Pacific basin, rather than flowing directly back into the Atlantic basin. In the single-basin model, the NADW streamfunction must connect to the upper cell in the channel to conserve volume. This explains the northerly flow of the tracer as it upwells in the Southern Ocean. However, there is also a significant volume of tracer in the channel’s lower cell in the deep Southern Ocean at T=1375 years. While, diffusion can explain some of this, it is likely that zonal variations in the flow are also responsible. There is a strong western boundary current of NADW as in the multi-basin model. This water may flow into the channel deeper than the global-average upper cell which could then return to the upper cell through upwelling in the basin.

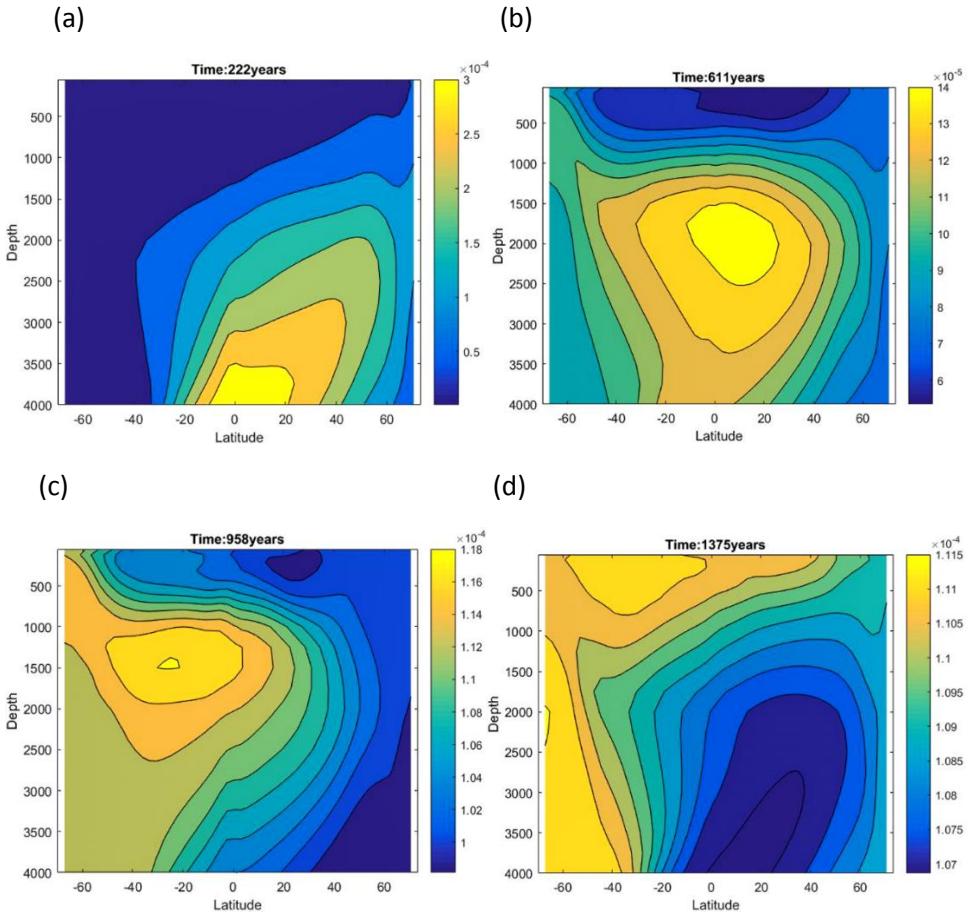

Fig 5.8: Single-basin model -1.96°C freezing point control experiment latitude-depth cross-sections showing the evolution of a passive tracer released at the bottom of the model in the far north at time, T=0 years. The tracer distribution is shown at (a) 222 years, (b) 611 years, (c) 958 years and (d) 1375 years after release. Note: the tracer concentration scale changes in each plot.

A tracer release experiment was performed in the multi-basin model using the 'warm' state sea-ice freezing point but with a zero southern channel (i.e. south of South Africa) zonal wind stress (see Fig 5.9). The MOC was shown previously in Chapter 4 in Fig 4.4a. NADW still flows into the channel all the way to the ocean floor before flowing into and upwelling in the Pacific basin. However, there is no longer a wind or eddy-induced channel circulation, with the residual circulation now approximately zero in the channel. Thus, instead of upwelling in the channel, NADW flows directly into the Pacific basin via zonal flows. This can be seen in the passive tracer plots with the tracer flowing south in the Atlantic basin upwelling by

diffusion but it is no longer pulled vertically towards the surface in the channel. The direct zonal flow into the Pacific basin is seen at T= 222 years.

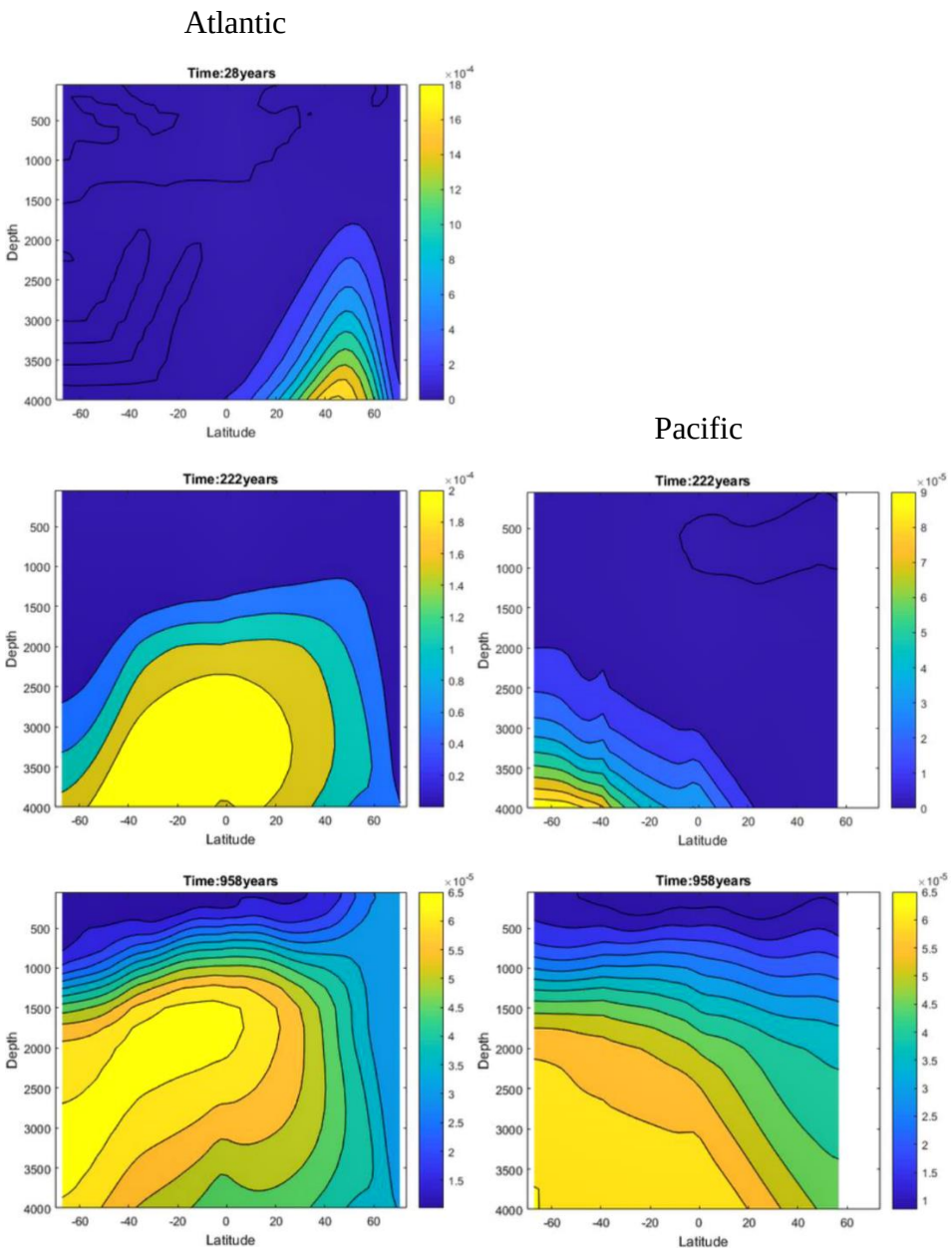

Fig 5.9: Multi-basin model 'warm' state with a zero Southern Ocean zonal wind stress experiment as in Chapter 4. Latitude-depth cross-sections showing the evolution of a passive tracer released at the bottom of the north Atlantic at time T=0 years. The Atlantic and Pacific sectors are displayed on the left and right respectively. From top to bottom the plots show the tracer distribution at 28 years, 222 years and 958 years after release.

These tracer release experiments help us to visualise the meridional overturning circulation and MOC pathways under varying forcings. It also highlights the important role played by diffusion in transporting passive tracers, in addition to the advective transport.

5.5. Conclusions

This chapter is concluded by summarising the results and answering each of the questions set out at the start of the Chapter. These are listed again below as a reminder:

- Why do single-basin models have a weaker NADW circulation than multi-basin simulations under all buoyancy forcings?
- How are single-basin models setup to attain a realistic overturning circulation, representative of the global-integrated MOC?
- How do variations in vertical ocean diffusivity, Southern Ocean winds and surface buoyancy fluxes alter the circulation in single-basin models?

The structure of the single-basin model MOC responds to varying Southern Ocean buoyancy forcing similarly to the global-average MOC in the multi-basin model simulation. The NADW cell shoals while the abyssal cell expands as Southern Ocean sea-ice formation is increased and a glacial state buoyancy forcing is approached. However, the single-basin model has a far weaker control NADW cell and the changes in strength in response to the buoyancy forcing perturbations are smaller. The NADW cell strength is significantly weaker than reality in all simulations using a realistic wind forcing and vertical diffusivity.

Model simulations were performed with varying geometries to understand the cause of the far weaker NADW cell in the single-basin model compared to the multi-basin model. A wide single-basin model with the same width as the multi-basin model generates a strong NADW cell, similar to the multi-basin model. This shows the important role played by diffusive-driven upwelling in generating a NADW cell with a realistic strength. The wider channel in

this model also leads to a stronger NADW cell due to enhanced wind-driven upwelling in the channel, although under the imposed realistic forcings this appears to play a lesser role.

In single-basin models forced by realistic external forcings (i.e. wind and buoyancy forcing), a NADW overturning with a strength similar to the present day is only obtained if an unrealistic enhanced ocean diffusivity profile is used. In the experiments performed here, this was implemented by using a constant diffusivity profile, with enhanced diffusivities in the upper ocean relative to the control, strengthening the NADW cell. This leads to a highly diffusive NADW circulation. It can also be strengthened by using an unrealistically large Southern Ocean zonal wind stress. In contrast, a lower vertical diffusivity or wind speed weaken the NADW cell.

The multi-basin model global-average (average over both the Atlantic and Pacific sectors) upper cell is highly diffusive in the 'warm' climate state, analogous to the upper NADW cell structure in the single-basin model. This similarity in structure between the multi-basin model global-average MOC and the single-basin model MOC, despite large differences in the individual basins of the multi-basin model is due to most of the NADW in this 'warm' state ultimately upwelling in the Pacific basin before returning to the Atlantic rather than upwelling along the direct wind-driven pathway. It is also due to the continuity requirement that in the global-average and the single-basin model, the upper cell in the channel must connect with the upper cell to the north of the channel with no overlap between the upper and lower cells. The actual structure of the NADW cell in the Atlantic basin of the multi-basin model differs substantially from the single-basin model, with a largely adiabatic flow into the channel.

Tracer release experiments help us to visualise the pathways taken by the MOC and how these differ between single and multi-basin models. The inter-basin transport in the multi-

basin model was shown, with the main pathway of NADW entering the channel flowing into the Pacific basin after adiabatic upwelling and transformation in the Southern Ocean in the 'warm' climate state. In contrast, in the single-basin model under the same buoyancy forcing, the NADW upwells adiabatically in the channel before flowing back to the north at the surface into the Atlantic basin. However, a significant concentration of tracer also sinks in the south of the basin entering the lower cell. This is unexpected and shows the importance of zonal asymmetries in the flow and diffusion when considering the transport of tracers through the ocean.

Chapter 6

Variations in atmospheric CO_2 and the carbon cycle during MOC transitions

This chapter analyses the variations in atmospheric CO_2 which occur during the buoyancy driven changes in the MOC described in Chapter 3 and also compares the changes in the single and multi-basin model. This will enable us to understand how changes in the MOC contribute to glacial-interglacial variations in atmospheric CO_2. The results in this section are currently minimal due to encountering a number of difficulties setting up the biogeochemistry model (based on Lauderdale et al. [2013] but updated with recent changes to the MITgcm) described in Chapter 2. A number of figures showing the change in some of the biogeochemical quantities are provided, although further analysis is needed to determine the contribution these changes have on the atmospheric CO_2 variation.

This chapter is structured as follows; firstly the main differences in the forcings and thus MOC in this biogeochemistry setup of the model are described, followed by a description of the biogeochemical tracer distributions in the control state. The change in these biogeochemical variables with perturbations to the buoyancy forcing and the transition to a glacial state is then briefly described. The accompanying changes in atmospheric CO_2 are also described. Finally, a comparison with the single-basin model experiments is made.

6.1. Comparison with the original setup

The response of the NADW cell strength in this biogeochemistry setup of the multi-basin model to the same variations of the sea-ice freezing point as in Chapter 3 is smaller, varying by only ~5.1 Sv from ~14.2 Sv in the 'warm' state (-1.96°C freezing point) to ~9.1 Sv in the glacial state (1°C freezing point). This is due to a change in the salinity boundary conditions, with both the salinity surface relaxation and net freshwater flux (i.e. neglecting the relaxation term) globally balanced at each time step to ensure the salinity is globally conserved, rather than simply relying on the salinity relaxation to prevent the salinity drifting significantly. Thus, the virtual salinity flux and hence the virtual flux of dissolved inorganic carbon (DIC) and total alkalinity (TA) (see Chapter 2.14) are globally conserved.

The main change in the NADW cell structure is a reduction in Atlantic basin upwelling in the 'warm' state, weakening the NADW cell under this buoyancy forcing relative to the 'warm' state MOC in Chapter 3 by ~5 Sv. The main changes in the pathways and thus strength of the MOC as the sea-ice freezing point and thus Southern sea-ice formation rate is increased is very similar to Chapter 3, with the exception of the changes in Atlantic upwelling. In particular, the interaction between the upper and lower cells, with these cells becoming isolated in the glacial state is still simulated. This is likely to play a key role in the variation of atmospheric CO_2. The MOC in these model simulations is not shown since it is very similar to the changes in Chapter 3 for the multi-basin model. The changes in the MOC of the single-basin model in this modified setup is also very similar to those described in Chapter 5, with a slight weakening and shoaling of the NADW cell as the sea-ice freezing point is increased.

The experiments performed here use a strong temperature relaxation to the monthly surface temperature fields obtained from the future 'warm' state experiment in Chapter 3, with the

temperature relaxation field held at these values regardless of the perturbations to the sea-ice freezing point made in this chapter. This ensures the temperature induced solubility effect is approximately zero in the model. By using a strong relaxation to the monthly varying surface temperature field ensures the seasonal changes in temperature and thus sea-ice are still captured by the model. This is particularly important given the important effect sea-ice has on biological production and air-sea CO_2 exchange.

6.2. Present-day control Experiment

The multi-basin model control experiment representative of the present-day state is obtained using a sea-ice freezing point of 0°C as in Chapter 3. The model is spun up over more than 10,000 years to allow the ocean carbon cycle to reach a steady equilibrium state. In this case, the control has an equilibrated atmospheric CO_2 of ~246 ppm. Although this is significantly lower than the pre-industrial atmospheric CO_2 concentration of ~278 ppm, the changes in CO_2 in response to perturbations in the buoyancy forcing are likely to be similar (perhaps slightly smaller). The structure of the Atlantic basin MOC in this control state is similar to the present-day. The NADW cell strength is ~12.8 Sv (smaller than the same freezing point in Chapter 3 as described in Section 6.1), with a significant overlap between the NADW cell and the channel's lower cell at the channel-basin boundary. Thus, a large volume of NADW flows into the channel's lower cell and consequently into the Pacific basin along the Pacific diffusive-driven pathway. There is also a significant volume of NADW upwelled along the wind-driven pathway, flowing back into the Atlantic basin after upwelling in the channel.

6.2.1. DIC, PO_4 and O_2 distributions

The biogeochemical tracers simulated in the setup used here are DIC, TA, PO_4, DOP and O_2 as described in Chapter 2, with the distribution of DIC and PO_4 in this control experiment at the surface and in latitude-depth space shown in Fig 6.1 and Fig 6.2 respectively.

The DIC and PO_4 concentrations at the surface increase polewards of the equator with the highest values in the Southern Ocean and the DIC also has high concentrations in the North Atlantic (see Fig 6.1). In latitude-depth space, the concentrations of DIC and PO_4 are low above 500 m except in the Southern Ocean. They increase southwards throughout the Atlantic below about 500 m, with maximum values of DIC and PO_4 of ~2.25 mol m^{-3} and ~1.8 mmol m^{-3} respectively in the Southern Ocean (see Fig 6.2a and c). In contrast to the Atlantic, the DIC and PO_4 concentrations increase to the north throughout the Pacific below about 500 m, with maximum values in the North Pacific of ~2.32 mol m^{-3} and ~2.5 mmol m^{-3} respectively (see Fig 6.2b and d).

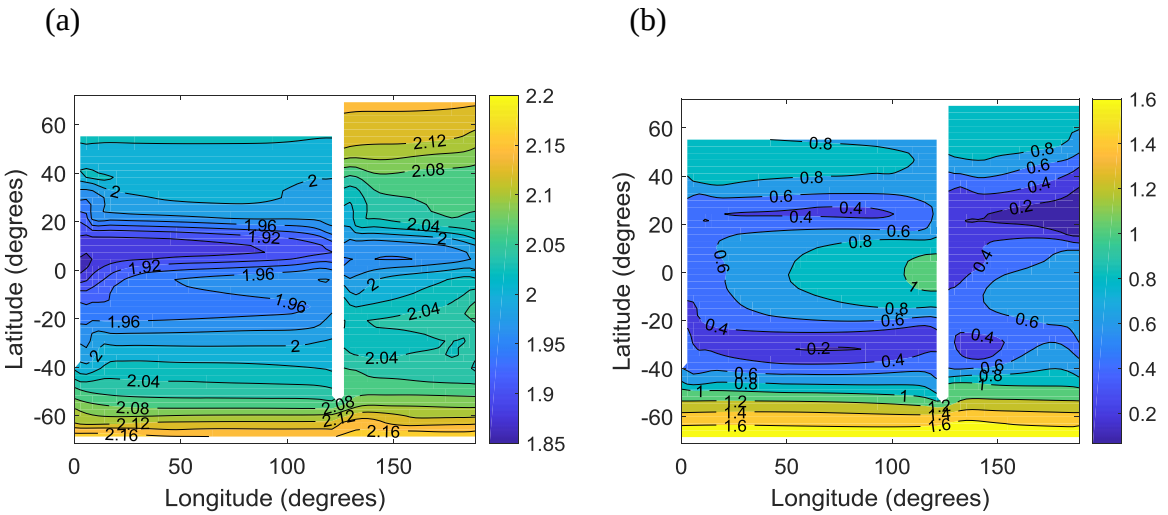

Fig 6.1: Surface distribution of (a) DIC (mol m^{-3}) and (b) PO_4 (mmol m^{-3}) in the present-day control experiment.

The modelled distribution of DIC and PO_4 can be explained by the structure of the MOC, biological productivity and remineralisation of organic matter as they are transported through the ocean, and also solubility effects. The MOC has a significant control on the distribution of these tracers, since it determines the transport pathway of these tracers from the surface, into and through the ocean interior, with the gradual remineralisation of organic matter as the waters flow through the interior.

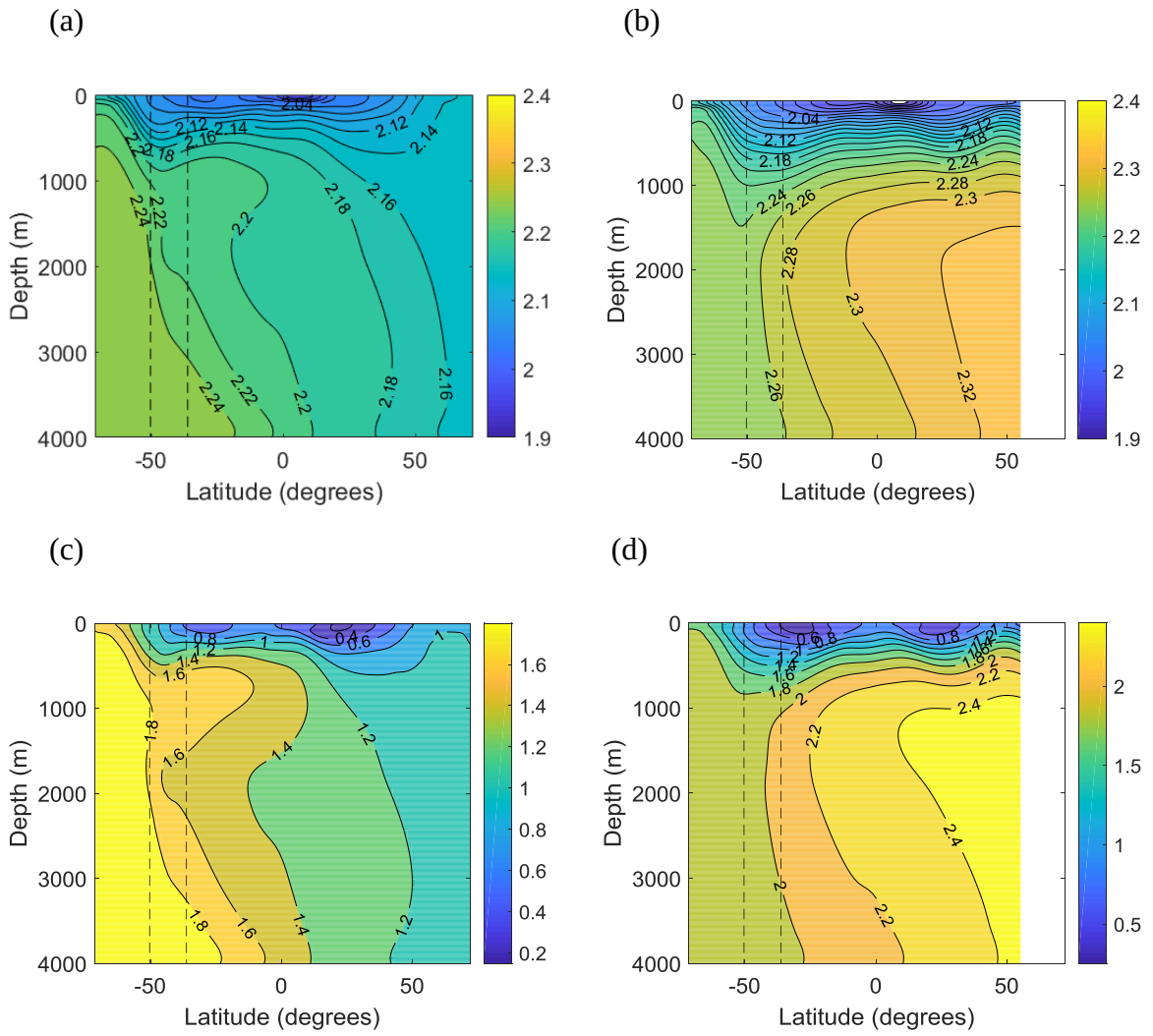

Fig 6.2: Zonally-averaged (over the Atlantic sector (left) and Pacific sector (right)) latitude-depth sections of (a),(b) DIC (mol m^{-3}), and (c),(d) PO_4 (mmol m^{-3}) in the present-day control experiment.

The transport of DIC (and nutrients (e.g. PO_4)) to the deep ocean due to biological productivity is known as the biological pump (Volk and Hoffert [1985]) with the soft-tissue and carbonate pump components due to the transport of organic carbon and calcite respectively into the deep ocean.

At the surface, the DIC and PO_4 distributions are similar although there are some differences. As described above, the highest values of both DIC and PO_4 are in the Southern Ocean. The North Atlantic and North Pacific also have higher concentrations than the subtropics, with DIC significantly higher in the North Atlantic than the North Pacific (Fig 6.1a). The large

increase of DIC at the surface of the North Atlantic is due to enhanced solubility as the surface temperature decreases towards the poles, increasing the uptake of atmospheric CO_2.

The high concentrations of both DIC and PO_4 at the surface of the Southern Ocean but lower values in the North Pacific are explained by the remineralisation of organic matter. In the zonally-averaged latitude-depth sections, the DIC and PO_4 concentration increases as NADW moves southwards through the Atlantic basin interior due to the remineralisation of organic matter, with enhanced concentrations at the surface in the Southern Ocean due to the wind-driven upwelling of NADW in this region. As discussed in Chapter 2, a significant volume of the NADW in the present-day flows south near the surface where it forms AABW and flows into the Pacific basin. However, only a proportion of the NADW actually appears to be exposed at the surface, and thus the concentration of DIC remains high in AABW (rather than being reset to be in equilibrium with the atmosphere). The AABW which does reach the surface and flows southwards is also believed to be underutilised by biological production since it flows southwards and forms AABW before biological production has enough time to utilise the DIC and PO_4 (Watson et al. [2015]). Sea-ice also likely plays a role in reducing the outgassing of carbon rich deep waters to the atmosphere. The DIC and PO_4 continue to increase as the AABW moves north through the deep Pacific basin, leading to a maximum value in the deep North Pacific.

The DIC and PO_4 distributions provide a reasonable approximation to the World Ocean Circulation Experiment (WOCE) transects of the Atlantic and Pacific Oceans. However, one notable discrepancy in our model is the surface DIC and PO_4 in the North Atlantic is too high compared to the observations. Although, it increases in the real world North Atlantic, the increase is too high. The WOCE transects show a significant vertical gradient in these tracers near the surface of the North Atlantic whereas Fig 6.2 shows only a very small vertical

gradient. This suggests the water is well mixed in this region. While this is expected due to NADW convection, it is likely the surface productivity is not high enough, at least in this region, which leads to almost no vertical gradient in these tracers due to the removal of DIC and PO_4 by biological productivity being too small. This lack of a vertical gradient is also seen in the preformed PO_4 described in Section 6.2.2 with a large outcropping of the contours in the North Atlantic. Further work will be needed to ensure these tracer distributions are representative of the real world ocean, and to ensure the productivity is set realistically since this will have a significant impact on the variations in atmospheric CO_2.

The Apparent Oxygen Utilisation (AOU) is also plotted in Fig 6.3. This helps us track the respiration and remineralisation of organic matter as the water masses move through the ocean since O_2 is used in this process. Therefore, the AOU distribution has a very similar structure to the DIC and PO_4 in Fig 6.2, with the AOU increasing in the Southern Ocean and deep Pacific basin (Fig 6.3b) as organic matter is respired, and thus O_2 becomes depleted.

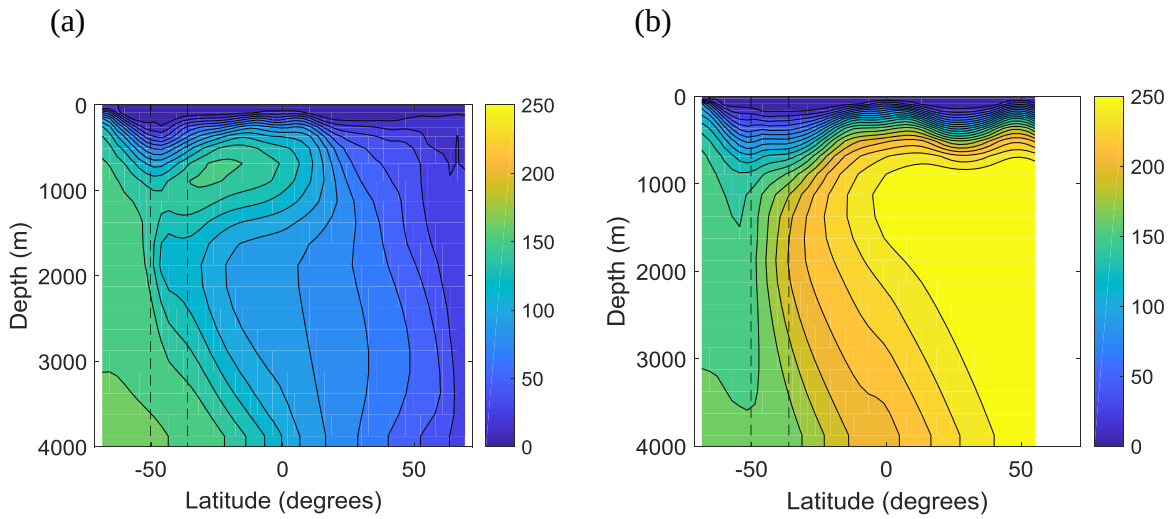

Fig 6.3: Zonally-averaged (over (a) the Atlantic sector (left) and (b) the Pacific sector (right)) latitude-depth sections of Apparent Oxygen Utilisation (AOU) [mmol m^{-3}] in the present-day control experiment. The surface is assumed saturated with O_2 relative to the atmosphere. Contour intervals of 12.5 mmol m^{-3}.

6.2.2. Preformed and regenerated PO_4

The phosphate (PO_4) concentration can be separated into the preformed and regenerated components, P_{pre} and P_{reg} respectively. The regenerated component is the PO_4 utilised during biological production which is later remineralised. The preformed PO_4 is the component which is transported through the ocean without being converted by biological production to organic matter. The efficiency of the soft-tissue pump (P*) can be obtained from the ratio of the regenerated PO_4, $P_{reg,}$ to the total PO_4, P_{tot}, following the method of Ito and Follows [2005]:

$$P^* = \frac{P_{reg}}{P_{tot}} \tag{6.1}$$

with the maximum efficiency being reached when P* = 1.

The regenerated PO_4 is calculated from the AOU as follows:

$$P_{reg} = r_{P:O2}\, AOU \tag{6.2}$$

where $r_{P:O2}$= 170 is the Redfield ratio of PO_4 to O_2.

The preformed PO_4 is then calculated as the residual of the total and regenerated PO_4. The distributions of P_{reg} and P_{pre} are plotted in Fig 6.4. As expected, P_{reg} has the same spatial pattern as the AOU (and DIC and PO_4) (Fig 6.4a and b). The P_{pre} has a very different distribution with the highest values at the surface of the Southern Ocean. This is as expected from observations with the Southern Ocean underutilising the nutrients (Watson et al. [2015]) during biological production and thus the soft-tissue pump has a low efficiency in the present-day in this region of the model.

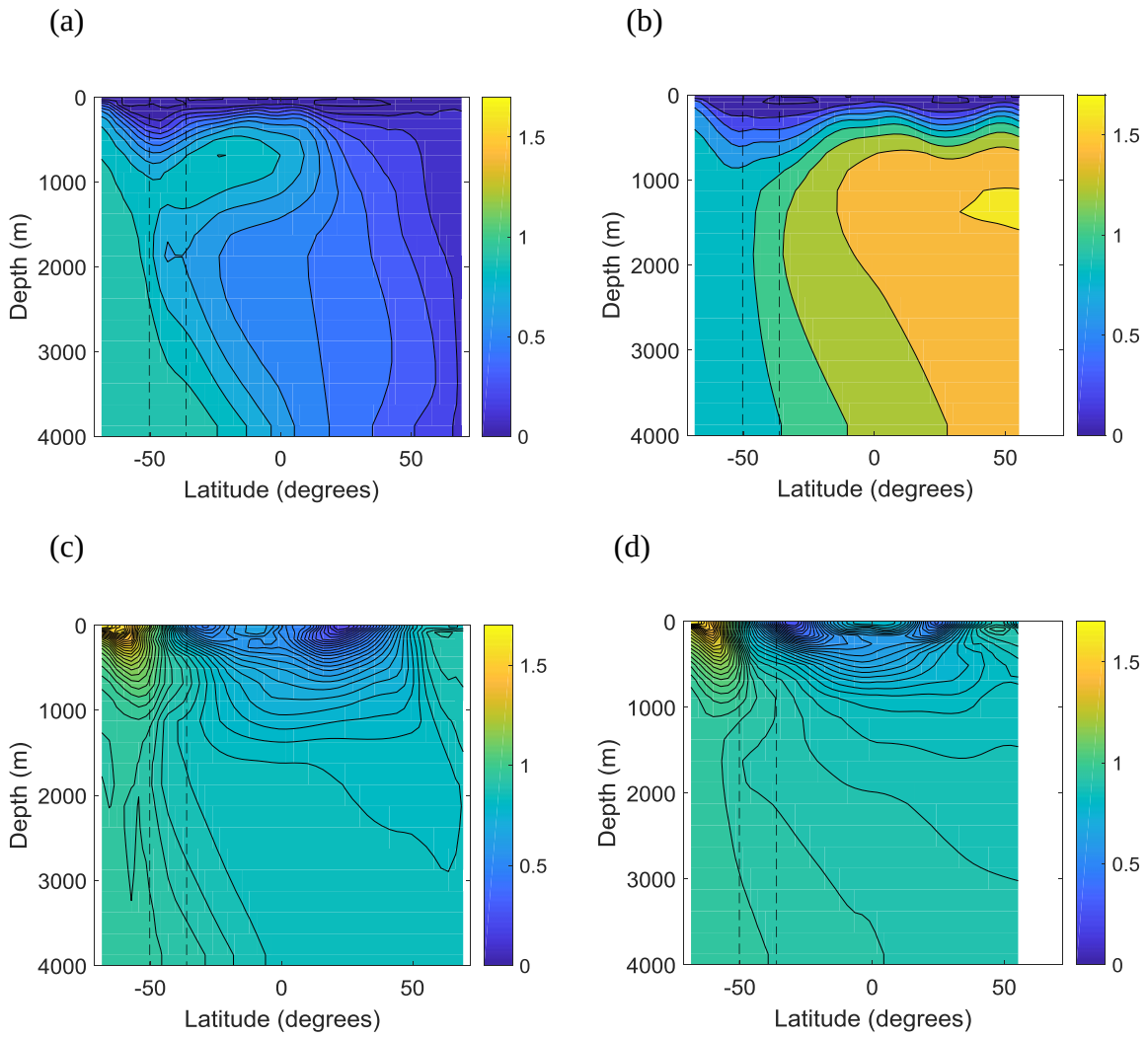

Fig 6.4: Zonally-averaged (over the Atlantic sector (left) and Pacific sector (right)) latitude-depth sections of (a),(b) regenerated phosphate, P_{reg} [mmol m^{-3}], and (c),(d) preformed phosphate, P_{pre} [mmol m^{-3}] in the present-day control experiment. Contour intervals of 0.05 mmol m^{-3}.

6.2.3. Air-sea CO_2 flux

The air-sea CO_2 flux controls the atmospheric CO_2 concentration by determining the exchange of CO_2 between the atmosphere and ocean. The annual-average air-sea CO_2 flux is plotted in Fig 6.5a and b. The air-sea CO_2 flux is negative (i.e. there is a net CO_2 outgassing by the ocean) in the warmer equatorial and subtropical regions, whereas the flux becomes positive (i.e. there is a net uptake of CO_2 by the ocean) towards the poles, especially in the North Atlantic (see Fig 6.5b). The southern channel absorbs CO_2 over most of the latitude range in the zonal-average, only becoming negative in the far south. However, there is large

zonal variation and particularly high values at the boundaries between the Atlantic and Pacific sectors. This is primarily due to the large zonal surface temperature gradients at these longitudes due to the Atlantic and Pacific temperature forcing being different.

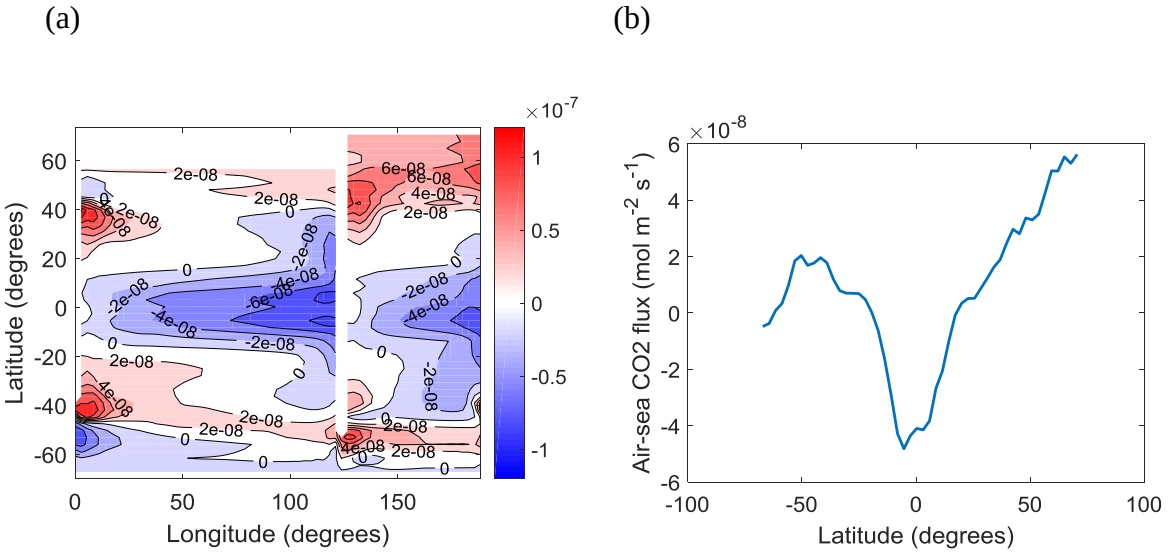

Fig 6.5: Annual-average air-sea CO_2 flux [mol m^{-2} s^{-1}] in the multi-basin model present-day control experiment for (a) latitude-longitude surface flux distribution, and (b) zonally-averaged flux against latitude.

6.3. Buoyancy flux perturbation experiments

6.3.1. Atmospheric CO_2 variations

The atmospheric CO_2 decreases by ~14 ppm to ~232 ppm when the sea-ice freezing point is increased from 0°C to 1°C, during which the MOC transitions to a glacial state (with an isolated NADW cell). In contrast, the atmospheric CO_2 increases by ~20 ppm to ~266 ppm when the sea-ice freezing point is reduced from 0°C to -1.96°C which transitions the MOC to a 'warm' state. The cause of these changes in CO_2 is an area I am currently investigating, although a few figures showing the change in tracer distributions in the glacial state are now shown.

6.3.2. Glacial state tracer variations

The variation in DIC and PO_4 between the present-day and glacial states are shown in Fig's 6.6 and 6.7. The main change in the surface distributions is a decrease in DIC and PO_4 over most of the domain. However, the decrease is greatest for PO_4 in the North Atlantic (perhaps due to a reduced northward flow of NADW), and there is an increase in DIC and PO_4 in the far south of the model. This increase is likely due to the increased upwelling of AABW to the surface in this region due to a northward shift in the upwelling of AABW.

The pattern of change in the zonal-average DIC and PO_4 concetrations in latitude-depth space is similar, with an increase in the deep North Atlantic (Fig 6.7a and c) and a decrease in the upper Atlantic and Pacific basins. The increase in the deep North Atlantic is most likely due to the expansion of the lower cell in this region as the NADW cell is shoaled.

(a) (b)

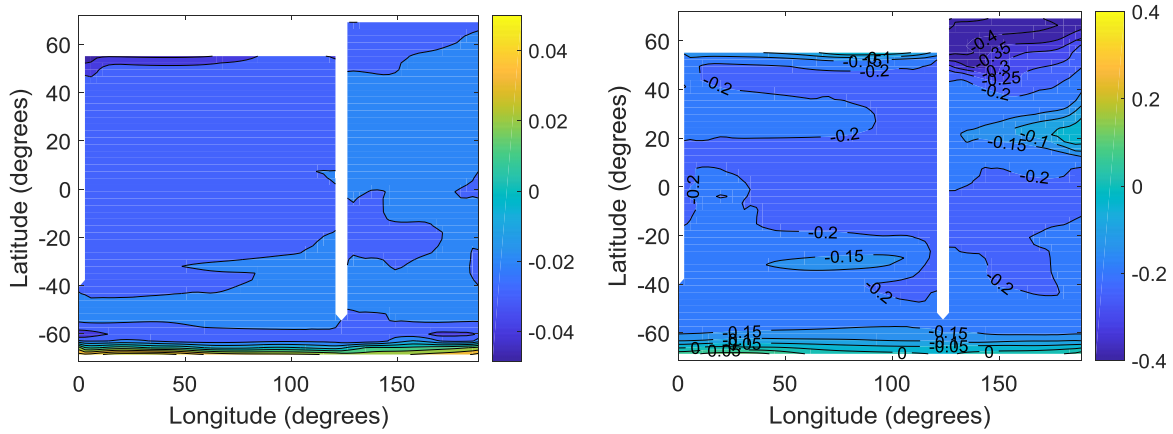

Fig 6.6: Surface distribution of the perturbation in (a) DIC (mol m^{-3}) and (b) PO_4 (mmol m^{-3}) in the glacial state experiment relative to the present-day state in Fig 6.1.

The importance of sea-ice in reducing biological production and also air-sea exchange of CO_2 needs to be analysed. To investigate the effect of sea-ice on atmospheric CO_2, the sea-ice concentration in the control was increased to one (i.e. 100% sea-ice cover) between 70°S and 50°S in the biogeochemistry model. The original sea-ice distribution (i.e. simulated by the

sea-ice model) is still used in the physical model, and thus the MOC remains unchanged. The atmospheric CO_2 increases by ~22 ppm suggesting that enhanced Southern Ocean sea-ice cover increases atmospheric CO_2 when the ocean circulation does not change. This is expected since the zonal-average air-sea CO_2 flux is positive over most of this region (Fig 6.5b) and sea-ice also blocks sunlight, preventing biological production under the sea-ice. However, this is an extreme case both in sea-ice concentration and in latitudinal sea-ice coverage. The results may be very different under more realistic changes in sea-ice.

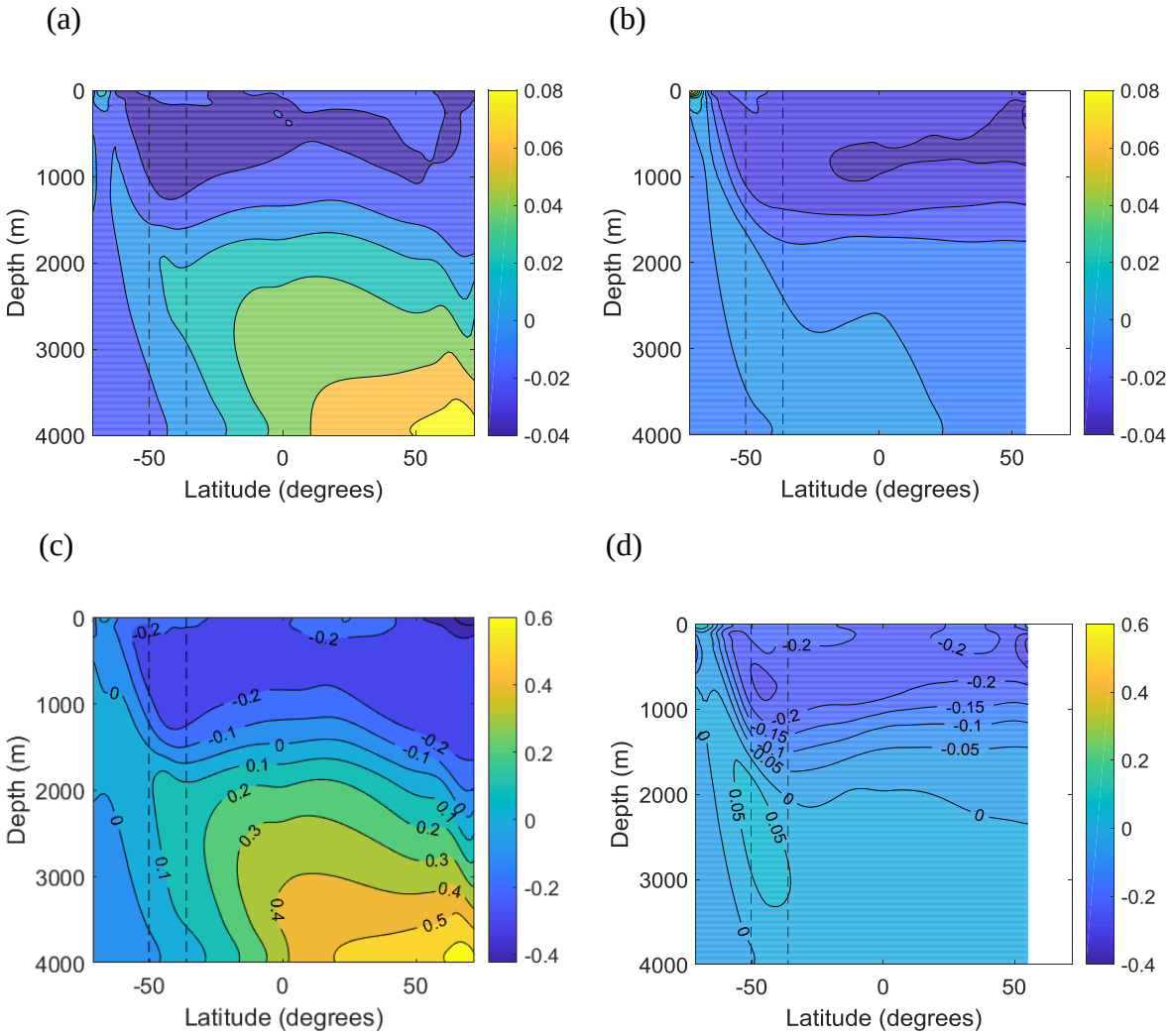

Fig 6.7: Zonally-averaged (over the Atlantic sector (left) and Pacific sector (right)) latitude-depth sections of the perturbation in (a),(b) DIC (mol m^{-3}), and (c),(d) PO_4 (mmol m^{-3}) in the glacial state experiment relative to the present-day state in Fig 6.2.

6.4. Single-basin model experiments

The tracer distributions in the single-basin model simulations are yet to be analysed. However, the decrease in atmospheric CO_2 for an increase in the sea-ice freezing point from -1.96°C to 1°C is only ~7 ppm from ~272 to ~265 ppm (i.e. ~27 ppm less than the corresponding change in the multi-basin model). This is despite the atmospheric box being scaled proportionally to the ocean volume in the models. This large difference is perhaps not surprising given the NADW cell is far weaker than reality in the single-basin model implemented here, with only a small weakening of ~2.8 Sv between the 'warm' and glacial states. Although, the NADW cell can be strengthened by enhancing the vertical diffusivity (as shown in Chapter 5), for a true comparison between these model setups, the diffusivity has been kept the same. The other major difference is the pathways taken in the single-basin model necessitate the NADW cell to be separated from the lower cell to conserve volume. The relative importance of these differences will be analysed in future work.

6.5. Conclusions

The buoyancy driven changes in the multi-basin model due to enhanced Southern Ocean sea-ice formation is shown to have a significant impact on atmospheric CO_2, with an increase of ~34 ppm between the 'warm' state and glacial state experiments. The exact cause of this change is being investigated, although the changes in sea-ice, biological production (and soft-tissue pump efficiency) and changes in the structure of the MOC are likely to play a key role.

In contrast, the single-basin model atmospheric CO_2 increases by only ~7 ppm for the same change in the sea-ice freezing point as in the multi-basin model. This far lower increase in CO_2 is likely due to differences in the structure of the MOC between single and multi-basin models discussed in Chapter 5.

Chapter 7

Semi-analytical model of the Bottom and Upper Cells of the Atlantic (SAMBUCA)

7.1. Introduction

In addition to the MITgcm used in previous chapters, a far simpler semi-analytical model of the ocean is also used to investigate glacial-interglacial cycle changes in the MOC and climate system. This work was carried out during the start of my PhD with the ambition of modifying the Semi-analytical Model of the Bottom and Upper Cells of the Atlantic (SAMBUCA) (Nikurashin and Vallis [2011; 2012]) to create a simplified semi-analytical Earth System Model (ESM). The model would include the major climate feedbacks believed to be responsible for the glacial-interglacial transitions in climate. These include the ice-sheet albedo feedback and the greenhouse feedback. The aim was to simulate the glacial cycle changes in ocean circulation and consequent changes in atmospheric CO_2 and climate in response to changes in solar radiation i.e. the Milankovitch Cycles. The small perturbation to the climate system and ocean circulation through this change could then lead to a transition to a glacial state via the aforementioned climate feedbacks and further changes in ocean circulation.

Although the aim of simulating glacial cycle changes in climate, ocean circulation and atmospheric CO_2 via these feedbacks was not attained, some interesting findings regarding the effect of orbital parameter variations and the ice-sheet albedo effect were obtained. In addition, a mechanism to transition the MOC to a glacial state via enhanced Southern Ocean

sea-ice formation and thus brine rejection was proposed and tested through very simple changes in the Southern Ocean buoyancy boundary conditions. This mechanism was published by Jansen and Nadeau [2016], and validated by their model results using the far more complex and realistic MITgcm. The SAMBUCA model simulates similar changes in the MOC via this mechanism (see Section 7.5.3), with these findings reached independently of Jansen and Nadeau [2016], prior to its publication.

The advantage of using a simpler model is the results are easier to interpret since fewer processes are accounted for in the model, and model runs are therefore far faster than a GCM. The proposed mechanism of enhanced sea-ice formation to transition the MOC to a glacial state used in the MITgcm simulations discussed in previous chapters is an example of how simple models can be used alongside the more complex GCM's to further our understanding.

SAMBUCA was created to develop a theory of the ocean's stratification and MOC (Nikurashin and Vallis [2011; 2012]) in which it was used to obtain scaling relations for the stratification and overturning strength under varying wind and diffusivity limits. More recently it was modified to include a carbon cycle with an atmospheric box to obtain glacial-interglacial atmospheric CO_2 variations through changes in Southern Ocean buoyancy fluxes (Watson et al. [2015]). A similarly structured model following on from SAMBUCA has also been used by Burke et al. [2015] to simulate the change in radioactively decaying tracer in the ocean in response to MOC changes. This enables them to investigate the 'mid-depth age bulge' in radiocarbon in the glacial South Atlantic Ocean.

The results from this work were limited and thus only a summary of the changes made to the model is provided here before the results are described.

7.2. Energy Balance Model

An energy-balance model (EBM) has been developed to provide the surface heat flux boundary condition in SAMBUCA. The use of an EBM rather than fixed temperature boundary conditions enables the effect of changes in the solar forcing (due to Milankovitch orbital variations) to be investigated. It also provides the potential for a greenhouse and ice-sheet albedo feedback to be added to the model, which would be required to simulate the glacial cycles. The coupling of SAMBUCA to an EBM (described in Section 7.3) also makes the simulations more realistic since changes in ocean circulation and consequent temperature changes are then able to interact with the atmosphere, changing the heat fluxes as in the real world.

The EBM used has been developed from scratch and it is based on several previous EBM's. The main structure of the EBM is based on the ocean-atmosphere EBM described by Vallis in Chapter 1 of "Stochastic Physics and Climate Modelling" (Palmer and Williams [2010]). This model is based on previous EBM's, notably the original Budyko-Sellers EBM (Budyko [1969]; Sellers [1969]), but with an atmosphere added (i.e. with a latitude and time dependent atmospheric temperature) to parameterise the present-day greenhouse effect, rather than choosing radiative constants to be used in the surface radiative flux calculation to parametrise it. This is more realistic and would enable a time dependent greenhouse forcing in response to changes in atmospheric CO_2 to be added more easily. The model created also has a latitude dependence as in the Budyko-Sellers model and thus a meridional diffusive heat transport is included in the models atmosphere. The solar constant has been set such that it can be made time dependent i.e. to add seasonality (North and Coakley [1979]) and it is dependent on the Earth's obliquity and eccentricity (McGehee and Lehman [2012]).

The EBM generates a realistic latitudinal variation in the zonal-average atmospheric and surface temperatures (when the surface is taken to have zero heat capacity). This realistic atmospheric and surface temperature distribution is set as an initial condition when the EBM is coupled to SAMBUCA to prevent the model becoming unstable.

7.3. Coupling of the EBM to SAMBUCA

The EBM will now provide the surface heat flux boundary conditions rather than using a restoring temperature north of the channel and an imposed buoyancy flux in the channel, as in the Watson et al. [2015] version of the model.

SAMBUCA is a single-basin model with a southern circumpolar channel, described in detail in Nikurashin and Vallis [2011; 2012]. The model uses theoretical assumptions to quantify the upper and lower cells of the MOC, and the deep stratification under varying surface forcing and diffusivity. The model accounts for the effects of Southern Ocean winds, mesoscale eddies and vertical diffusivity with the dynamics treated differently in three regions; the southern channel, main ocean basin and the northern convective region. A schematic of SAMBUCA is shown in Fig 7.1, with the main ocean processes in the three aforementioned regions depicted.

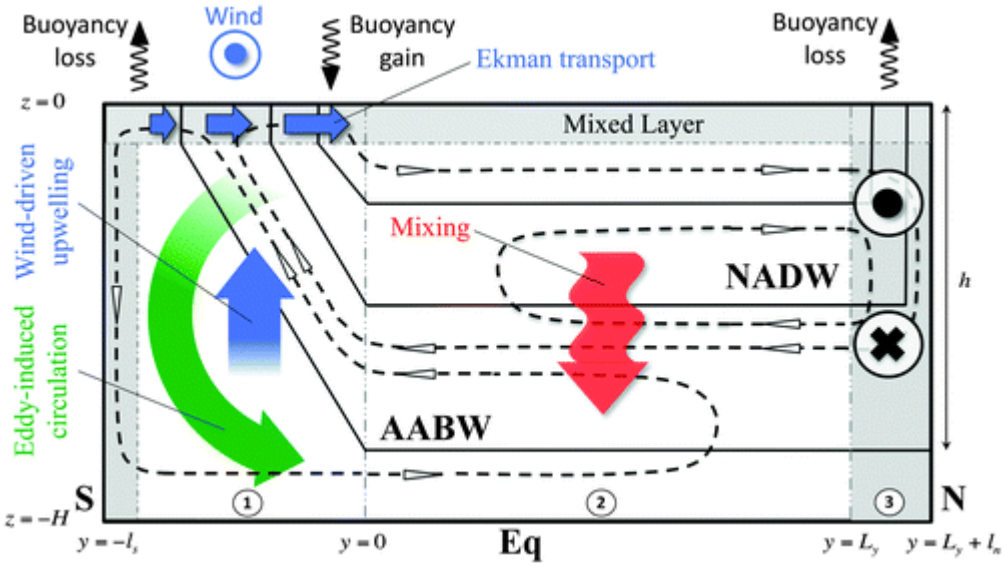

Fig 7.1: SAMBUCA model schematic taken from Nikurashin and Vallis [2012] with the three dynamical regions labelled, (1) the Southern channel, (2) the main ocean basin and (3) the northern convective region. The dashed lines are the residual streamlines of the MOC and the solid lines are isopycnals.

The model is based on the equations of motion and the buoyancy evolution equation, using the Transformed Eulerian Mean (TEM) theory (Andrews and McIntyre [1976; 1978]) which enables the equations to be written in terms of a residual overturning streamfunction. The model simulates the residual circulation in the southern circumpolar channel, as in Marshall and Radko [2003], with a balance between the wind-driven and eddy-induced circulations. At high northern latitudes where isopycnals outcrop, the NADW overturning strength is determined from the meridional buoyancy gradient via the thermal wind balance, while its depth is attained by calculating the depth of the highest density isopycnal at the northern edge of the southern circumpolar channel, which outcrops in the north of the basin.

The dependence of the abyssal and mid-depth overturning cells and deep stratification on various parameters in the wind and mixing-driven limits was explored by Nikurashin and Vallis [2011; 2012]. The scalings obtained using the theoretical model for the streamfunction and stratification are consistent with simulations using a course-resolution ocean GCM.

The abyssal circulation is dependent on the strength of the vertical diapycnal mixing in the ocean basin to the north of the southern channel, while the deep stratification is primarily dependent on the relative strength of the wind and eddies in the southern channel, since they determine the slope of the isopycnals in the channel (Nikurashin and Vallis [2011]).

In simulations with an abyssal and mid-depth cell (representative of the present-day Atlantic Ocean) in Nikurashin and Vallis [2012], the dependence of the mid-depth circulation and stratification on the model parameters was investigated. In a wind-driven limit (i.e. small diapycnal diffusivity, representative of the modern ocean), the mid-depth circulation scales with the wind stress over the Southern Ocean, while the mid-depth stratification depends on

the wind stress and the rate of deep water formation in the northern convective region. In a mixing-driven limit, the mid-depth circulation and stratification are dependent on the diapycnal diffusivity and the rate of deep water formation (Nikurashin and Vallis [2012]).

The coupling of the EBM to SAMBUCA must be considered separately in the three different dynamical regions of the model, as described in the following subsections. The SAMBUCA model code is changed in the surface mixed layer equations but remains unchanged below this depth.

7.3.1. Southern channel

In this region between 50°S and 70°S in which there are no meridional boundaries, the overturning is determined from the net effect of the wind-driven and eddy-induced circulations. A surface buoyancy flux alters the surface mixed layer buoyancy, along with buoyancy advection and diffusion. In the original SAMBUCA model (Nikurashin and Vallis [2011; 2012]) the buoyancy flux was imposed as a relaxation boundary condition to an imposed buoyancy distribution. This was updated in Watson et al. [2015] to investigate the effect of changes in the buoyancy fluxes by imposing a buoyancy flux here which is set as an initial condition and fixed. In the modified version, the buoyancy fluxes in this region are now calculated by the EBM at every model time step by converting the calculated rate of change in surface temperature to a buoyancy flux using the linear equation of state (there is no salinity variable in the original SAMBUCA model, although I have added this to the modified model as described later).

The EBM's atmosphere and the surface layer of SAMBUCA are therefore coupled with changes in the atmospheric temperature altering the surface temperature and vice-versa, through changes in the radiative fluxes.

7.3.2. Main ocean basin

In this region of the model, the isopycnals are assumed to be flat, extending north from the northern boundary of the southern channel. This is similar to observations of the ocean's density (e.g. World Ocean Circulation Experiment (WOCE) meridional ocean sections). In this region, an advective-diffusive balance is assumed for the buoyancy in the vertical while the meridional advection is zero due to the isopycnals being horizontal. However, in order to determine the latitudes of convection in the north of the model, a surface buoyancy distribution is set for the latitudes north of the channel as a boundary condition determined by the EBM. If the surface buoyancy is greater than the buoyancy in the layers below it, convective columns form.

As mentioned above, the surface buoyancy (or temperature) is now calculated from the EBM rather than being a fixed boundary condition as in the original model. The horizontal advection of the surface temperature is ignored in this region. This is due to the wind-driven gyres which are responsible for surface transport at lower latitudes not being simulated in the model and also due to there being no salinity variable (this will be added later), which in reality would oppose the buoyancy changes due to temperature advection to some degree. The addition of a salinity variable into the model is described in Section 7.4. Therefore, the surface temperature (and buoyancy) is taken to be the steady state value from the EBM with no ocean surface advection. This surface buoyancy is used to determine the latitudes of convection in the north of the model.

7.3.3. Northern convective region

In this region of the model, the surface density is greater than in the layers below, and thus convective columns form (with isopycnals outcropping vertically to the surface) over which the buoyancy is constant with depth and set equal to the surface buoyancy. The vertical

advection and diffusion of buoyancy is zero within the convective columns, with the advective-diffusive balance assumed in the vertical below them as in the main ocean basin. However, there is now a horizontal advection of buoyancy across the vertical isopycnals and convective columns. The surface heat flux is then recalculated in the EBM at each time step, with the depth of the convective columns at each latitude accounted for in these calculations (i.e. by changing the surface layer depth and thus the ocean column heat capacity).

7.4. Further modifications

In order to investigate the effects of variations in sea-ice formation on the MOC, a salinity variable is added to the model in order to represent brine rejection, potentially an important glacial-interglacial feedback. The buoyancy is thus dependent on both salinity and temperature. This was implemented by adding a salinity variable, using the same numerical schemes used by Watson et al. [2015] to simulate the biogeochemical variables, which are diffused and advected over the whole domain. The salinity is initialised at 35 ppt throughout the ocean and a salinity flux is imposed as a surface boundary condition. The salinity flux is calculated using the latitude dependent freshwater flux of Wolfe and Cessi [2014] to represent the effects of precipitation and evaporation. The flux is then modified in the south of the domain to represent the additional salinity flux due to sea-ice formation. The freshwater flux is normalised over the domain such that average value is zero to conserve salinity.

The buoyancy flux in the southern channel and northern convective region is now dependent on the salinity flux in addition to the heat flux. The contribution of salinity to the buoyancy is then removed to determine the updated surface temperature to use in the EBM before recalculating the buoyancy using the salinity and the updated surface temperature from the EBM.

The EBM was modified to include a meridional dependent albedo which could be used to represent the ice-sheet albedo feedback. It also has been extended in the north of the model to account for the blocking effects of sea-ice on the heat flux by reducing it in regions of sea-ice cover. Sea-ice occurs in the model at temperatures below 0.5°C and has full cover at 0°C. This is an unrealistic sea-ice freezing temperature, although it enables the effects of sea-ice on the heat flux to be included in the semi-analytical model.

Although the coupled atmosphere-ocean SAMBUCA model is simplistic compared to a GCM, the simulations can be run quickly with about 125 model years run per minute (when the biogeochemistry is removed). The results obtained using the modified model are now described.

7.5. Results

The first results described are the attempts to simulate the glacial cycles by perturbing the solar orbital parameters and varying the surface albedo to represent the northern hemisphere ice-sheets.

Watson et al. [2015] showed changes in the Southern Ocean buoyancy fluxes can transition the MOC between glacial and present-day states, with accompanying changes in atmospheric CO_2. The buoyancy fluxes in the Southern Ocean were imposed in the model rather than being simulated. In the modified model used in this chapter, the effect of changes in the orbital parameters on the MOC is studied. Only the effect of changes in the annual-average solar irradiance due to obliquity and eccentricity changes are investigated here. Seasonal variations in the solar irradiance are also investigated in a separate experiment, although only for the present-day orbital parameters. The effect of changes in the seasonal cycle due to perturbations in precession and obliquity have not been studied.

7.5.1. Variation in orbital parameters: obliquity and eccentricity

The control simulation, representing the present-day climate uses present-day orbital parameters with an eccentricity of 0.017 and an obliquity of 23.44° (see Fig 7.2a). The NADW cell is ~4.2 Sv, significantly weaker than reality which is not unexpected given the findings in previous chapters comparing single- and multi-basin models, and this is similar to the present-day strength in Watson et al. [2015]. The lower overturning cell has a strength of ~6.1 Sv near the surface, although only ~4 Sv in the deep ocean.

Changes in either the obliquity from 22.25° to 24.5°, or the eccentricity from 0.005 to 0.06 which correspond to realistic Milankovitch variations (Imbrie et al. [1993]) produce no discernible change in the MOC. This is not surprising since climate feedbacks are believed to amplify the initial small solar forced perturbations in surface temperature. Seasonal changes which are not considered here are also believed to be critical in causing the glacial cycles. The focus of the simulations performed here is on changes in the obliquity rather than the eccentricity since the eccentricity is not believed to cause the glacial cycles, instead it modulates the magnitude of the precessional cycles (which only leads to seasonal changes in solar radiation). The focus is thus on changes in the obliquity which is proposed as the cause of the 41 Kyr periodicity of glacial cycles prior to ~800 Kyrs ago.

The effect of large changes in obliquity are analysed. Despite being unrealistic, this is interesting since it enables the direction of change in the MOC that would be caused by a small perturbation in obliquity to be determined, and it helps understand how the model responds to changes in the solar radiation. These simulations do not have salinity as a variable in the model and thus buoyancy is dependent only on temperature (i.e. only the direct effects of temperature changes are considered).

The obliquity is increased and decreased to 30° and 15° relative to the control respectively. There is a significant shoaling and deepening of the NADW cell in these respective experiments, with an accompanying weakening and strengthening respectively (see Fig 7.2b and c). The deepening of the NADW cell at low obliquity is due to the annual-average radiation and thus surface temperature decreasing at latitudes polewards of 43° with a greater decrease at higher latitudes (Loutre et al. 2004). Therefore, the surface temperature reduction in the far north of the domain is greater than over most of the channel which is at a lower latitude (and sea-ice also reduces the temperature decrease in the far south). In particular, the decrease is greater in the far north than at the latitude in the channel with the same surface temperature (or the same isopycnal outcrop). This deepening of the northern convective columns and thus the NADW cell also increases the depth over which there is meridional temperature gradient (which is used to determine the streamfunction via thermal wind balance) in the north of the domain. This factor along with an increase in the meridional temperature gradient at lower obliquity leads to a strengthening of the NADW cell by ~0.9 Sv to ~5.1 Sv. As the obliquity is increased, the changes are in the opposite direction with a shoaling and weakening of the NADW cell, decreasing by ~0.9 Sv to ~3.3 Sv at 30° obliquity, due to the greater increase in temperature in the north of the domain than at the equivalent isopycnal outcrop in the southern channel. The lower cell expands slightly but also weakens to ~3.5 Sv due to reduced AABW formation. This is likely due to the Southern Ocean surface warming and also perhaps due to enhanced Southern Ocean stratification.

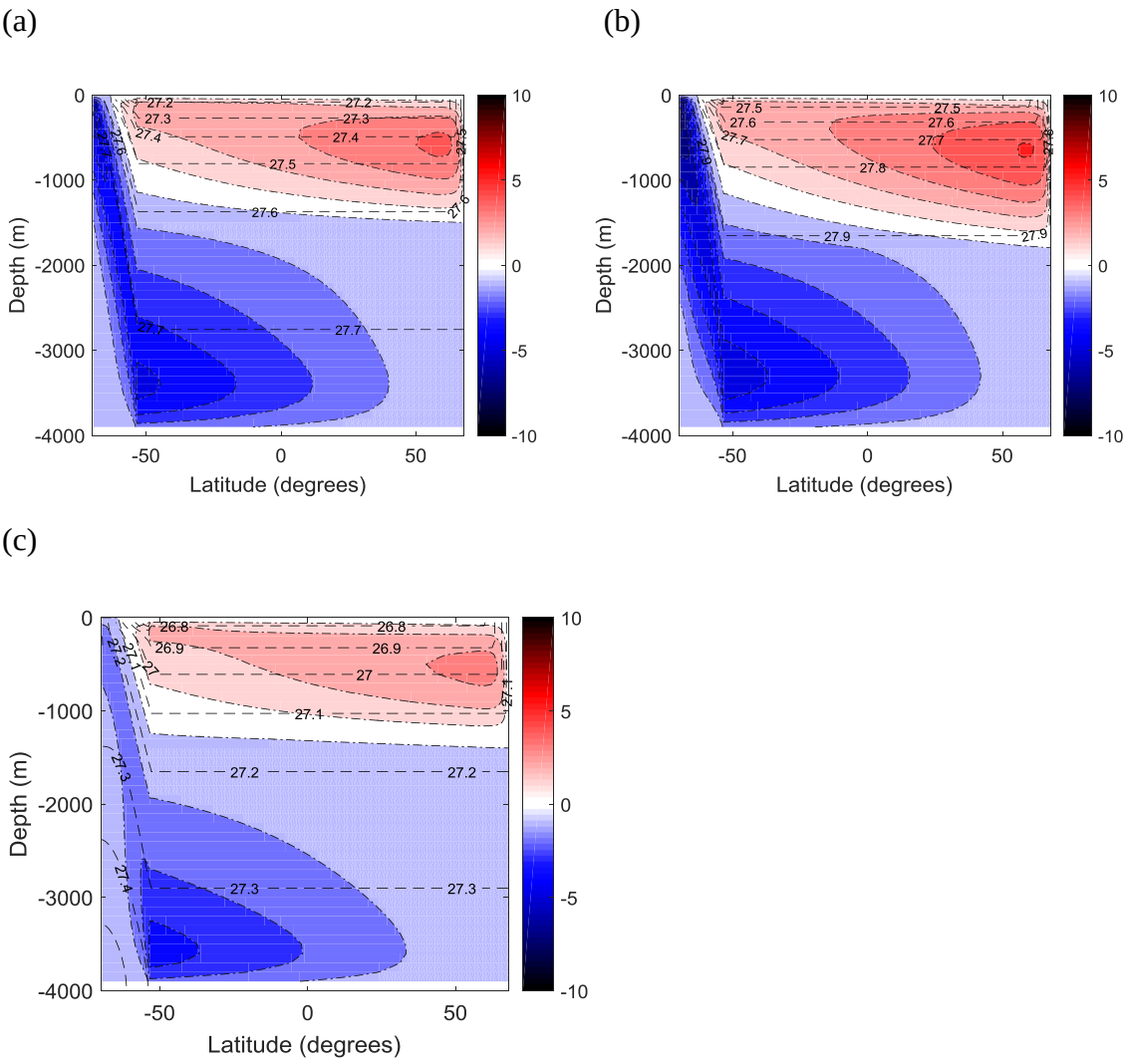

Fig 7.2: Zonal-average residual overturning streamfunction (1 Sv contour intervals) in the single-basin atmosphere-ocean annual-average SAMBUCA model with density dependent only on temperature (salinity assumed constant at 35 ppt to determine potential density) for (a) present-day obliquity (23.44°), (b) reduced obliquity of 18° and (c) enhanced obliquity of 30°. The red (positive) and blue (negative) streamfunctions are clockwise and anti-clockwise circulations respectively, with the 0 Sv contour marked by the change from blue to white shading. Potential density contours are represented by thin dash black lines. The colorbar on the righthandside is the stremfunction shading magnitude.

The obliquity cycle varies between 22.25° and 24.5°, about a one degree change from the present-day value of 23.44°. An increase of one degree leads to only a small decrease of ~0.1 Sv in the NADW cell strength and a decrease of ~0.8 Sv in the AABW cell, with the same magnitude but opposite direction of change in these cells for reduced obliquity. Although this

is only a small change in the NADW cell, it could instigate the transition to a glacial state through climate feedbacks. However, at the LGM the obliquity actually decreased to 22.9° (Pausata et al. [2011]), which strengthens the NADW cell in the model.

The seasonal cycle shall now be simulated in the model. It is important to consider the seasonal cycle since seasonal variations in solar radiation due to changes in obliquity and precession are likely to play an important role during glacial cycles. However, the original SAMBUCA model is setup to simulate the steady state MOC, and thus it is unlikely to be suitable to realistically simulate the seasonal variability in the MOC. The MOC in the model is highly sensitive to the buoyancy at the surface in the north of the model and the depth of this buoyancy contour at the channel-basin boundary, which depends on the Southern Ocean surface buoyancy (among other factors). Therefore, the seasonal variation in surface temperature causes large changes in the MOC, with a deeper, stronger NADW cell in the winter months and a shallower, weaker NADW cell in the summer months (see Fig 7.3). The NADW cell strength and depth is minimum at the Autumn equinox (Fig 7.3b) and maximum at the Spring equinox (Fig 7.3d) since the temperature difference between the north and south of the model is greatest due to the seasonal cycle in surface temperature lagging that of the solar radiation due to the large ocean heat capacity.

These significant changes in the MOC appear to be reasonable, given the AMOC does have a significant seasonal cycle as seen in the time series of the AMOC recorded by the Natural Environment Research Council (NERC) RAPID array. However, the model used here is very simplistic with an instantaneous adjustment of the density throughout the ocean to perturbations in the surface temperature. This is highly unrealistic and thus if seasonal effects were to be considered in the model, they should only be used in the ice-sheet component of the model (see Section 7.5.2), not for determining seasonal variations in the MOC. In reality it takes significantly longer for the ocean circulation to adjust to these surface temperature

variations (timescale of decades) whereas wind-driven changes are believed to largely control the seasonal variations observed in the MOC as inferred by a number of modelling studies (e.g., Willebrand et al. [1980]; Jayne and Marotzke [2001]; Köhl [2005]; Hirschi et al. [2007]). However, Johnson and Marshall [2002] and Hirschi et al. [2007] show that density variations do play a role in the seasonal variations of the MOC in the upper ocean although their focus is confined to the upper ocean meridional transports. Hirschi et al. [2007] suggest the meridional transport changes in the GCM they use are local and are not driven by changes at high latitudes. In contrast Johnson and Marshall [2002] use a highly idealised model to suggest the changes are driven by density changes at high northern latitudes with Kelvin waves propagated along the western boundary to the equator. Nonetheless, wind-driven changes are believed to dominate the seasonal MOC variations and the rapid seasonal changes in the deep ocean isopycnals simulated in the seasonal SAMBUCA setup not seen in more realistic dynamical models.

The model has a time step of 20 days (with a model year of 360 days) over which the streamfunction is calculated. The streamfunction is plotted at the Summer and Winter solstices (Fig 7.3a and c), and the Autumn and Spring equinoxes (Fig 7.3b and d) to illustrate the seasonal variation of the MOC.

The streamfunction is minimum at the Autumn equinox and maximum at the Spring equinox (even if the streamfunction is plotted every 20 days). Thus the greatest contrast in surface temperature between the north and south of the model is at these times of the seasonal cycle (with the north warmer (cooler) than the south at the Autumn (Spring) equinox). The solar radiation is highest and lowest in the Northern Hemisphere at the summer and winter solstices respectively. However, the ocean surface (or mixed layer) temperature lags behind due to the oceans large heat capacity as described previously.

The simulated MOC changes are not realistic as described above and thus the model should only be used to determine the steady state annual-average MOC. This is one of the major difficulties encountered when attempting to simulate the glacial cycles in the SAMBUCA model.

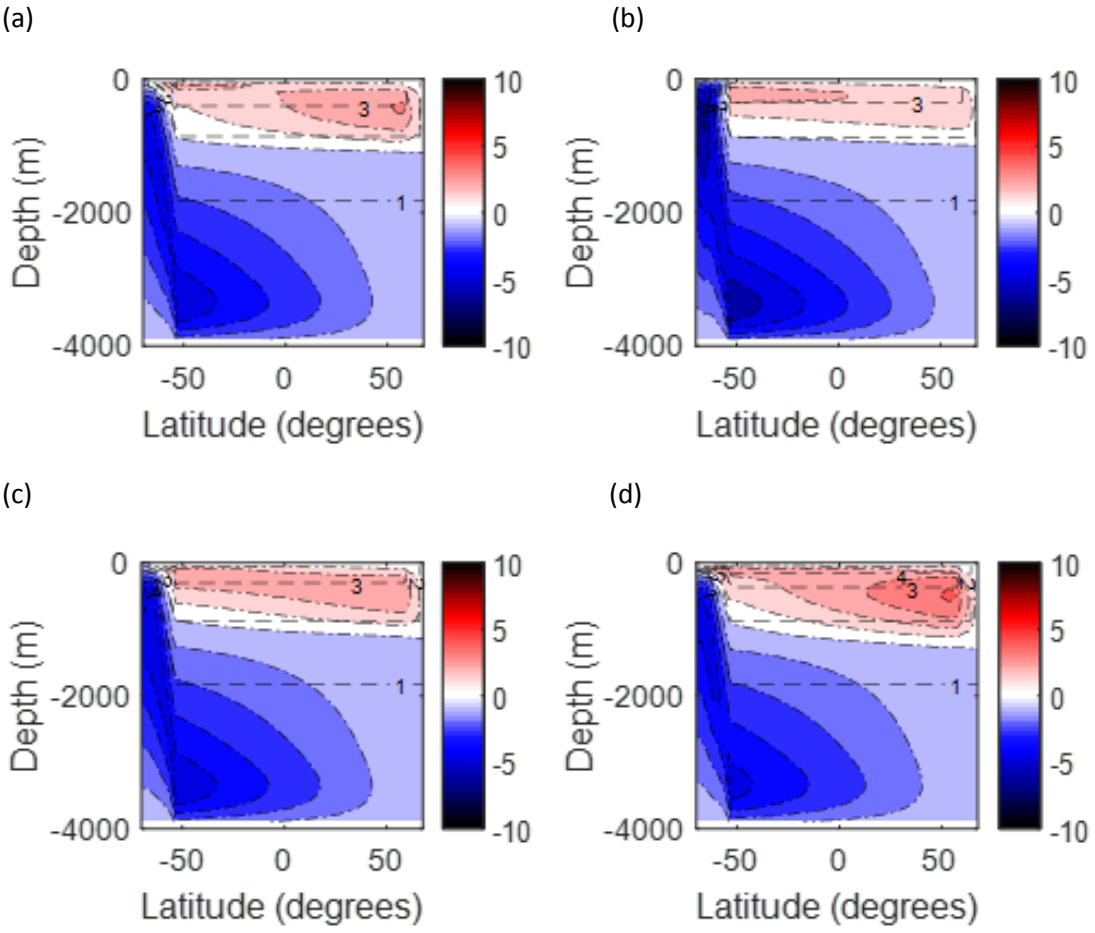

Fig 7.3: Zonal-average residual overturning streamfunction (1 Sv contour intervals) in the single-basin atmosphere-ocean seasonal SAMBUCA model with density dependent only on temperature. Plots show time-variation of MOC at (a) Summer solstice, (b) Autumn equinox, (c) Winter solstice and (d) Spring equinox. Colours and contours are as in Fig 7.2, except the thin dashed lines are now isotherms (°C).

7.5.2. Ice albedo effect: Northern Hemisphere ice-sheets

The growth and melt of the Northern Hemisphere ice-sheets during the transition to a glacial and interglacial state respectively is a major climate feedback. Although the increase in elevation as the ice-sheet grows is an important feedback, an ice-sheet model would be

needed to capture this. Instead, the effect of enhanced Northern Hemisphere albedo, representative of increased ice-sheet coverage during glacial periods is first tested to determine the effect on the MOC. The albedo is held at 30% over most of the domain as in the control (Fig 7.4a). However, it is now increased between 51°N and 56°N to represent the growth of an ice-sheet. However, this is problematic since the model is unable to calculate the convective columns correctly and ultimately blows up if the temperature in the north of the model becomes warmer than the temperature just to the south. Thus, the albedo in this region can only be increased to 32%. This leads to only a very small increase (~0.1 Sv) in the NADW cell strength (Fig 7.4b).

To further investigate the changes in Northern Hemisphere albedo, the albedo is increased at all latitudes north of 51°N which enables a higher albedo to be implemented. The NADW cell again strengthens when the albedo is increased from 0.3 to 0.35 over latitudes north of 51°N (Fig 7.4c) to ~6 Sv. This very small change in albedo has a significant effect on NADW cell strength, showing the high sensitivity of the MOC to albedo in the model. Although, the annual-average surface temperature decreases globally, the local decrease in temperature at latitudes with increased albedo is greater. This leads to a greater cooling in the north of the model than in the Southern Ocean, leading to a deepening and strengthening of the NADW cell. These changes in the MOC are in the opposite direction to that expected in glacial times. This is not surprising given the simplicity of the model but these experiments suggest the ice-sheet feedback due to Northern Hemisphere ice-sheet growth cannot provide the forcing required to weaken the NADW cell. In the latter experiment, the enhanced depth of isopycnal columns and enhanced meridional temperature gradient in the north of the model both contribute to the strengthening of the NADW cell.

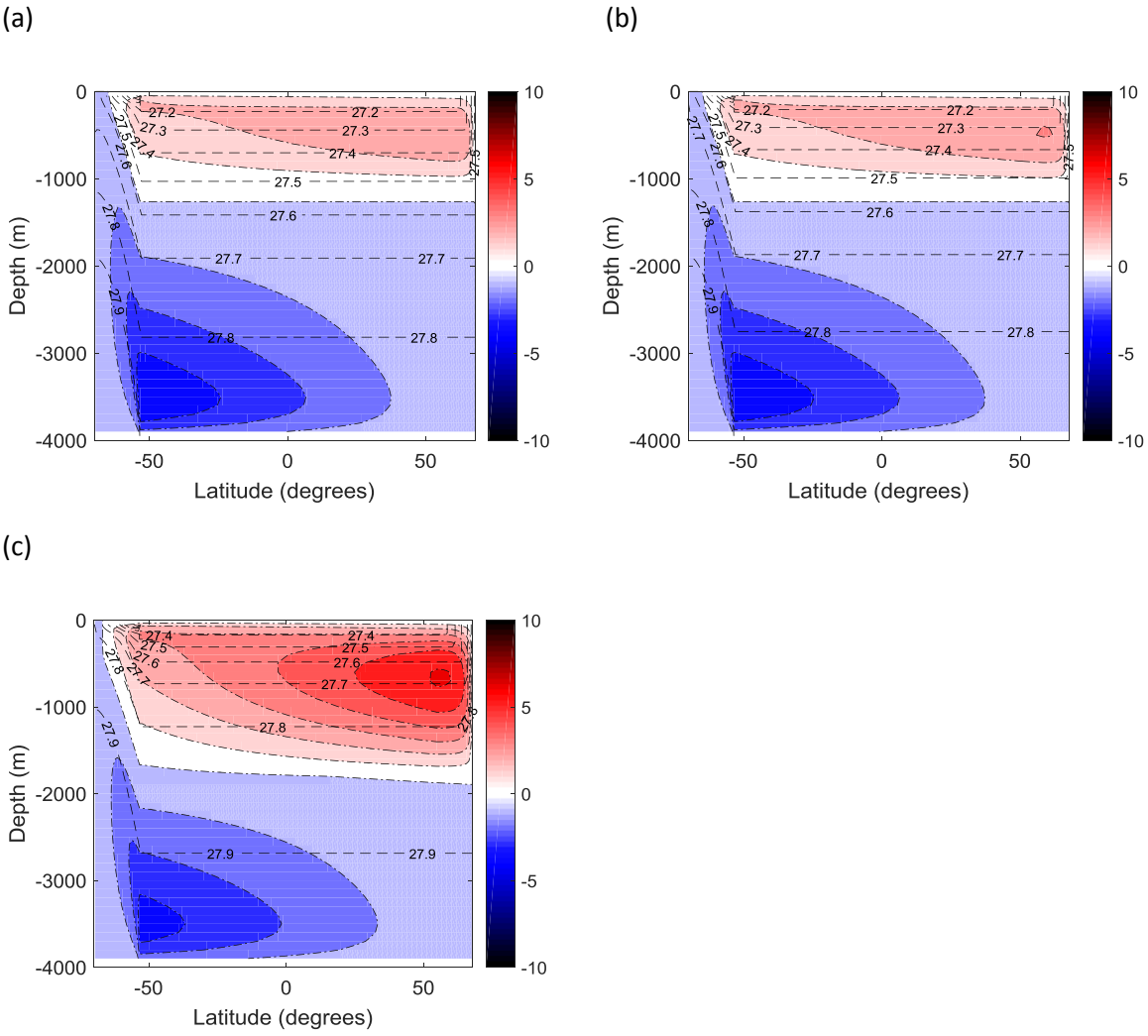

Fig 7.4: Zonal-average residual overturning streamfunction (1 Sv contour intervals) in the single-basin atmosphere-ocean annual-average SAMBUCA model for varying surface albedos of (a) 0.3 everywhere, (b) 0.32 between 51°N and 56°N and 0.3 elsewhere, (c) 0.35 north of 51°N and 0.3 elsewhere. The density is dependent only on temperature and the reduction in the heat flux in regions of sea-ice cover north of the channel is not accounted for in the setup used here. Colours and contours are as in Fig 7.2.

7.5.3. Changes in Southern Ocean sea-ice formation

Since changes in surface temperature from perturbations in solar radiation and surface albedo are unable to cause the transition of the present-day MOC to a glacial state in the model, an alternative mechanism or feedback is required to explain the shoaling and weakening of the NADW cell. The importance of Southern Ocean sea-ice formation and melt in determining the buoyancy forcing and water mass transformations at these high latitudes in the present-

day is evident (e.g. Abernathey et al. [2016]). In the Southern Ocean there is a significant northward export of sea-ice by the wind-driven Ekman flow, and thus a significant brine rejection from sea-ice formation. Thus, the effects of enhanced Southern Ocean sea-ice formation in glacial times could drive the transition of the NADW cell to a glacial state. A number of studies have suggested changes in the Southern Ocean boundary conditions are important in the transition to glacial climates (e.g., Shin et al. [2003], Liu et al. [2005], Ferrari et al. [2014], Sun et al. [2016], Jansen and Nadeau [2016], and Jansen [2017]). The latter study of Jansen [2017] provides MOC and salinity distribution plots which are in agreement with the results from SAMBUCA described below despite the more complex MITgcm being used in that study.

A salinity variable is added to the model as described previously enabling the surface salinity (and thus buoyancy) flux to be perturbed to crudely represent the effects of changes in Southern Ocean sea-ice formation on the salinity. The present-day control circulation is generated using the same control EBM inputs as described previously but now the buoyancy is dependent on temperature and salinity (see Fig 7.5a and c). A surface salinity boundary condition is set to the normalised evaporation-precipitation (E-P) flux of Wolfe and Cessi [2014], with a reduction in the south of the domain to account for the additional flux due to Southern Ocean sea-ice formation. The E-P flux is then modified in the South of the domain between 70°S and 64.6°S to be more positive (i.e. increase the salinity flux). In the control this additional 'sea-ice' E-P flux is taken to be 0.85 m yr^{-1} over these southern latitudes, with this value increased to 4.73 m yr^{-1} to obtain a glacial state, approximately a 5.5 fold increase. This leads to a shoaling and weakening of the NADW cell from ~5.9 Sv in the control (Fig 7.5a) to ~4.6 Sv in the glacial state (Fig 7.5b), and an expansion and slight strengthening of the AABW cell from ~6.1 Sv to ~6.3 Sv in the respective buoyancy states (Fig 7.5a and b). The equatorward shift in upwelling of the lower AABW cell in the Southern Ocean proposed

as a mechanism to draw down atmospheric CO_2 by Watson at al. [2015] is also simulated. Thus enhanced Southern Ocean sea-ice formation as the global temperature decreases could provide a major climate feedback and a mechanism to transition the MOC to a glacial state.

This mechanism has been used in previous chapters to obtain a glacial state and has been analysed and discussed in detail by Jansen and Nadeau [2016] and Jansen [2017]. It also alters the ocean's salinity distribution. The salinity range in the control varies from 34.4 ppt to 35.6 ppt with a maximum at the surface of the North Atlantic (see Fig 7.5c), a similar distribution with a slightly smaller range than present-day observations from WOCE of the Atlantic Ocean (Koltermann et al. [2011]). In the glacial state, the salinity range varies from 33.1 ppt to 35.8 ppt, with the highest salinity now at depth in the Southern Ocean. This increase in salinity at depth in the AABW cell (see Fig 7.4d) is similar to the glacial distribution inferred from proxy evidence (Adkins et al. [2002]) and modelled by Jansen [2017].

The enhanced brine rejection from enhanced sea-ice formation sinks in the south of the domain, which is then circulated in the lower cell, increasing the salinity in the deep Southern Ocean leading to the redistribution of salinity in Fig 7.5d. The simulations are very similar to the study of Jansen [2017] despite the many simplifications made in SAMBUCA compared to the MITgcm used in the aforementioned study. This validates the simulations of the MOC made using this simplified model and shows the importance of using both simple and more complex models to improve our understanding of the MOC and the glacial cycles.

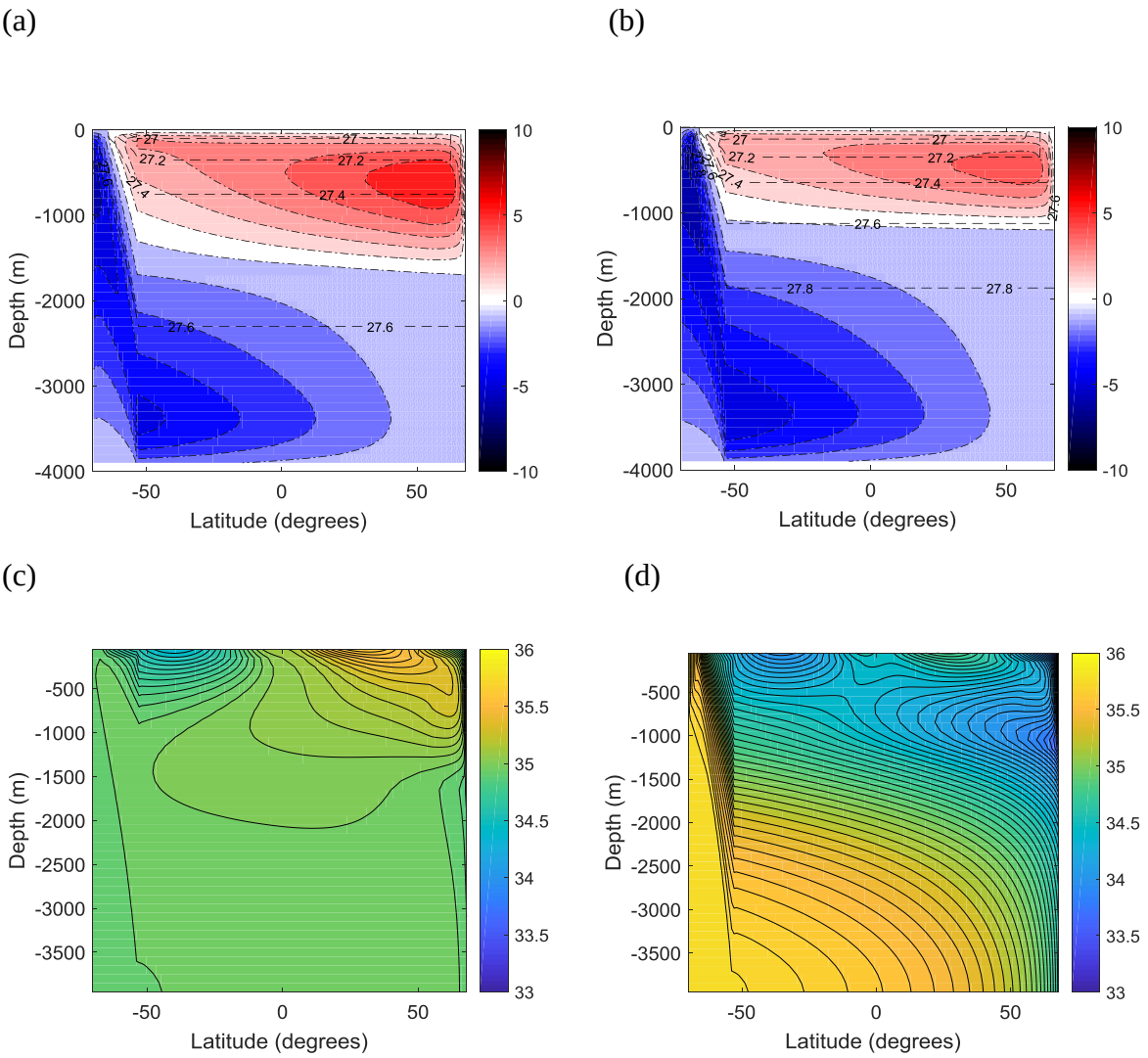

Fig 7.5: Zonal-average residual overturning streamfunction (top) (1 Sv contour intervals) and salinity distribution (bottom) (0.05 ppt contour intervals) in the single-basin atmosphere-ocean annual-average SAMBUCA model for varying Southern Ocean salinity (and buoyancy) forcing representative of (a),(c) present-day and (b), (d) glacial state with enhanced southern salinity flux. The density is now dependent on both temperature and salinity. Colours and contours are as in Fig 7.2.

7.6. Conclusions

The semi-analytical SAMBUCA model (Nikurashin and Vallis [2011; 2012]) extended by Watson at al. [2015] has been further modified by coupling the ocean model to an Energy Balance Model, enabling the simulation of surface buoyancy forcings in SAMBUCA. The buoyancy forcing has been made dependent on the solar orbital parameters, surface albedo

and also an imposed salinity forcing. Increases in obliquity lead to a strengthening and deepening of the annual-average MOC while reduced obliquity had the opposite effect. A seasonal dependence was added to the model, although this is shown to be unrealistic due to the semi-analytical nature of the model. Instead it should only be used to obtain the annual-average steady state MOC. This fact in addition to the Northern Hemisphere ice-sheet albedo and obliquity changes in glacial times having the opposite effect to those observed lead us to look for alternative climate feedback and changed the direction of this PhD project.

The model was further advanced by adding a salinity variable enabling the surface freshwater forcing in addition to heat flux changes to alter the surface buoyancy forcing and MOC. Changes in the Southern Ocean sea-ice formation rate is suggested as a mechanism for glacial-interglacial transitions in the MOC and confirms the findings of Jansen [2017] in this basic model. This mechanism was used to obtain a glacial state in previous chapters using the MITgcm. The limitations and application of this semi-analytical single-basin model to investigate MOC variations is apparent, showing the importance of using both simple and more complex models.

Chapter 8

Conclusions

8.1. Summary

In this thesis, both a simple and a more complex ocean model have been used to investigate the response of the MOC and atmospheric CO_2 to variations in surface forcing, with a particular focus on the glacial cycle variations. An idealised two-basin general circulation model connected by a southern circumpolar channel suggests a change in Southern Ocean buoyancy fluxes due to enhanced Southern Ocean sea-ice formation can cause the MOC to transition from a present-day to a glacial state, whereas a reduction in the Southern Ocean westerly wind stress is unable to cause the glacial shoaling of the NADW cell. The buoyancy forcing mechanism for the glacial cycle MOC variations supports the studies of Watson and Garabato [2006], Ferrari et al. [2014], and Jansen and Nadeau [2016].

The pathways taken by the MOC have been analysed under varying Southern Ocean buoyancy and zonal wind forcing, and Pacific basin vertical diffusivity in the two-basin model. The components are separated by determining the volume flow rates between the residual circulations in each basin and the global-average residual circulation in the channel. The direct zonal pathways between the Atlantic and Pacific basins are also accounted for.

The present-day NADW cell in the model is driven both by wind-driven upwelling in the Southern Ocean and by diffusion in the Pacific and Atlantic. In a cooler climate with enhanced sea-ice, the shoaled NADW cell can no longer flow directly into the channel's lower cell, reducing the Pacific diffusively-driven pathway of NADW. This leads to a

substantial weakening of the NADW cell and the isolation of the upper and lower cells. In contrast, in a future warmer climate with reduced AABW formation, the NADW cell strengthens and deepens, becoming increasingly driven by diffusive upwelling in the Pacific basin, with a smaller role played by wind-driven upwelling.

The NADW cell strengthens (weakens) with enhanced (reduced) Southern Ocean zonal wind stress and Pacific diffusivity under all buoyancy forcings. The sensitivity of the NADW cell to Pacific diffusivity increases as the buoyancy forcing is varied from a 'cold' glacial to a 'warm' state, due primarily to a greater change in the Pacific diffusively-driven pathway of NADW in the 'warm' state and also a greater change in Atlantic upwelling as the NADW cell deepens. In contrast, the NADW cell is more sensitive to changes in Southern Ocean wind stress when the buoyancy forcing is varied from a 'warm' to a present-day or glacial state due to a greater variation in the wind-driven pathway of NADW in these latter states.

At low wind speeds, the NADW cell only weakens slightly in the 'warm' and present-day states due to the maintenance of the Pacific diffusively-driven pathway through zonal flows of NADW between the Atlantic and Pacific basins, and the expansion of the channel's lower cell.

These findings help to explain the inability of single-basin models to simulate a realistic overturning circulation under realistic surface forcings and vertical ocean diffusivity, with the NADW cell being far weaker than in the real world. The stronger NADW cell simulated by the two-basin model under the same forcings is primarily due to its wider domain which allows for enhanced diffusive upwelling. The wider channel also strengthens the NADW cell through enhanced wind-driven upwelling in the channel.

The atmospheric CO_2 also varies as the MOC changes in response to changes in Southern Ocean sea-ice formation. The two-basin model is found to vary by ~34 ppm between the

‘warm’ state and glacial states, whereas it only varies by ~7 ppm in the single-basin model for the same variation in the sea-ice freezing point and thus a similar change in the sea-ice formation rate. These differences are likely due to the difference in the pathways taken by the MOC between these models although further work is needed to determine whether this is the case.

This thesis has improved our understanding of the MOC in the present-day and how it varies in response to perturbations in forcings and ocean vertical diffusivity. It extends our understanding of the mechanisms responsible for glacial-interglacial cycles and also highlights the potential future changes in the MOC in a warmer climate. The direct comparison between single and multi-basin models highlights important differences in their abilities to simulate realistic changes in the MOC, with the importance of using a hierarchy of models with differing complexites evident.

8.2. Further Work

The change in atmospheric CO_2 in response to enhanced Southern Ocean sea-ice formation and the consequent transition to a glacial state MOC needs further analysis to determine the exact cause of the changes in CO_2. This will be accomplished through a separation of the carbon components in the model and through a more thorough analysis of the role played by sea-ice on the biological productivity and atmosphere-ocean CO_2 exchange. The change is also lower than the proxy record glacial-interglacial variations in atmospheric CO_2. While, this is in part due to carbonate compensation, solubility effects due to temperature variations and some other processes not being accounted for, it is likely that a more realistic change could be obtained if the biological productivity is enhanced. For example, the theory of Watson et al. [2015] relies on biological productivity being able to occur under sea-ice or in

polynyas in the Southern Ocean. This is not possible in the current setup of the MITgcm used in this thesis.

There is also scope for an extension of the work on the MOC pathways. Further experiments could be performed with both wind and vertical diffusivity perturbations for each buoyancy state, since these perturbations were only varied in isolation. This could enable a more complete understanding of the response and sensitivity of the MOC to variations in buoyancy and wind forcing, and vertical diffusivity. It would also be interesting to use the method proposed in this study to quantify the pathways taken by the MOC in a global setup of the MITgcm, the complex ocean model used in this thesis, and also global climate models to investigate whether the same conclusions are obtained as in the model used in this thesis and how the various models differ.

Bibliography

Abernathey R., J. Marshall and D. Ferreira, 2011: The dependence of Southern Ocean meridional overturning on wind stress. *J. Phys. Oceanogr.*, **41**, 2261–78, https://doi.org/10.1175/JPO-D-11-023.1.

Abernathey, R., I. Cerovečki, P. R. Holland, E. Newsom, M. Mazloff, and L. D. Talley, 2016: Southern Ocean Water Mass Transformation Driven by Sea Ice. *Nature Geoscience*, **9**, 596–601, https://doi.org/10.1038/ngeo2749.

Adams J. M., Faure H., Faure-Denard L., McGlade J. M. and Woodward F. I., 1990: Increases in terrestrial carbon storage from the last glacial maximum to the present. *Nature*, **348**, p. 711–714.

Adcroft, A., C. Hill and J. Marshall, 1997: The Representation of Topography by Shaved Cells in a Height Coordinate Model. Month. *Weath. Rev.*, **125**, 2293-2315.

Adkins, J. F., K. McIntyre, and D. P. Schrag, 2002: The salinity, temperature, and $\delta_{18}O$ of the glacial deep ocean. *Science*, **298**, 1769–1773, https://doi.org/10.1126/science.1076252.

Altabet M.A. and Curry W. B., 1989: Testing models of past ocean chemistry using foraminifera $^{15}N/^{14}N$. *Glob. Biogeochem. Cycles*, **3**, pp. 107–119.

Altabet M. A. and Francois R., 1994: Sedimentary nitrogen isotopic ratio as a recorder for surface ocean nitrate utilization. *Glob. Biogeochem. Cycles*, **8**, pp. 103-116.

Anderson, L. A. and J. L. Sarmiento, 1994: Redfield ratios of remineralization determined by nutrient data analysis. *Global Biogeochem. Cycles*, **8**, 65–80.

Andersen, K., Azuma, N., Barnola, J. *et al.*, 2004: High-resolution record of Northern Hemisphere climate extending into the last interglacial period. *Nature*, **431,** pp. 147–151.

Andrews D. G. and McIntyre M. E., 1976: Planetary waves in horizontal and vertical shear: The generalized Eliassen–Palm relation and the mean zonal acceleration. *J. Atmos. Sci.*, **33**, pp. 2031–2048.

Andrews D. G. and McIntyre M. E., 1978: Generalized Eliassen–Palm and Charney–Drazin theorems for waves on axisymmetric mean flows in compressible atmospheres. *J. Atmos. Sci.*, **35**, pp. 175–185.

Arakawa, A., 1966: Computational design for long-term numerical integration of equations of fluid motion: Two dimensional incompressible flow. Part I. *J. Comput. Phys.*, **1**, 119–143.

Arakawa A. and Lamb VR., 1977: Computational design of the basic dynamical processes of the UCLA general circulation model. *Methods Comput. Phys.*, **17**, 173-265.

Archer D. and Maier-Reimer E., 1994: Effect of deep-sea sedimentary calcite preservation on atmospheric CO_2 concentration. *Nature*, **367**, pp. 260-263.

Archer D., Winguth A., Lea D., and Mahowald N., 2000a: What caused the glacial/interglacial atmospheric pCO2 cycles? *Rev. Geophys.*, **38**, pp. 159–189.

Baker J. A., A. J. Watson and G. K. Vallis, 2020: Meridional Overturning Circulation in a multi-basin model Part I: Dependence on Southern Ocean buoyancy forcing. https://doi.org/10.1175/JPO-D-19-0135.1.

Batjes N.H., 1996: Total carbon and nitrogen in the soils of the world. *European Journal of Soil Science*, **47**, pp. 151-163.

Berger A., 1978: Long-term variations of daily insolation and Quaternary climatic changes. *Journal of Atmospheric Science*, **35**, pp. 2362-2367.

Bishop, S. P., P. R. Gent, F. O. Bryan, A. F. Thompson, M. C. Long, and R. Abernathey, 2016: Southern Ocean Overturning Compensation in an Eddy-Resolving Climate Simulation. *J. Phys. Oceanogr.*, **46**, 1575-1592, https://doi.org/10.1175/JPO-D-15-0177.1.

Bond, G., W. S. Broecker, S. Johnson, J. McManus, L. Labeyrie, J. Jouzel, and G. Bonani, 1993: Correlations between climate records from North Atlantic sediments and Greenland ice, *Nature*, **365**, pp. 143–147.

Bopp L., Kohfeld K.E., Le Quéré C. and Aumont O., 2003: Dust impact on marine biota and atmospheric CO_2 during glacial periods. *Paleoceanography*, **18**, pp. 1046.

Bouttes N., Paillard D., Roche D. M., Brovkin V., and Bopp L., 2011: Last Glacial Maximum CO2 and δ_{13}C successfully reconciled. *Geophys. Res. Lett.*, **38**, L02705.

Boyle E.A., Keigwin L.D., 1987: North Atlantic thermohaline circulation during the past 20,000 years linked to high-latitude surface temperature. *Nature*, **330**, pp. 35-40.

Broecker W. S. and Henderson G. M, 1998: The sequence of events surrounding Termination II and their implications for the cause of glacial-interglacial CO_2 changes. *Paleoceanography*, **13**, pp. 352-364.

Broecker W. S., 1982: Ocean chemistry during glacial time. *Geochim. Cosmochim. Acta*, **46**, pp. 1689-1706.

Broecker, W.S. and T.-H. Peng, 1982: Tracers in the Sea, *Eldigio Press*, 690, https://doi.org/10.1016/0016-7037(83)90075-3.

Broecker, W. S., T. Takahashi, and T. Takahashi, 1985: Sources and flow patterns of deep-ocean waters as deduced from potential temperature, salinity, and initial phosphate concentration. *J. Geophys. Res.*, **90**, 6925-6939.

Broecker, W.S., 1987: The biggest chill**,** *Natural History Magazine*, **97**, 74-82.

Bryan, K., and L. J. Lewis, 1979: A water mass model of the world ocean. *J. Geophys. Res.*, **84**, 2503–2517, https://doi.org/10.1029/JC084iC05p02503.

Bryan, F., 1987: Parameter sensitivity of primitive equation ocean general circulation models. *J. Phys. Oceanogr.*, **17**, 970–985, https://doi.org/10.1175/1520-0485(1987)017<0970:PSOPEO>2.0.CO;2.

Budyko M. I., 1969: The effect of solar radiation variations on the climate of the earth. Tellus, 2I, pp. 611–619.

Burke, A., A. L. Stewart, J. F. Adkins, R. Ferrari, M. F. Jansen, and A. F. Thompson, 2015: The glacial mid-depth radiocarbon bulge and its implications for the overturning circulation. *Paleoceanography*, **30**, 1021–1039, https://doi.org/10.1002/2015PA002778.

Campin, J.-M., A. Adcroft, C. Hill, and J. Marshall, 2004: Conservation of properties in a free-surface model. *Ocean Modell.*, **6**, 221–244.

Carter A.J. and Scholes R.J., 2000: Spatial Global Database of Soil Properties. IGBP Global Soil Data Task CD-ROM. International Geosphere-Biosphere Programme (IGBP) Data Information Systems.

Catubig N. et al., 1998: Global deep-sea burial rate of calcium carbonate during the last glacial maximum. *Paleoceanography*, **13**, pp. 298-310.

Cessi, P., 2019: The global overturning circulation. *Annual Review of Marine Science*, **11**, 249-270, https://doi.org/10.1146/annurev-marine-010318-095241

Charette, M.A., and W.H.F. Smith, 2010: The volume of Earth ocean. *Oceanography*, **23**, 112–114.

Chisholm S. W. and Morel F. M. M., 1991: What controls phytoplankton production in nutrient-rich areas of the open sea? *Limnol. Oceanogr.*, **36**, pp. 1507-1970.

Chisholm S. W., 2000: Stirring times in the Southern Ocean. *Nature*, **407**, pp. 685–687.

CLIMAP Project Members, 1981: Seasonal reconstructions of the Earth's surface at the last glacial maximum. *Geol. Soc. Am. Map Chart Ser.*, **36**, pp. 1–18.

Codispoti L., 1995: Biogeochemical cycles—Is the ocean losing nitrate. *Nature*, **376**, 724.

Crowley T.J., 1995: Ice-Age terrestrial carbon changes revisited. *Glob. Biogeochem. Cycles*, **9**, pp. 377-389.

Curry, W., and D. Oppo, 2005: Glacial water mass geometry and the distribution of $\delta^{13}C$ of ∑CO2 in the Western Atlantic Ocean. *Paleoceanography*, **20**, PA1017, https://doi.org/10.1029/2004PA001021.

Danabasoglu G. and J. Marshall, 2007: Effects of vertical variations of thickness diffusivity in an ocean general circulation model, *Ocean Modell.*, **18**, 122-141, https://doi.org/10.1016/j.ocemod.2007.03.006.

Dansgaard W. *et al*., 1993: Evidence for general instability of past climate from a 250-kyr ice-core record. *Nature*, **364**, pp. 218−220.

De Fries R.S., Field C.B., Fung I., Collatz G.J., and Bounoua L., 1999: Combining satellite data and biogeochemical models to estimate global effects of human-induced land cover change on carbon emissions and primary productivity. *Global Biogeochemical Cycles*, **13**, pp. 803-815.

Delmotte M., Chappellaz J., Brook E., Yiou P., Barnola J.M., Goujon C., Raynaud D., Lipenkov V.I., 2004: Atmospheric methane during the last four glacial-interglacial cycles: Rapid changes and their link with Antarctic temperature. *J Geophys Res*, **109**, 1–13.

Doos, K., and A. Coward, 1997: The Southern Ocean as the major upwelling zone of North Atlantic Deep Water. *International WOCE Newsletter,* **27**, 3–4.

Downes, S.M., and A. MC. Hogg, 2013: Southern Ocean circulation and eddy compensation in CMIP5 models. *Journal of Climate*, **26**, 7198-7220, https://doi.org/10.1175/JCLI-D-12-00504.1.

Dufour C.O, J. Le Sommer, J.D. Zika, M. Gehlen, J.C. Orr, et al. 2012: Standing and transient eddies in the response of the Southern Ocean meridional overturning to the southern annular mode. *J. Clim.* **25**, 6958–74, https://doi.org/10.1175/JCLI-D-11-00309.1.

Duplessy, J., N. Shackleton, R. Fairbanks, L. Labeyrie, D. Oppo, and N. Kallel, 1988: Deepwater source variations during the last climatic cycle and their impact on the global deepwater circulation. *Paleoceanography*, **3**, 343-360, https://doi.org/10.1029/PA003i003p00343.

Dutkiewicz, S., A. Sokolov, J. Scott, and P. Stone, 2005: A three-dimensional ocean-seaice carbon cycle model and its coupling to a two-dimensional atmospheric model: Uses in climate change studies., Tech. Rep. Report 122 , Joint Program of the Science and Policy of Global Change, M.I.T., Cambridge, MA.

Eady, E. T., 1957: The general circulation of the atmosphere and oceans. In D. R. Bates, Ed., *The Earth and its Atmosphere*, 131-151. New York, Basic Books.

EPICA-Community-Members, 2004: Eight glacial cycles from an Antarctic ice core. *Nature*, **429**, pp. 623–628.

Farneti R., S.M. Downes, S.M. Griffies, S.J. Marsland, E. Behrens, et al. 2015: An assessment of Antarctic Circumpolar Current and Southern Ocean meridional overturning circulation during 1958–2007 in a suite of interannual CORE-II simulations. *Ocean Model.*, **93**, 84–120, https://doi.org/10.1016/j.ocemod.2015.07.009.

Farrell J. W., Pedersen T. F., Calvert S. E. and Nielsen B., 1995: Glacial-interglacial changes in nutrient utilization in the equatorial Pacific Ocean. *Nature*, **377**, pp. 514-517.

Ferrari, R., M. F. Jansen, J. F. Adkins, A. Burke, A. L. Stewart, and A. F. Thompson, 2014: Antarctic sea ice control on ocean circulation in present and glacial climates. *Proc. Natl. Acad. Sci. USA*, **111**, 8753–8758, https://doi.org/10.1073/pnas.1323922111.

Ferrari, R, L. P. Nadeau, D. P. Marshall, L. C. Allison, H. L. Johnson, 2017: A model of the ocean overturning circulation with two closed basins and a reentrant channel. *J. Phys. Oceanogr*. **47**, 2887–906, https://doi.org/10.1175/JPO-D-16-0223.1.

Follows M., T. Ito and S. Dutkiewicz, 2006: Solving the carbonate chemistry system in ocean biogeochemistry models. *Ocean Modeling*. **12**, 290-301.

Francois, R., M. A. Altabet, E.-F. Yu, D. M. Sigman, M. P. Bacon, M. Frank, G. Bohrmann, G. Bareille, and L. D. Labeyrie, 1997: Contributions of Southern Ocean surface-water stratification to low atmospheric CO2 concentrations during the last glacial period. *Nature*, **389**, 929–935.

Garcia, H. E. and L. I. Gordon, 1992: Oxygen solubility in seawater: Better fitting equations. *Limnol. Oceanogr.*, **37**, 1307-1312.

Gent, P. R., 2016: Effects of southern hemisphere wind changes on the meridional overturning circulation in ocean models, *Ann. Rev. Mar. Sci.*, **8**, 79–94, https://doi.org/10.1146/annurev-marine-122414-033929.

Gent, P. R., J. Willebrand, T. J. McDougall, and J. C. McWilliams, 1995: Parameterizing eddy-induced tracer transports in ocean circulation models, *J. Phys. Oceanogr.*, **25**, 463-474, https://doi.org/10.1175/1520-0485(1995)025<0463:PEITTI>2.0.CO;2.

Gent, P. R., and J. C. McWilliams, 1990: Isopycnal mixing in ocean circulation models. *J. Phys. Oceanogr.*, **20**, 150–155, https://doi.org/10.1175/1520-0485(1990)020<0150:IMIOCM>2.0.CO;2.

Gent, P. R., 2016: Effects of Southern Hemisphere wind changes on the meridional overturning circulation in ocean models. *Annu. Rev. Mar. Sci.*, **8**, 79–94, https://doi.org/10.1146/annurev-marine-122414-033929.

Gerdes, R., C. Koberle, and J. Willebrand, 1991: The influence of numerical advection schemes on the results of ocean general circulation models, *Clim. Dynamics*, **5**, 211-226, https://doi.org/10.1007/BF00210006.

Gherardi J.M., Labeyrie L., Nave S., Francois R., McManus J. F., and Cortijo E., 2009: Glacial-interglacial circulation changes inferred from $^{231}Pa/^{230}Th$ sedimentary record in the North Atlantic region. *Paleoceanography*, **24**, PA2204.

Gnanadesikan, A., 1999: A simple predictive model for the structure of the oceanic pycnocline. *Science*, **283**, 2077–2079, https://doi.org/10.1126/science.283.5410.2077.

Gnanadesikan, A., A. M. de Boer, and B. K. Mignone, 2007: A simple theory of the pycnocline and overturning revisited, in *Ocean Circulation: Mechanisms and Impacts*, Geophys. Monogr. Ser.173, Washington, DC, American Geophysical Union, 19–32.

Gordon, A. L., 1986: Interocean exchange of thermocline water, *Journal of Geophysical Research*, **91** (C4), 5037-5046, https://doi.org/10.1029/JC091iC04p05037.

Gregg, M. C., 1989: Scaling turbulent dissipation in the thermocline. *J. Geophys. Res.*, **94**, 9686–9698, https://doi.org/10.1029/JC094iC07p09686.

Griffies, S. M., 1998: The Gent-McWilliams skew flux, *J. Phys. Oceanogr.*, ***28***, 831-841.

Griffies, S.M. and Coauthors, 2000: Developments in ocean climate modelling. *Ocean Modell.*, **2**, 123–192.

Grootes, P., Stuiver, M., White, J. et al., 1993: Comparison of oxygen isotope records from the GISP2 and GRIP Greenland ice cores. *Nature*, **366,** 552–554.

Gruber N.and Sarmiento J. L.,1997: Global patterns of marine nitrogen fixation and denitrification. *Glob. Biogeochem. Cycles*, **11**, pp. 235-266.

Haney, R. L., 1971: Surface thermal boundary condition for ocean circulation models, *J. Phys. Oceanogr.*, **1**, 241-248, https://doi.org/10.1175/1520-0485(1971)001<0241:STBCFO>2.0.CO;2.

Hays J., Imbrie J. and Shackleton N., 1976: Variations in the earth's orbit: Pacemaker of the ice ages. *Science*, **194**, pp. 1121–1132.

Hibler, III, W. D., 1979: A dynamic thermodynamic sea ice model, *J. Phys. Oceanogr.*, **9**, 815-846, https://doi.org/10.1175/1520-0485(1979)009<0815:ADTSIM>2.0.CO;2.

Hibler, III, W. D., 1980: Modeling a variable thickness sea ice cover, *Mon. Wea. Rev.*, **1**, pp. 1943-1973, https://doi.org/10.1175/1520-0493(1980)108<1943:MAVTSI>2.0.CO;2.

Hirschi, J., and J. Marotzke, 2007: Reconstructing the meridional overturning circulation from boundary densities and the zonal wind stress. *J. Phys. Oceanogr.*, **37**, pp. 743-763.

Hopcroft, P., Valdes, P., O'Connor, F. et al., 2017: Understanding the glacial methane cycle. *Nat. Commun.*, **8**, 14383.

Huybers P. J. and Wunsch C., 2005: Obliquity pacing of the late Pleistocene glacial terminations. *Nature*, **434**, pp. 491-494.

Huybers P., 2006: Early Pleistocene glacial cycles and the integrated summer insolation forcing. *Science*, **313**, pp. 508 – 511.

Imbrie J., and Imbrie J.Z., 1980: Modelling the climatic response to orbital variations. *Science*, **207**, pp. 943–953.

Imbrie J. et al., 1993: On the structure and origin of major glaciation cycles: 2. The 100,000-year cycle. *Paleoceanography*, **8**, pp. 699– 735.

IPCC, 2007: Climate Change 2007: The Physical Science Basis, Contribution of Working Group I to the Fourth Assessment Report of the Intergovernmental Panel on Climate Change [Solomon S., Qin D., Manning M., Chen Z., Marquis M., Averyt K.B., Tignor M. and Miller H.L. (eds.)] Cambridge University Press, Cambridge, United Kingdom and New York, NY, USA.

IPCC, 2013: Climate Change 2013: The Physical Science Basis. Contribution of Working Group I to the Fifth Assessment Report of the Intergovernmental Panel on Climate Change [Stocker, T.F., D. Qin, G.-K. Plattner, M. Tignor, S.K. Allen, J. Boschung, A. Nauels, Y. Xia, V. Bex and P.M. Midgley (eds.)]. Cambridge University Press, Cambridge, United Kingdom and New York, NY, USA, 1535 pp.

Ito, T., and M. Follows, 2005: Preformed phosphate, soft tissue pump and atmospheric CO2.

Journal of Marine Research, **63**, 813-839.

Ito, T., and J. Marshall, 2008: Control of lower-limb overturning circulation in the Southern Ocean by diapycnal mixing and mesoscale eddy transfer. *J. Phys. Oceanogr.*, **38**, 2832–2845, https://doi.org/10.1175/2008JPO3878.1.

Jansen, M. F., and L. P. Nadeau, 2016: The effect of Southern Ocean surface buoyancy loss on the deep-ocean circulation and stratification. *J. Phys. Oceanogr.* **46,** 3455–70, https://doi.org/10.1175/JPO-D-16-0084.1.

Jansen, M. F., 2017: Glacial ocean circulation and stratification explained by reduced atmospheric temperature. *Proc. Natl. Acad. Sci.,* **114(1)**, 45-50, https://doi.org/10.1073/pnas.1610438113.

Jansen, M. F., L. P. Nadeau, and T. M. Merlis, 2018: Transient versus Equilibrium Response of the Ocean's Overturning Circulation to Warming. *J. Climate,* **31**, 5147–5163, https://doi.org/10.1175/JCLI-D-17-0797.1.

Jayne, S. R., and J. Marotzke, 2001: The dynamics of ocean heat transport variability. *Rev. Geophys.,* **39,** pp. 385–411.

Jeffreys, H., 1925: On fluid motions produced by differences of temperature and humidity. *Q.J.R. Meteorol. Soc.,* **51**, 347 – 356.

Jeffreys H., 1926: On the dynamics of geostrophic winds. *Quart. J. Roy. Meteor. Soc.*, **51**, pp. 85–104.

Jochum, M., and C. Eden, 2015: The connection between Southern Ocean winds, the Atlantic meridional overturning circulation, and Indo-Pacific upwelling. *J. Climate*, **28**, 9250–9257, https://doi.org/10.1175/JCLI-D-15-0263.1.

Johnson, H. L., and D. P. Marshall, 2002: A theory of the surface Atlantic response to thermohaline variability. *J. Phys. Oceanogr.,* **32,** pp. 1121–1132.

Jouzel J. et al., 2007: Orbital and millennial Antarctic climate variability over the last 800,000 years. *Science,* **317**, pp. 793-796.

Kalnay et al., 1996: The NCEP/NCAR 40-year reanalysis project, *Bull. Amer. Meteor. Soc.*, **77**, 437-470, https://doi.org/10.1175/1520-0477(1996)077<0437:TNYRP>2.0.CO;2.

Kim S.J., Flato G.M. and Boer G.J., 2003: A coupled climate model simulation of the Last Glacial Maximum, part 2: approach to equilibrium. *Climate Dynamics*, **20**, pp. 635–661.

Knox F. and McElroy M., 1984: Changes in atmospheric CO_2: influence of the marine biota at high latitude. *J. Geophys. Res.*, **89**, pp. 4629-4637.

Kobayashi H., Abe-Ouchi A., and Oka A., 2015: Role of Southern Ocean stratification in glacial atmospheric CO_2 reduction evaluated by a three-dimensional ocean general circulation model. *Paleoceanography*, **30**, pp. 1202–1216,

Kohfeld K. E. and Tegen I., 2007: The record of soil dust aerosols and their role in the earth system, in Treatise on Geochemistry Update 1, **4.13**, pp. 1–26.

Kohfeld K.E. and Ridgwell A., 2009: Glacial-interglacial variability in atmospheric CO_2. Surface Ocean-Lower Atmosphere Processes (eds C. L. Quéré and E. S. Saltzman), American Geophysical Union, Washington D.C.

Kohfeld K.E., Graham R.M., de Boer A.M., Sime L.C., Wolff E.W., Quéré C.L. and Bopp L., 2013: Southern Hemisphere westerly wind changes during the Last Glacial Maximum: Paleo-data synthesis. *Quat. Sci. Rev.* **68**, pp. 76–95.

Köhl, A., 2005: Anomalies of meridional overturning: Mechanisms in the North Atlantic. *J. Phys. Oceanogr.*, **35,** pp. 1455–1472.

Köhler P., Fischer H., Munhoven G. and Zeebe R. E., 2005: Quantitative interpretation of atmospheric carbon records over the last glacial termination. *Global Biogeochem. Cycles*, **19**, GB4020.

Koltermann, K.P., V.V. Gouretski and K. Jancke, 2011: Hydrographic Atlas of the World Ocean Circulation Experiment (WOCE). Volume 3: Atlantic Ocean (eds. M. Sparrow, P. Chapman and J. Gould). International WOCE Project Office, Southampton, UK.

Kuhlbrodt, T., A. Griesel, M. Montoya, A. Levermann, M. Hofmann, and S. Rahmstorf, 2007: On the driving processes of the Atlantic meridional overturning circulation. *Rev. Geophys.*, **45**, RG2001, https://doi.org/10.1029/2004RG000166.

Kumar N., Anderson R. F., Mortlock R. A., Froelich P. N., Kubik P., Dittrich-Hannen B. and Suter M., 1995: Increased biological productivity and export production in the glacial Southern Ocean. *Nature*, **378**, pp. 675–680.

Lauderdale, J. M., A. C. N. Garabato, K. I. C. Oliver, M. J. Follows, and R. G. Williams, 2013: Wind-driven changes in Southern Ocean residual circulation, ocean carbon reservoirs and atmospheric CO_2. *Climate Dyn.*, **41**, 2145–2164, https://doi.org/10.1007/s00382-012-1650-3.

Lee, T., D. E. Waliser, J.-L. F. Li, F. W. Landerer, and M. M. Gierach, 2013: Evaluation of CMIP3 and CMIP5 Wind Stress Climatology Using Satellite Measurements and Atmospheric Reanalysis Products. *J. Climate*, **26**, 5810 –5826, https://doi.org/10.1175/JCLI-D-12-00591.1.

Ledwell, J. R., A. J. Watson, and C. S. Law, 1993: Evidence for slow mixing across the pycnocline from an open-ocean tracer release experiment. *Nature*, **364**, 701–703, https://doi.org/10.1038/364701a0.

Levitus, S., and T. P. Boyer, 1994a: World Ocean Atlas 1994 Volume 3: Salinity, Tech. rep., NOAA Atlas NESDIS 3.

Levitus, S., and T. P. Boyer, 1994b: World Ocean Atlas 1994 Volume 4: Temperature, Tech. rep., NOAA Atlas NESDIS 4.

Li, C. and A. Born, 2019: Coupled atmosphere-ice-ocean dynamics in Dansgaard-Oeschger events. *Quaternary Science Reviews*, **203**, 1-20.

Lisiecki L. E. and Raymo M. E., 2005: A Pliocene-Pleistocene stack of 57 globally distributed benthic $\delta_{18}O$ records. *Paleoceanography*, **20**, PA1003.

Liu, Z., S. Shin, R. Webb, W. Lewis, and B. Otto-Bliesner, 2005: Atmospheric CO2 forcing on glacial thermohaline circulation and climate. *Geophys. Res. Lett.*, **32**, https://doi.org/ 10.1029/2004GL021929.

Lorenz EN., 1960: Energy and numerical weather prediction. *Tellus*, **12**, 364-373.

Losch, M., D. Menemenlis, J.-M. Campin, P. Heimbach, and C. Hill, 2010: On the formulation of sea-ice models. Part 1: Effects of different solver implementations and parameterizations, *Ocean Modelling*, **33(1-2)**, 129-144, https://doi.org/10.1016/j.ocemod.2009.12.008.

Loulergue, L. et al., 2007: New constraints on the gas age-ice age difference along the EPICA ice cores, 0–50 kyr. *Clim. Past*, **3**, pp. 527–540.

Loutre, M. F., D. Paillard, F. Vimeux, and E. Cortijo, 2004: Does mean annual insolation have the potential to change the climate? *Earth Planet. Sci. Lett.*, **221**, pp. 1-14, https://doi.org/10.1016/S0012-821X(04)00108-6.

Lumpkin, R., and K. Speer, 2007: Global ocean meridional overturning. *J. Phys. Oceanogr.*, **37**, 2550–2562, https://doi.org/10.1175/JPO3130.1.

Lüthi D., Le Floch M., Bereiter B., Blunier T., Barnola J.M., Siegenthaler U., Raynaud D., Jouzel J., Fischer H., Kawamura K. and Stocker T.F., 2008: High-resolution carbon

dioxide concentration record 650,000-800,000 years before present. *Nature*, **453**, pp. 379-382.

Lynch-Stieglitz, J., W. B. Curry, and N. Slowey, 1999: Weaker Gulf Stream in the Florida Straits during the Last Glacial Maximum. *Nature*, **402**, 644–648, https://doi.org/10.1038/45204.

Marchal O. et al., 1998a: A latitude-depth circulation-biogeochemical ocean model for paleoclimate studies. *Tellus*, **B50**, pp. 290–316.

Marchitto T., Lynch-Stieglitz J. and Hemming S. R., 2005: Deep Pacific $CaCO_3$ compensation and glacial-interglacial atmospheric CO_2. *Earth and Planetary Science Letters*, **231**, pp. 317-336.

Marotzke, J., 1997: Boundary mixing and the dynamics of the three-dimensional thermohaline circulation. *J. Phys. Oceanogr.*, **27**, 1713 – 1728, https://doi.org/10.1175/1520-0485(1997)027<1713:BMATDO>2.0.CO;2.

Marshall J. and Radko T., 2003: Residual mean solutions for the Antarctic Circumpolar Current and its associated overturning circulation. *J. Phys. Oceanogr.*, **33,** pp. 2341–2354.

Marshall J. and Radko T., 2006: A model of the upper branch of the meridional overturning of the Southern Ocean. *Prog. Oceanogr.*, **70,** pp. 331–345.

Marshall, J. and K. Speer, 2012: Closure of the meridional overturning circulation through Southern Ocean upwelling. *Nat. Geosci.*, **5**, 171–80, https://doi.org/10.1038/ngeo1391.

Marshall, J., A. Adcroft, C. Hill, L. Perelman, and C. Heisey, 1997a: A finite-volume, incompressible Navier Stokes model for studies of the ocean on parallel computers. *J. Geophysical Res.*, **102(C3)**, 5753-5766, https://doi.org/10.1029/96JC02775.

Marshall, J., C. Hill, L. Perelman, and A. Adcroft, 1997b: Hydrostatic, quasi-hydrostatic, and nonhydrostatic ocean modelling. *J. Geophysical Res.*, **102(C3)**, 5733-5752, https://doi.org/10.1029/96JC02776.

Marshall, J. and T. Radko, 2003: Residual mean solutions for the Antarctic Circumpolar Current and its associated overturning circulation. *J. Phys. Oceanogr.*, **33,** 2341–2354, https://doi.org/10.1175/1520-0485(2003)033<2341:RSFTAC>2.0.CO;2.

Marotzke, J., S. A. Cunningham, and H. L. Bryden, 2002: Monitoring the Atlantic Meridional Overturning Circulation at 26.5°N (Southampton Oceanography Centre, Southampton, U.K).

Martin, J. H., G. A. Knauer, D. M. Karl, and W. W. Broenkow, 1987: VERTEX: Carbon cycling in the northeast Pacific. *Deep Sea Res.*, **34**, 267-285.

Martin, J. H., R. M. Gordon, S. Fitzwater, and W. W. Broenkow, 1989: VERTEX: Phytoplankton/iron studies in the Gulf of Alaska, Deep-Sea Res., **36**, 649-680.

Martin J.H., 1990: Glacial-interglacial CO_2 change: The iron hypothesis. *Paleoceanography*, **5**, pp. 1-13.

Martin J.H. et al., 1991: Testing the iron hypothesis in ecosystems of the equatorial Pacific Ocean. *Nature*, **371**, pp. 123-129.

Mashayek A., Ferrari R., Nikurashin M. and Peltier W. R., 2015: Influence of enhanced abyssal diapycnal mixing on the ocean stratification and overturning circulation. *J. Phys. Oceanogr.*, **45**, pp. 2580–2597.

Masson-Delmotte V. et al., 2006: Past and future polar amplification of climate change: Climate model intercomparisons and ice-core constraints. *Clim. Dyn.*, **26**, pp. 513 – 529.

McGehee, R. and Lehman C., 2012: A paleoclimate model of ice-albedo feedback forced by variations in Earth's orbit. *SIAM Journal on Applied Dynamical Systems*, **11**, pp. 684-707.

McManus, J., R. Francois, J. M. Gherardi, L. Keigwin, and S. Brown-Leger, 2004: Collapse and rapid resumption of Atlantic meridional circulation linked to deglacial climate changes. *Nature*, **428**, 834–837, https://doi.org/10.1038/nature02494.

Mignot, J., A. Levermann, and A. Griesel, 2006: A decomposition of the Atlantic meridional overturning circulation into physical components using its sensitivity to vertical mixing. *J. Phys. Oceanogr.*, **36**, 636–650, https://doi.org/10.1175/JPO2891.1.

Mikolajewicz, U. and E. Maier-Reimer, 1994: Mixed boundary conditions in ocean general circulation models and their influence on the stability of the model's conveyor belt. *J. Geophys. Res.*, **99**, 22633–22644, https://doi.org/10.1029/94JC01989.

Milankovitch M., 1941: Kanon der Erdbestrahlung und seine Andwendung auf das Eiszeiten-problem. Royal Serbian Academy, Belgrade.

Monnin E., Indermühle A., Dällenbach A., Flückiger J., Stauffer B., Stocker T.F., Raynaud D., Barnola J.M., 2001: Atmospheric CO_2 concentrations over the last glacial termination. *Science*, **291**, pp. 112-114.

Mooney H., Roy J. and Saugier B., 2001: Terrestrial Global Productivity: Past, Present and Future. Academic Press, San Diego.

Munday, D., H. Johnson, and D. Marshall, 2013: Eddy saturation of equilibrated circumpolar currents. *J. Phys. Oceanogr.*, **43**, 507–532, https://doi.org/10.1175/JPO-D-12-095.1.

Munk, W., 1966: Abyssal recipes. *Deep-Sea Res.*, **13**, 707–730, https://doi.org/10.1016/0011-7471(66)90602-4.

Munk, W., and C. Wunsch, 1998: Abyssal recipes II: Energetics of tidal and wind mixing. *Deep Sea Res.*, Part I, **45**, 1977–2010, https://doi.org/10.1016/S0967-0637(98)00070-3.

Nadeau, L.-P., R. Ferrari & M. F. Jansen, 2019: Antarctic sea ice control on the depth of North Atlantic Deep Water. *J. Clim.*, **32**, 2537–2551, https://doi.org/10.1175/JCLI-D-18-0519.1.

Najjar, R. G. and J. C. Orr, 1998: Design of OCMIP-2 simulations of chlorofluorocarbons, the solubility pump and common biogeochemistry, 19 pp, http://www.cgd.ucar.edu/oce/OCMIP/design.pdf.

Nikurashin, M., and R. Ferrari, 2010: Radiation and dissipation of internal waves generated by geostrophic motions impinging on small-scale topography: Theory. *J. Phys. Oceanogr.*, **40**, 1055–1074, https://doi.org/10.1175/2009JPO4199.1.

Nikurashin, M., and G. Vallis, 2011: A theory of deep stratification and overturning circulation in the ocean. *J. Phys. Oceanogr.*, **41**, 485–502, https://doi.org/10.1175/2010JPO4529.1.

Nikurashin, M., and G. Vallis, 2012: A theory of the interhemispheric meridional overturning circulation and associated stratification. *J. Phys. Oceanogr.*, **42**, 1652–1667, https://doi.org/10.1175/JPO-D-11-0189.1.

North G.R. and Coakley J.A. Jr, 1979: Differences between seasonal and mean annual energy balance model calculations of climate and climate sensitivity. *J Atmos Sci*, **36**, 1189–1204.

Oka, A., H. Hasumi, and A. Abe-Ouchi, 2012: The thermal threshold of the Atlantic meridional overturning circulation and its control by wind stress forcing during glacial climate. *Geophys. Res. Lett.*, **39**, L09709, https://doi.org/10.1029/2012GL051421.

Oppo D.W. and Lehman S.J., 1993: Mid-depth circulation of the subpolar North Atlantic during the last glacial maximum. *Science*, **259**, pp. 1148 – 1152.

Otto-Bliesner B. et al., 2006: Last Glacial maximum and Holocene climate in CCSM3. *Journal of Climate*, **19**, pp. 2526–2544.

Otto-Bliesner B. L., Hewitt C., Marchitto T., Brady E., Abe-Ouchi A., Crucifix M., Murakami S., and Weber S., 2007: Last Glacial Maximum ocean thermohaline circulation: PMIP2 model intercomparisons and data constraints. *Geophys. Res. Lett.*, **34**, L12706.

Palmer, T. and P. Williams (Eds), 2010: Stochastic Physics and Climate Modelling, Cambridge University Press, Cambridge, UK.

Parekh, P., M. J. Follows, and E. Boyle, 2005: Decoupling of iron and phosphate in the global ocean, *Global Biogeochem. Cycles*, **19**, https://doi.org/10.1029/2004GB002280.

Paulson, C. A., and J. J. Simpson, 1977: Irradiance measurements in the upper ocean. *J. Phys. Oceanogr.*, **7**, 953–956, https://doi.org/10.1175/1520-0485(1977)007%3C0952:IMITUO%3E2.0.CO;2.

Pausata, F. S. R., C. Li, J. J. Wettstein, M. Kageyama, and K. H. Nisancioglu, 2011: The key role of topography in altering North Atlantic atmospheric circulation during the last glacial period. *Clim. Past*, **7**, pp. 1089-1101, https://doi.org/10.5194/cp-7-1089-2011.

Peltier, W. R., 2004: Global glacial isostasy and the surface of the ice-age Earth: The ICE-5G (VM2) model and GRACE, *Annu. Rev. Earth Planet. Sci.*, **32**, pp. 111–149, doi:10.1146/annurev.earth.32.082503.144359.

Peng, T.-H., and W. S. Broecker, 1987: C/P ratios in marine detritus. *Global Biogeochem. Cycles*, **I**, 155-161.

Petit J. R., Jouzel J., Raynaud D. et al., 1999: Climate and atmospheric history of the past 420,000 years from the Vostok ice core, Antarctica. *Nature*, **399**, pp. 429-436.

Pisias N. and Moore T., 1981: The evolution of Pleistocene climate: A time series approach. *Earth Planet. Sci. Lett.*, **52**, pp. 450 – 458.

Prentice I.C., Heimann M. and Sitch S., 2000: The carbon balance of the terrestrial biosphere: Ecosystem models and atmospheric observations. *Ecological Applications*, **10**, pp. 1553-1573.

Pride C. et al., 1999: Nitrogen isotopic variations in the Gulf of California since the last deglaciation: Response to global climate change. *Paleoceanography*, **14**, pp. 397-409.

Raven J. A. and Falkowski P. G., 1999: Oceanic sinks for atmospheric CO2. *Plant Cell Environ*,. **22**, pp. 741-755.

Raymo M. E. and Nisancioglu K., 2003: The 41 kyr world: Milankovitch's other unsolved mystery. *Paleoceanography*, **18**, 1011.

Rea D. K., 1994: The paleoclimatic record provided by eolian deposition in the deep sea: The geologic history of wind. *Rev. Geophys.*, **32**, pp. 159–195.

Redfield A. C., 1934: On the proportions of organic derivations in sea water and their relation to the composition of plankton. James Johnstone Memorial Volume, pp. 177–192.

Redfield A. C., Ketchum B. H. and Richards F. A., 1963: The influence of organisms on the composition of seawater. The Sea (ed. Hill M. N.), **2**, Interscience, New York, pp. 26-77.

Redi, M. H., 1982: Oceanic isopycnal mixing by coordinate rotation. *Journal of Physical Oceanography*, **12**, 1154-1158, https://doi.org/10.1175/1520-0485(1982)012<1154:OIMBCR>2.0.CO;2.

Richardson, P. L., 2008: On the history of meridional overturning circulation schematic diagrams. *Prog. Oceanogra.* **76**, 466–486, https://doi.org/10.1016/j.pocean.2008.01.005.

Rojas M. et al., 2009: The southern westerlies during the Last Glacial Maximum in PMIP2 simulations. *Climate Dynamics*, **32**, pp. 525–548.

Rooth C.G.H. and Östlund H.G., 1972: Penetration of tritium into the Atlantic thermocline. *Deep Sea Res.*, **19**, pp. 481-492.

Röthlisberger R., Bigler M., Wolff E.W., Joos F., Monnin E., and Hutterli M. A., 2004: Ice core evidence for the extent of past atmospheric CO2 change due to iron fertilisation. *Geophys. Res. Lett.*, **31**, L16207.

Ruttenberg K. C., 1993: Reassessment of the oceanic residence time of phosphorous. *Chem. Geol.*, **107**, pp. 405- 409.

Saltzman J., Wishner K. F., 1997: Zooplankton ecology in the eastern tropical Pacific oxygen minimum zone above a seamount: 2. vertical distribution of copepods. *Deep Sea Res. I*, **44**, 931–954.

Sandström J. W., 1916: Meteorologische Studien im Schwedischen Hochgebirge, Göteborgs K. Vetensk. *Vitterhetssamhällets Handkl.*, **27**.

Sarmiento J. L. and Toggweiler J. R.,1984: A new model for the role of the oceans in determining atmospheric pCO2 . *Nature*, **308**, pp. 621-624.

Schmittner A., Galbraith E. D., Hostetler S. W., Pedersen T. F., and Zhang R., 2007: Large fluctuations of dissolved oxygen in the Indian and Pacific oceans during Dansgaard-Oeschger oscillations caused by variations of North Atlantic Deep Water subduction. *Paleoceanography*, **22**.

Schmitz Jr., W.J., 1995: Interbasin Thermohaline Exchange. *Rev. Geophys.* **32**, 151—173, https://doi.org/10.1029/95RG00879.

Sellers W. D., 1969: A global climatic model based on the energy balance of the earth-atmosphere system. *Journal of Applied Meteorology*, **8**, 392– 400.

Shackleton N. J. and Hall M., 1984: Oxygen and carbon isotope stratigraphy of Deep-Sea Drilling Project hole 552a: Plio-Pleistocene glacial history, Initial Rep. Deep Sea Drill. Proj., **81**, pp. 599 – 609.

Shakespeare, C. J. and A. M. Hogg, 2012: An analytical model of the response of the meridional overturning circulation to changes in wind and buoyancy forcing. *J. Phys. Oceanogr.*, **42**, 1270-1287, https://doi.org/10.1175/JPO-D-11-0198.1.

Shin, S.-I., Z. Liu, B. L. Otto-Bliesner, J. E. Kutzbach, and S. J. Vavrus, 2003: Southern Ocean sea-ice control of the glacial North Atlantic thermohaline circulation. *Geophys. Res. Lett.*, **30**, 1096, https://doi.org/10.1029/2002GL015513.

Siegenthaler U. and Wenk T.,1984: Rapid atmospheric CO2 variations and ocean circulation. *Nature* **308**, pp. 624-626.

Sigman D. M., McCorkle D. C. and Martin W. R., 1998: The calcite lysocline as a constraint on glacial/ interglacial low-latitude production changes. *Glob. Biogeochem. Cycles*, **12**, pp. 409-427.

Sigman D. M. and Boyle E. A., 2000: Glacial/interglacial variations in atmospheric carbon dioxide. *Nature*, **407**, pp. 859–869.

Sigman D.M., Hain M.P., and Haug G.H., 2010: The polar ocean and glacial cycles in atmospheric CO_2 concentration. *Nature*, **466**, pp. 47-55.

Stephens B. B. and Keeling R. F., 2000: The influence of Antarctic sea ice on glacial-interglacial CO_2 variations. *Nature*, **404**, pp. 171–174.

Sun, S., I. Eisenman, and A. L. Stewart, 2016: The influence of Southern Ocean surface buoyancy forcing on glacial-interglacial changes in the global deep ocean stratification. *Geophys. Res. Lett.*, **43**, 8124–8132, https://doi.org/10.1002/2016GL070058.

Takahashi, T., W. S. Broecker, and S. Langer, 1985: Redfield ratio based on chemical data from isopycnal surfaces. *J. Geophys. Res.*, **90**, 6907- 6924.

Talley, L. D., 2013: Closure of the global overturning circulation through the Indian, Pacific, and Southern Oceans: Schematics and transports. *Oceanography*, **26**, 80–97, https://doi.org/10.5670/oceanog.2013.07.

Thompson, A. F., A. Stewart, and T. Bischoff, 2016: A multibasin residual-mean model for the global overturning circulation. *J. Phys. Oceanogr.* **46**, 2583–604, https://doi.org/10.1175/JPO-D-15-0204.1.

Timmermann, A., and H. Goosse, 2004: Is the wind stress forcing essential for the meridional overturning circulation? *Geophys. Res. Lett.*, **31**, L04303, https://doi.org/10.1029/2003GL018777.

Toggweiler J. R. and Sarmiento J. L., 1985: Glacial to interglacial changes in atmospheric carbon dioxide: The critical role of ocean surface water in high latitudes, in The Carbon Cycle and Atmospheric $C0_2$: Natural Variations Archean to Present. Geophys. Monogr. Ser., **32**, pp. 163-184.

Toggweiler, J. R., and B. Samuels, 1993: New radiocarbon constraints on the upwelling of abyssal water to the ocean's surface. *The Global Carbon Cycle*, **15**, 334–366, https://doi.org/10.1007/978-3-642-84608-3_14.

Toggweiler J. R., and B. Samuels, 1995: Effect of Drake Passage on the global thermohaline circulation. *Deep-Sea Res.*, **42**, 447–500, https://doi.org/10.1016/0967-0637(95)00012-U.

Toggweiler J.R. and Samuels B., 1998: On the ocean's large scale circulation in the limit on no vertical mixing. *J. Phys. Oceanogr.*, **28**, pp. 1832–1852.

Toggweiler J.R., 1999: Variation of atmospheric CO_2 by ventilation of the ocean's deepest water. *Paleoceanography*, **14**, pp. 571 – 588.

Toggweiler, J. R., J. L. Russell, and S. R. Carson, 2006: Midlatitude westerlies, atmospheric CO_2, and climate change during the ice ages. *Paleoceanography*, **21**, https://doi.org/10.1029/2005PA001154.

Toole, J. M., K. L. Polzin, and R. W. Schmitt, 1994: Estimates of diapycnal mixing in the abyssal ocean. Science, **264**, 1120– 1123, https://doi.org/10.1126/science.264.5162.1120.

K.E. Trenberth, L. Smith, 2005: The mass of the atmosphere: a constraint on global analyses. *J. Climate*, **18**, 864-875.

Tyrrel T., 1999: The relative influences of nitrogen and phosphorus on oceanic primary production. *Nature*, **400**, pp. 525-531.

Vallis, G. K., 2000: Large-scale circulation and production of stratification: Effects of wind, geometry, and diffusion. *Journal of Physical Oceanography*, **30**, 933-954, https://doi.org/10.1175/1520-0485(2000)030<0933:LSCAPO>2.0.CO;2.

Vallis, G. K., 2017: *Atmospheric and Oceanic Fluid Dynamics*, Cambridge Univ. Press, 946pp., https://doi.org/10.1017/9781107588417.

Volk, T., and M. I. Hoffert, 1985: Ocean carbon pumps: Analysis of relative strengths and efficiencies in ocean-driven atmospheric CO2 changes, in *The Carbon cycle and atmospheric CO2: Natural variations Archean to present*, edited by T. Sundquist and W. Broecker, *Geophysical monograph series*, **32**, pp. 99-110, American Geophysical Union, Washington, D.C.

Wang, W., and R. X. Huang, 2005: An experimental study on thermal circulation driven by horizontal differential heating. *J. Fluid Mech.*, **540**, 49–73, https://doi.org/10.1017/S002211200500577X.

Watson A. J., Bakker D. C. E., Ridgwell A. J., Boyd P. W. and Law C. S., 2000: Effect of iron supply on Southern Ocean CO_2 uptake and implications for glacial atmospheric CO_2. *Nature*, **407**, pp. 730-733.

Watson, A. J., and A. C. Naveria Garabato, 2006: The role of Southern Ocean mixing and upwelling in glacial–interglacial atmospheric CO2 change. *Tellus B,* **58**, 73–87, https://doi.org/10.1111/j.1600-0889.2005.00167.x.

Watson, A. J., G. K. Vallis, and M. Nikurashin, 2015: Southern Ocean buoyancy forcing of ocean ventilation and glacial atmospheric CO_2. *Nat. Geosci.*, **8**, 861–864, https://doi.org/10.1038/ngeo2538.

WBGU, (Wissenschaftlicher Beirat der Bundesregierung Globale Umweltveränerungen), 1988. Die Anrechnung biolischer Quellen und Senken in Kyoto-Protokoll: Fortschritt oder Rückschlang für den globalen Umweltschutz Sondergutachten.

Weber S. L., Drijfhout S. S., Abe-Ouchi A., Crucifix M., Eby M., Ganopolski A., Murakami S., Otto-Bliesner B. and Peltier W. R., 2007: The modern and glacial overturning circulation in the Atlantic ocean in PMIP coupled model simulations. *Climate of the Past*, **3**, pp. 51-64.

Willebrand, J., G. H. Philander, and R. C. Pacanowski, 1980: The oceanic response to large-scale atmospheric disturbances. *J. Phys. Oceanogr.*, **10,** 411–429.

William A. Gough & Tatiana Allakhverdova, 1998: Sensitivity of a coarse resolution ocean general circulation model under climate change forcing. *Tellus A: Dynamic Meteorology and Oceanography*, **50**, 124-133.

Williams R.G. and Follows M.J., 2011: Ocean Dynamics and the Carbon Cycle: Principles and Mechanisms. Cambridge University Press.

Wolfe, C. L., and P. Cessi, 2009: Overturning circulation in an eddy-resolving model: The effect of the pole-to-pole temperature gradient. *J. Phys. Oceanogr.*, **39**, 125–142, https://doi.org/10.1175/2008JPO3991.1.

Wolfe C.L. and P. Cessi: 2010: What sets the strength of the middepth stratification and overturning circulation in eddying ocean models? *J. Phys. Oceanogr.*, **40**, 1520–38, https://doi.org/10.1175/2010JPO4393.1.

Wolfe, C. L., and P. Cessi, 2011: The adiabatic pole-to-pole overturning circulation. *J. Phys. Oceanogr.*, **41**, 1795–1810, https://doi.org/10.1175/2011JPO4570.1.

Wolfe, C.L. and Cessi P., 2014: Salt feedback in the adiabatic overturning circulation. *Journal of Physical Oceanography*, **44**, pp.1175-1194, https://doi.org/10.1175/jpo-d-13-0154.1

Wunsch, C., 2003: Determining paleoceanographic circulations, with emphasis on the Last Glacial Maximum. *Quat. Sci. Rev.*, **22**, 371–385, https://doi.org/10.1016/S0277-3791(02)00177-4.

Wunsch C., 2003(1): The spectral description of climate change including the 100ky energy. *Clim. Dyn.*, **20**, pp. 353–363.

Wunsch, C., and R. Ferrari, 2004: Vertical mixing, energy, and the general circulation of the oceans. *Annu. Rev. Fluid Mech.*, **36**, 281–314, https://doi.org/10.1146/annurev.fluid.36.050802.122121.

Wyrwoll K., Dong B. and Valdes P., 2000: On the position of Southern Hemisphere westerlies at the Last Glacial Maximum: an outline of AGCM simulation results and evaluation of their implications *Quaternary Science Reviews*, **19**, pp. 881–898.

Zeebe R. E. and Wolf-Gladrow, 2001: CO_2 in Seawater: Equilibrium, Kinetics, Isotopes. Elsevier Oceanography Series, **65**, pp. 346.

Yamanaka, Y. and E. Tajika, 1997: Role of dissolved organic matter in the marine biogeochemical cycle: studies using an ocean biogeochemical general circulation model. *Global Biogeochem. Cycles*, **11**, 599-612.

Zhang, J., and Hibler, III, W. D., 1997: On an efficient numerical method for modeling sea ice dynamics. *J. Geophys. Res.*, **102(C4)**, 8691-8702, https://doi.org/10.1029/96JC03744.

Zhang, J., R. Schmitt, and R. Huang, 1999: The relative influence of diapycnal mixing and hydrologic forcing on the stability of the thermohaline circulation. *J. Phys. Oceanogr.*, **29**, 1096–1108, https://doi.org/10.1175/1520-0485(1999)029<1096:TRIODM>2.0.CO;2.